The Convergence of Heat, Groundwater & Fracture Permeability:

Innovative Play Fairway Modelling Applied to the Tularosa Basin

DOE Award #DE-EE0006730

■ FINAL PROJECT REPORT ■

October 20, 2020

Submitted By:

Ruby Mountain Inc.

Salt Lake City ■ El Paso ■ Seattle ■ Newport Beach

and

EGI Energy & Geoscience Institute AT THE UNIVERSITY OF UTAH

TABLE OF CONTENTS

This material is based upon work supported by the Department of Energy, Office of Energy Efficiency and Renewable Energy (EERE), under Geothermal Technologies Office Award Number DE-EE0006730.

The Convergence of Heat, Groundwater & Fracture Permeability: **Innovative Play Fairway Modelling Applied to the Tularosa Basin**

■ PHASE 1 PROJECT REPORT ■

This report summarizes the activities and key findings of the project team occurring during Phase 1 (August 2014 – October 2015) of the Tularosa Basin Geothermal Play Fairway Analysis Project.

Questions regarding the contents of this document should be directed to:
RMI Senior Project Manager Carlon R. Bennett at carlonbennett@gmail.com

Submitted By:

Ruby Mountain Inc.

Carlon R. Bennett, Project Manager
2373 East 1300 South, Salt Lake City, UT 84108
801-538-5003 ● rubymountaininc.com

And

EGI Energy & Geoscience Institute
AT THE UNIVERSITY OF UTAH

Gregory D. Nash, Ph.D. Principal Investigator
423 Wakara Way #300, Salt Lake City, UT 84108
801-581-5126 ● egi.utah.edu

TABLE OF CONTENTS

■ ACKNOWLEDGEMENTS

Ruby Mountain Inc. and EGI wish to thank the following individuals and organizations for their cooperation, support and assistance throughout the implementation of Phase 1 of this project:

- U.S. Department of Energy (DOE) for its financial support, oversight, and guidance through Contract # DE-EE0006730;
- U.S. DOE Geothermal Technologies Office (GTO) & Staff - Eric Haas, Director;
- Fort Bliss Directorate of Public Works (DPW) & Staff - Alfredo Riera, Director;
- Fort Bliss Directorate of Public Works (DPW) - B. J. Tomlinson, Chief, Sustainability & Energy Division;
- Fort Bliss Directorate of Public Works - Environmental Division (DPW-E) Staff;
- Fort Bliss Office of the Staff Judge Advocate;
- White Sands Missile Range – Samuel O. Sanchez, April E. Banks & Craig Collins;
- El Paso Water Utilities - Alfredo Ruiz, Associate Hydrogeologist;
- University of Texas at El Paso - Diane Doser, UTEP Department of Geologic Sciences;
- New Mexico Environment Department - Water Quality Bureau;
- Fort Bliss Water;
- City of Alamogordo Water Utilities;
- New Mexico Office of the State Engineer – District IV;
- Alamogordo Public Schools;
- Michael Hillesheim, Sr. Systems Engineer - National Renewable Energy Laboratory; and,
- Mr. Dennis Wike, in his capacity as a civilian contractor to Fort Bliss DPW.

■ PROJECT TEAM

Mike Weathers, DOE Golden Field Office Contract Manager

Ruby Mountain Inc.

- Carlon R. Bennett, Project Manager
- Jon Lear, RMI Principal
- Phil L. Jones, Project Administrative & Research Assistant
- Dan Lear, Staff Attorney
- Brigitte Swanson, Consultant

Energy & Geoscience Institute at the University of Utah

- Gregory Nash, Ph.D., Project Principal Investigator
- Joseph Moore, Ph.D., Research Professor
- Stuart Simmons, Ph.D. Research Professor
- Rasoul B. Sorkhabi , Ph.D., Research Professor
- Adam Brandt, Student Research Assistant
- Nancy Taylor, Assistant Business Manager
- Benjamin Barker, Ph.D., Consultant

EXECUTIVE SUMMARY

The Convergence of Heat, Groundwater & Fracture Permeability: Innovative Play Fairway Modelling Applied to the Tularosa Basin

The Tularosa Basin Play Fairway Analysis (PFA) project tested two distinct geothermal exploration methodologies covering the entire basin within South Central New Mexico and Far West Texas. Throughout the initial phase of the project, the underexplored basin proved to be a challenging, yet ideal test bed to evaluate effectiveness of the team's data collection techniques as well as the effectiveness of our innovative PFA.

Phase 1 of the effort employed a low-cost, pragmatic approach using two methods to identify potential geothermal plays within the study area and then compared and contrasted the results of each method to rank and evaluate potential plays. Both methods appear to be very effective and highly transferable to other areas.

The first method was a deterministic approach developed by the petroleum industry and the second a stochastic method (weights of evidence) that has been used for mineral exploration and which has seen some use in geothermal exploration. To support PFA, an exhaustive data collection was undertaken to stock a geographic information system (GIS) with geospatial data to support the development of evidential layers representing heat of the earth, fracture permeability, and ground water for the transfer of heat. Data was also added to support future marketing.

Data for PFA would ideally be evenly spaced and contiguous throughout the study area. However, a significant and technically sufficient dataset was created covering large parts of the study area.

The deterministic petroleum industry PFA was modified for geothermal use and it identified eight plays, including a known geothermal resource at McGregor Range. Certainty was also assessed deterministically based upon the spatial distribution and correlation of input data representing heat.

The weights of evidence (WoE) PFA required training data representing known geothermal systems and hot springs. A paucity of sites within the study area led to the use of training sites elsewhere in New Mexico, Utah, and Nevada. WoE statistically evaluates the relationships of the input data with the training sites, calculates weights for each dataset, and produces a posterior probability raster surface (PFA model) and supporting statistics. This PFA identified ten plays, six of which were also identified using the aforementioned deterministic method, including the known resource at McGregor Range. WoE analysis also produces a confidence map which showed the plays area being relatively high confidence. However, data constrained within the study area was examined using probability kriging to create an additional certainty layer which was more conservative.

Considering the proximity to control data and certainty analyses, four of the twelve identified plays were considered to be from medium to high priority. The remaining plays lack certainty primarily due to a lack of certain evidential data at these locations.

Support work was also done to help better understand the geology of the region and to aid in marketing. This included:

- Economic analysis of the higher priority plays;

- Basement structure analysis;
- Strain surrogate (Z/R ratio) calculations;
- Geochemistry;
- Surface thermal anomaly mapping;
- Hydrothermal alteration mapping; and,
- Mineralogy mapping to map brittle v non-brittle rock (future EGS support).

Phase 1 of this study has not only exponentially increased the level of understanding of the basin from a geothermal resource perspective, but could very well lay the groundwork for a clean energy future in the region. Several distinct potential markets for geothermal energy exist within the Tularosa Basin, including three of our nation's premier military installations (Fort Bliss, White Sands Missile Range and Holloman Air Force Base) as well as the El Paso, Texas metropolitan area (home to over two million people).

In large part, the PFA team developed the project due to the potential marketability of geothermal power to these distinct areas. As an example, due to the vastness of both Fort Bliss and White Sands, both installations require power in numerous remote training locations and currently purchase power from major utilities in Texas and New Mexico, and also from several different small electric cooperatives. The power purchased in these remote areas can sometimes be costly (up to 17-21 cents per kWh in some instances) and on occasion is subject to frequent interruption.

DOE funding for this project facilitated the identification of geothermal resources for the first time on a Tularosa Basin-wide scale bringing a substantial amount of disparate data into a common database for analysis. The project team believes that this study could have a significant impact toward reducing geothermal exploration costs, and by doing so, lead to the development of new geothermal resources.

The project team, led by Ruby Mountain Inc. and The Energy and Geoscience Institute at the University of Utah, had no significant departure from stated goals or methods and brought Phase 1 to a successful conclusion on budget and on time while substantially exceeding cost sharing targets.

SECTION 1: INTRODUCTION

1.1 Geothermal Play Fairway Analysis (PFA) For Risk Reduction

Play fairway analysis (PFA) was developed by the petroleum industry to reduce risk over basin-wide areas by identifying small areas that meet play criteria (Fraser, 2001). PFA has already crossed-over into the geothermal arena, although prior to this DOE GTO initiative it had not been widely applied.

There are two basic model types of geothermal PFA: (1) knowledge-based (deterministic), where genetic geothermal data are considered through direct spatial correlation and (2) data driven, often stochastic, statistical models where data from training sites provide evidence to support probability calculations.
Nash et al. (1996) reported results of an early DOE supported effort, covering part of Nevada, where limited data was used in a knowledge-based model based upon genetic relationships of the input data to known geothermal occurrences within the study area. Coolbaugh (2003) used a greatly expanded GIS database, including numerous training sites, for weights of evidence (WoE) and density function calculations coupled with weighted fuzzy modelling, for models covering the Great Basin. Sabin et al. (2004) discuss the merits of geothermal Occurrence Models based on co-occurrence of geothermal associated phenomena and using these to identify other localities with similar co-occurrences. Younes et al. (2007, 2007) discuss the use of feature distances from producing geothermal wells as evidence and integrate these into a knowledge-based weighted-sum model, which yielded 97% accuracy based upon the prediction of known occurrences in kita and Iwate prefectures, Japan.

Fry analysis, spatial association analysis, and evidential belief functions were applied for geothermal modeling in West Java, Indonesia by Carranza et al, 2008. In this study 127 training sites were used. A similar study was carried out by Moghaddam et al. (2013) for Akita and Iwate, where numerous training sites were required. Hossein et al (2007, 2010), applied a knowledge-based method, using Boolean logic on vector evidence layers, to create a geothermal model for Iran, where layers were combined using Intersect and Union techniques in ArcGIS.

All models rely on the spatial correlation of data known to be directly associated with geothermal systems. The chief strength of statistical models is that they are not biased by the user and that probabilities may be derived. However, the results are sometimes not trusted by explorationists, decision makers, and investors. Additionally, statistical models require significant amounts of training data from known geothermal systems or hot springs, which can be limited. The chief strength of knowledge-based modelling is that training sites/data are not required because they rely on the knowledge of experienced explorationists. In frontier areas, with few if any training sites, this type of model would be the practical choice. Additionally, this type of model is more easily understood by decision makers and investors and the contribution of each factor is easily extracted. Finally, there is currently no evidence that knowledge-based or statistical models are superior.

PFA can lead to the discovery of new geothermal resources by reducing large formidable regions to smaller more focused areas for exploration. This reduces risk and up-front expenses. Both of the PFA methods used in the project have excellent potential for application, not only in the Tularosa Basin but in other areas as well – a very important consideration for the cost effective identification and development of geothermal resources across the entire United States.

1.2 Tularosa Basin Project Objectives

The overriding objectives of this project are to: (1) develop a knowledge-based PFA applying petroleum industry logic; (2) develop a stochastic WoE model; and, (3) compare and contrast the results. Additional objectives include economic modeling for the highest priority identified plays and development of a GIS database to support the project and marketing with the final future objective of power production.

1.3 Overview of Study Area

The Tularosa Basin is a graben located in the southern Rio Grande Rift (Fig. 1). The study area covers approximately 6500 km^2, much of which is underexplored. Several factors went into the selection of the Tularosa Basin. It was primarily chosen because it is a challenging, yet ideal test bed to evaluate effectiveness of PFA.

Additionally, Tularosa Basin is home to several military installations including White Sands Missile Range and Fort Bliss, which are the first and second largest U.S. Army bases in the United States, together covering more than 10,000 km^2 of southeastern New Mexico. The much smaller Holloman Air Force Base also lies within the study area. Geothermal development in this area could help the military achieve its Net Zero Energy goals.

1.4 Study Area Characteristics

The Tularosa Basin study area has a complex tectonic history beginning with Paleozoic siliciclastic sedimentation on a once low-lying shelf of the North American Craton. This was followed by periods of crustal shortening, including Late Paleozoic deformation related to Ancestral Rocky Mountains uplift and the Late Cretaceous Laramide Orogeny. The current landscape has been shaped by extensional tectonics, with the resultant development of the Rio Grande Rift. Extension began in the Late Paleogene and is accompanied by high heat flow. However, seismic activity is infrequent, relative to that in the Great Basin to the northwest, indicating that extension may be slowing in this area.

Figure 1. Tularosa Basin study area, about half of which is military lands.

Historical earthquakes in the area are, in general, clustered in the northern part of the basin, suggesting that the basin opened on the southern end and active rifting is now focused in the northern reaches (Fig. 2).

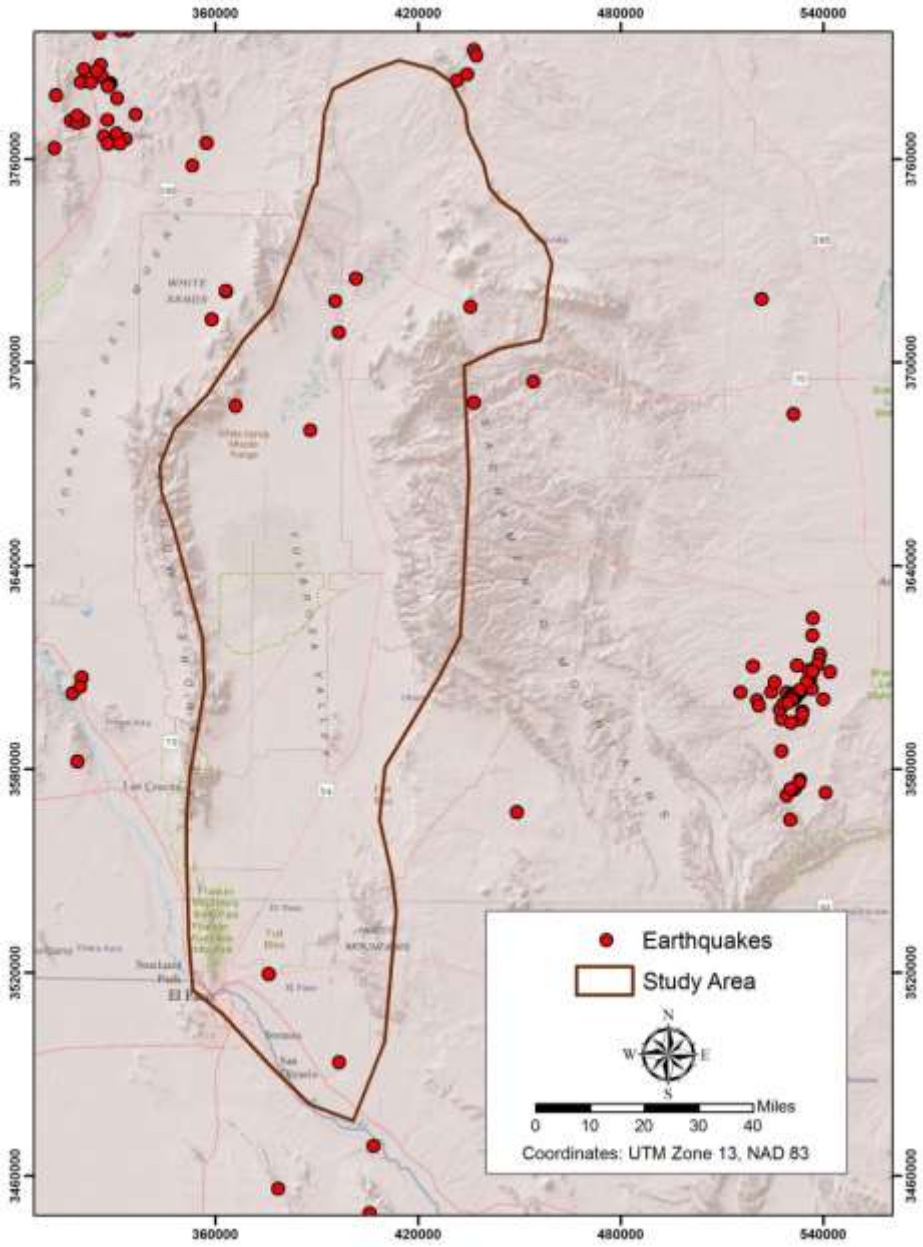

Figure 2. Tularosa Basin earthquakes, which tend to cluster at the north end of the valley, suggesting that active extension is migrating northwardly.

Four slim holes drilled in a 1997 SANDIA sponsored program near Davis Dome, in the southeastern part of the basin (Fig. 3), recorded high temperatures between 170°F and ~190°F (Finger and Jacobson, 1997) suggesting the presence of a promising geothermal system. More recently a study of McGregor Range, Fort Bliss, sponsored by the U.S. Department of Energy Geothermal Technologies

Office and implemented by Ruby Mountain Inc., resulted in the drilling of a new test well, RMI 56-5, again near Davis Dome, that reached a depth of 3,030 feet and encountered a high temperature near 200°F. Initial tests suggest a production rate of 300 gpm (Barker et al, 2015) and water chemistry suggests a reservoir temperature of 235°F (Barker et al., 2014).

The presence of a known geothermal system, Quaternary faults, and relatively high heat flow, suggest that additional geothermal systems may be present in the study area. This, along with military needs for green energy, gave rise to the need of basin-wide PFA to determine if additional promising plays exist.

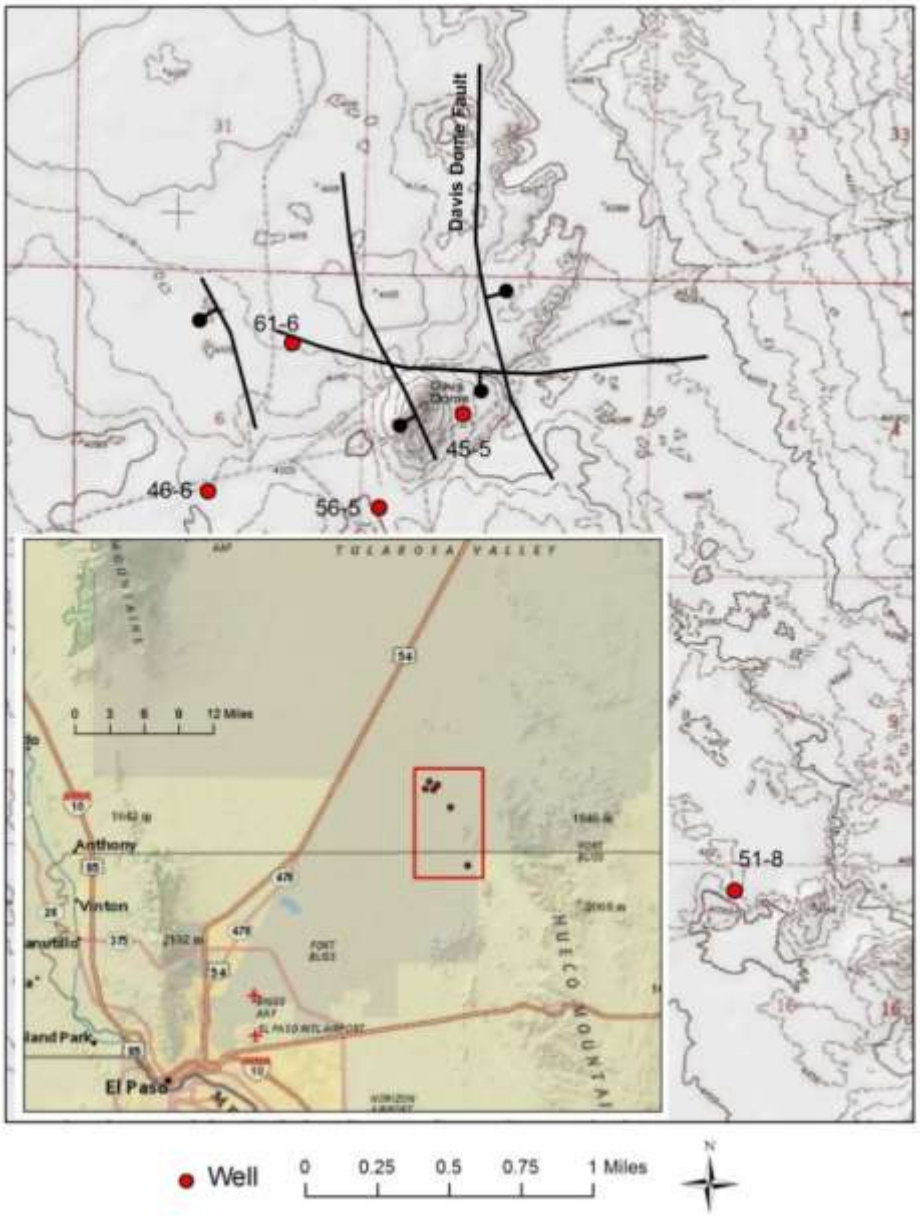

Figure 3. SANDIA slimholes 51-8, 46-6, 61-6, and 45-5 and RMI 56-5.

SECTION 2: DATA ACQUISITION & PROJECT DATABASE

2.1 Data Collection

From the onset of the Tularosa Basin PFA effort, the most daunting challenge was the accumulation of adequate data in the underexplored Tularosa Basin. Lack of credible data in adequate quantity would have posed a barrier to PFA model development. Through a variety of means, the project team was able to collect more data than thought possible at commencement of the effort.

As per DOE guidelines, all datasets used in Phase 1 of this study were derived from existing databases/repositories, previously published literature and existing unpublished data collected from local/regional sources. An exhaustive data collection effort was undertaken to support the development of layers of evidence for heat of the Earth, the presence of ground water for heat transfer, and the presence of faults for fracture permeability.

Operating on the assumption that increased outreach to, and cooperation from, potential stakeholders would lead to greater data collection success, the project team worked with key organizations and military reservations within the project study area to collect data and help facilitate information exchange about the Play Fairway Analysis effort.

Rather than having a single project kickoff meeting with all potential stakeholders invited, the team opted to meet with key stakeholder groups individually to brief them on the PFA concept in general, our project specifically, and to assess their level of interest in geothermal energy development in the area, and obviously to submit formal data requests. Specifically the following actions were undertaken as part of the data collection effort:

1. Internet literature review
   RMI initiated the data gathering process in mid-August of 2014, scouring the internet and online databases for data relevant to the effort as requested by EGI's Dr. Greg Nash. Almost 500 papers and websites were reviewed which resulted in collection of almost 60 relevant documents, 45 web links to online research, heat flow maps and several water well maps - the most expansive of which was from the NM State Engineer's Office.

2. Review of pertinent data on existing databases
   RMI also located 15 searchable online databases and sent links to those websites to Dr. Nash at EGI. In addition, Dr. Nash accessed and collected information from several additional online databases including the NGDS, USGS, the State of New Mexico Geothermal Resources Database among others.

3. Collection of local/regional data
   Early on in the effort, RMI began to reach out to an initial set of stakeholders in the region for purposes of data collection. Initial contacts made included: Fort Bliss, El Paso Water Utilities, the University of Texas at El Paso, New Mexico State University and Mike Hillesheim with the National Renewable Energy Laboratory, White Sands Missile Range, the City of Alamogordo Water Utilities, Alamogordo Public Schools, the New Mexico State Engineer's Office – District IV, the New Mexico Environment Department's Water Quality Bureau in Las Cruces, Fort Bliss Water and the U.S. Army Corps of Engineers.

RMI collected a substantial amount of useful data from El Paso Water Utilities which included well locations, temperatures, well logs and water chemistry data for dozens of locations throughout El Paso County in the southern part of the study area, including several locations where warm water is known to exist. Although data was received from many sources, the cooperation from El Paso Water Utilities was by far the most successful during Phase 1.

Lastly, the project team realized that despite the extensive desktop reconnaissance and outreach efforts to key local agencies, there would likely be gaps in the data collection. To address this issue, RMI created an extensive list of additional contacts for agencies in New Mexico and for communities/utilities and water districts throughout the Tularosa Basin. This was done so that RMI could reach out to those agencies to infill data throughout the study area. RMI contacted many agencies on the list to help address data gaps, however not all agencies were responsive and additional follow up is planned for Phase 2.

2.2 Liaison with Military

While Fort Bliss was made aware of the PFA project upon initial implementation of the effort, a formal presentation to relevant staff was delivered on Wednesday, January 7, 2015. A copy of that presentation was previously submitted to DOE. Representatives from various directorates (departments) on the Post attended the meeting and it was determined that a Memorandum of Agreement (MOA) was needed for purposes of collaboration and information exchange. RMI drafted an MOA for submittal to the Office of the Staff Judge Advocate at Fort Bliss and it was executed by both parties.

Subsequent to execution of the MOA, RMI continued to brief our Fort Bliss staff contacts on project progress, and in fact, our project point of contact even accompanied Project Manager Carlon Bennett to White Sands Missile Range in order to help facilitate information exchange. Fort Bliss was very helpful during Phase 1 of the effort in setting up project briefings/data collection meetings with Fort Bliss Water and El Paso Water Utilities as well as arranging contact with the Army Corps of Engineers.

Concurrently with the efforts at Fort Bliss, a dialogue was opened up with White Sands Missile Range staff to both assess their interest in geothermal development and to gather any pertinent information which might be helpful in PFA development. Several meetings were held with WSMR staff and the Post has agreed to share results of some upcoming data collection with our project team.

Facilitating ongoing information exchange and maintaining positive working relationships with the Army is significant to the project. This is true not only because most of the identified geothermal plays up to this point are located on military lands, but also because the military is likely the largest beneficiary of geothermal development within the basin.

Any effective PFA methodology developed through this project will be a valuable tool for the geothermal industry interested in developing geothermal resources, but this is particularly true for DoD energy managers/decision makers who are charged with making significant, long-term energy investments with limited access to reliable, understandable geothermal data.

At present RMI and EGI estimate that over two dozen military installations – most located in the Western U.S. - are projected to have some level of geothermal power production potential.

2.3 Project Database Development

As stated previously, an exhaustive desktop reconnaissance effort was undertaken to gather and review data on the region. The principal goals of this effort were to:

- find data that are a direct indication of heat including temperature gradients, heat flow, and water chemistry to facilitate the calculation of geothermometers;
- find geologic data that may indicate fracture permeability; and,
- locate data indicating the presence of ground water.

The SMU Geothermal Laboratory 2011 heat flow map was also added (Blackwell et al., 2011). These data were collected in a digital format from multiple websites and in analog form from publications. The majority of data collected was evaluated and integrated into the project GIS, which was developed and maintained by EGI.

From our Phase 1 effort, 99 temperature gradient points, 414 water chemistry analyses with good charge balance, Quaternary faults, Pleistocene Lake Otero, and 6,192 water wells which penetrated ground water were added to the GIS. References to the data sources are listed in the GIS shapefile tables and/or metadata which are to be uploaded to the U.S. Department of Energy Geothermal Data Repository (GDR).

Supporting data were also added to the GIS for project support and to aid in future marketing efforts. These included land ownership, geology, shaded relief, regional Bouguer gravity, regional total magnetics, earthquakes, average temperature, depth to ground water, and volcanic age maps. Digital elevations models were also incorporated.

Additionally, both day and night acquisition ASTER (Advanced Spaceborne Thermal Emission and Reflection Radiometer) data were added and used to (1) map possible surface temperature anomalies, (2) relative outcrop clay, calcite, silica, and gypsum concentrations (mineralogic EGS implications), and (3) hydrothermal alteration.

Data collected during Phase 1 has been added directly into a GIS database or reformatted as necessary to allow its incorporation. All data will be carefully georeferenced to a common coordinate system, projection, and datum to facilitate model integration. Potential error and uncertainty related to the sources will be noted in the metadata and attribute tables.

SECTION 3: APPROACH TO PHASE 1 PFA DEVELOPMENT

3.1 Deterministic Play Fairway Analysis: Petroleum Logic Approach

The first PFA completed in the project was based upon petroleum industry logic. For petroleum PFA development, data representing charge, reservoir, and seal are integrated into representative composite risk segment (CRS) maps, which are then in turn integrated into the final PFA. In our geothermal PFA effort, we substitute heat of the Earth, ground water for heat transfer, and fracture permeability for the three CRS layers. Seal is not of great consequence because our PFA is designed to locate areas with high potential for fault related fracture permeability rather than permeable rock reservoirs upon which petroleum systems rely.

Classification rules for petroleum industry logic PFA are relatively simple and easy to understand. If all three CRS layers have the same risk class, then the final PFA class is the same. If a single CRS risk class is of higher risk, then the final PFA class is of the higher risk class. Examples can be seen in (Table 1).

Table 1. Petroleum PFA classification rule examples.

Charge CRS Class	Reservoir CRS Class	Seal CRS Class	Final PFA Class
Low Risk	Low Risk	Low Risk	Low Risk
Low Risk	Low Risk	Medium Risk	Medium Risk
Low Risk	High Risk	Low Risk	High Risk
Medium Risk	Medium Risk	Medium Risk	Medium Risk
Medium Risk	Medium Risk	High Risk	High Risk
High Risk	High Risk	Low Risk	High Risk

This simple classification scheme works well where a relatively even spatial distribution of all input data sets is present. However, modifications were necessitated because this was not the case for our study area. The modifications will be elucidated throughout the following descriptions of CRS and PFA development.

Heat of the Earth CRS

To develop this CRS, temperature data points representing temperature gradients and quartz Geothermometers were interpolated into statistical surfaces using the deterministic IDW (inverse distance weighted) technique found in the ArcGIS software package. The statistical surfaces were then classified in the ArcGIS map document using Layer Properties>Symbology as follows:

Temperature gradients (Fig. 4):
0 ^{o}C/km – 60 ^{o}C/km = High Risk
60 ^{o}C/km – 80 ^{o}C/km = Medium Risk
>80 ^{o}C/km = Low Risk

Quartz Geothermometer (Fig. 5):
0 ^{o}C – 60 ^{o}C = High Risk
60 ^{o}C – 80 ^{o}C = Medium Risk

>80 ^{o}C = Low Risk

The ArcGIS Reclassify tool was then used to permanently apply these classes to new output files (ArcToolbox>Spatial Analyst Tools>Reclass). The output raster files were then vectorized (ArcToolbox>Converation Tools>From Raster>Raster to Polygon) for CRS integration.

Heat flow (Fig 6) was digitized as vector data directly from the SMU 2011 heat flow map (Blackwell et al., 2011). It was classified as follows (mW/m^2):
55 – 70 = High Risk
70 – 85 = Medium Risk
>85 = Low Risk

New fields were then added to each of the three CRS input file tables, with field heading names unique to the given dataset (e.g. TempGrad_Class), and populated with risk classes. These will be carried over in the following Union process, which is the next step.

The ArcGIS Union overlay method (Geoprocessing>Union) was then applied to the three heat CRS input vector layers. This produces a “spaghetti map” (Fig 7). A new Final_Class field was then added to the table of the output “spaghetti” vector file. Data queries were then be run to select sets of data for classification, e.g. "Qtz_Risk" = 'Low' AND "TG_Risk" = 'Low' AND "HF_Risk" = 'Low', and, for the records selected, the new Final_Class field was populated as Low Risk in this example.

This initially followed the petroleum PFA classification rules. However, since there is an uneven spatial distribution of data, the heat CRS was overlain with input temperature gradient and quartz geothermometer data points and the vectorized heat flow map to help classify problematic areas. For instance a polygon may have input classes of (1) temperature gradient = High Risk, (2) heat flow = Low Risk, and 3) quartz geothermometer = Low Risk. This, according to petroleum industry logic, would make the polygon High Risk. However, upon inspection of the input data, if no temperature gradient control points were found within or nearby the polygon, this dataset would have been considered low priority. Conversely, if geothermometer control points, in the Low Risk class, were found within the polygon this data would be assumed high priority. This would give the quartz geothermometer dataset precedence and the polygon would have been classified as Low Risk. This requires additional work and data observation, but we believe that is it appropriate and so this method was used to classified questionable polygons. It takes more time, but it also helps the explorationist become better acquainted with the data.

The ArcGIS Dissolve method (ArcToolbox>Data Management Tools>Generalization> Dissolve) is then applied, based on the final risk field, to simplify the polygons for the final Heat CRS (Fig. 8).

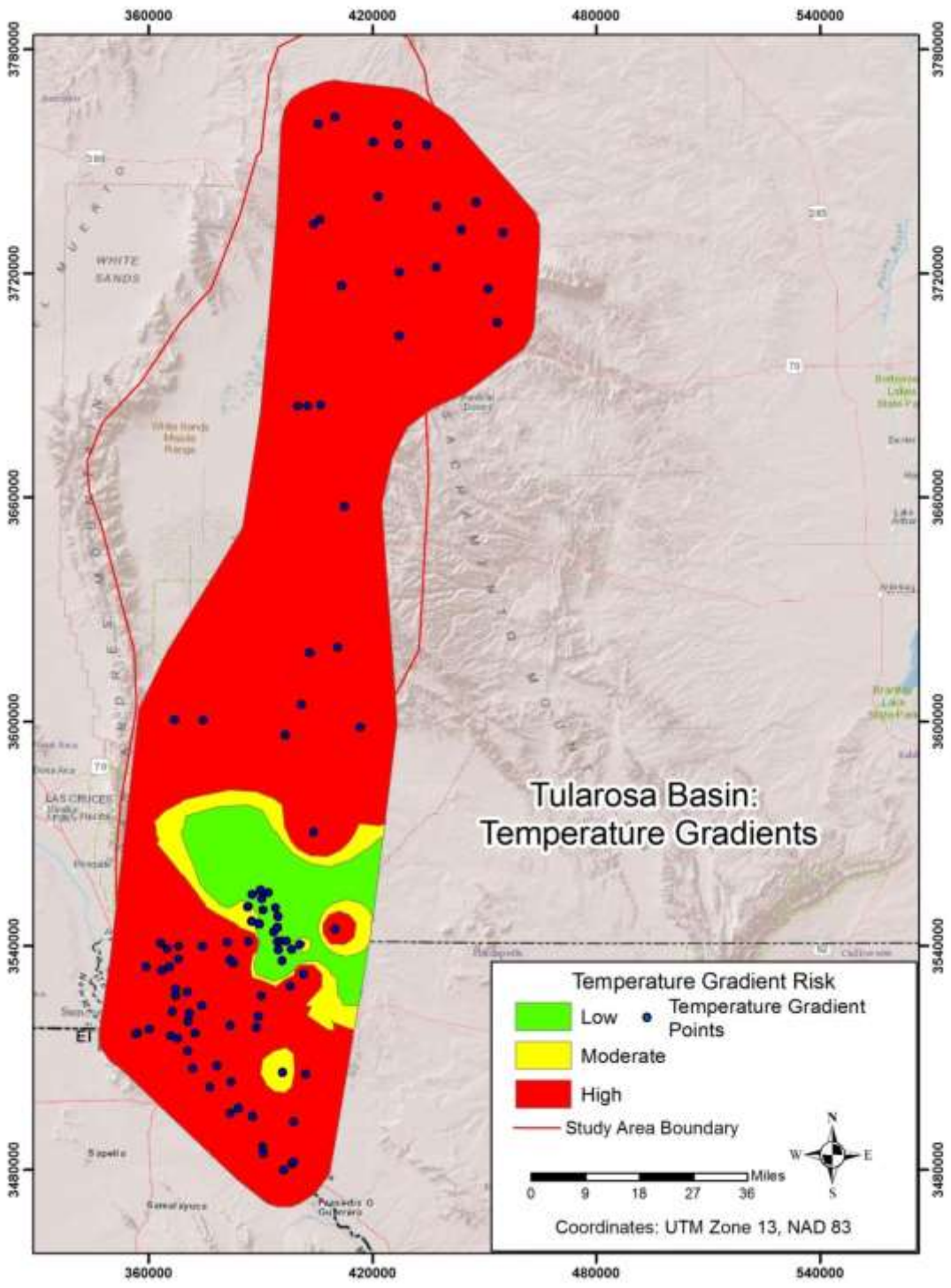

Figure 4. Heat risk -- temperature gradients.

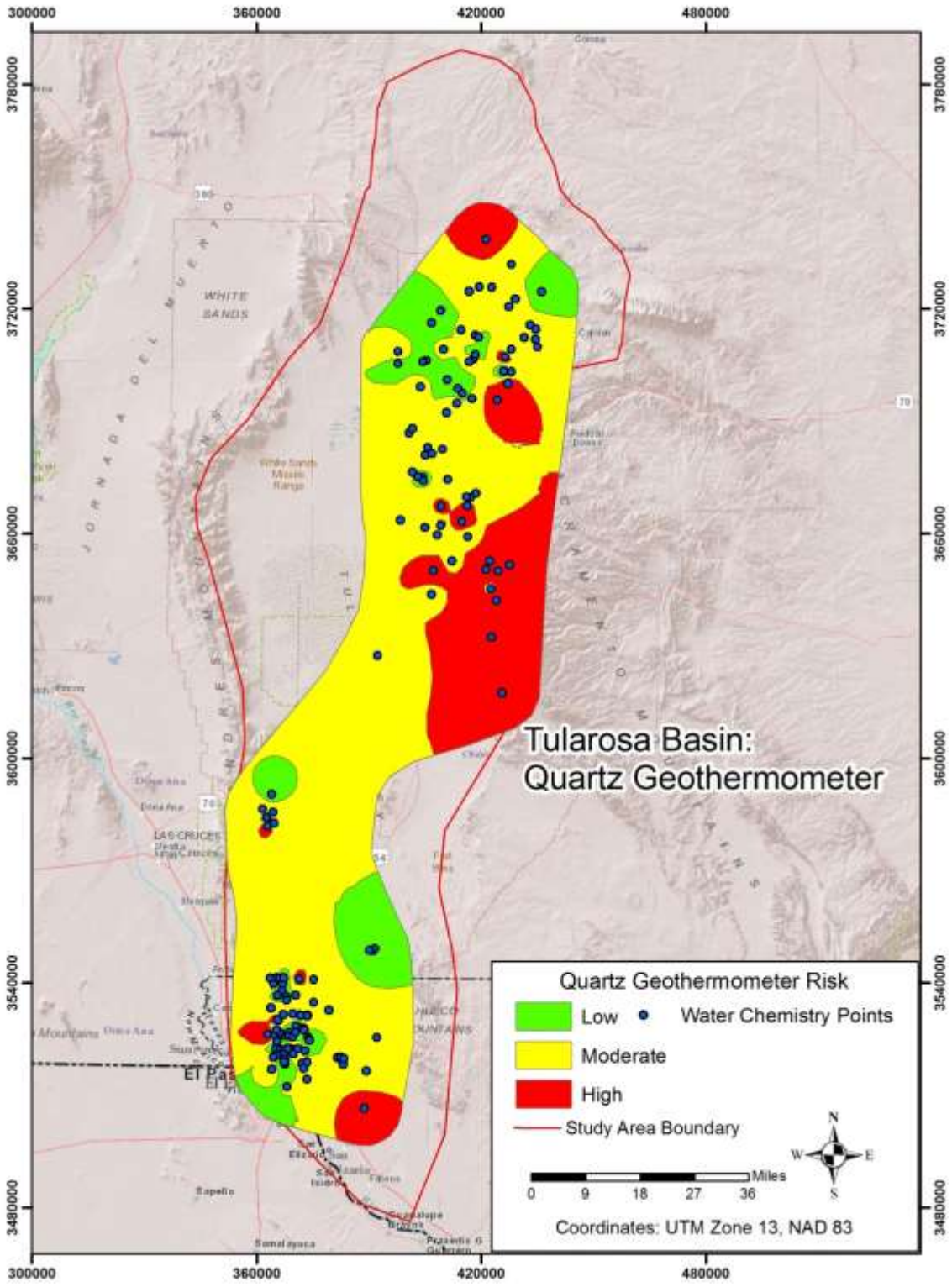

Figure 5. Heat risk – quartz geothermometers.

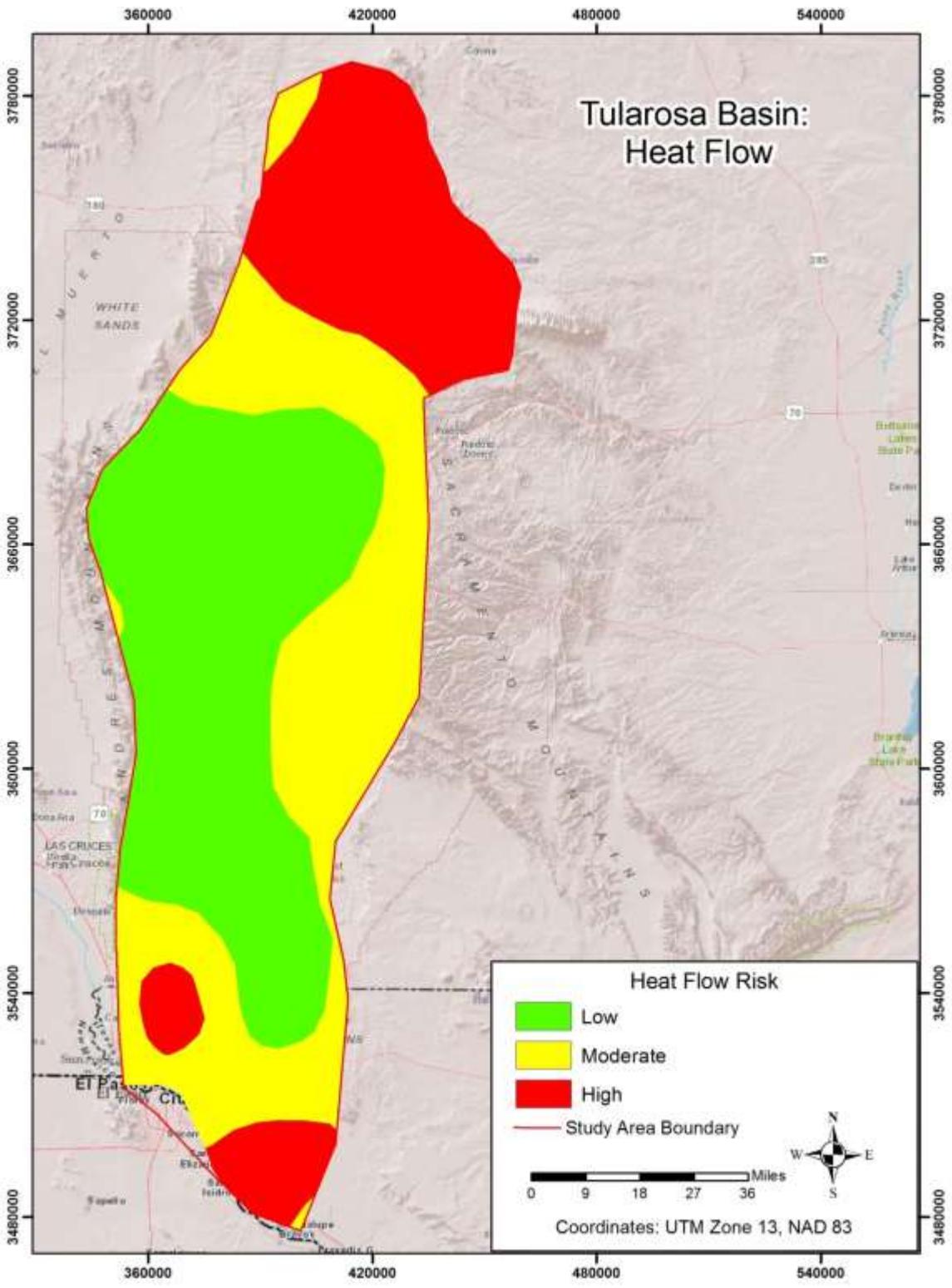

Figure 6. Heat risk – heat flow.

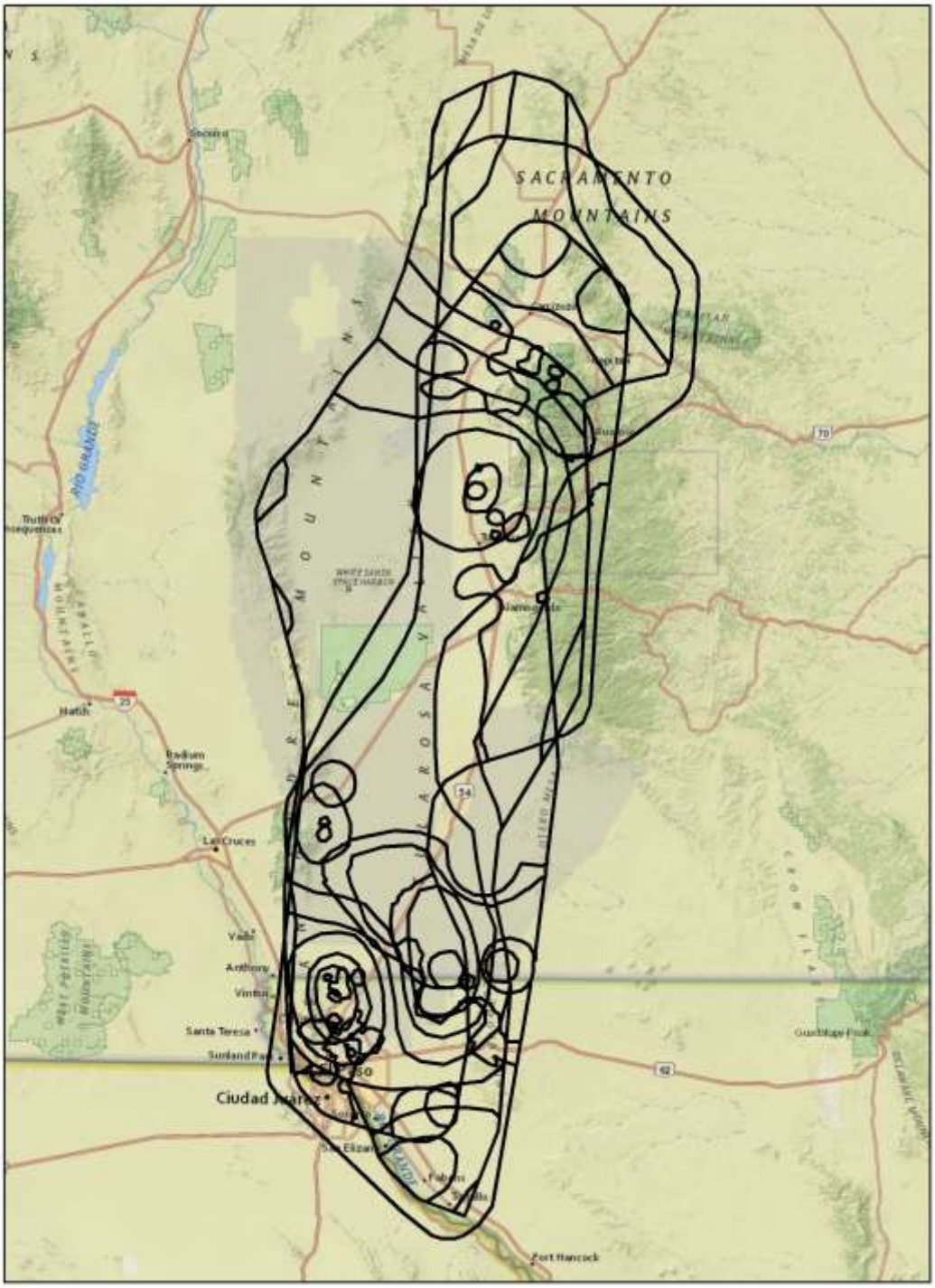

Figure 7. Graphic showing the spaghetti like polygons created using the Union overlay method.

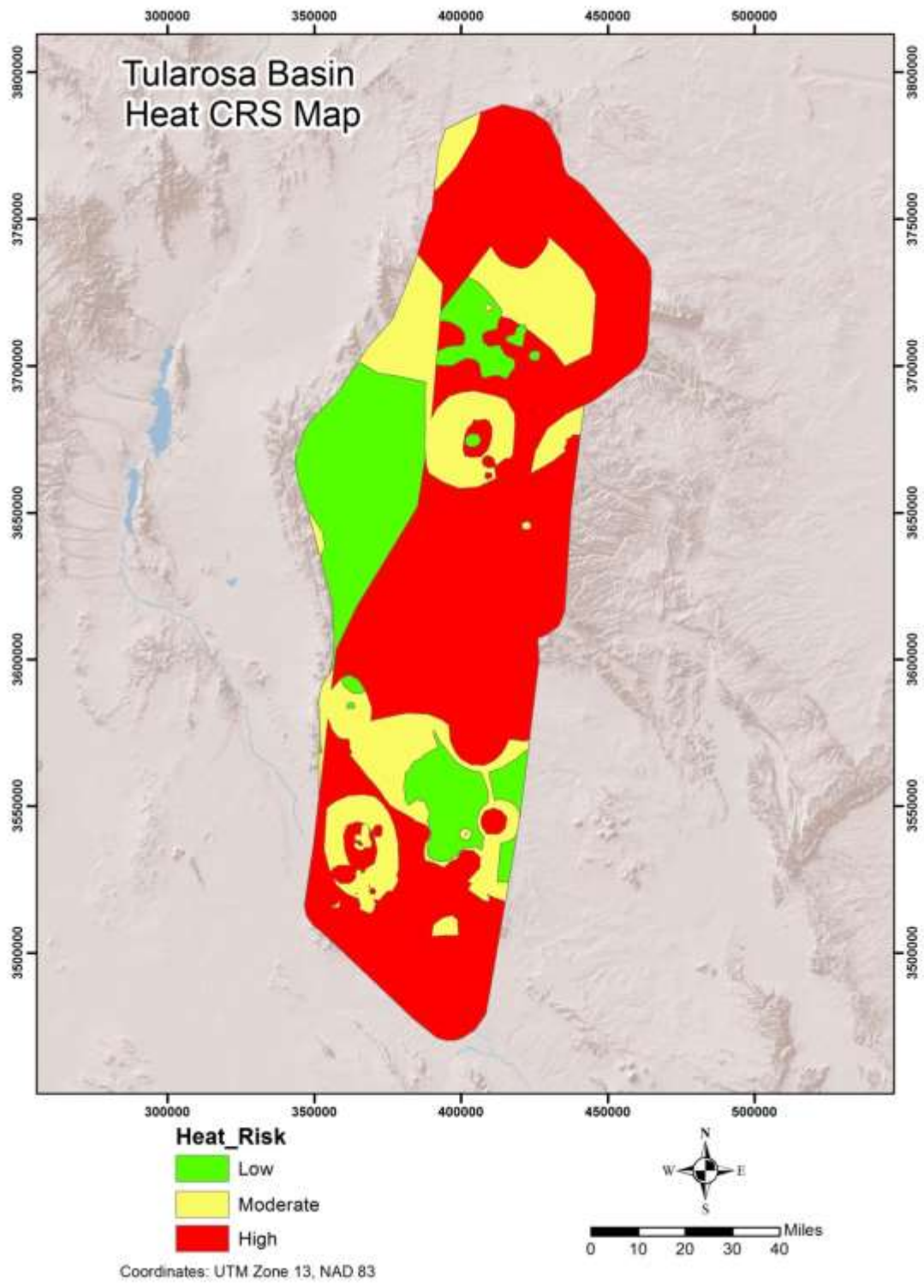

Figure 8. Final heat CRS after application of the Dissolve method.

Fracture Permeability CRS

This CRS was developed using Quaternary faults and zones of critical stress (Fig. 9) (Faulds et al., 2006, 2010, 2013). Quaternary faults were derived from the USGS Quaternary Fault and Fold Database of the United States. These were in a polyline shapefile. These data were Clipped to fit the study area (Geoprocessing>Clip) and the clipped lines were then buffered at a distance of 1 km. The resultant polygons were then all classified as Medium Risk. Quaternary faults and recent seismic actively are known to be related to permeability in geothermal systems, but fault slippage can both open and close fractures. Therefore, we believed that Quaternary faults needed to be represented, but not as Low Risk.

Zones of critical stress form in structural settings such as fault step-overs, terminations, apexes, intersections, and accommodation zones. Critical stress zones were mapped using analysis of aerial photography, Bouguer gravity, and total magnetic data. Each zone was considered to be encompassed within a 5 km diameter circle, except where evidence indicated that a larger area may be impacted. Resultant polygons were classified as Low Risk

The ArcGIS Union method was applied to the 1 km buffered Quaternary faults and the critical stress zones polygons and a new field was added to the result to hold the final classifications. The ArcGIS dissolve method was then applied to simplify the polygons, the results of which can be seen in Fig. 10.

Ground Water CRS

This CRS was developed using data from a point of diversion (POD) water shapefile obtained from the New Mexico office of the State Engineer and from drainage basin analysis in the Sacramento Mountains. Wells that had penetrated ground water and springs were extracted from the POD data and merged with water chemistry points were not redundant, and buffered at a distance of 2 km. The Pleistocene Lake Otero shoreline was also buffered at a distance of 2 km and this was Union overlain with the other water data. A trivial amount of new area was also edited in based upon the results of the drainage basin analysis. Dissolve was applied to simplify the resultant polygons. These polygons were given a class of Low Risk (Fig.11). All other areas in the basin were considered to be High Risk, although a good deal of the High Risk area may contain ground water, there is just no data to support it.

Final Petroleum Industry Logic PFA

The final deterministic PFA was created by applying a Union overlay to the three CRS layers. This was followed by Dissolve to simplify the polygons. The PFA, which identified eight plays, can be seen on Figure 12. The methodology is detailed on a flow chart located in Appendix C.

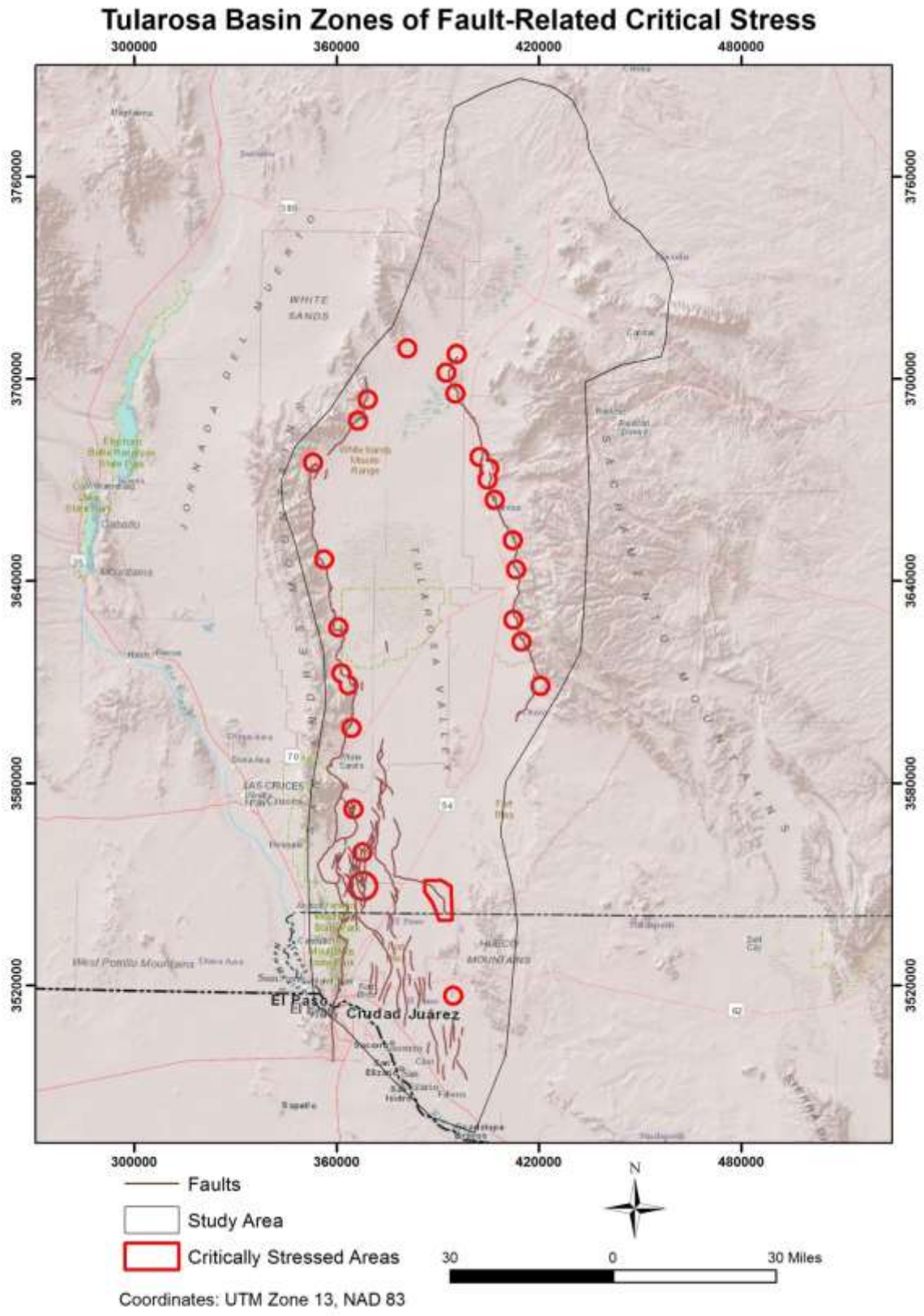

Figure 9. Study area Quaternary faults and zones of critical stress.

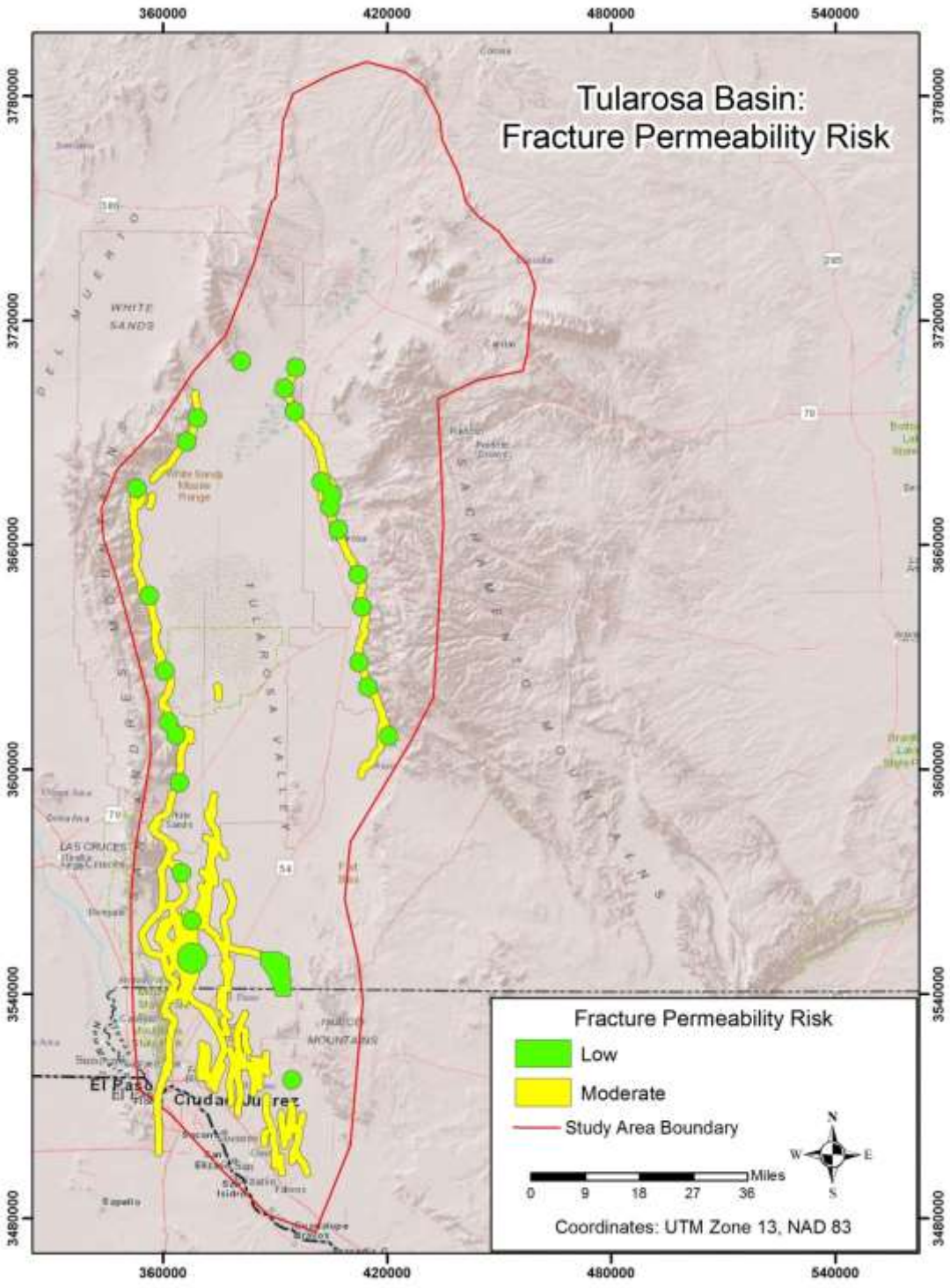

Figure 10. Fracture permeability risk CRS: Integration of Quaternary faults with a 1 km buffer (each side of fault) and 5 km diameter zones of critical stress. All areas within the study area boundary that are not colored are high risk.

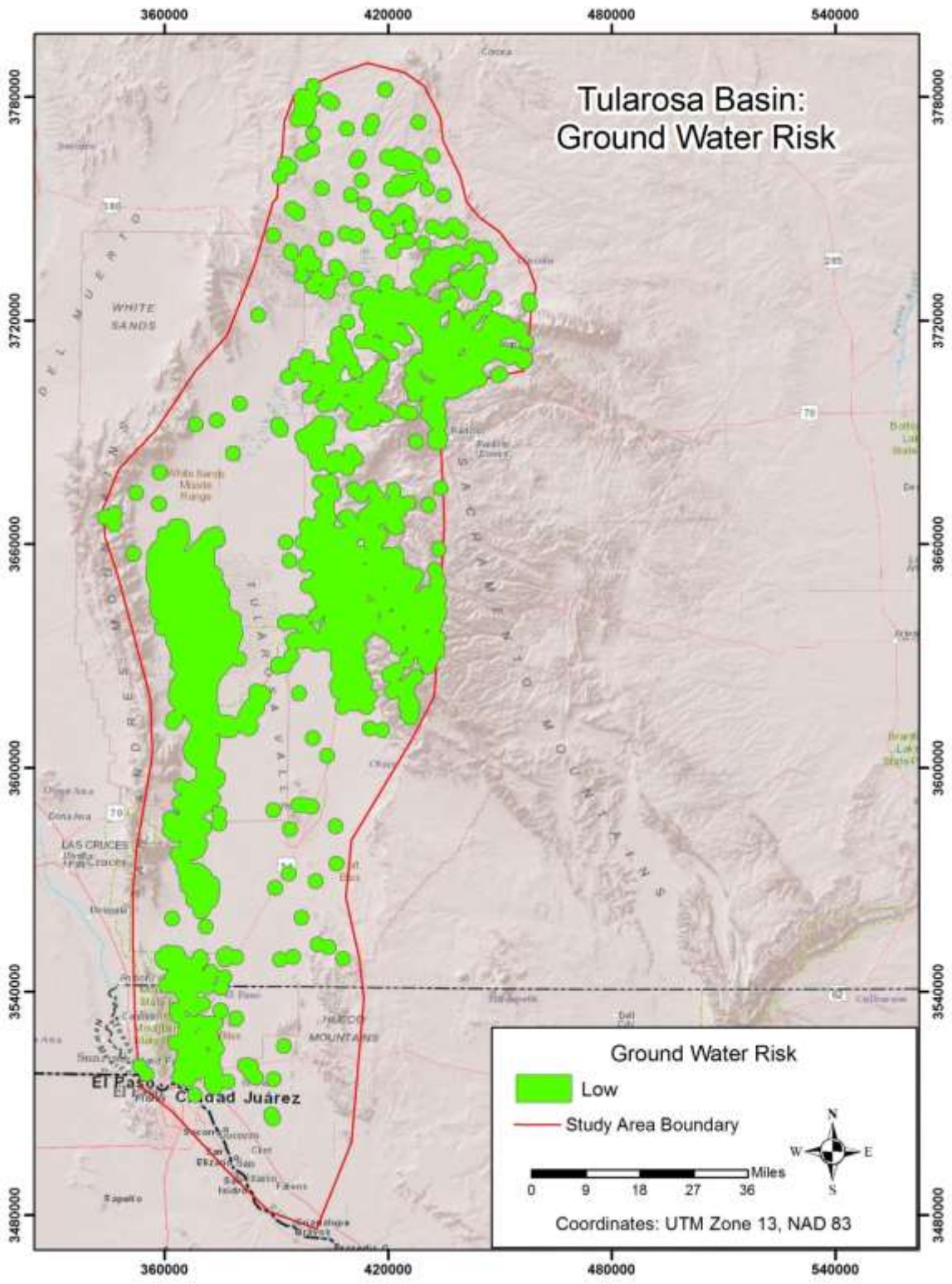

Figure 11. Ground water risk. All areas of the study area not colored in were considered to be high risk.

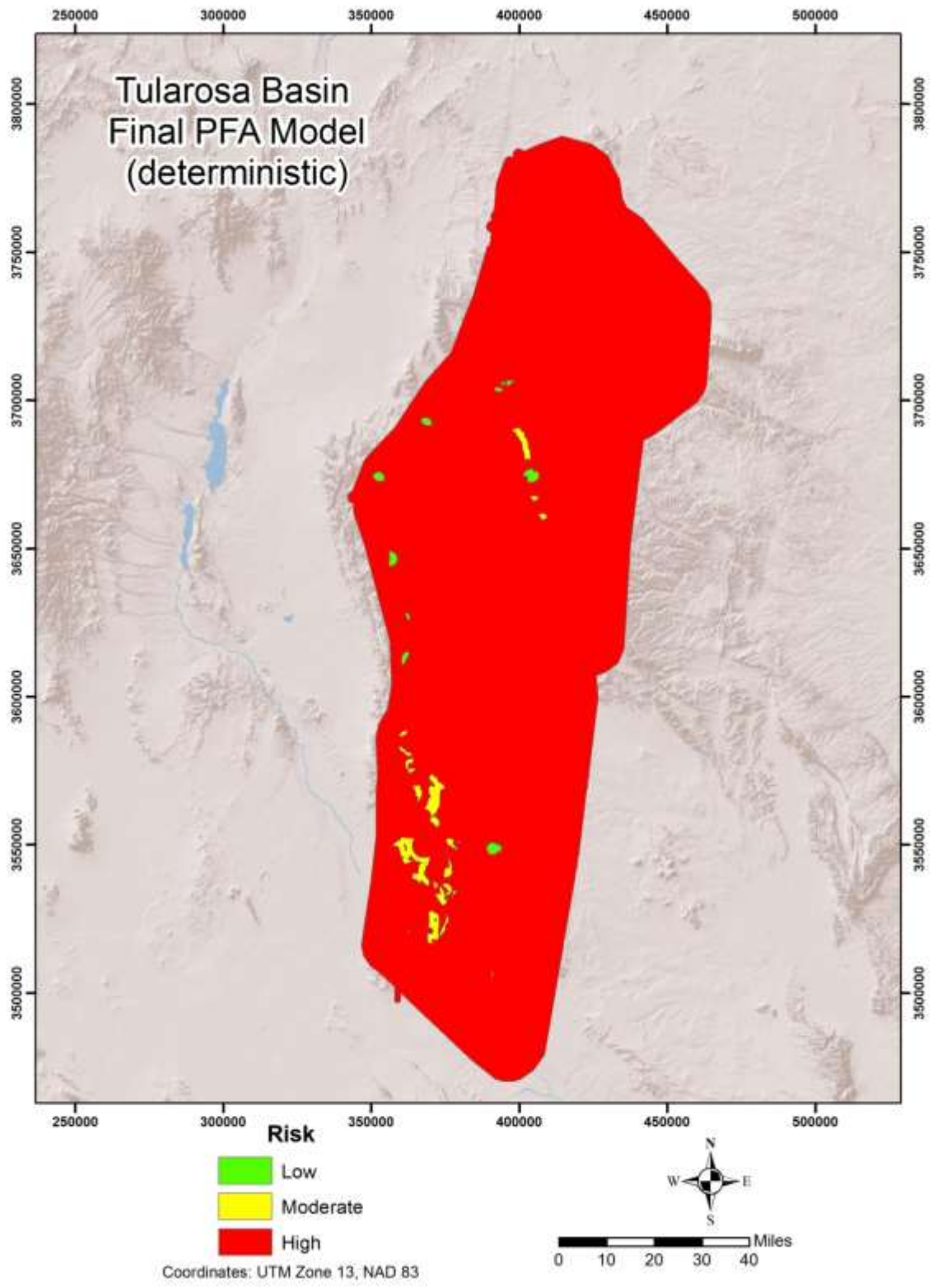

Figure 12. Final petroleum industry logic PFA. This model identified eight plays including the known geothermal system.

PFA Certainty

Certainty for this deterministic model was addressed in a deterministic way. Some data, such as fault traces, wells penetrating ground water, and zones of critical stress may have some elements of error, but this would be very difficult to ascertain in a desk-top exercise using existing data. However, there were several sources of heat data from a number of different sources and it was felt that confidence was bolstered for areas where all data sets were present.

Therefore, considering Heat CRS polygons, the following certainty classes were ascertained:

- All three heat data sets present: High Certainty
- Two heat datasets present: Moderate Certainty
- Only one heat dataset present: Low Certainty

The results can be seen on Figure 13. The low certainty areas were only represented by heat flow data because this is the only map covered the entire study.

3.2 Stochastic Play Fairway Analysis: Weights of Evidence Approach

The weights of evidence (WoE) method was used in this PFA because Moghaddam et al., 2013, found it to be the superior stochastic method, out of several tested, for geothermal exploration model development. This technique examines multiple layers of evidence, calculates weights for each evidential layer based upon the spatial relationships of training points, which are located at known geothermal systems and hot springs (in this case), and then produces a posterior probability raster surface and other related statistics.

A problem with applying this method in the Tularosa Basin was a lack of training sites. This was addressed by creating statistical surfaces for training that covered Nevada, Utah, and New Mexico. This gave access to ample known geothermal areas and hot springs for training. Spatial Data Modeler was used for the WoE analysis (Sawatzky et al., 2009)

Evidence of Heat

Water chemistry was compiled into an ArcGIS shapefile from the Great Basin Groundwater Geochemical Database from the Nevada Bureau of Mining and Geology (http://www.nbmg.unr.edu/Geothermal/GeochemDatabase.html) and additional data from the Oregon Institute of Technology Geo-Heat Center (http://www.oit.edu/orec/geo-heat-center). Redundant points were removed and the quartz (conductive) geothermometer (Fournier, 1991) was calculated. The inverse distance weighted (IDW) interpolation method was then applied to the quartz geothermometers using ArcGIS to create a raster statistical surface (Fig. 14).

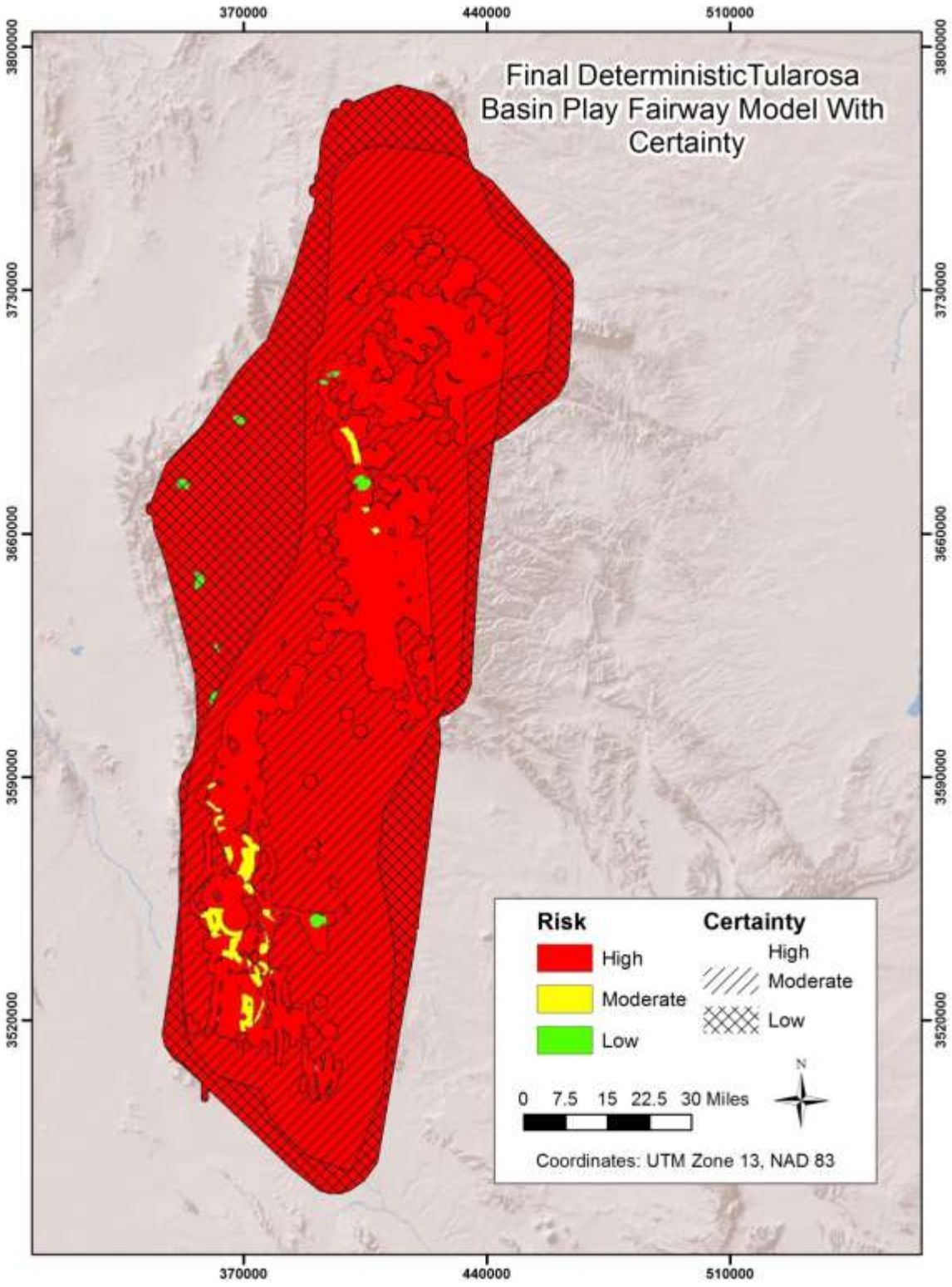

Figure 13. Deterministic certainty draped over the final deterministic PFA model.

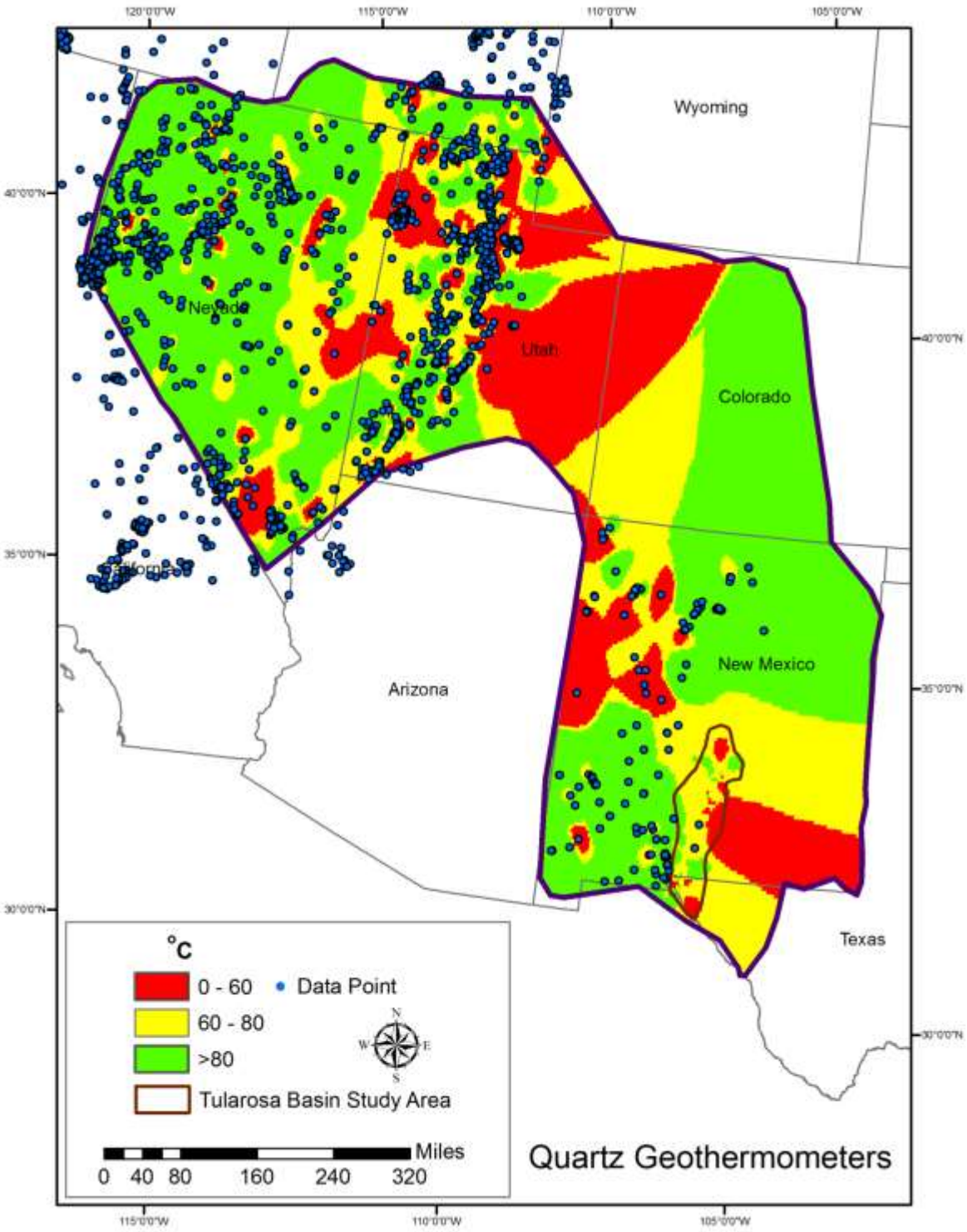

Figure 14. Quartz geothermometer evidential layer overlain with data points. Extrapolation was allowed beyond data points, but training area were all in data rich areas.

Extrapolation was allowed into areas with no data for this evidential layer. However, training sites were only chosen in data rich areas where the statistical surface was very accurate.

The same process was also applied to heat flow and temperature gradient data, originating from the SMU Geothermal Laboratory (http://www.smu.edu/dedman/academics/programs/geothermallab). The temperature gradient statistical surface produced for use in the previously discussed deterministic model, which was created with additional data, was then integrated into the new temperature gradient surface. The results of which can be seen in Figures 15 and 16.

Fracture Permeability

Evidence of fracture permeability was once again represented by the Quaternary faults from the USGS Quaternary Fault and Fold Database and the Faulds Structural Inventory of Great Basin Geothermal Systems and Definition of Favorable Structural Settings (http://en.openei.org/datasets/dataset/structural-inventory-of-great-basin-geothermal-systems-and-definition-of-favorable-structural-setti2). The Faulds data were converted into a shapefile and integrated with the critical stress zones points mapped in the Tularosa Basin. Points with unknown conducive structural settings were removed and the remaining points buffered to 5 km. This was then integrated into a training data boundary layer where zones of critical stress were classified as 1 and other areas as 0 (Fig. 17). This was then converted into a raster layer (Fig. 18).

Quaternary faults were once again buffered to 1 km on each side of the trace. The buffer polygons were then classified as one and integrated with the boundary polygon (value 0). The resultant shapefile was then converted to a raster layer (Fig 19).

Training Sites

Fifty training sites were chosen, scattered through New Mexico, Utah, and Nevada, for use in WoE analysis. Steamboat Springs and the Dixie Valley production area in Nevada were left out because it was very doubtful that a similar system exists in the Tularosa Basin. The sites that were used can be seen in Table 2, Appendix B and the points seen on a map in Figure 20.

Weights of Evidence

In weights of evidence, positive weights indicate a significant contribution by the data whereas a negative value indicates no contribution. Therefore, an examination of class weights can help give a better idea of the data relationships to geothermal systems.

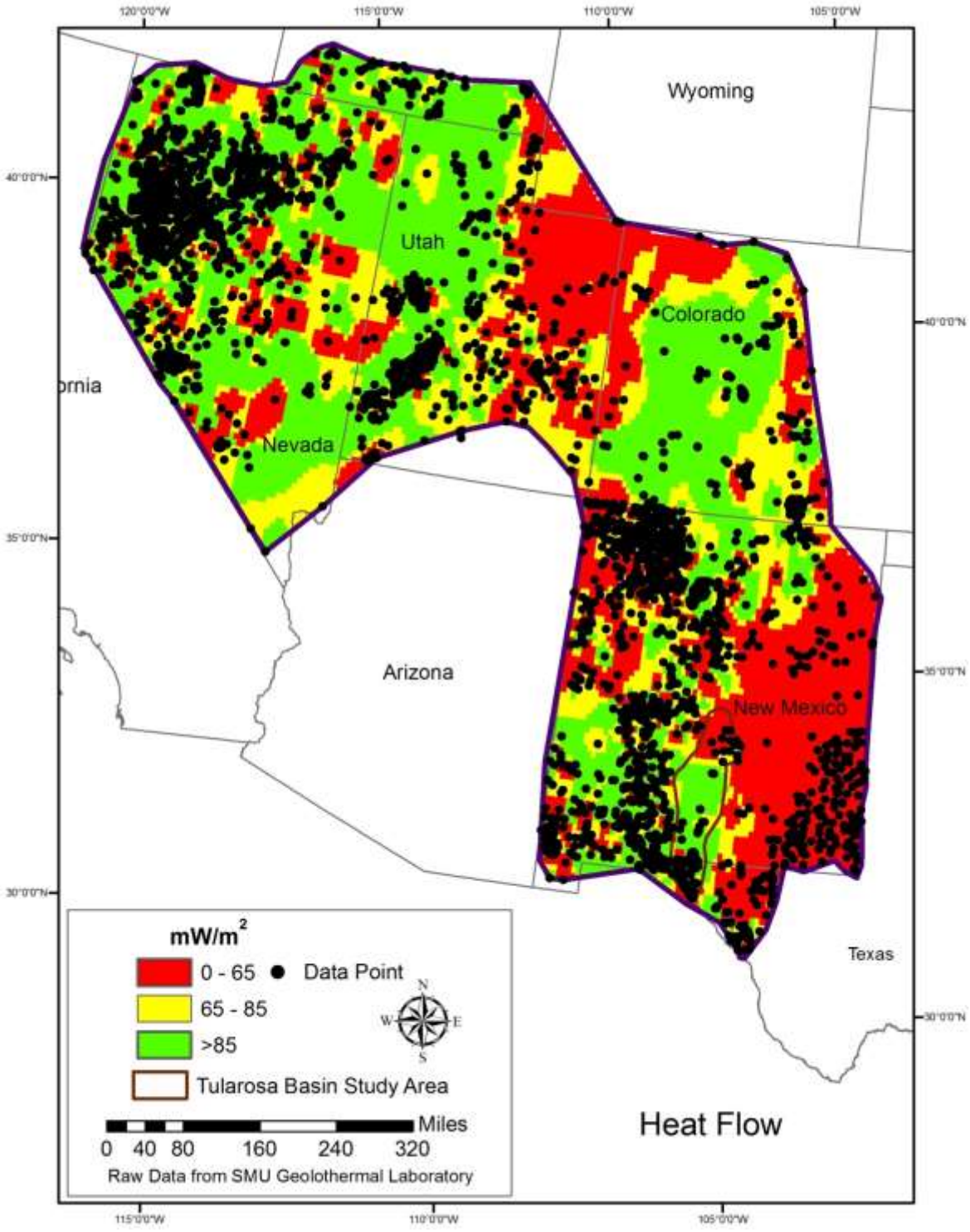

Figure 15. Heat flow evidential layer overlain with data points.

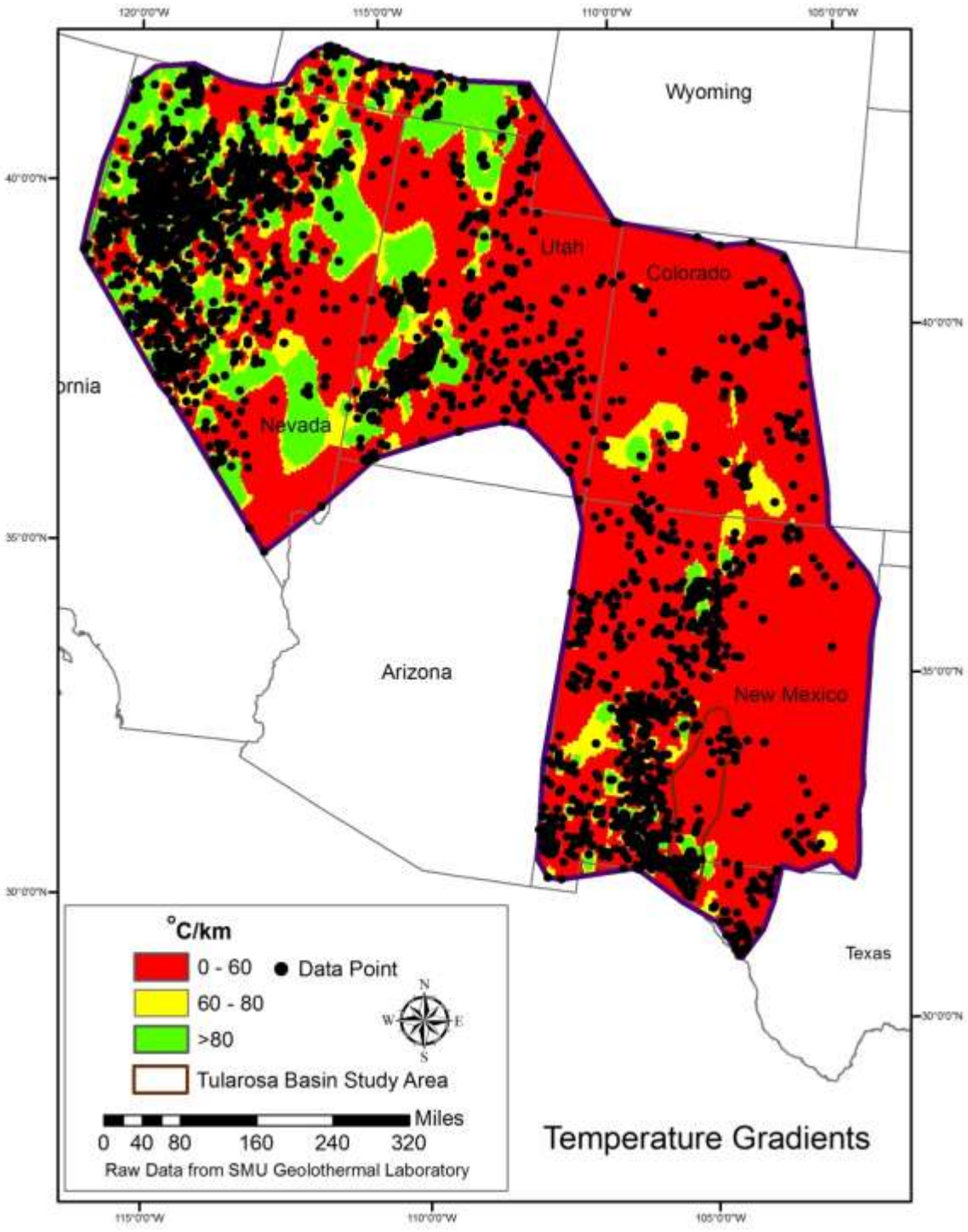

Figure 16. Temperature gradients evidential layer overlain with data points.

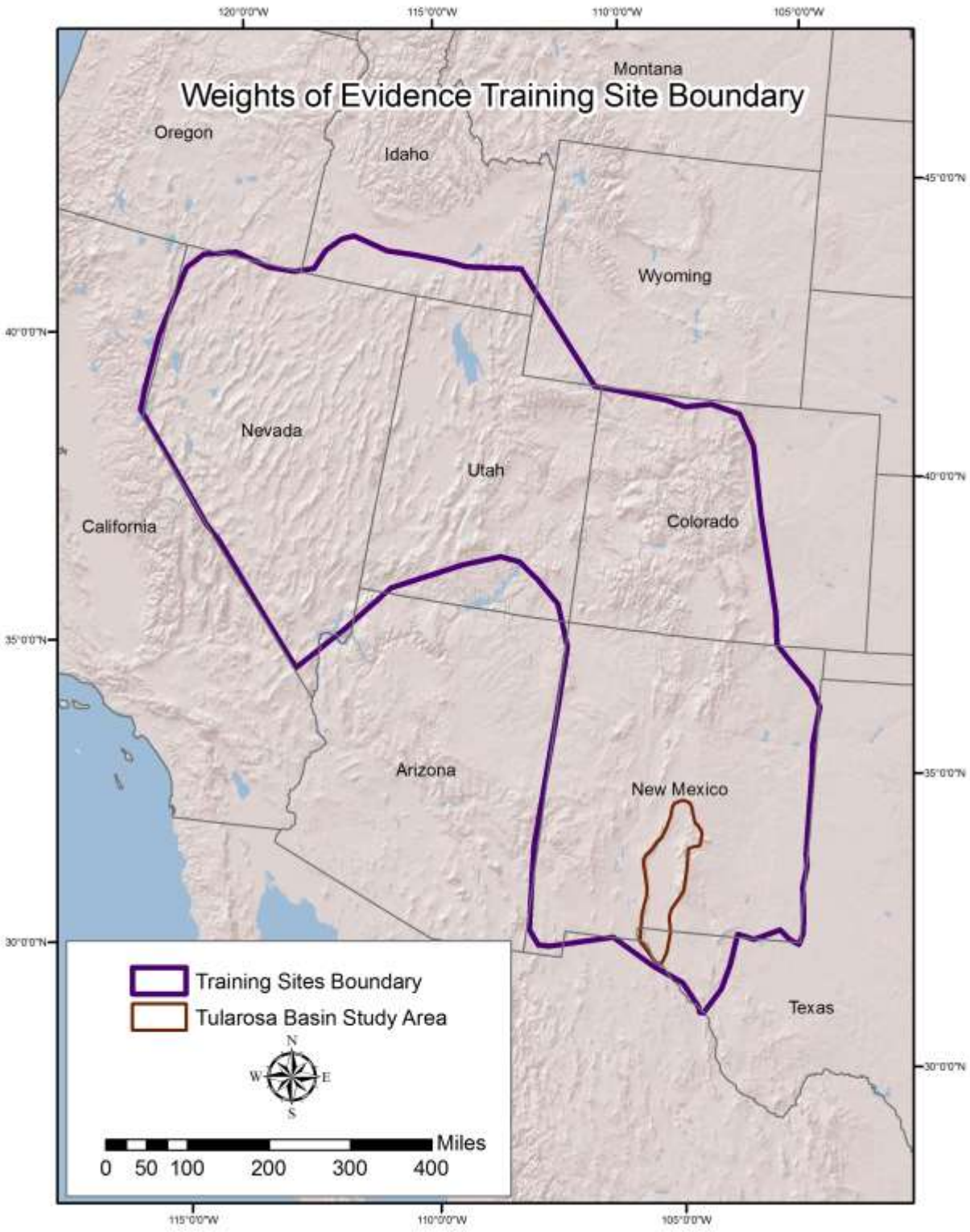

Figure 17. WoE training data boundary.

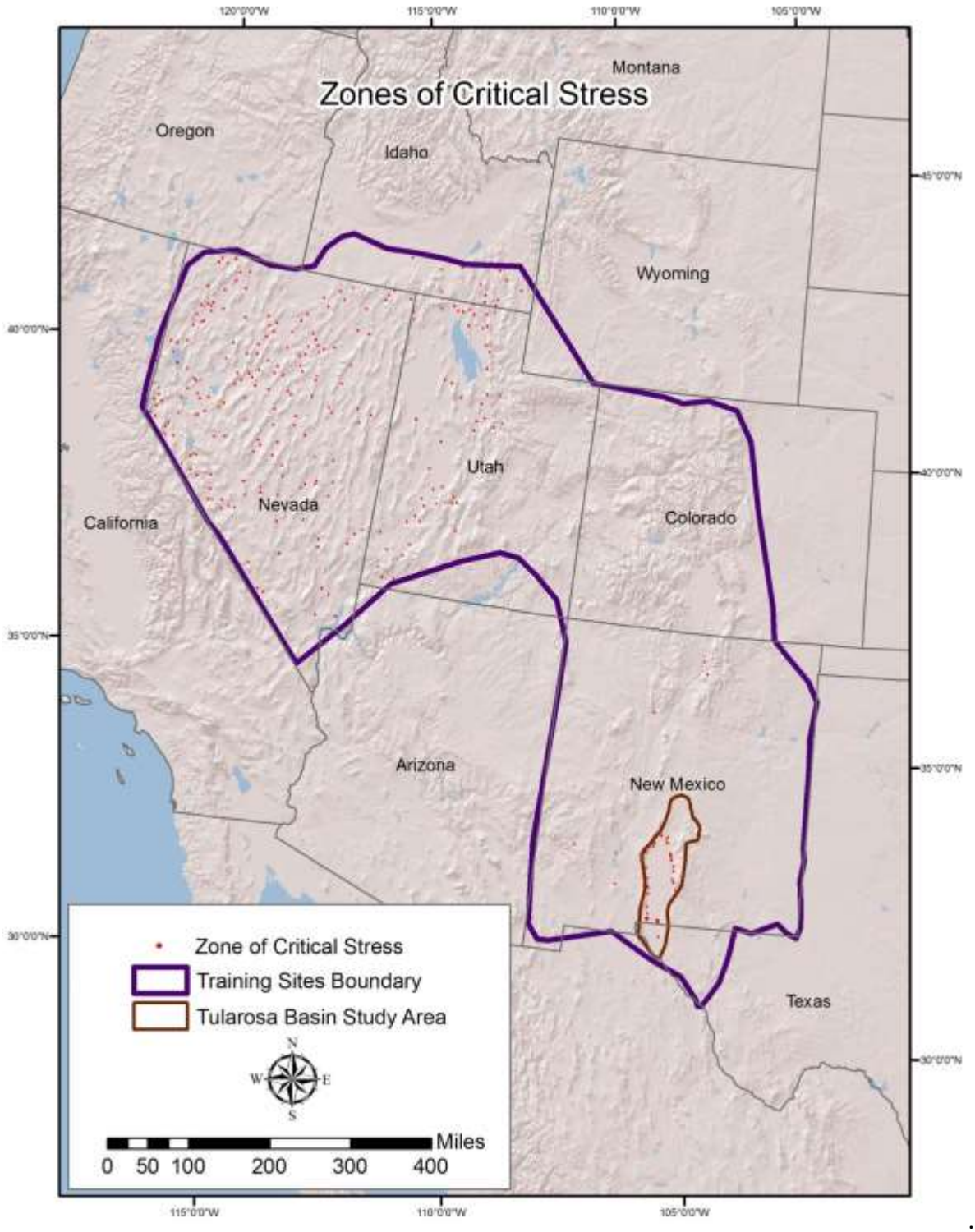

Figure 18. Zones of critical stress.

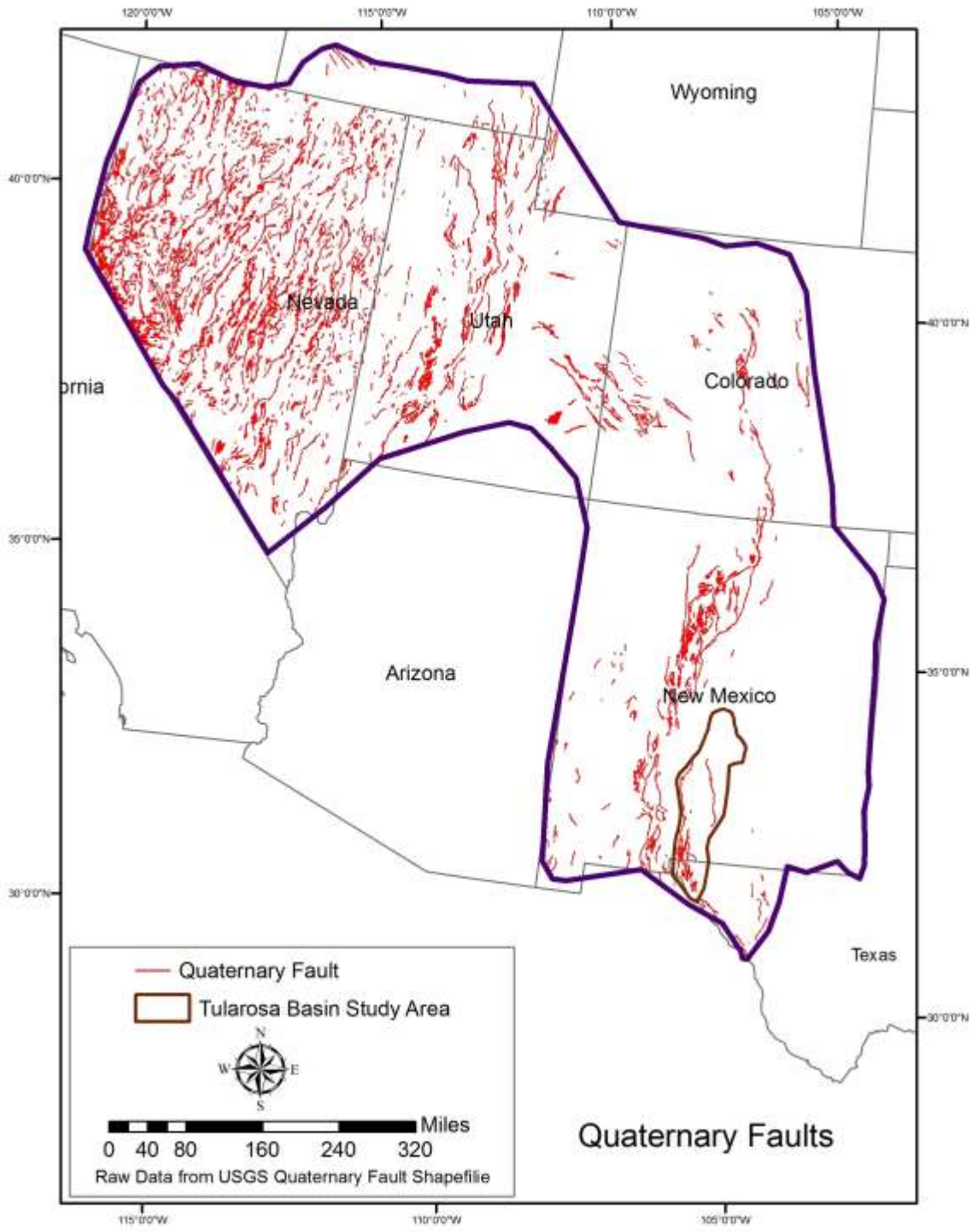

Figure 19. Quaternary faults buffered to 1 km (both sides of fault trace).

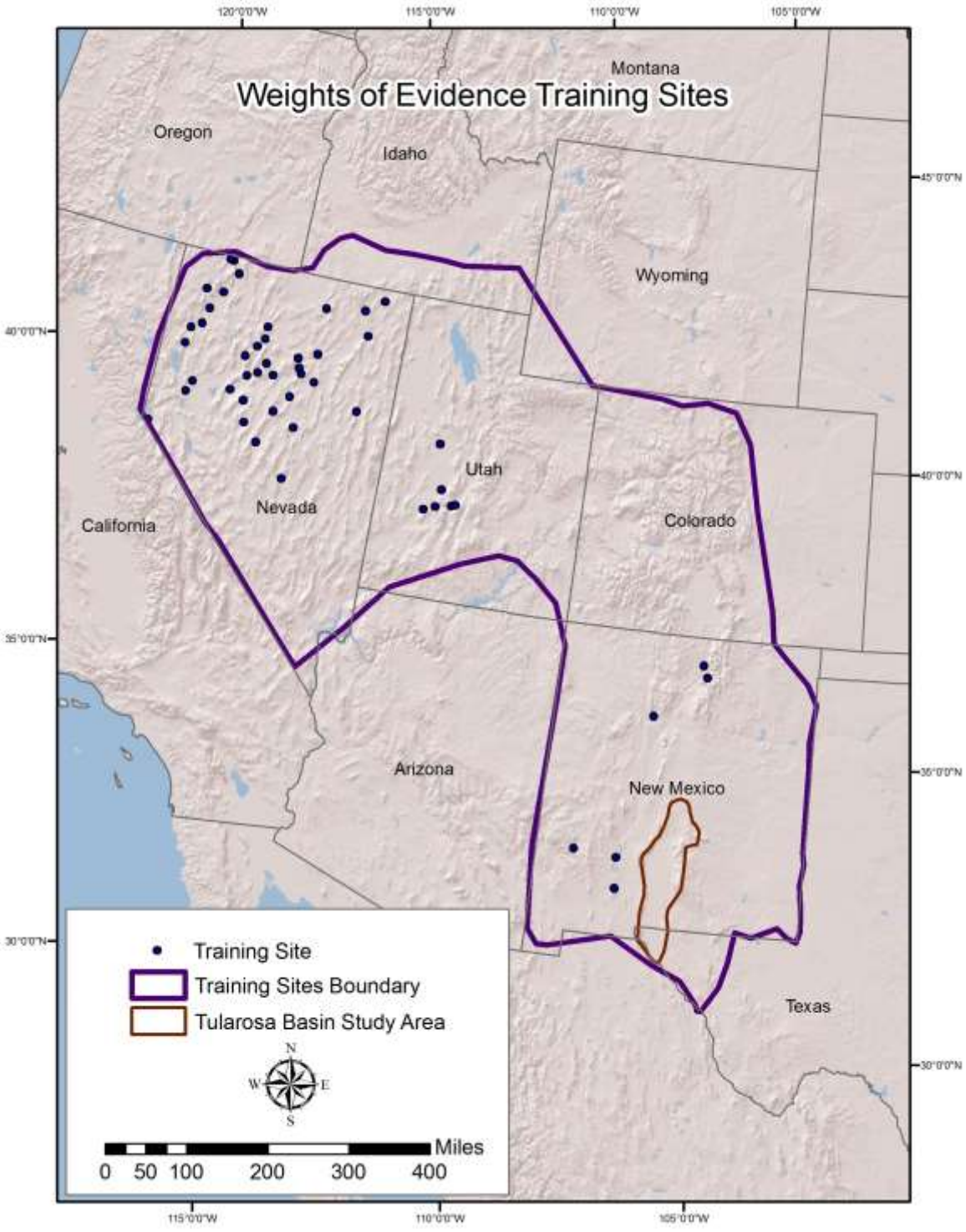

Figure 20. WoE training sites located at hot springs and known geothermal systems.

Heat Flow

The heat flow surface was divided into 15 classes using equal intervals. Positive weights were only produced for three classes:
Class 7, Range = 164 – 189 mW/m^2, Weight = 1.8805
Class 10, Range = 241 - 166 W/m^2, Weight = 2.6463
Class 13, Range = 319 – 343 W/m^2, Weight = 2.7381.

This indicates that in general, there is little relationship between hot springs and geothermal areas and temperature gradients lower than 164 mW/m^2 on the statistical surface.

Temperature Gradients

The temperature gradient surface was divided into 11 classes using equal intervals. Positive weights were generated for only four of these classes:

Class 5, Range = 80 – 100 $^oC/km$, Weight = 0.8071
Class 9, Range = 160 – 180 $^oC/km$, Weight = 1.9264
Class 10, Range = 180 – 200 $^oC/km$, Weight = 2.6685
Class 11, Range = >=200 $^oC/km$, Weight = 2.3096.

This indicates that in general, there is little relationship between hot springs and geothermal areas and temperature gradients lower than 160 $^oC/km$ on the statistical surface.

Quartz Geothermometers

The quartz geothermometers surface was divided into 5 classes using equal intervals. A positive weight was only produced for one class: Class 5, Range = >=100 ^oC, Weight = 1.0452.
This indicates that over the entire training area, hot springs and known geothermal areas generally have quartz Geothermometers higher than 100 ^oC.

Quaternary Faults
The Quaternray fault layer of evidence was a binary dataset. It produced the following weights:
Class 0 = -0.7771
Class 1 = 1.9035.

This indicates a good correlation between Quaternary faults and the training points (hot springs and known geothermal areas).

Zones of Critical Stress
The zones of critical stress layer of evidence was also a binary dataset. It produced the following weights:
Class 0 = -3.2137
Class 1 = 5.2212.

This shows that the critical stress layer of evidence had a very strong correlation with the training points (hot springs and known geothermal areas).

WoE Results

In general, based upon the WoE weightings, the Tularosa Basin would not be as likely as some areas (e.g. Dixie Valley and McGinnis Hills) elsewhere within the training data boundary, to contain a high enthalpy system. However, a new Dixie Valley was never expected and lower temperature plays, similar to the known McGregor Range system, can provide important energy to the military.

WoE identified ten plays (Fig. 21), six of which correlated with plays identified by the deterministic method and four which did not (Fig. 22). Of the four plays that were unique to the WoE method, two were given a low priority due to relatively low probabilities, and two were given medium-high priority due to relatively high probabilities, spatial relationships to input data points with permissible values, and certainty (Fig. 23). Water was also considered, although not inherently as part of the WoE. The ground water potential map created for the deterministic model was overlain on the WoE results and it was determined that all WoE plays have a good potential for groundwater (Fig. 24).

Certainty

A confidence surface was generated as a default part of the WoE analysis using Spatial Data Modeler and the result can be seen on Fig. 25, where all play areas have relatively high confidence. However, this was based upon the data for the large area used for training (Fig. 17).

Data specific to the Tularosa Basin study area boundary were also used to calculate probabilistic certainty using probability kriging on the three datasets for heat. The following thresholds were applied:
Geothermometers = 80 ^{o}C
Heat flow = 85 mW/m^{2}
Temperature Gradients = 80 ^{o}C/km

However, since the water chemistry data was clustered to three relatively specific areas, these points were split out into three separated datasets prior to kriging and probability kriging was then applied to each area. After probability kriging was completed on all of the datasets, the resultant probability raster images were classified as follows:
0.0 – 0.6 = Low Certainty
0.6 - 0.8 = Moderate Certainty
0.8 – 1.0 = High Certainty

The classified probability raster images were then vectorized. This was followed by a Union overlay and Dissolve to simplify the polygons. The results can be seen on Figure 26, where it can be seen that using localized data resulted in a more conservative layer of certainty.

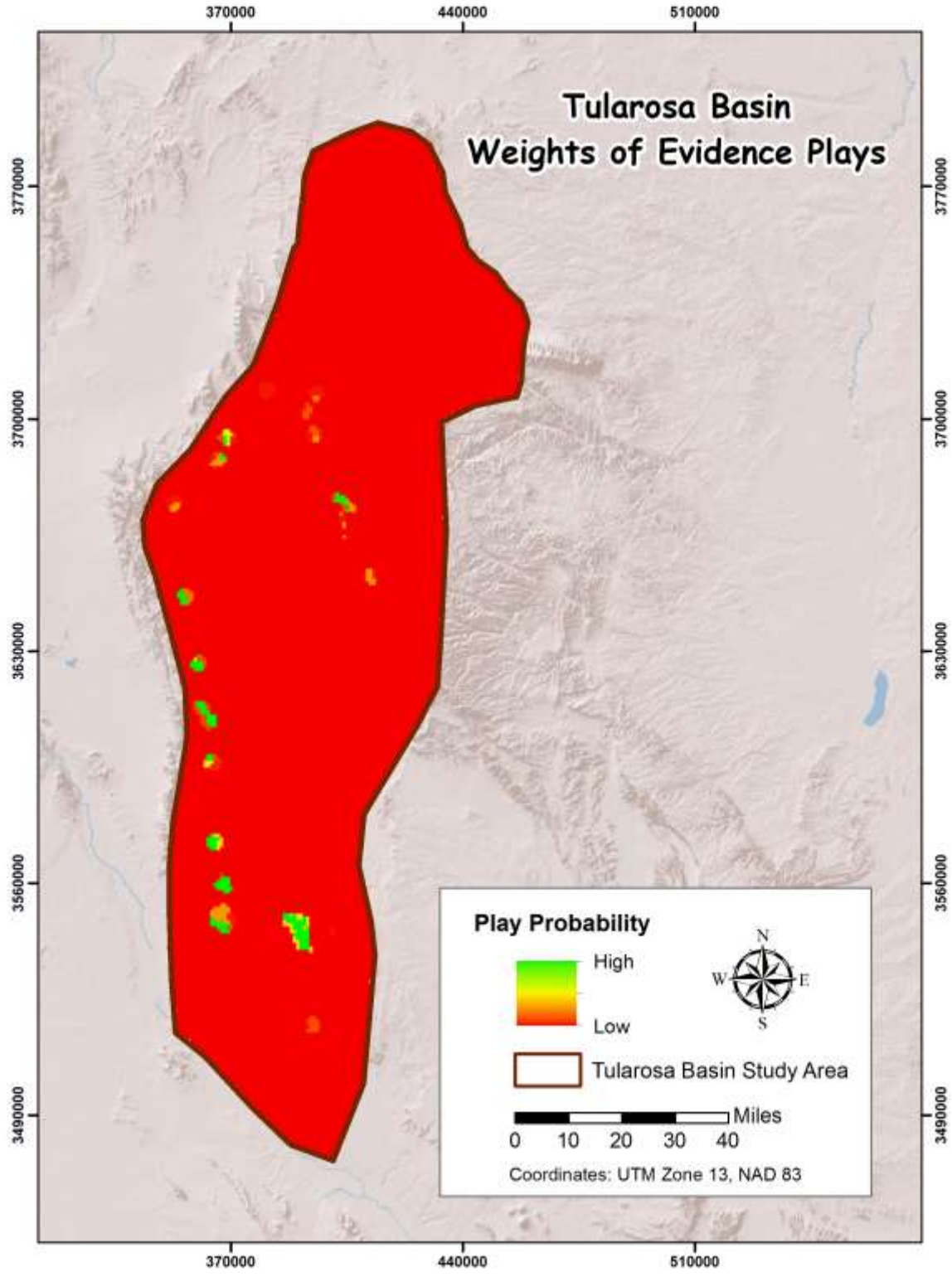

Figure 21. WoE final play probability map.

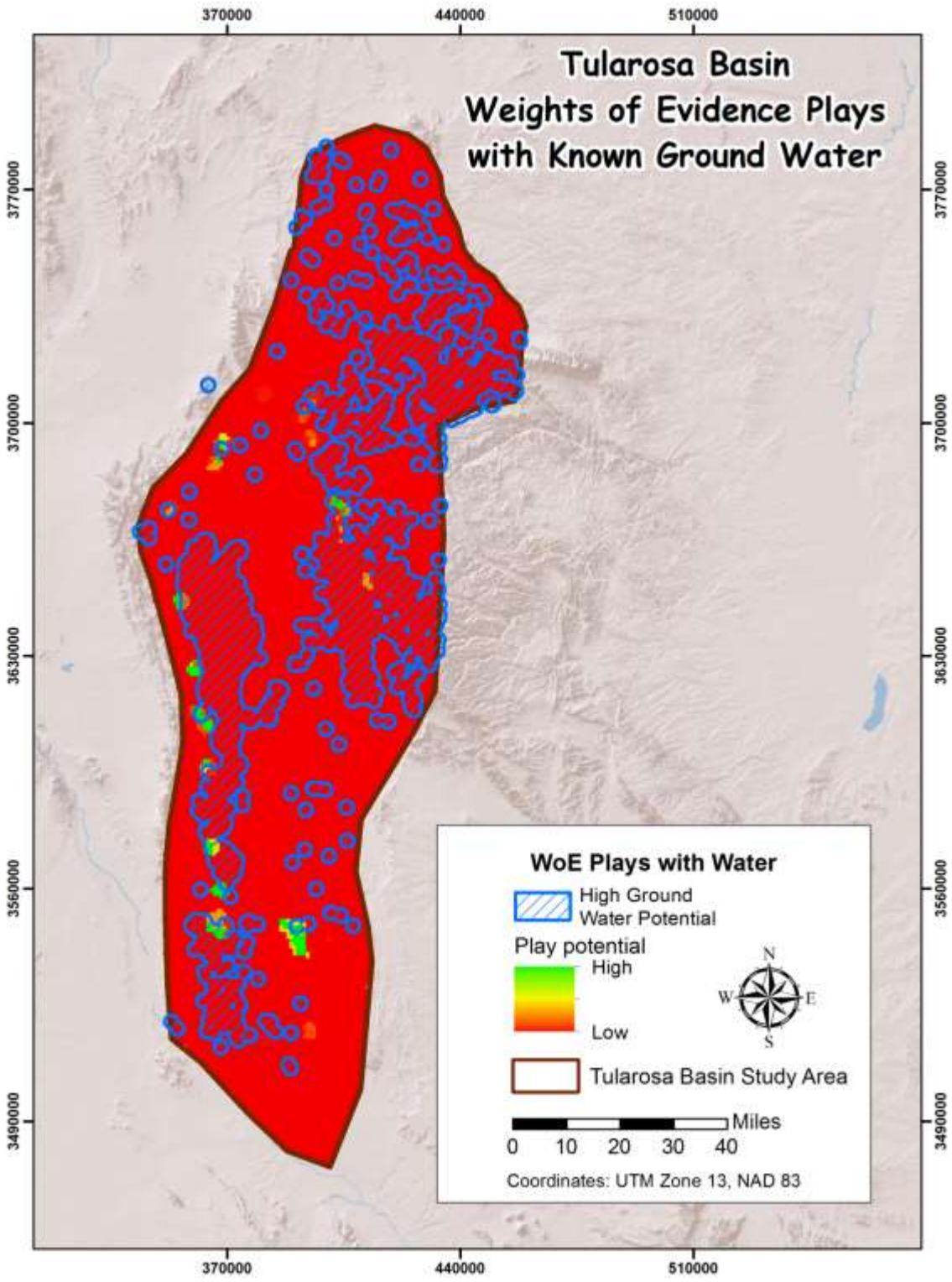

Figure 22. Ground water potential from the deterministic model overlain on WoE plays. Ground water potential is high on or bounding all plays.

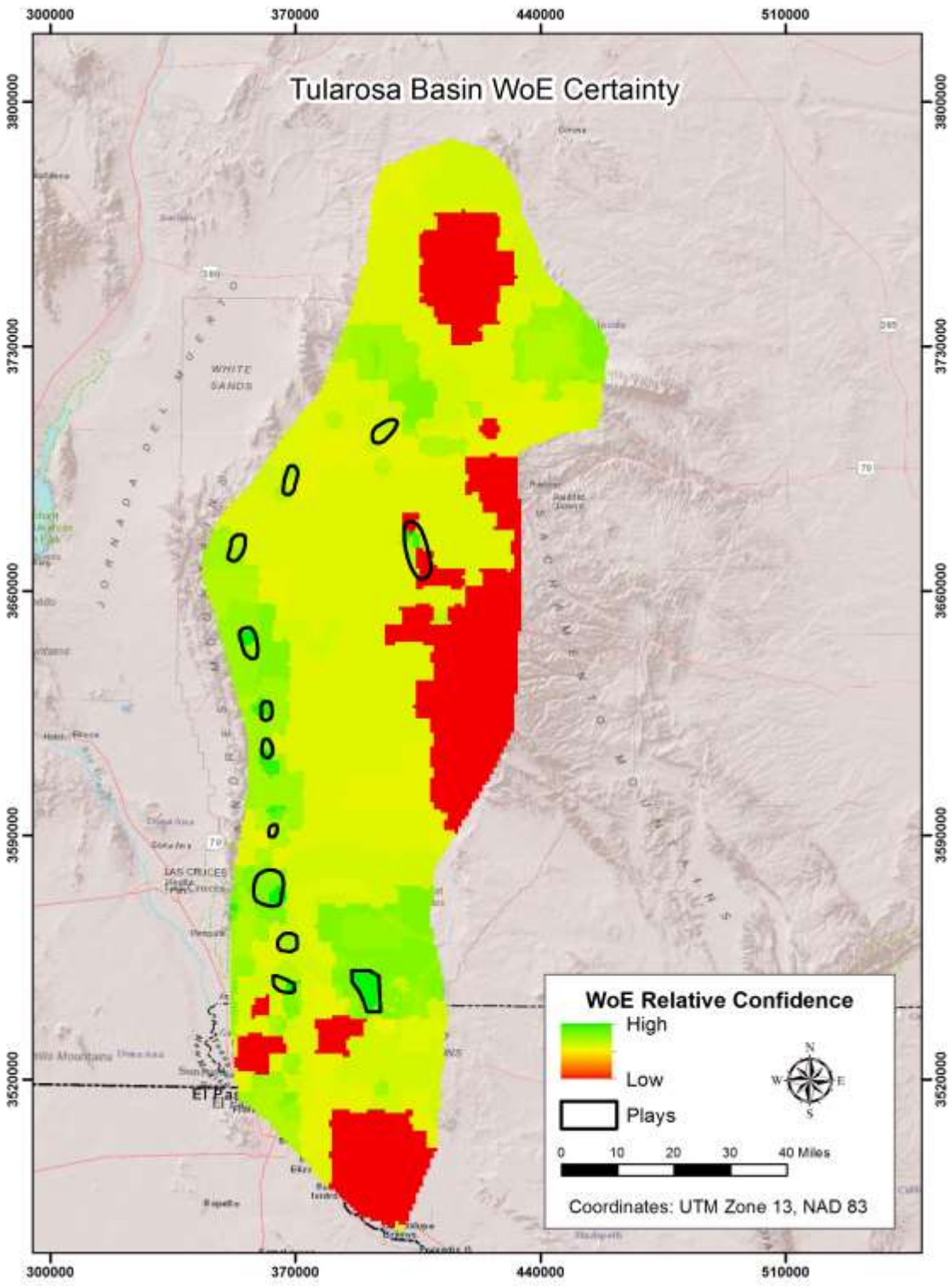

Figure 23. WoE confidence layer generated using the Spatial Data Modeler. All plays are in medium high to high confidence areas; although a single play also has low confidence areas included bounding a high confidence area.

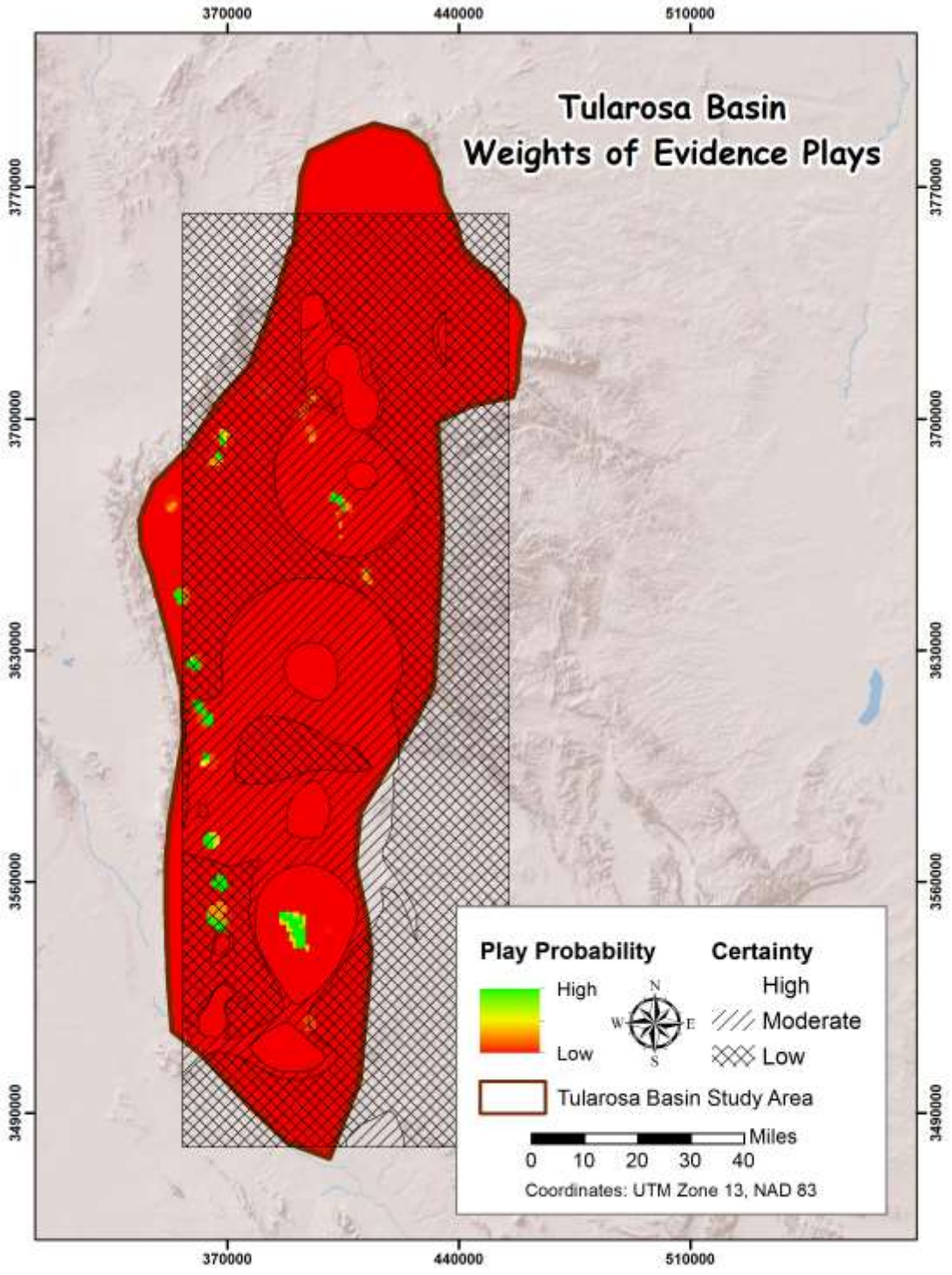

Figure 24. Certainty based upon probability kriging. Heat layers of evidence were used in this analysis, the results of which are more conservative than the WoE confidence surface with only the McGregor Range play having high certainty and three other plays having moderate certainty. Areas outside of the certainty polygon lack control data.

4.3 Compare and Contrast of Methods

Both the deterministic petroleum industry logic PFA, converted for geothermal use, and the WoE PFA methods identified potential plays. Six plays were identified by both methods with two additional plays being identified by the deterministic method and four additional plays being identified using WoE.

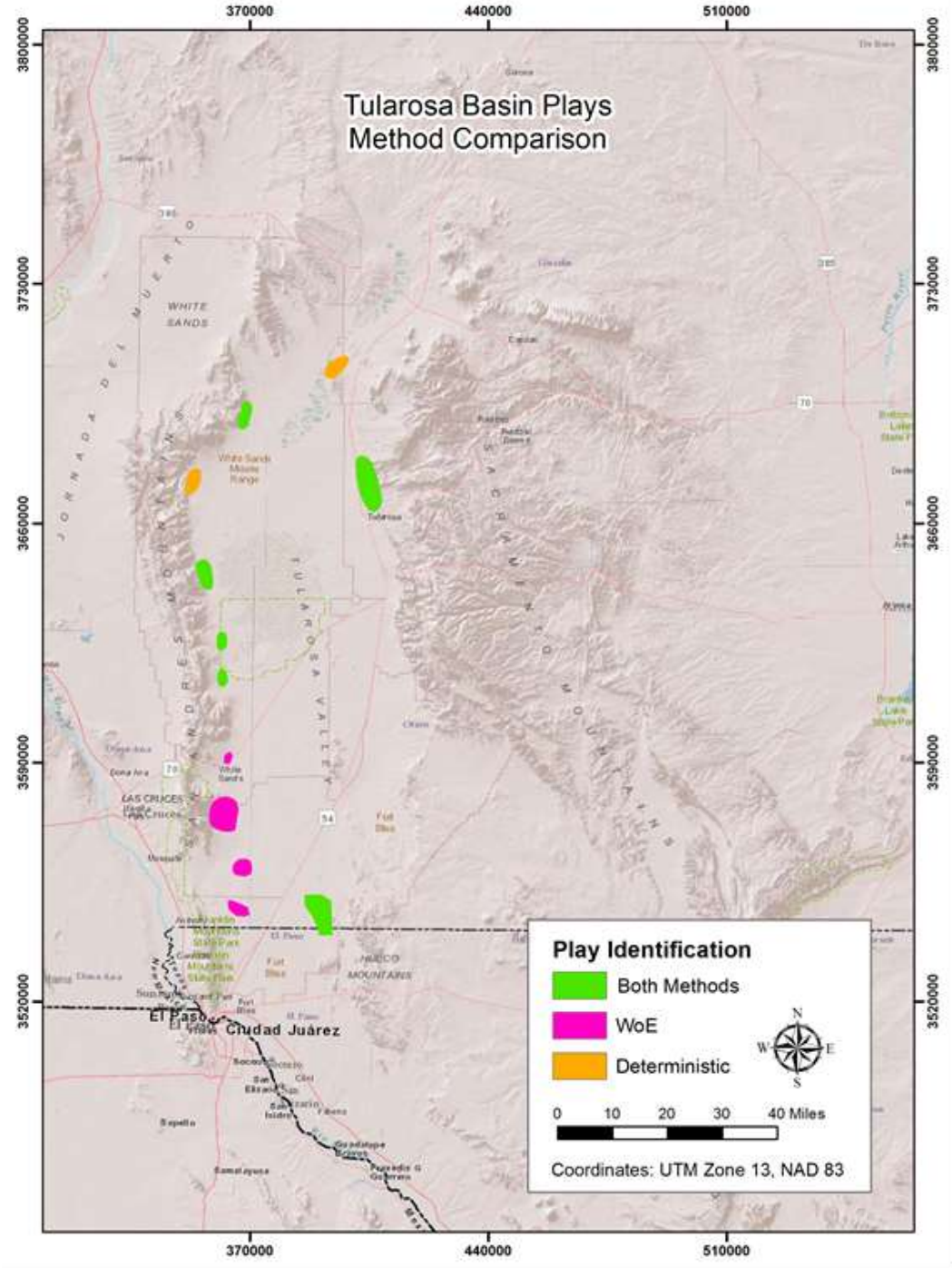

Figure 25. Plays identified by method. Twelve total plays were identified, six by both methods, two additionally by the deterministic method, and four additional by WoE.

In finality, only additional work will allow a definitive comparison of these methods. However, it is our opinion at this time that it would be prudent to apply both methods if possible. What one overlooks the other may see.

Additionally, this redundancy could give more confidence where there is agreement. However, the deterministic approach works and it would be an excellent tool in areas where adequate training sites and supporting data cannot be obtained for use in stochastic PFA.

See Appendix C for flow charts detailing the methodologies. The flow charts will also be uploaded to the GDR in larger formats for easier reading.

SECTION 4: FINAL TULAROSA BASIN PLAY RANKINGS

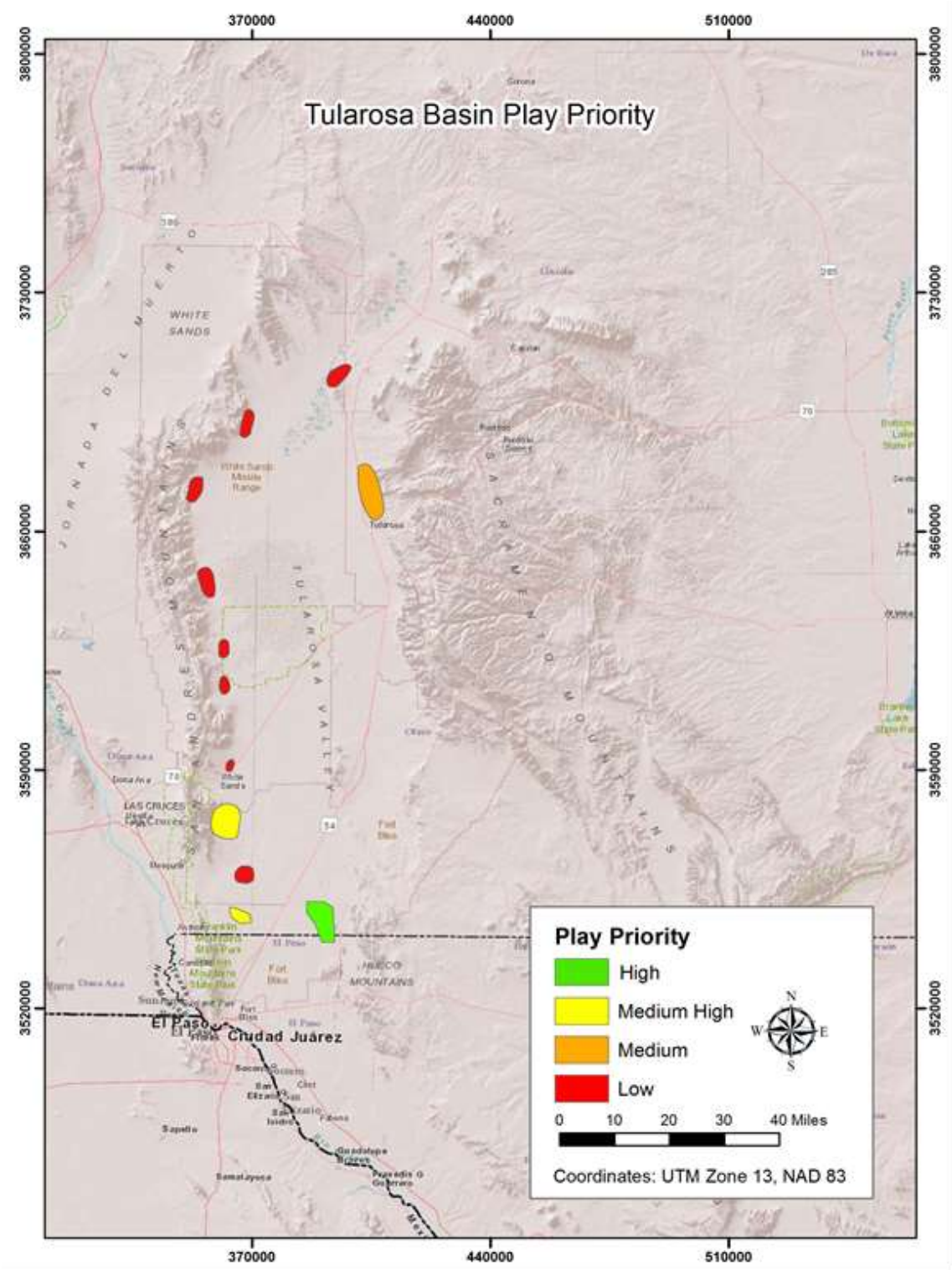

Figure 26. Play priority based upon structure, WoE probability, and proximity to permissible data points.

SECTION 5: ASSESSMENT OF RISK & REWARD FACTORS

5.1 Assessment Methodology

Background

A hallmark of the best use of PFA for effective decision making is the integration of incomplete data sets in a way that consistently weighs the uncertainty associated with the various measurements. In the petroleum industry the use of fully probabilistic geo-statistical modeling has been very successful (c.f., Journel, A.G.).

In practice, the vagaries of budget cycles, survey and drilling equipment availability, investor philosophy, and so on, mean that some mix of deterministic and probabilistic methods is almost always used. At this preliminary stage of data collection, the resources are not available to rigorously demonstrate the ideal industrial-strength analysis. This section will illustrate the analysis using largely deterministic values, with remarks on the potential for applying a probabilistic approach at key points.

This Phase 1 analysis also differs from the real world in that we are considering a scenario in which exploration data is available for analysis in a single package that would actually be acquired over a period of months or years. Iterative analysis of collected data and new data as it is discovered is the norm in industry. Most managers of the authors' acquaintance consider it essential to focusing exploration dollars on areas having the highest probability of success.

Estimation of Productive Area

Continuously processing new information allows for fluidity of the valuation of a project. In this early phase of data collection and analysis of existing data, a simpler deterministic approach to several parameters was sufficient to demonstrate the ability of PFA to identify attractive prospects in the Tularosa Basin.

The area for exploration and eventual development for production for each of the play was estimated using the following steps:

1. The total area of the play, as defined in the preliminary study of the basin, was considered to be a target for further geological, geochemical and geochemistry (GGG) studies. These are collectively referred to as surface exploration studies. As the three plays selected are of similar size, a total cost of $350k was assigned to each.

2. The surface exploration work provides the information necessary to select the portion of each play with the most favorable conditions for further expenditures. In this example we arbitrarily used 50% as the cull fraction. In practice, this fraction will be dependent on the actual results. We would, for example, expect the cull fraction to be small near Yellowstone and quite large in the Appalachians. The next step in exploration is temperature gradient well (TGW) drilling. For this example we used a TGW density of 1 well/km^2.

3. Refine the area for exploratory well drilling by eliminating areas of low temperature gradient from further consideration. This will normally be accomplished in concert with geostatistical modeling as described in the background discussion above. In the present case a simpler approximation was developed assuming normally distributed gradient values. The gradients measured in several hundred TG wells throughout the Tularosa Basin range from 25-140°C/km. If we assume this range covers about 95% of the possible values, we can construct a normal distribution curve with 25°C/km and 140°C/km assigned to probability values of -2σ and +2σ, respectively. The high risk threshold for CRS is defined as 60°C/km, so we excluded areas with a gradient ≤ 60°C/km. The cumulative probability of a gradient exceeding 60°C/km is 78% for the distribution as described, so exploratory wells will be drilled on 78% of the area passing the initial surface screening in step (2). For this example, a density of two exploratory wells per ten square kilometers was assumed.

4. Estimate the likelihood of successful exploration well drilling. This lends itself to Monte Carlo simulation if no experiential data exists for the play in question. For this example, a probability of success of 45% was used, based on the initial drilling experience reported in Indonesia (Sanyal and Morrow). The reported success rate increased to nearly 70% with experience, but the small size of the subject plays makes choosing a lesser value prudent. We acknowledge the vast geologic differences between the Tularosa Basin and Indonesia, but find that the reported drilling success rates are consistent with the proprietary domestic industrial experience of which we are aware.

To illustrate the process of this approach to narrowing the focus of the study to the most prospective area, the table below summarizes the percentages applied to each activity phase for all the plays identified.

Table 2. Percentages Applied to Each Activity Phase

Area Selected from Total Play				
	Surface Exploration	**Temperature Gradient Wells**	**Exploration Wells**	**Successful Development Wells**
Activity applies to:	**100%**	**50%**	**39%**	**18%**

5.2 Cost and Revenue Calculations

Gross Revenue

A target plant capacity of 10 MW per 10 sq. km. was used as the basis for gross revenue calculations. Plant and well field parasitic load was assumed at 25%, based on industrial experience (Verkis Consulting Engineers). Flash plants normally show records of 4% to 7% parasitic loads while binary plants' parasitic loads may range from 15% to 40%, or higher depending on the high use of pumps to flow the wells.

Net present value of future annual revenue estimate is calculated as the product of the Estimated Net Generation and the electricity price over a lifetime of 30-years. A discount rate of 2%, the average US inflation rate from 2010 to 2014, was used in the calculation.

Cost of Exploration

Well exploration cost was estimated using the formula defined in The 2011 Geothermal Well Cost Update (Mansure and Blankenship), which calculated to around US $3 million per well. The total cost of exploration for all three plays ranged from $1,360 to $1,516 per kW installed capacity.

Development and Plant Cost

An additional five (5) production wells and two (2) injection wells for a 10-MW plant capacity per 10 km^2 was used in constructing a deterministic cost profile for each play. These are representative values from existing Basin & Range plants but we would expect more sophisticated probabilistic modeling to be used when the surface exploration and TGW data are in hand.

Operating cost assumptions and plant cost estimates were provided by industry experts and validated by information taken from an Icelandic review of low temperature geothermal power plants (Verkis Consulting Engineers). The figure below summarizes the data used as assumptions in the exercise.

Table 3. Expected Value of Plays – Elements of Calculation

	Unit	**Play #1 (McGregor)**	**Play #2**	**Play #9**
Area of Play	sq. km	70.00	86.00	73.00
Reservoir Thickness	m	914.63	914.63	914.63
Minimum Temperature	°C	90.00	75.00	85.00
Maximum Temperature	°C	110.00	85.00	100.00
Depth to reach Minimum Temperature	m	909.09	727.27	848.48
Depth to reach Maximum Temperature	m	1,151.52	848.48	1,030.30
Target Depth of Wells at 400m into reservoir	m	1,309.00	1,127.00	1,248.00
Drill TG wells on 50% of Explored Area	sq. km	35.00	43.00	36.50
Area for Exploration Drilling	sq. km	27.41	33.67	28.58
Number of Temperature Gradient Wells	ea	35	43	37
Number of Exploration Wells	ea	5	7	6
Number of Production Wells	ea	6	8	6
Number of Injection Wells	ea	2	3	3
Target Capacity in Identified Play	MW	12.70	15.61	13.25
Plant Availability	%	95	95	95
Plant & Wellfield Parasitic Loads	%	25	25	25
Electricity Price	$/kWh	0.1724	0.1724	0.1724
Number of Operating Years	yrs	30	30	30
NPV Discount rate	%	2	2	2

Results

The Levelized Cost of Power (LCP) ($/kWh) was calculated as the initial capital investment, including exploration costs plus the cumulative present value of future costs discounted by the assumed inflation rate, divided by the cumulative power generation over the project life. LCP for all three plays was about $0.08/kWh.

The analysis described herein dispenses with some sophistication in modeling parameters for which reasonable values can be assigned. This is appropriate for an initial screening exercise in which the object is to learn whether there is sufficient economic attractiveness to pursue further work in a basin. The results clearly demonstrate that the unusual market conditions (i.e., $/kWh price) in the Tularosa Basin make all three plays viable candidates for exploration and development. The results are similar for all three plays identified by the PFA process. The figure below shows each has an expected net present value greater than $120 million.

Table 4. Net Present Value of Plays

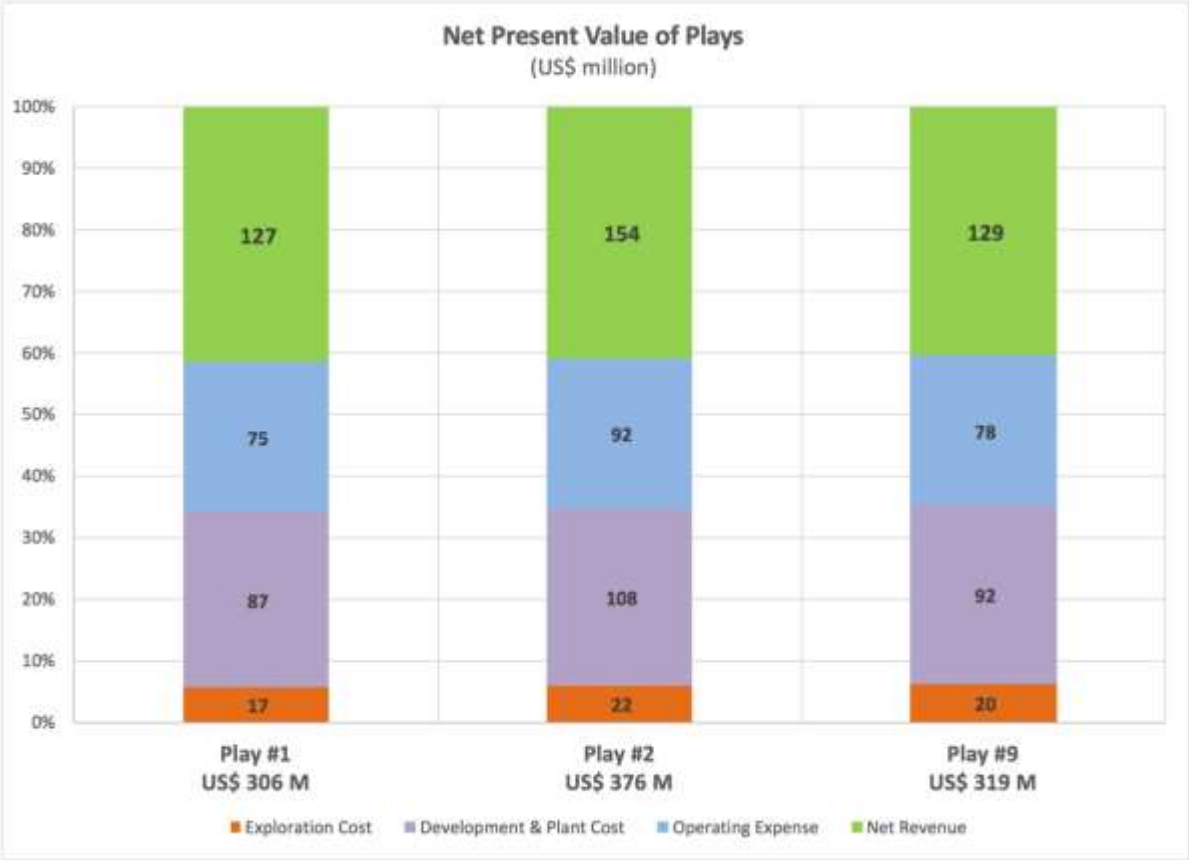

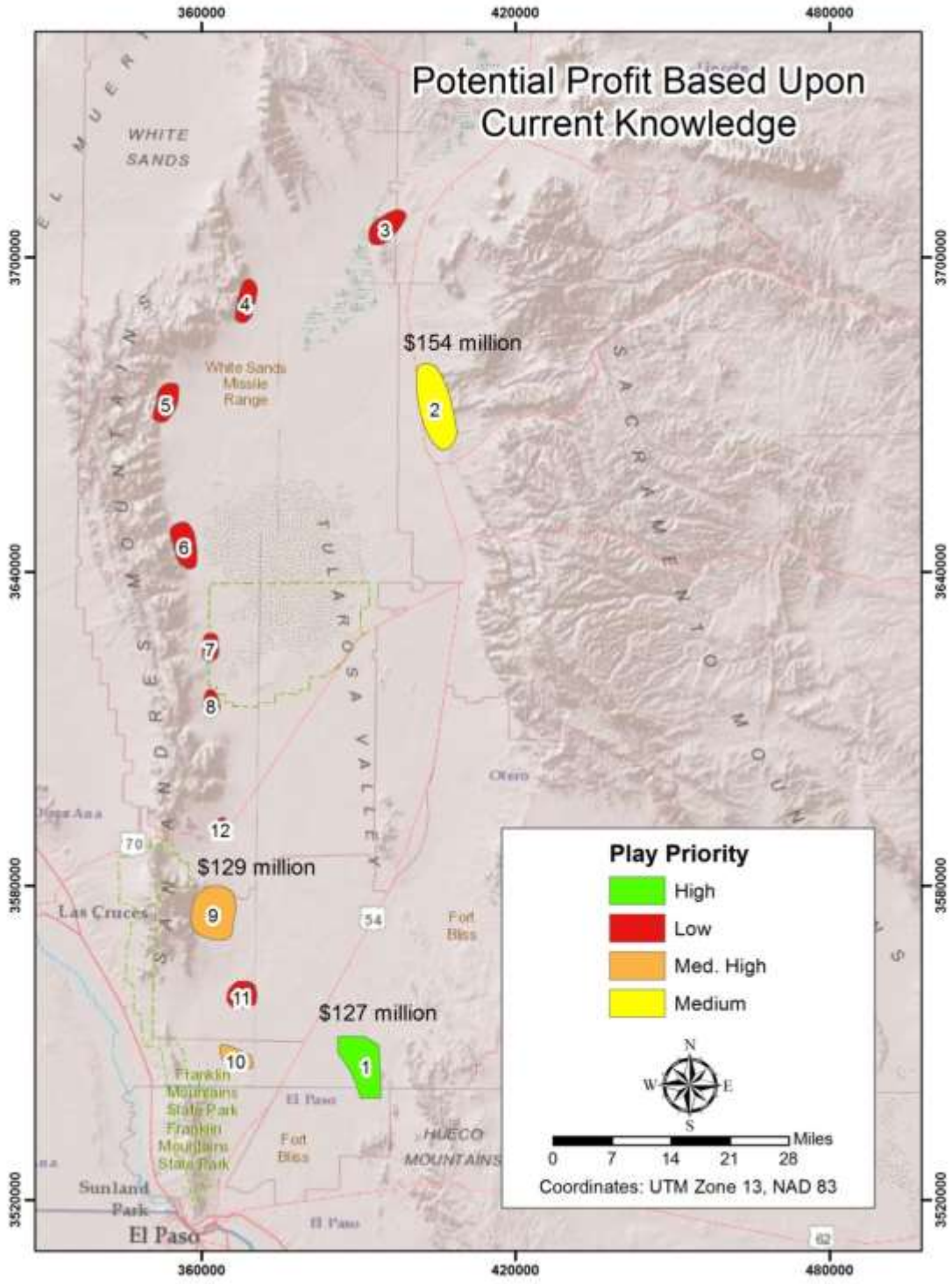

Figure 27. Profit potential of medium to high priority plays. Please note that Play 1 is the most data rich (low uncertainty), yet needs additional work to substantiate economic analysis. Plays 2 and 9 are relatively data poor and need considerably more work to facilitate refinement of this preliminary economic analysis. Please note that Play 10, although considered to be of Medium High priority, has low certainty due to critical data paucity, so no economic analysis was done for this play. Phase 2 addresses additional data needs that will allow better economic modeling.

Table 5. Levelized Cost of Power and Expected Net Present Value of Plays

	Unit	Play #1 (McGregor)	Play #2	Play #9
Area of Play	Sq. Km	70.00	86.00	73.00
Area for Development Drilling	sq. km	12.33	15.15	12.86
Target Capacity in Identified Play	MW	12.70	15.61	13.25
Annual Net Generation	MWhr/yr	79,288	97,411	82,686
Cumulative Net Generation Over Project Life	MWhr	2,378,644	2,922,334	2,480,586
Annual Gross Revenue	$/yr	13,669,274	16,793,680	14,255,100
Cumulative Net Present Value of Gross Revenue	$/project life	306,143,292	376,118,902	319,263,719
Surface Exploration & Exploration Drilling Cost		17,280,829	22,299,324	20,085,930
Surface Exploration	$	350,000	350,000	350,000
Temperature Gradient Wells	$	700,000	860,000	740,000
Exploration Well Cost based on Depth	$/ea	3,246,166	3,012,761	3,165,988
Total Cost of Exploration Wells	$	16,230,829	21,089,324	18,995,930
Surface Exploration and Expl. Drilling Cost Ratio	$/kW	1,360	1,429	1,516
Development & Plant Costs		86,945,540	108,054,001	92,083,376
Production & Injection Wells	$	25,969,326	33,140,366	28,493,896
Pipeline & Facilities	$/kW	16,514,391	20,289,109	17,222,151
Binary Plant & Pump Cost	$/kW	44,461,823	54,624,525	46,367,330
Annual Operating Expense	$	3,338,448	4,101,521	3,481,524
Cumulative Net Present Value of O&M Expense	$	74,769,396	91,859,544	77,973,799
Levelized Cost of Power	$/kWh	0.075	0.076	0.077

5.3 Next Steps

A more refined valuation using Monte Carlo Analysis will suit well Phase 2 of the project when more detailed data can be coupled with practical parameters based on the further study of the plays.

USGS Methods in the Assessment of Identified Geothermal Resources will be used as a way of evaluating reserves versus a conservative density assumption in Phase 1 of the project.

Further studies and information within the Tularosa Basin, like, financing, permitting, transmission details and a defined exploration and development strategy will add more granularity to the next valuation phase. Also, an iterative process of data input and output discussions will provide an environment where research data intersect with actual historical industry performance.

SECTION 6: MARKET TRANSFORMATION

Getting the results of this project in front of geothermal exploration/development companies and military energy decisions makers is a priority for the project team. While market transformation began with our Phase 1 reporting and presentation efforts described below, should we be funded into Phase 2, the project team will expand our efforts through targeted outreach to those two key constituencies.

6.1 Phase 1 Market Transformation Activities

As stated in our original project funding proposal, the project team initiated limited market transformation activities in Phase 1 by presenting our preliminary findings for comment to the DOE Geothermal Peer Review and the Geothermal Resources Council (GRC) in 2015.

For the 2015 Peer Review, a project summary was prepared and a presentation given for comment by the Technical Monitoring Team. The comments received were very helpful and some adjustments in PFA representation made as a result. Also, in 2015 a paper was accepted to GRC and a presentation was given by Dr. Greg Nash. Posters were presented at GRC in both 2014 and 2015. Some promising contacts were made as a result of those presentations. Specifically, during Phase 1, the following market transformation activities were completed:

- **Poster Presentation:** ***Innovative Play Fairway Modelling Applied to the Tularosa Basin***
  Authors: Gregory D. Nash, Ph.D., EGI & Carlon R. Bennett, Sr. Project Mgr., RMI
  Poster Presentation Given at the 2014 Geothermal Resources Council Annual Meeting, Portland, OR, September 2014

- **Publication:** ***Adaptation of a Petroleum Exploration Tool to Geothermal Exploration: Preliminary Play Fairway Model of Tularosa Basin***
  Authors: Gregory D. Nash, Ph.D., EGI & Carlon R. Bennett, Sr. Project Mgr., RMI
  Paper Published and Formal Presentation given at the 2015 Geothermal Resources Council Annual Meeting, Reno, NV, September, 2015

- **Presentation:** ***Preliminary Findings - Innovative Play Fairway Modelling Applied to the Tularosa Basin***
  U.S. Dept. Of Energy Geothermal Technologies Office Peer Review, Westminster, CO, May, 2015

- **Publication:** ***Adaptation of a Petroleum Exploration Tool to Geothermal Exploration: Preliminary Play Fairway Model of Tularosa Basin***
  Authors: Gregory D. Nash, Ph.D., EGI & Carlon R. Bennett, Sr. Project Mgr., RMI
  Paper Published and Formal Presentation given at the 2015 Geothermal Resources Council Annual Meeting, Reno, NV, September, 2015

- **Poster Presentation:** ***Adaptation of a Petroleum Exploration Tool to Geothermal Exploration: Preliminary Play Fairway Model of Tularosa Basin***
  Authors: Gregory D. Nash, Ph.D., EGI & Carlon R. Bennett, Sr. Project Mgr., RMI
  Poster Presentation Given at the 2015 Geothermal Resources Council Annual Meeting, Reno, NV, September, 2015

Additionally in 2015, an article regarding the Tularosa Basin PFA Project was published on EGI's "Ask EGI" website with distribution to 65 energy companies and Ruby Mountain made several presentations on the PFA methodology to military energy management staff.

Since so many agencies were involved in our data collection process at the beginning of Phase 1, Ruby Mountain is in process of planning a meeting to present the final Phase 1 Tularosa Basin PFA Model to stakeholders en masse. Military representatives, government officials, local utility staff and likely some industry representatives will be invited to the presentation which is tentatively scheduled for the first week in December 2015.

Additionally, individual separate meetings will be held with military installation energy staff located within the Tularosa Basin Study area to encourage additional collaboration, collect more information, and most importantly, address how this geothermal exploration methodology can assist them in addressing both current and future installation energy needs.

6.2 Expanded Market Transformation Activities

The project team believes that the play fairway methodology being developed by our project, that while complex, has the unique ability to be easily understood by the educated layman, makes the most of existing data, and is highly replicable. Put simply, getting valuable time in front of key civilian government officials and/or military energy staff is not an easy task, but doing so with a full complement of scientists and researchers in tow is even more difficult. Time with key decision makers is always at a premium and the methodology being proven out by this effort offers a low-cost, pragmatic approach to geothermal exploration which can be easily understood by non-industry, non-academic decision makers.

For that reason, if funded to Phase 2, the project team will develop a market transformation approach for our PFA process which, over the course of the next few years, will offer some near-term market penetration for PFA to facilitate increased geothermal exploration and/or development. Increase market transformation for PFA will require a targeted, multi-faceted approach, but in summary:

- Continued Reporting and Publication of Results through Conference Posters and Presentations;
- Outreach to Industry through EGI;
- Direct collaboration with one or more industry partners;
- Targeted outreach to military energy managers, key installation energy staff and subject matter experts; and,
- Continued exploration / validation of our PFA modelling methodology through expanded project implementation.

At this time, the project team is planning a submittal to the 2016 Stanford Geothermal Conference regarding comparison of the Weights of Evidence PFA Method and Deterministic PFA Methods, and a subsequent paper (topic not yet determined) will be submitted to the 2016 GRC for consideration. Additionally, we are contemplating recruitment of one or more industry partners to assist with validation of the Tularosa Basin methodology(ies) and identifying at least one DoD Energy Conference for which to submit a paper or make a presentation on this project.

SECTION 7: PHASE 1 CONCLUSIONS

The project team has developed the following conclusions through the end of Phase 1 of the Tularosa Basin Play Fairway Analysis Project:

Conclusion #1
The project team successfully developed and compared two methods - deterministic and stochastic – for purposes of creating a play fairway analysis for the Tularosa Basin.

Conclusion #2
Twelve total plays were identified, six by both methods, two additionally by the deterministic method, and four additionally by the WoE method.

Conclusion #3
Significantly, both methods tested identified the known McGregor Range Geothermal system, so this is an indicator that they are effective tools for geothermal exploration. New work suggested for Phase 2 will provide further proof of their veracity. It is our opinion at this time that it would be prudent to apply both methods where possible - what one method overlooks the other method may see.

Conclusion #4
The project team believes that the play fairway methodology developed by our project, while complex, has the unique ability to be easily understood by the educated layman, makes the most of existing data, and is highly replicable.

Conclusion #5
The project team incorporated economic analysis into the top plays identified by both methods finding what appear at this point to be multiple valuable and marketable plays.

Conclusion #6
Data collection efforts exceeded expectations and individual outreach to key stakeholders yielded significant results in terms of integrating previously unpublished data into the project database. Phase 1 of this study has exponentially increased the level of understanding of the basin from a geothermal resource perspective and could very well lay the groundwork for a clean energy future in the region.

Conclusion #7
DOE funding for this project facilitated the identification of geothermal resources for the first time on a basin-wide scale, bringing a substantial amount of disparate data into a common database for analysis.

Conclusion #8
A comprehensive approach to data collection, and the accompanying GIS database development, can be an effective means of assembling preexisting data (published and unpublished) to assess geothermal potential on a basin (or regional) scale.

Conclusion #9
The project team, led by Ruby Mountain Inc. and The Energy and Geoscience Institute at the University of Utah, had no significant departure from stated goals or methods and brought Phase 1 to a successful conclusion on budget and on time while substantially exceeding cost sharing targets

SECTION 8: OVERVIEW OF PHASE 2 RECOMMENDATIONS

Verifying the existence of the plays identified in this Phase 1 ("ground-truthing") was not done because field work and generation of new data were not part of the allowed work scope. However, Phase 2 will be geared toward collecting data that will provide significant confirmation. These will include (1) mapping detailed surface geology, (2) collecting additional water samples for geothermometry, and (3) measuring temperature gradients in existing wells. The project team also suggests high resolution gravity surveys over the high priority plays to facilitate enhanced structural model development and an MT survey covering the McGregor Range (Play 1) to better characterize the system, which will help us develop a better 3D geothermal system model.

Specifically, we recommend the following activities in Phase 2:

1. Geologic field work. For higher priority plays, surface geologic mapping at high resolution and a fracture study at the outcrop level. For lower priority plays, field reconnaissance to determine if any surficial evidence can be located indicating historic geothermal activity. This work often results in the discovery of subtle geothermal manifestations, as well as a better understanding of the site specific geology.

2. Additional water sample collection. Samples should be gathered from all plays where water chemistry is lacking. The samples will be used for geothermometry and isotopic analysis. Down-hole temperatures can be measured during water sampling to improve the temperature and temperature gradient data bases.

3. Gravity data infill for the highest priority plays. Phase I relied on regional-scale gravity data. Surveys on finer grids will provide additional structural information and help gain a better understanding of the relationships of basement faulting to Quaternary surface fault expressions and zones of permeability.

4. An MT survey on the highest priority play, McGregor Range. This will help characterize the system and identify up-flow. This will be integrated into a 3D geothermal model with existing lithologic and new structural data.

5. A flow test of well RMI 56-5 at the McGregor Range. A comprehensive flow test will determine its viability for power production, will indicate resource volume, and may detect boundaries. A concerted effort is under way to obtain a portion of funding for this test (50-75 percent) from other sources.

6. Update the GIS database and PFA models and upload all new data to the GDR.

7. Conduct advanced probabilistic economic modeling in high priority plays based upon Phase 2 results.

8. Develop a market transformation approach for our PFA processes. The objective is to facilitate the early adoption of effective PFA methods by the geothermal industry. Near-term market penetration for PFA will be encouraged by a successful project.

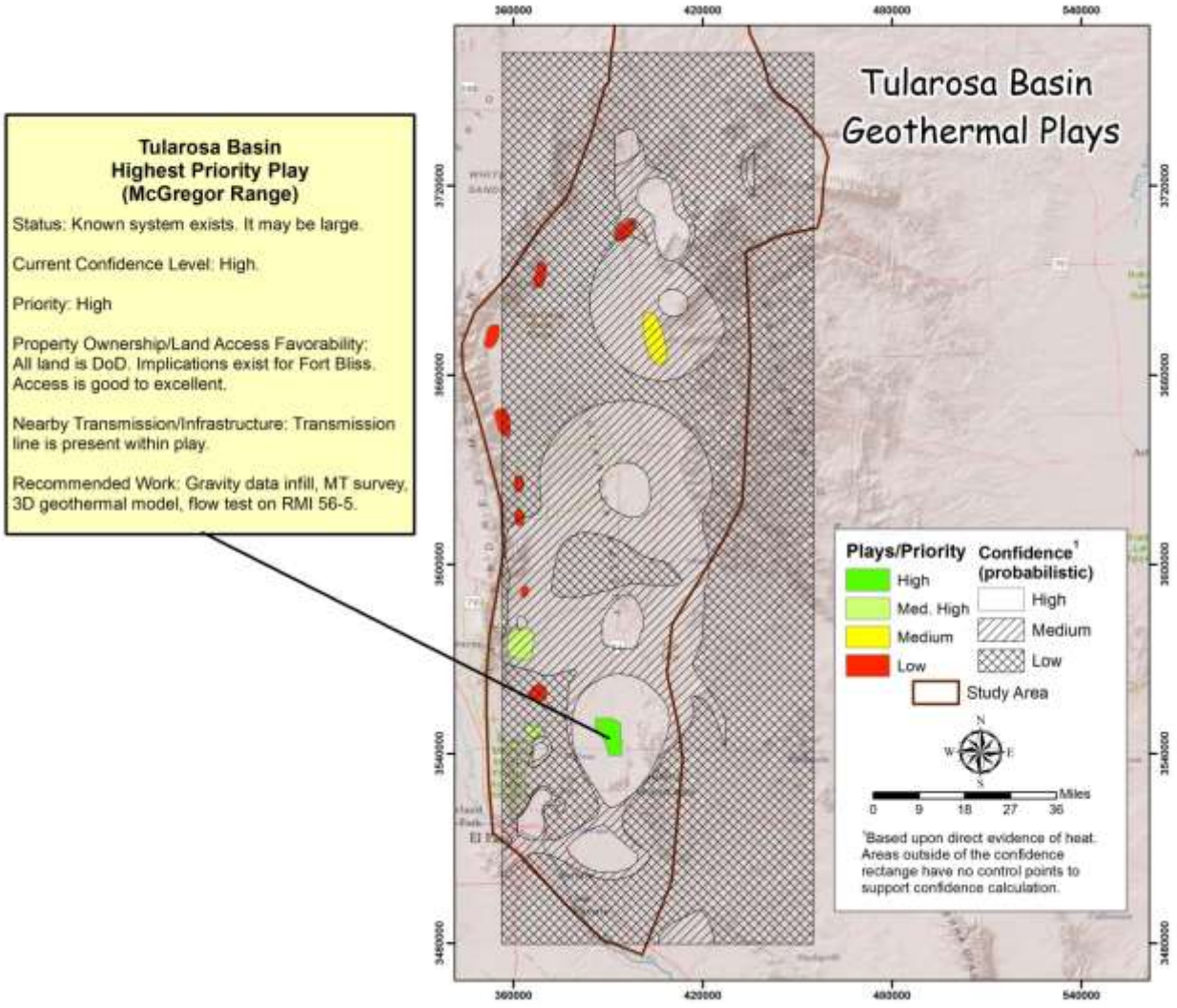

Figure 28. Phase 2 work suggested for the highest priority play.

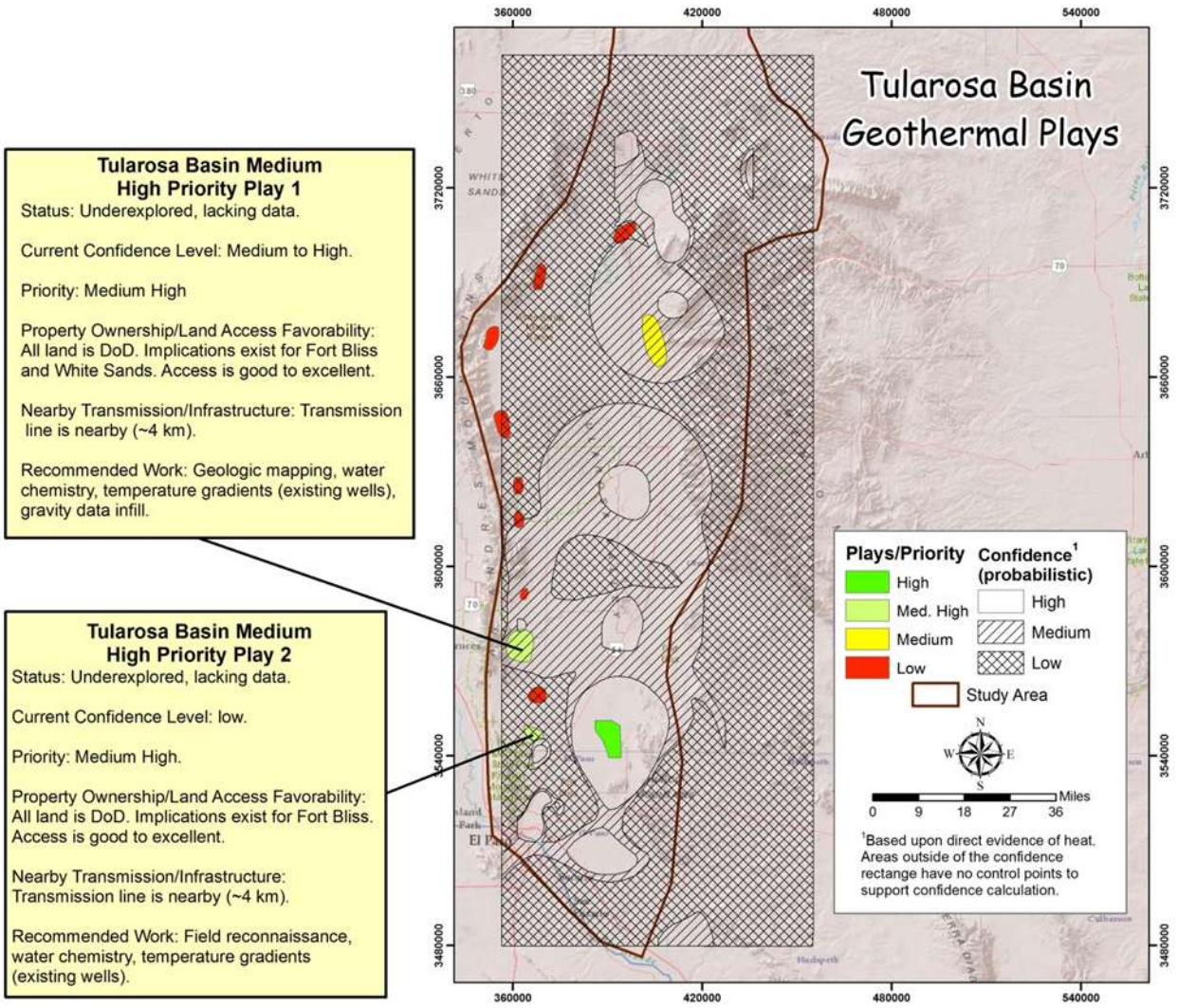

Figure 29. Suggested Phase 2 work for medium-high priority plays. Note that the southernmost play has low certainty which is largely due to a lack of data in the immediate area, so collecting more evidence of heat here would be recommended to raise certainty.

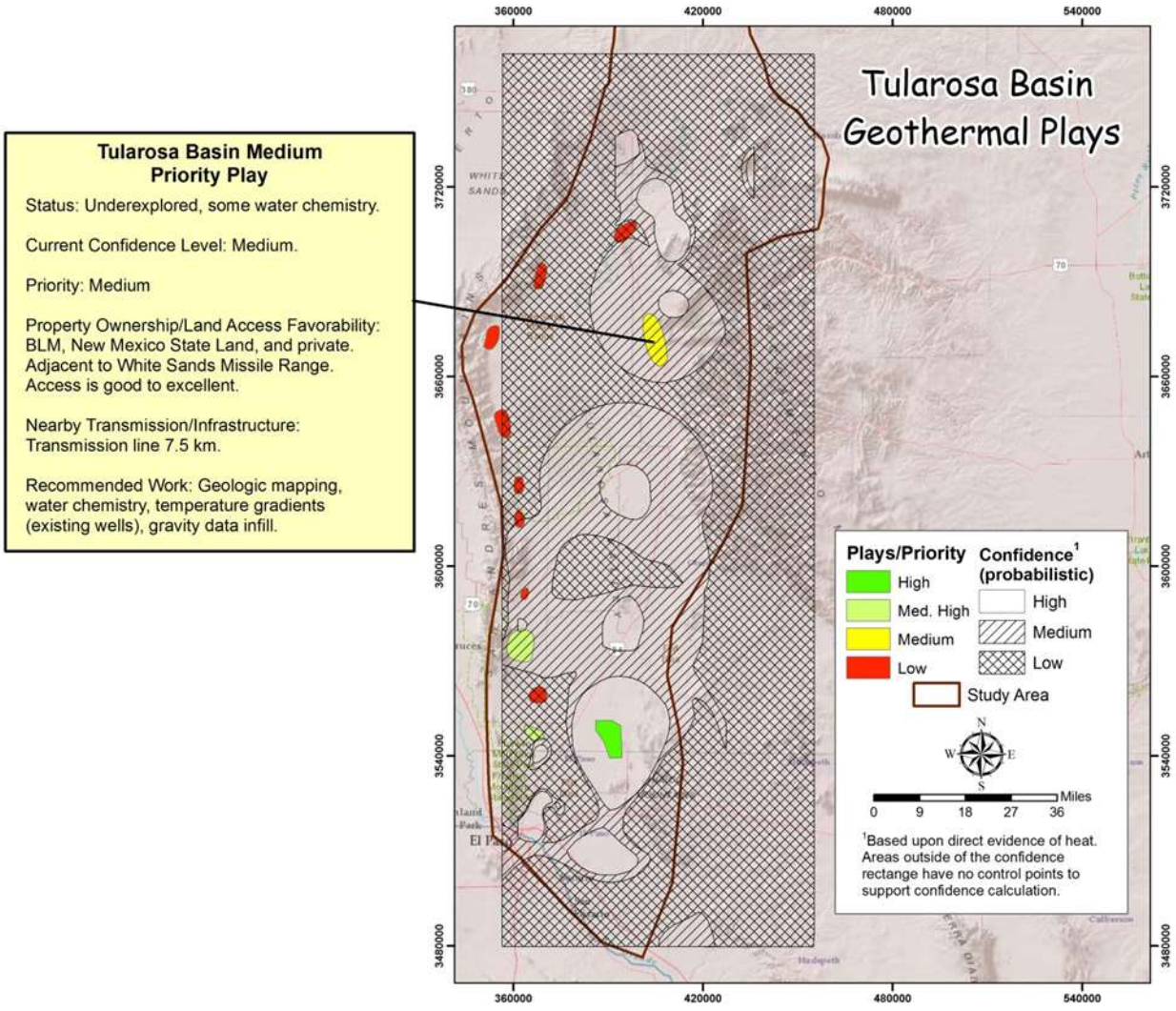

Figure 30. Suggested Phase 2 work for the medium priority play.

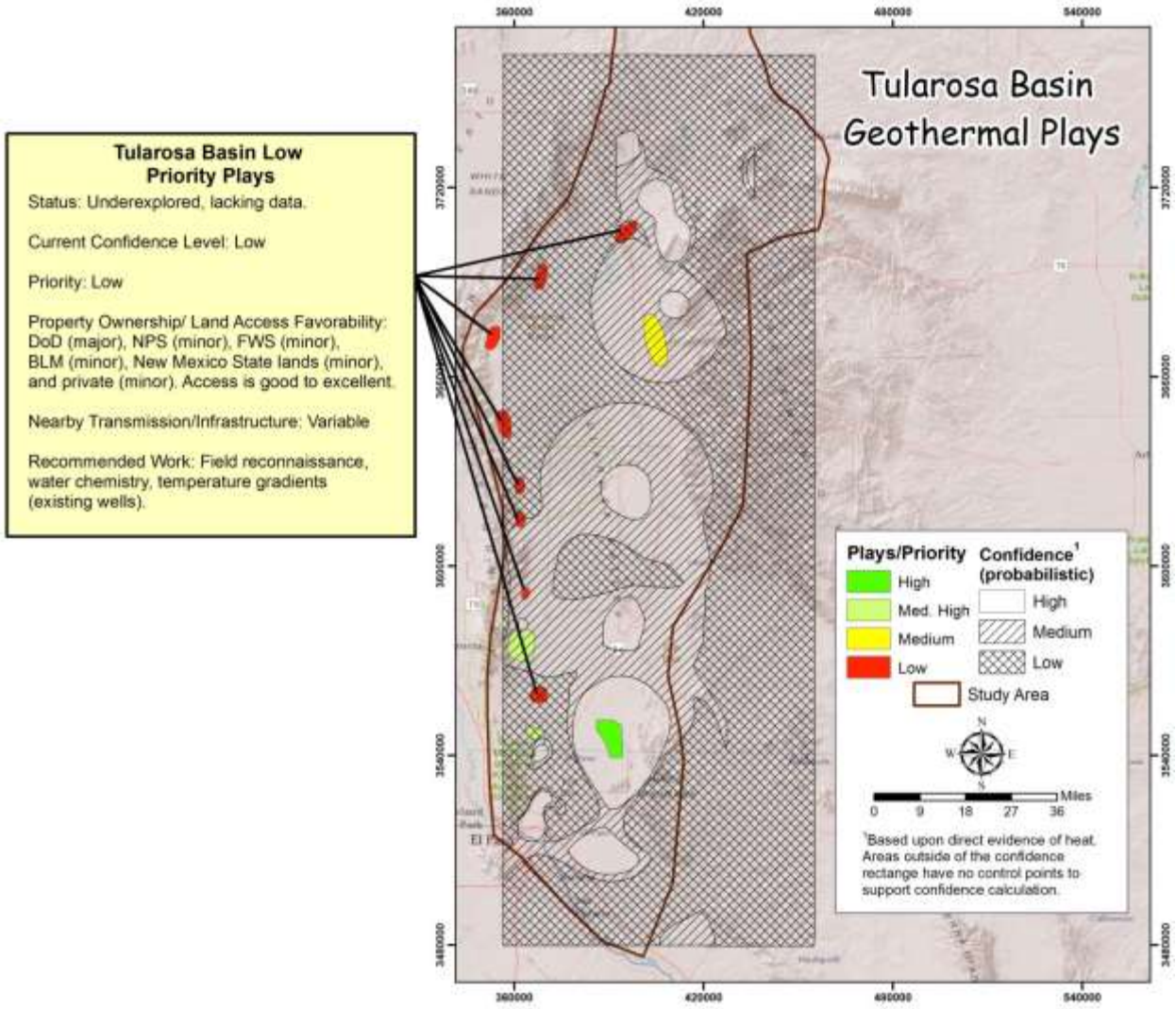

Figure 31. Suggest Phase 2 work for low priority plays.

REFERENCES

Barker, B., Nash, G., Moore, J., and Bennett, C., 2015, Multimodal geothermal development in the Tularosa Basin, NM: Proceedings, 40th Workshop on Geothermal Reservoir Engineering Stanford University, Stanford, California, January 26-28, 2015, SGP-TR-204.

Blackwell, D. D., M. C. Richards, Z. S. Frone, J. F. Batir, M. A. Williams, A. A. Ruzo, and R. K. Dingwall, 2011. SMU Geothermal Laboratory heat flow map of the coterminous United States.

Bonham-Carter, G., 1994. Geographic information systems for geoscientists: modelling with GIS. Pergamon press.

Coolbaugh, M. F., 2003: the prediction and detection of geothermal systems at regional and local scales in Nevada using a geographic information system and thermal infrared imagery. Dissertation, University of Nevada, 172 p.

Coolbaugh, M, C. Kratt, A. Fallacara, W. M. Calvin, and J. V. Taranik, 2007. Detection of geothermal anomalies using Advanced Spaceborne Thermal Emission and Reflection Radiometer (ASTER) thermal infrared images at Bradys Hot Springs, Nevada, USA, *Remote Sensing of Environment*, v. 106, i. 3, p. 350-359.

Cronin, V., Olds, S., Pratt-Sitaula, B., Resor, P., West, N., Hammond, W., & Kreemer, C. (2014). Infinitesimal Strain Analysis Using GPS Data: Module for Structural Geology or Geophysics Course. *UNAVCO, Geodetic Education Resources.* Retrieved from http://www.unavco.org/education/resources/educational-resources/lesson/majors-gps-strain/majors-gps-strain.html#development.

Powell, T and W, Cumming 2010. Spreadsheets for Geothermal Water and Gas Geochemistry. Thirty-Fifth Workshop on Geothermal Reservoir Engineering, Stanford University, Stanford, California, February 1-3, 2010. SGP-TR-188.

Dudley, E.A. and G.D. Nash, 2003. **"**Using Thermal Infrared (TIR) Data to Identify Geothermal Anomalies." Geothermal Resources Council *Transactions* vol. 27, 645-647.

Eneva, M, M. Coolgaugh, S. Bjornstad, and J. Combs, 2007. In search for thermal anomalies in the Coso Geothermal Field (California) using remote sensing and field data, *Proceedings*, Thirty-Second Workshop on Geothermal Reservoir Engineeing, Stanford University, SGP-TR-183.

Faulds, J., M. Coolbaugh, G. S. Vice, and M. L. Edwards, 2006. Characterizing structural controls of geothermal fields in the northwestern Great Basin: A Progress Report, GRC *Transactions,* v. 30, p. 69-76.

Faulds, J., M. Coolbaugh, V. Bouchot, I. Moeck, and K. Oguz, 2010. Characterizing Structural Controls of Geothermal Reservoirs in the Great Basin, USA, and Western Turkey: Developing Successful Exploration Strategies in Extended Terranes, *Proceedings*, World Geothermal Congress, Bali, Indonesia, p. 1-10.

Faulds, J. E., N. H. Hinz, C. Kreemer, and M. Coolbaugh, 2012. Regional patterns of geothermal activity in the Great Basin region, western USA: Correlation with strain rates, GRC *Transactions*, v. 36, p. 897- 901.

Faulds, J. E., N. H. Hinz, G. M. Dering, and D. L. Siler, 2013. The hybrid model – the most accommodating structural setting for geothermal power generation in the Great Basin, western USA: *GRC Transactions*, 37, 3-10.

Federal Register, v. 79, no. 55, Friday, March 21, 2014, p. 15732–15733.

Flyn, T. and P.K. Buchanan, 1993, Pleistocene origin of geothermal fluids in the Great Basin, western United States: *Resource Geology*, v. 16, p. 60-68.

Formento-Trigilio, M. L. and F. J. Pazzaglia, 1998, Tectonic Geomorphology of the Sierra Nacimiento: traditional and new techniques in assisting long-term landscape evolution in the Southern Rocky Mountains, *The Journal of Geology*, v. 106, p. 433-453.

Fournier, R. O., 1991, Water geothermometers applied to geothermal energy: in Applications of Geochemistry in Geothermal Reservoir Development, UNITAR-UNDP (ed. F. D'Amore), p. 37-69.

Fraser, A. J., 2001, Vining, B.A. & Pickering, S. C. (eds) Petroleum Geology: From Mature Basins to New Frontiers – Proceedings of the 7th Petroleum Geology Conference, 791–800. DOI: 10.1144/0070791# Petroleum Geology Conferences Ltd. Published by the Geological Society, London, p. 791-800.

Garg, S. K. and J. Combs, 2010. Appropriate ues of volumetric “heat in place” method and Monte Carlo calculations, Proceedings, Thirty-Fourth workshop on Geothermal Reservoir Engineering, Stanford Unicersity, California, SGP-TR-188.

Giggenbach, W. F., 1991, Chemical techniques in geothermal exploration: in Applications of Geochemistry in Geothermal Reservoir Development, UNITAR-UNDP (ed. F. D'Amore), p. 119-144.

Grant, S., N. Milton, and M.Thompson, 1996. Play fairway analysis and risk mapping: an example using the Middle Jurassic Brent Group in the northern North Sea, *Norwegian Petroleum Society Special Publications*, v. 6, Elsevier, p. 167-181.

Hulen, J.B., Nash, G.D., and Deymonaz, J., 2005. Geology of the Emigrant geothermal prospect, Esmeralda County, Nevada, Geothermal Resources Council, *Transactions*, v. 29, 15 p.

Journel, A. G., *Combining knowledge from diverse sources: An alternative to traditional data independence hypotheses*, MATHEMATICAL GEOLOGY, 2002; 34 (5): 573-596.

Mansure, J. and D. A. Blankenship, *The Geothermal Well Cost Update*, GRC Transactions, Vol. 35, 2011.

Mamer, E. A., B. T. Newton, D. J. Koning, S. S. Timmons, and S. A. Kelly, 2014. Northeastern Tularosa Basin Regional Hydrogeology Study, New Mexico, New Mexico Bureau of Geology and Mineral Resources, Open-File Report 562, 78 p.

Mars, J. C. and Rowan, L. C., 2006, Regional mapping of phyllic- and argillic-altered rocks in the Zagros magmatic arc, Iran, using Advanced Spacebourne Thermal Emission and Reflection Radiometer (ASTER) data and logical operator algorithms, *Geosphere*, v. 2, p. 161-186.

Moghaddam, M. K., Y. Noorollahi, F. Samadzadegan , M. A. Sharifi, and R. Itoi, 2013: Spatial data analysis for exploration of regional scale geothermal resources, *Geothermics*, Elsevier, p. 69–83.

Nash, G. D. and P. M. Wright, 1996. Remote sensing and geographic information systems (GIS) - tools for geothermal exploration in the Great Basin, U. S. A.: Sandia National Laboratories, Final Report, Contract #AB-6807, 74 p.

Nash, G. D. and G.W. Johnson, 2003. "Conceptualization and implementation of a tectonic geomophology study for geothermal exploration in the Great Basin, U. S. A." Geothermal Resources Council *Transactions* v. 27, 663-667.

Purelsy, J., S. L. Bilek, and C. J. Ruhl, 2013. Earthquake catalogs for New Mexico and bordering areas: 2005–2009, *New Mexico Geology*, vol. 35, no. 1, p. 3–12.

Rowan LC, Hook SJ, Abrams MJ & Mars JC. 2003. Mapping hydrothermally altered rocks at Cuprite, Nevada, using the Advanced Spacebourne Thermal Emission and Reflection Radiometer (ASTER), a new satellite-imaging system. Economic Geology 98:1019–1027.

Rowan L. C. & Mars J. C. 2003. Lithologic mapping in the Mountain Pass, California area using Advanced Spaceborne Thermal Emission and Reflection Radiometer (ASTER) data, *Remote Sensing of Environment* v. 84, p. 350–366.

Ruby Mountain, Inc., electricity cost data reported by Fort Bliss, 2015

Sabins, A. E., D. J. Walker, J. Unruh and F. C. Monastero, 2004. Toward the Development of Occurrence Models for Geothermal Resources in the Western United States: Geothermal Resources Council *Transactions*, vol. 28, p. 41 – 46.

Sanyal, Subir K. and James W. Morrow, *Quantification of Geothermal Resource Risk—A Practical Perspective*, GRC Transactions, Vol. 34, 2010.

Sawatzky, D.L., Raines, G.L., Bonham-Carter, G.F., and Looney, C.G., 2009, Spatial Data Modeler (SDM): ArcMAP 9.3 geoprocessing tools for spatial data modelling using weights of evidence, logistic regression, fuzzy logic and neural networks. http://arcscripts.esri.com/details.asp?dbid=15341.

Verkis Consulting Engineers, *Geothermal Binary Power Plants: Preliminary Study of Low Temperature Utilization,* Reykjavik, 2014, Retrieved from http://www.verkis.com/media/pdf/iceida-geothermal-binary-overview.pdf

Williams, C. F., M. J. Reed, R. H. Mariner, *USGS Assessment of Identified Geothermal Resources*; Open-File Report 2008-1296

Younes Noorollahi, Ryuichi Itoi, Hikari Fujii, Toshiaki Tanaka, 2007a. GIS model for geothermal resource exploration in Akita and Iwate prefrctures, northern Japan: *Computers and Geosciences*, vol. 33, Issue 8, Pergamon Press, Inc, p. 1008 – 1021.

Younes Noorollahi, Ryuichi Itoi, Hikari Fujii, Toshiaki Tanaka, 2007b. GIS integration model for geothermal exploration and well siting: *Geothermics*, vol 37 issue 2, Elsevier, p. 107-131.

Yousfi, H., S. Ehara, Y. Noorollahi, 2007. Geothermal potential site selection using GIS in Iran: *Proceedings*, Thirty-Second Workshop on Geothermal Reservoir Engineering Stanford University, Stanford, California, SGP-TR-183.

Yousfi, H., S. Ehara, Y. Noorollahi, 2010. Developing the Geothermal Resources Map of Iran, *Geothermics*, vol. 30, issue 2, Elsevier, p. 140-151.

Zehner, R. E., M. F. Coolbaugh, L. Shevenell, 2006. Regional groundwater geochemical trends in the Great Basin: implications for geothermal exploration, GRC *Transactions*, v. 30, p. 117-124.

.

APPENDICES

Appendix A – Supporting Work and Data

Appendix B – PFA Associated Data

Appendix C - Methodology Flow Charts

Appendix A
Supporting Work and Data

Geochemistry

Waters from the play fairway display a broad range of chemical compositions. The chemical analyses are compiled in an ArcGIS shapefile that will be uploaded to the NGR. As an initial check on the analytical quality of the data, the charge balance for each sample was calculated using the Powell and Cummings (2010) geochemical spreadsheet. Charge balances that exceeded 5% were removed from further consideration to minimize the possibility of misinterpreting the data. We consider the most important analyses to be the anions, Cl, SO_4, and HCO_3, which are major constituents of the fluids and thus most likely to be a major contributor to the poor charge balances, and SiO_2. A total of 1644 samples were evaluated and of these, 414 were considered to have acceptable charge balances.

The anion contents of the samples are shown on Figures 1-3. The data are divided into three regions. The northern region lies along the eastern side of the play fairway north of Alamogordo. Mamer et al. (2014) provide a detailed discussion of the hydrology and geochemistry of this area and their work is summarized below. The central and southern regions are located on the western side of the play fairway. Fort Bliss lies within the southern region and data from this site are summarized by Barker et al. (2015). For each region, the compositions of the fluids in terms of their relative contents of Cl, HCO_3 and SO_4 were plotted on a ternary diagram (Figs. 4-6) to determine the dominant water types and to evaluate possible mixing relationships among the waters.

Northern Region

The dominant anions in waters from the northern region are HCO_3 or SO_4 (Figs. 1-4). Cl is a minor component. Ca is the dominant cation, followed by Na and then Mg. Most of the waters can be classified as Ca-SO_4 in composition. SO_4 concentrations are higher in the well waters (mean of 1040 mg/L) compared to the springs (mean of 797 mg/L) and streams (mean of 666 mg/L) but the mean HCO_3 values are similar in all three sample types (mean values range from 209 mg/L for wells to 230 mg/L for springs). Although there is some scatter in the analyses, the waters generally define a linear trend on Figure 4, indicating mixing between two end member waters; one enriched in HCO_3 and the other in SO_4.

Figures 2 and 3 indicate there are systematic changes in the HCO_3 and SO_4 across the region. Overall, HCO_3 contents decrease from east to west whereas the SO_4 contents increase in this direction. The lowest SO_4 contents are found on the western slope of the Sacramento Mountains. These waters have SO_4 contents less than about 650 mg/L. Water from the Tularosa Basin contain up to approximately 3000 mg/L SO_4.

The origins of the waters from the northern Tularosa Basin and the effects of water-rock interactions were examined by Mamer et al. (2014). They concluded the HCO_3 and SO_4 resulted from interactions with limestone and gypsum respectively. Gypsum is common in the evaporate deposits of the basin and is a likely source of the SO_4 occurring in the basin waters. Interactions with limestone, which is present in the range and beneath the basin floor, are considered to be the source of the HCO_3.

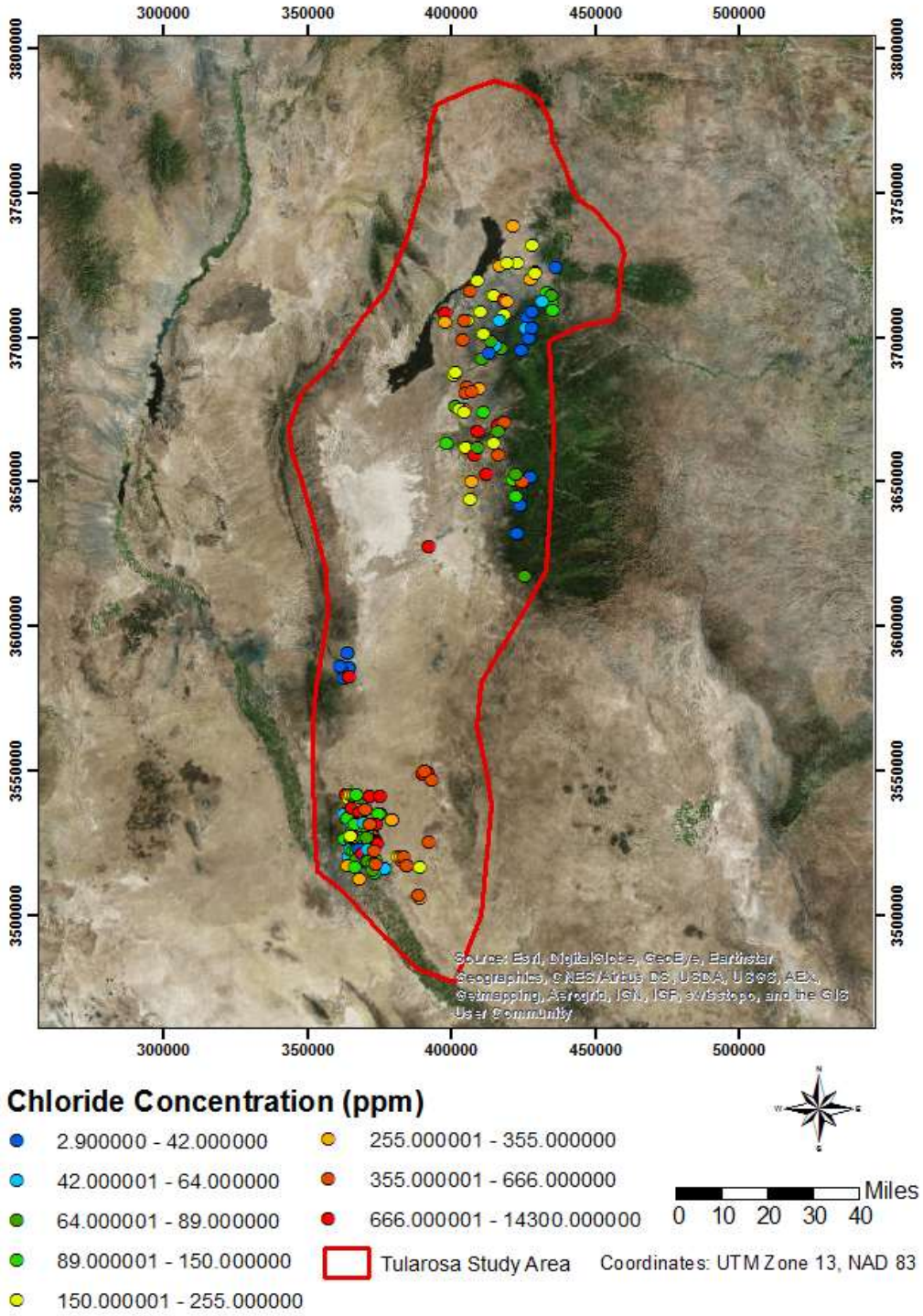

Figure 1. Chloride (Cl) contents of play fairway waters.

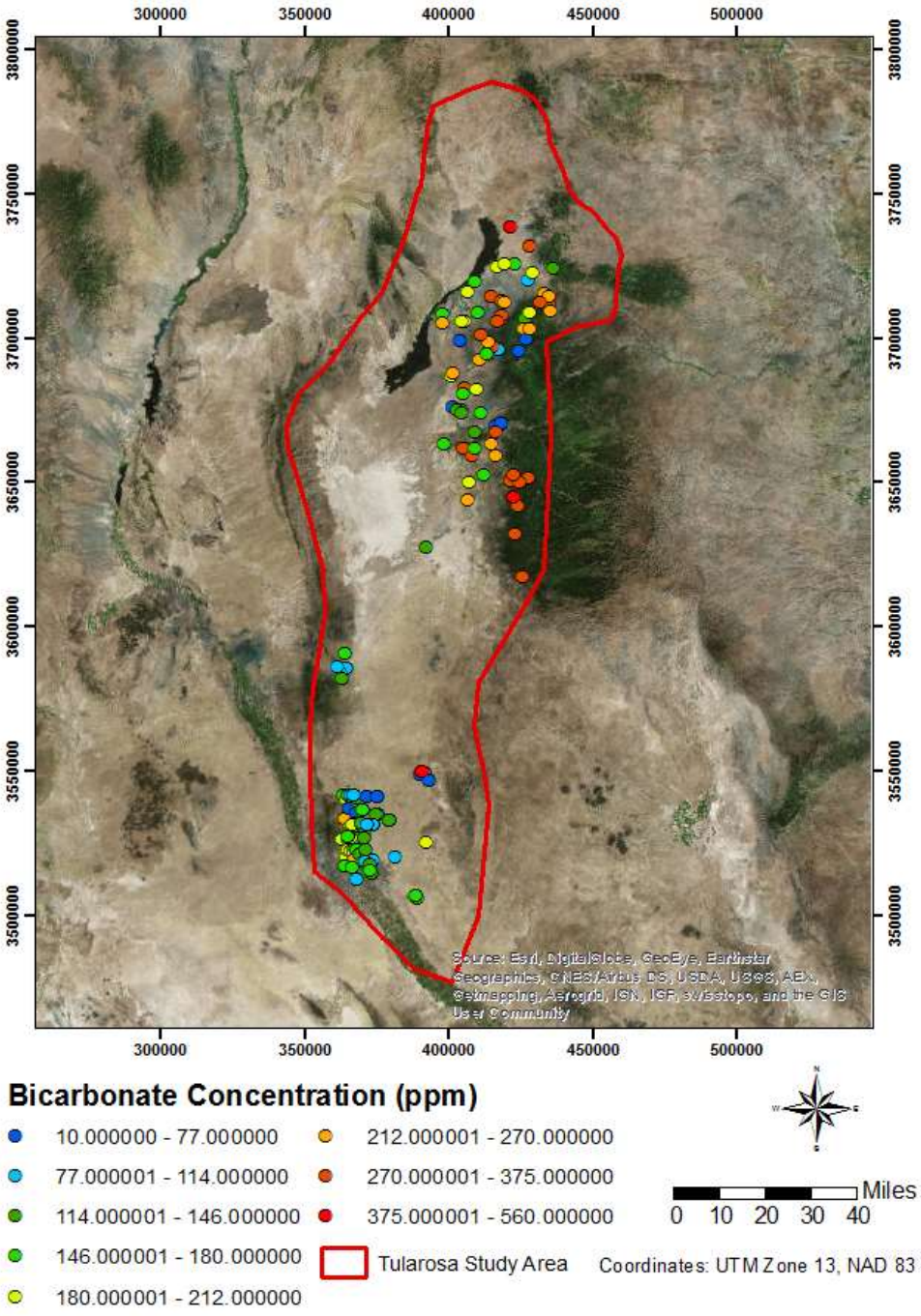

Figure 2. Bicarbonate (HCO_3) contents of play fairway waters.

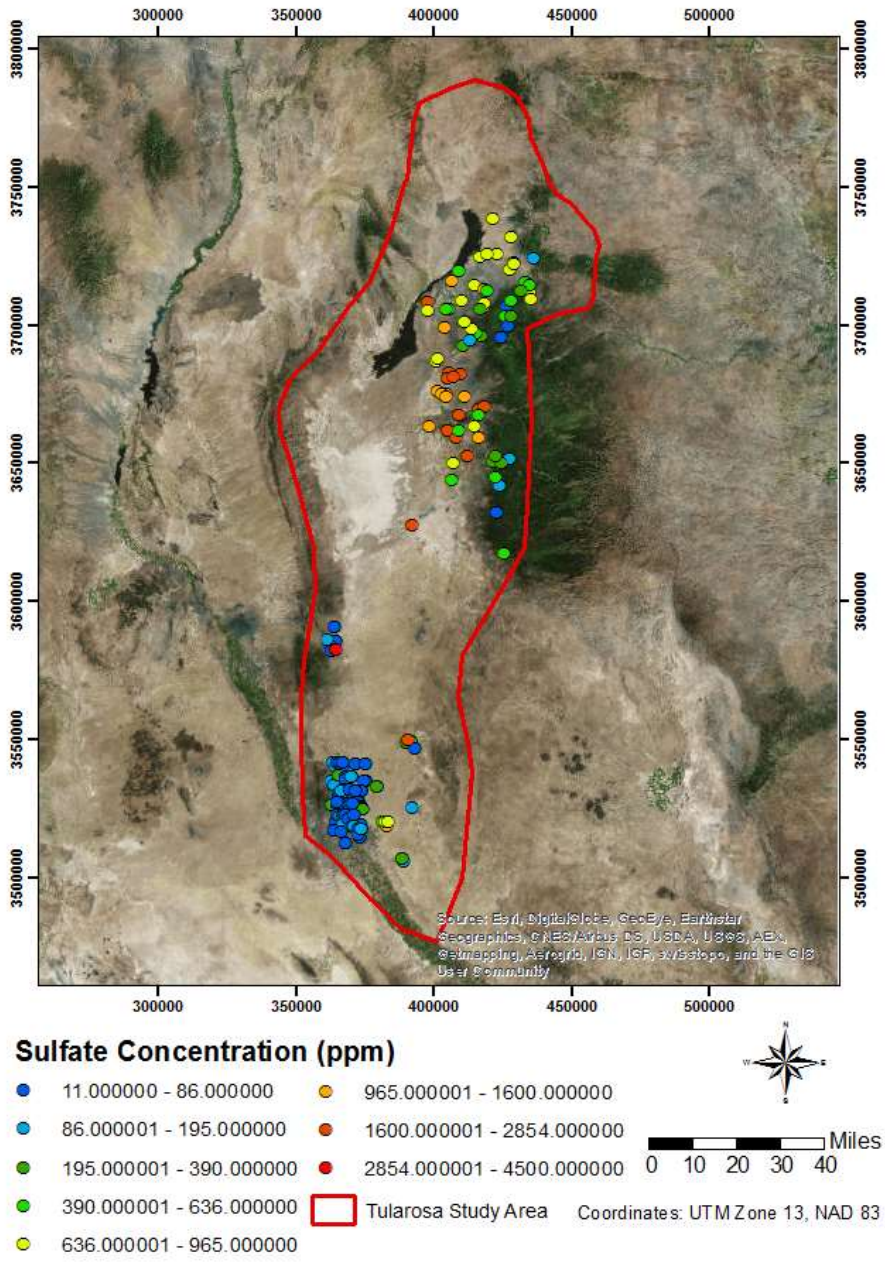

Figure 3. Sulfate (SO_4) contents of play fairway waters.

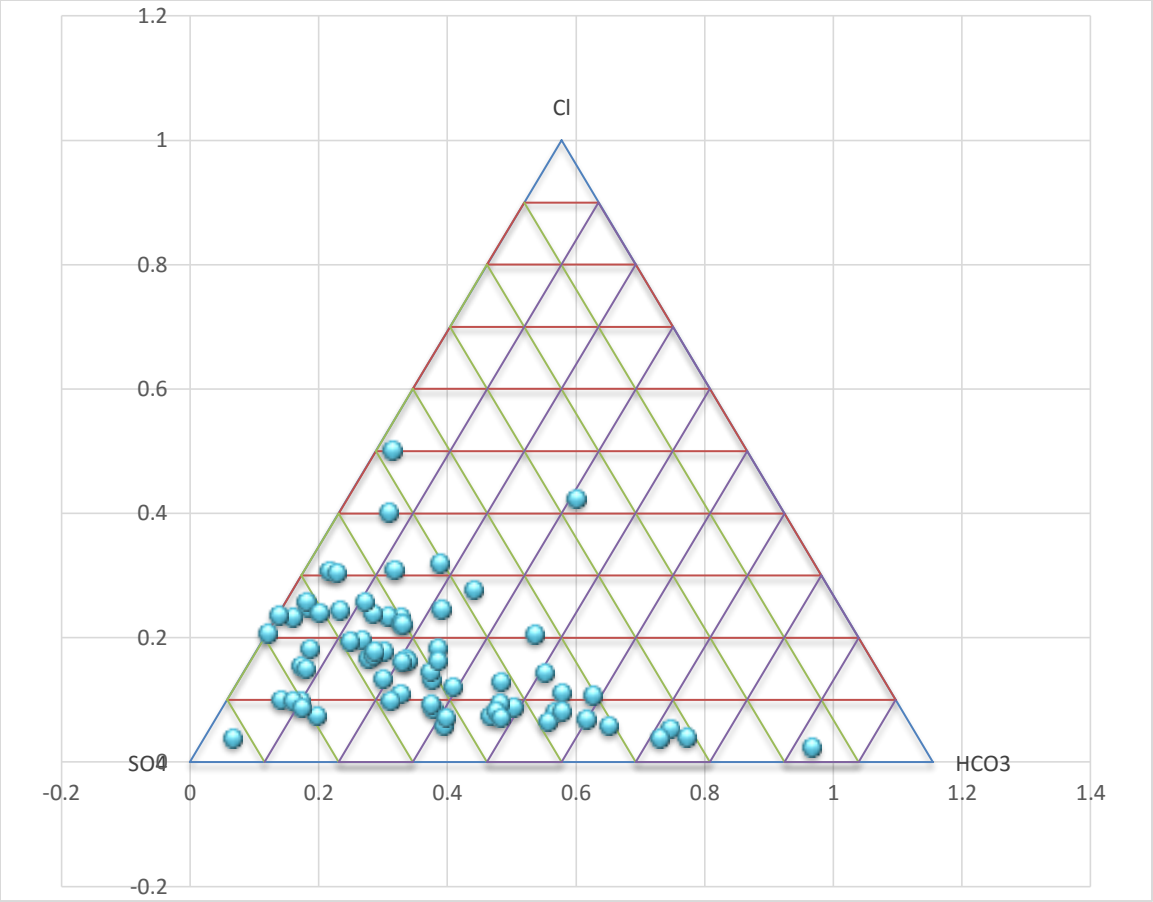

Figure 4. Relative Cl-SO_4-HCO_3 contents of waters from the northern region of the play fairway.

The Cl contents of the waters typically range up to several hundred mg/L, with most samples having a Na/Cl molar ratio of 1. The Cl concentrations display a spatial trend similar to that shown by SO_4, with the lowest Cl contents in the range and the highest in the basin. Mamer et al. (2014) suggested dissolution of halite was the primary source of the Cl and much of the Na based on the Na and Cl ratios.

Mamer et al. (2014) used tritium, ^{14}C and CFC data to assess the residence times of the waters. They concluded that most of the waters recharged hundreds to thousands of years ago and that there is no correlation between the age of the waters and their location.

Central Region

Water samples from the central region are primarily dilute HCO_3 waters with HCO_3 contents up to 150 mg/L, although one brine containing nearly equal amounts of SO_4 (4500 mg/L) and Cl (4100 mg/L) was analyzed (Fig. 5). The dominant cations are Na and Ca or K and Ca. The linear trend defined by the samples suggest they represent mixtures of HCO_3 and SO_4 rich waters, similar to the waters from the northern region.

Southern Region

In contrast to water from other portions of the fairway, the dominant anions in samples from the southern region are HCO_3 and Cl (Fig. 6). Na, followed by Ca, is the dominant cation. With the exception of the samples from the Ft. Bliss wells, waters from the southern region are relatively dilute, with total

dissolved solid contents of 1000-2000 mg/L. The linear relationship displayed on Figure 6 suggests they represent mixtures of Cl- and HCO_3-rich end members. Figures 1 and 2 show that the highest HCO_3 and lowest Cl concentrations are found in the western part of this area, whereas the highest Cl and lowest HCO_3 concentrations occur within the basin to the east. SO_4 concentrations tend to be relatively low, with concentrations less than 100/mg/L in most samples.

In contrast to the remainder of the southern region, Ft. Bliss well waters have total dissolved solids contents close to 10,000 mg/L (1 wt %) (Barker et al., 2015). These waters contain 4000-5500 mg/L Cl and concentrations of SO_4 close to 1000 mg/L. The high SO_4 contents suggest interactions with evaporate deposits; a conclusion consistent with fluid-mineral equilibrium calculations suggesting the water sampled at a depth of 1290 ft in well 56-5 is supersaturated with respect to barite (Barker et al., 2015). In contrast, water from 2960 ft is undersaturated in barite even though both the shallow and deep water contain similar concentrations of Cl and SO_4 (4220 vs 4270 mg/L and 846 vs 834 mg/L respectively). However, no SO_4 deposits (e.g. deposits containing barite, gypsum, or anhydrite) were observed in the cuttings samples from the Ft. Bliss wells. Thus, interactions with evaporate deposits may have occurred in the near-surface environment during wetter climates when lakes were present in the basin.

These chemical relationships suggest the compositions of the HCO_3-rich waters in the southern region are dominated by interactions with limestone beneath the western edge of the fairway whereas the composition of the Cl-rich waters is strongly influenced by evaporate deposits in the basin.

Geothermometry

Cation geothermometers are widely used to estimate reservoir temperatures but can yield inappropriate results if not interpreted with care. This is especially true for low- to moderate-temperature resources. To assess their applicability, standard geothermometer temperatures were calculated for the Ft. Bliss waters by Barker et al. (2015). These waters are appropriate for testing the reliability of the geothermometers because thermal data from Ft. Bliss indicates the wells were drilled into a convecting hydrothermal system. Barker et al. (2015) concluded that the quartz (conductive) geothermometer (Fournier, 1991) temperatures most closely matched the measured well temperatures, which ranged from 78^o to approximately 100^{o}C, and thus, could be considered “reliable”. The chalcedony geothermometer, which is often appropriate for low- to moderate- temperature waters (Fournier, 1991), yielded temperatures that are significantly lower than the measured temperature. In contrast, the Na/K and K/Mg geothermometers yielded values that were 80^o to >100^{o}C and 20^o to 30^{o}C hotter, respectively, than the measured temperatures (Giggenbach, 1991). The chalcedony, Na/K and K/Mg geothermometers were all considered unreliable.

Figure 7 presents the SiO_2 contents of the fairway waters. Quartz geothermometer temperatures are shown in Figure 8. The highest geothermometer temperatures, ranging from 100^o to 121^{o}C, are found in the northern and southern regions. However, geothermometer temperatures ranging from 80^o to 100^{o}C are found throughout the fairway, suggesting potential targets are present in all three regions.

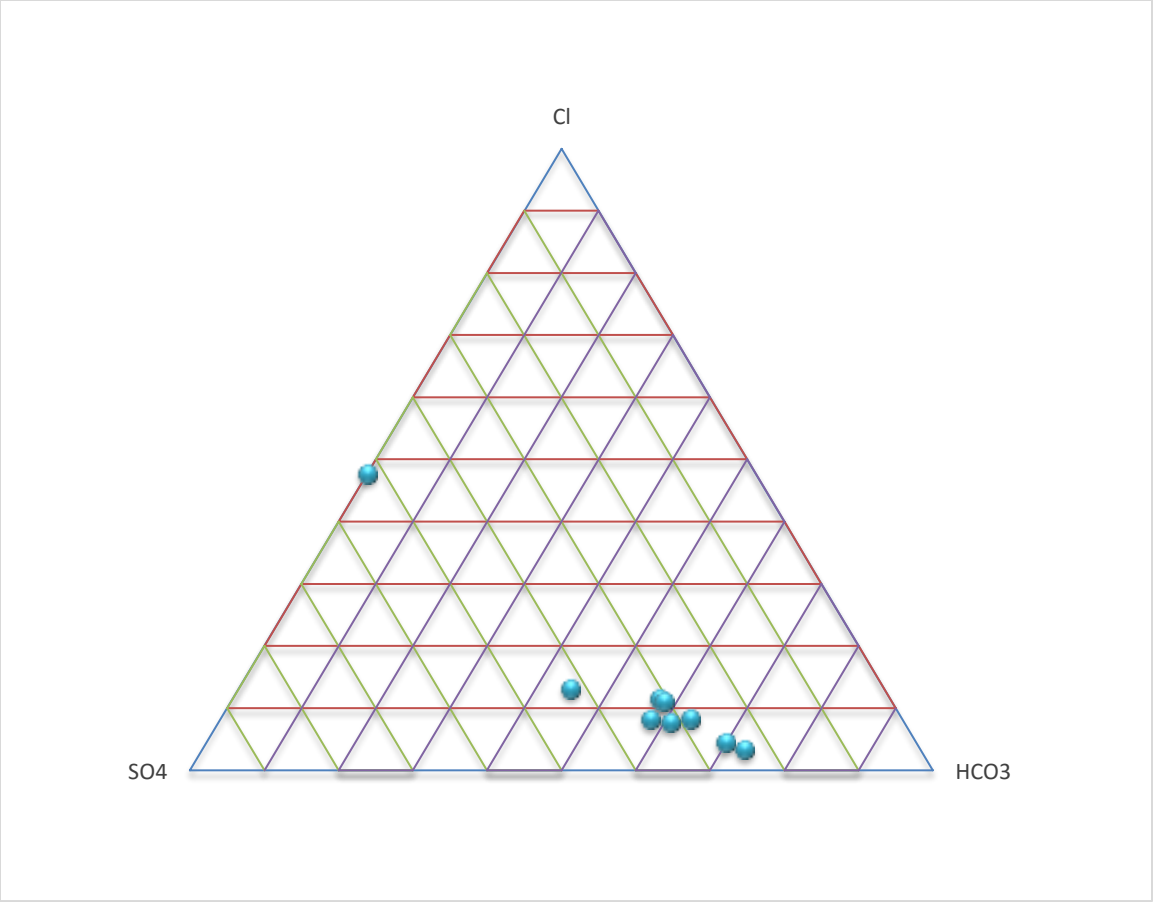

Figure 5. Relative Cl-SO_4-HCO_3 contents of waters from the central region of the play fairway

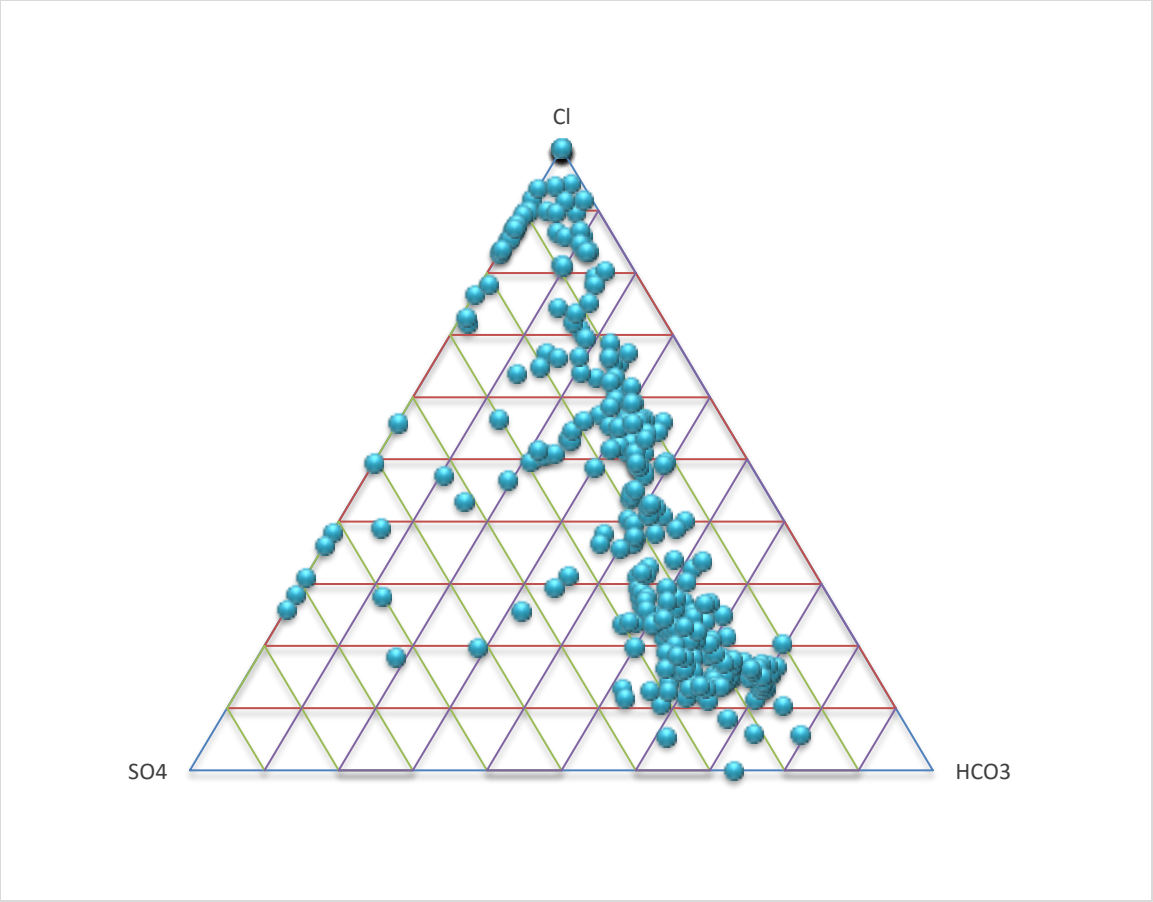

Fig. 6. Relative Cl-SO_4-HCO_3 contents of waters from the southern region of the play fairway.

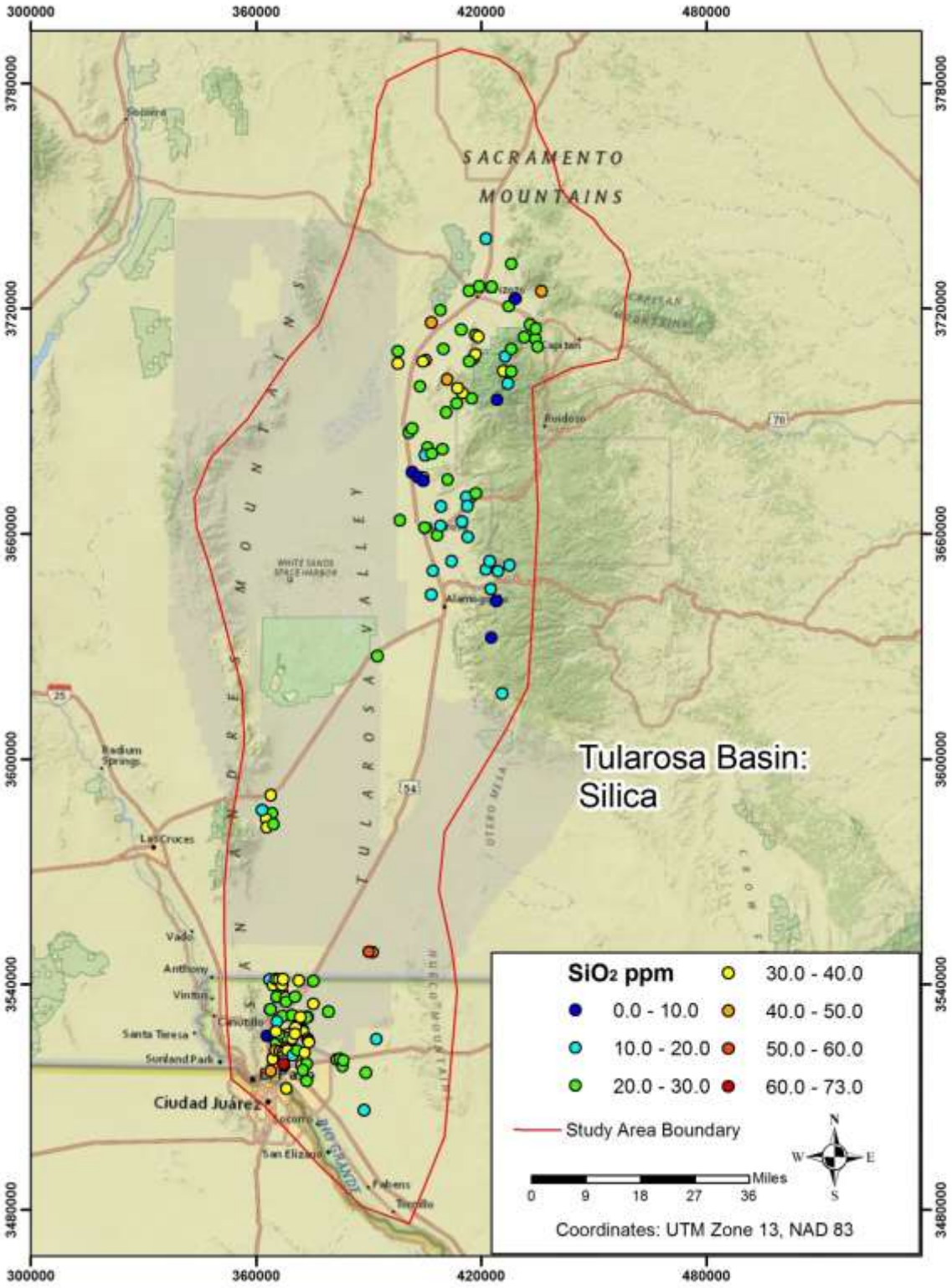

Fig. 7. Silica (SiO_2) contents of play fairway waters.

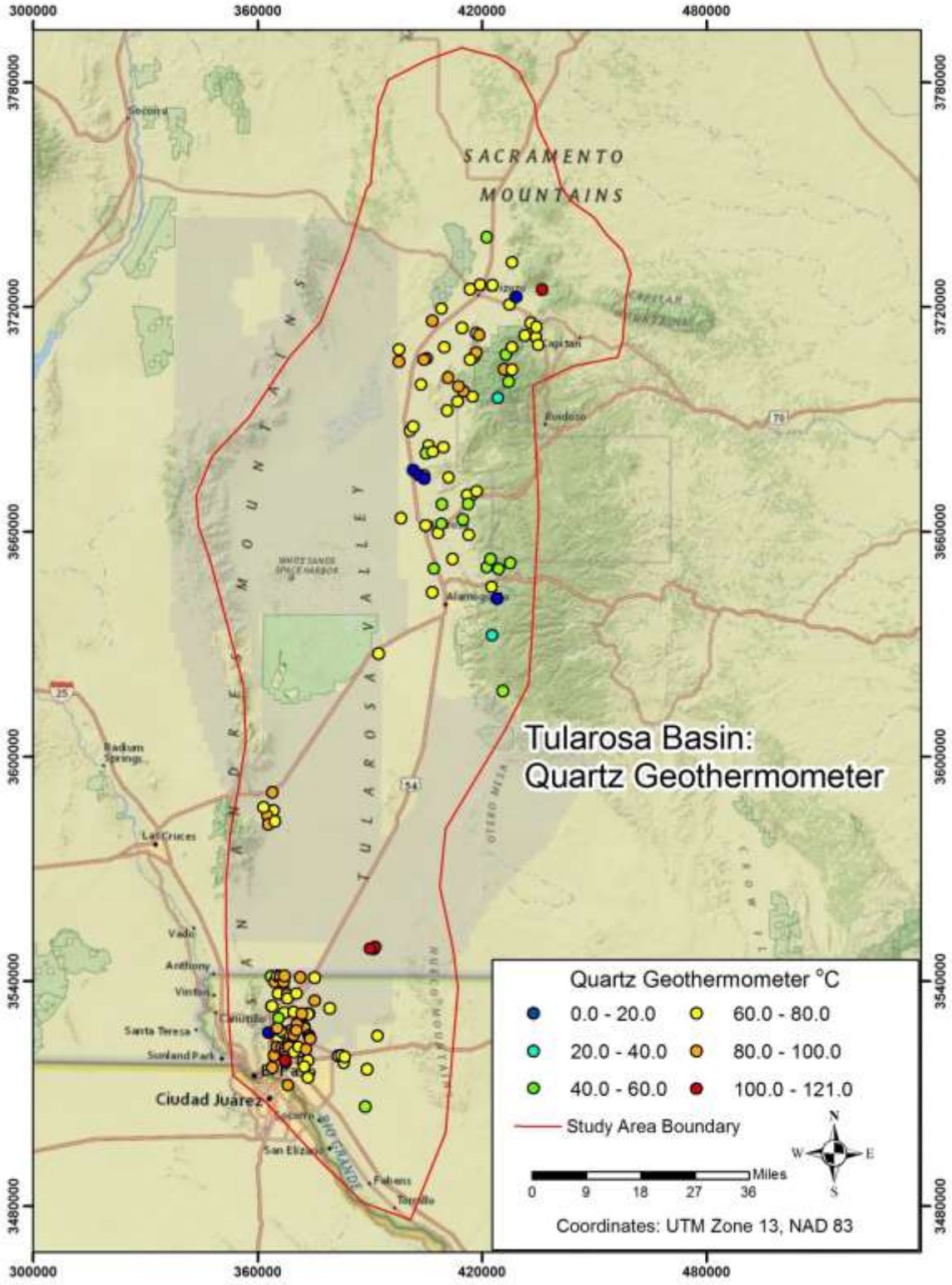

Fig. 8. Quartz (conductive) geothermometer temperatures.

Strain

Strain is an important consideration in PFA and was considered in this project. However, few GPS stations were available. Therefore, the ZR Ratio was applied to produce surrogates of strain within given areas of the study area.

Geothermal systems in the Great Basin are commonly related to relatively high strain rates (Faulds et al., 2012) and this should apply throughout the Basin and Range. The ZR ratio of Formento-Trigilio and Pazzaglia (1998) can be used to predict strain rates. In order to calculate ZR ratios, a large 10 m resolution DEM of the Tularosa basin was divided into twelve zones, shown in Figure 1, and then calculations proceeded as follows, for each zone.

Calculate local mean elevation (Ź), where $\sum_n Z_r$ is the sum of elevation values within a zone *r* and *n* is the number of elevation values within the zone.

$$\acute{Z} = \sum_n Z_r/n$$

Calculate the local mean relief ($\acute{R}$).

$$\acute{R} = (Z_{max} - Z_{min})$$

Calculate the ZR ratio.

$$ZR = \frac{\acute{Z}}{\acute{R}}$$

The results are shown on Figure 2. A minimum ZR ratio is 0.75 (Zone 4), and maximum is 1.92 (Zone 8). The mean ZR ratio is 1.146035 and the standard deviation is 0.35. Zone 8 is nearly two standard deviations greater the mean, while Zone 10 is about one and a half standard deviation greater. These zones have very high strain relative rates. Zones 1, 2 and 11 also have above average strain rates, though they are less than one standard deviation from the mean. That leaves Zones 3, 4, 5, 6, 7, 9, and 12, which are all below average and within one standard deviation of the mean.

The Tularosa Basin is large, roughly 30,000 sq. km, and so it is likely that strain rates vary throughout the basin. By clipping the basin into twelve equal zones, the variation in strain can be seen with better resolution than the infinitesimal strain rate calculations that can be made from GPS velocity vector triangles given the few stations available. It is permissible that the zones with relatively high strain rates will be more likely to have zones of high permeability, and therefore are more accommodating to geothermal systems. This analysis suggests that the northern and southern parts of the basin are the areas of greatest strain. This was taken into consideration, among many factors, in play prioritization.

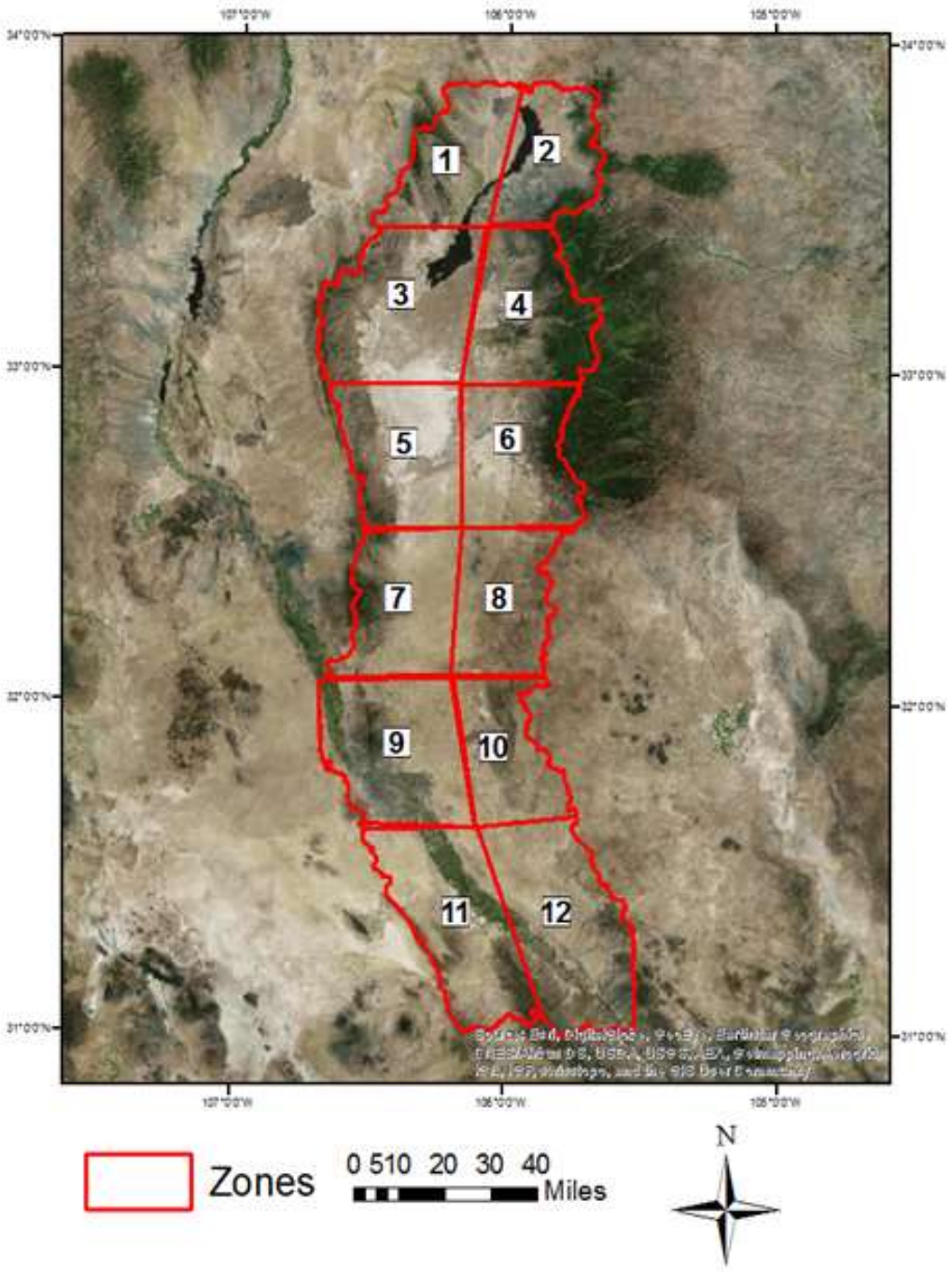

Figure 1. Tularosa Basin, divided into 12 zones for ZR ratio comparisons. Zone 8 and 10 have relatively high strain rates.

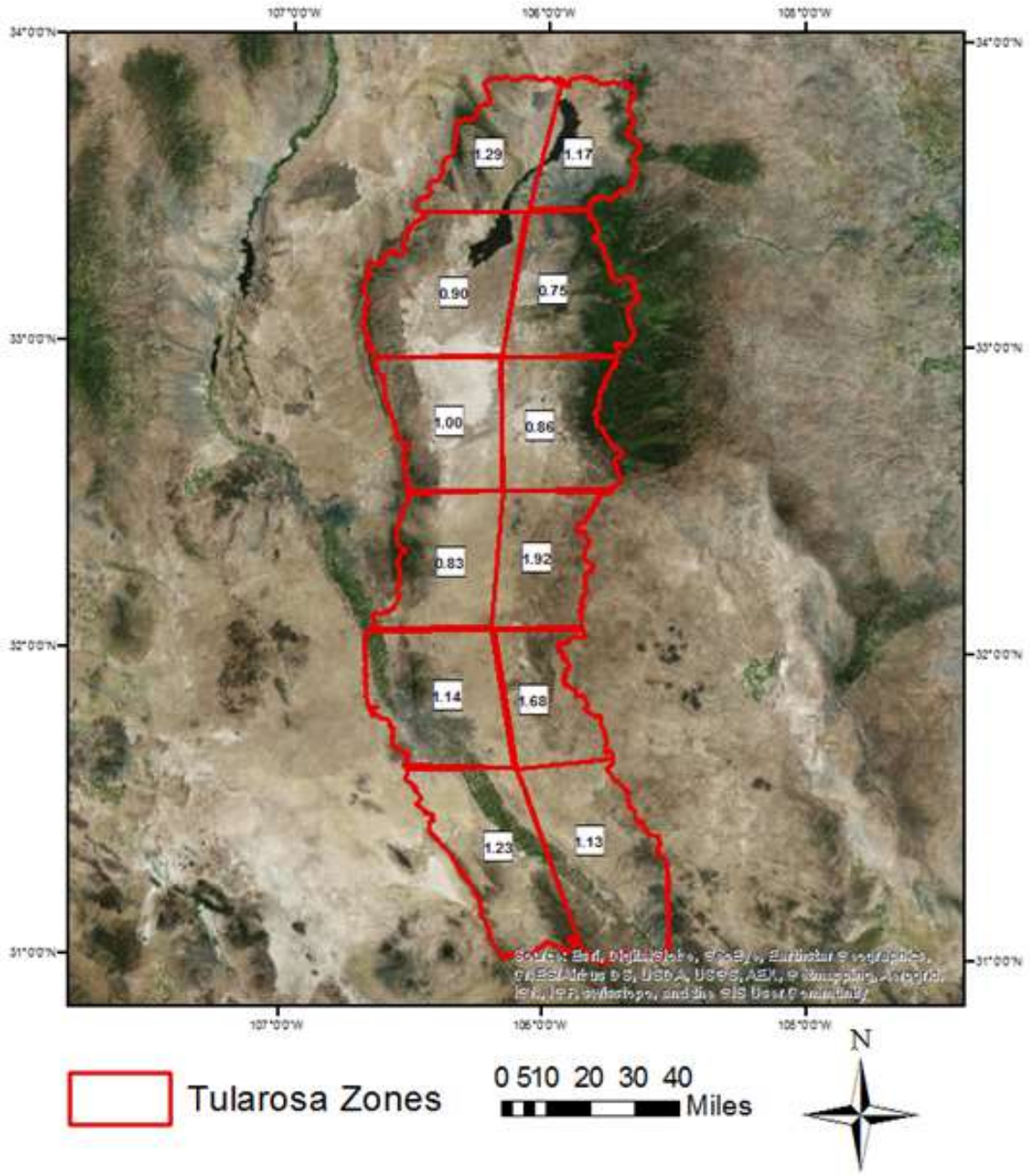

Figure 2. ZR Ratio values per zone. Higher values suggest greater strain and potentially better zones of permeability.

Basement Structure

Remote Sensing

Day and night time Advanced Spaceborne Thermal Emission and Reflection Radiometer (ASTER) data, covering most of the study area, was obtained to (1) map surface temperature anomalies, (2) map mineralogy as related to rock brittleness to support possible future EGS, and (3) map areas of hydrothermal alteration. The properties of this data are shown in Figure 1. These data have been shown to be useful for general geological mapping (Hulen et al., 2005); lithologic mapping (Rowan and Mars, 2003); hydrothermal mineralogy mapping (Rowan et al., 2003; Mars and Rowan, 2006); and temperature anomaly mapping (Eneva, 2007).

First surface temperatures were calculated from ASTER emissivity data. These 90 m spatial resolution data were used to determine if any anomalous temperatures could be found along the fault-bounded basin margins. Figure 1 show the results. A few areas show up along the base of the Sacramento Range, but they are not associated with plays. However, on the west side of the valley there are anomalies that either are or could be associated with plays. Field work is needed for verification.

To map the mineralogy that can affect EGS (fracing), band ratios, using diagnostic absorption features in the shortwave and thermal infrared, were used to highlight calcite and silica (brittle rocks) and clay (softer rocks) and gypsum representing evaporite beds that can be problematic in fracing. Relative concentrations of these minerals were recorded in a shapefile per mapped rock unit. The results can be seen in Figure 2. The classification was conservative and a large percentage of the rock in the area was rated as high risk. This was often the result of potential evaporite beds. Where this was not the case high risk was due to high clay content. This data, however, has not been field verified.

Hydrothermal alteration was not found to be prevalent in the study area. It was mapped in the Jarilla Mountains near Orogrande, in a small area in the Sacramento Mountains south-southeast of Oscura, and it was suggested in Mesoproterozoic granite alone the eastern margin of the San Andreas Range (Fig. 3), but this could be from weathering or hydrothermal alteration or both and needs to be field verified to determine if any alteration related to geothermal activity.

Table 1. ASTER VNirSwir band characteristics. Band numbers are in parentheses.

Spectral Region	Bandwidth (microns)	Spatial Resolution	Quantization Level
Visible Green (1)	0.52-0.60	15 m	8 bits
Visible Red (2)	0.63-0.69	15 m	8 bits
Near Infrared (3)	0.78-0.86	15 m	8 bits
Shortwave (4)	1.60-1.70	30 m	8 bits
Shortwave (5)	2.145-2.185	30 m	8 bits
Shortwave (6)	2.185-2.225	30 m	8 bits

Shortwave (7)	2.235-2.285	30 m	8 bits
Shortwave (8)	2.295-2.365	30 m	8 bits
Shortwave (9)	2.360-2.430	30 m	8 bits
Thermal infrared (10)	8.125-8.475	90m	12 bits
Thermal infrared (11)	8.475-8.825	90m	12 bits
Thermal infrared (12)	8.925-9.275	90m	12 bits
Thermal infrared (13)	10.25-10.95	90m	12 bits
Thermal infrared (14)	10.95-11.65	90m	12 bits

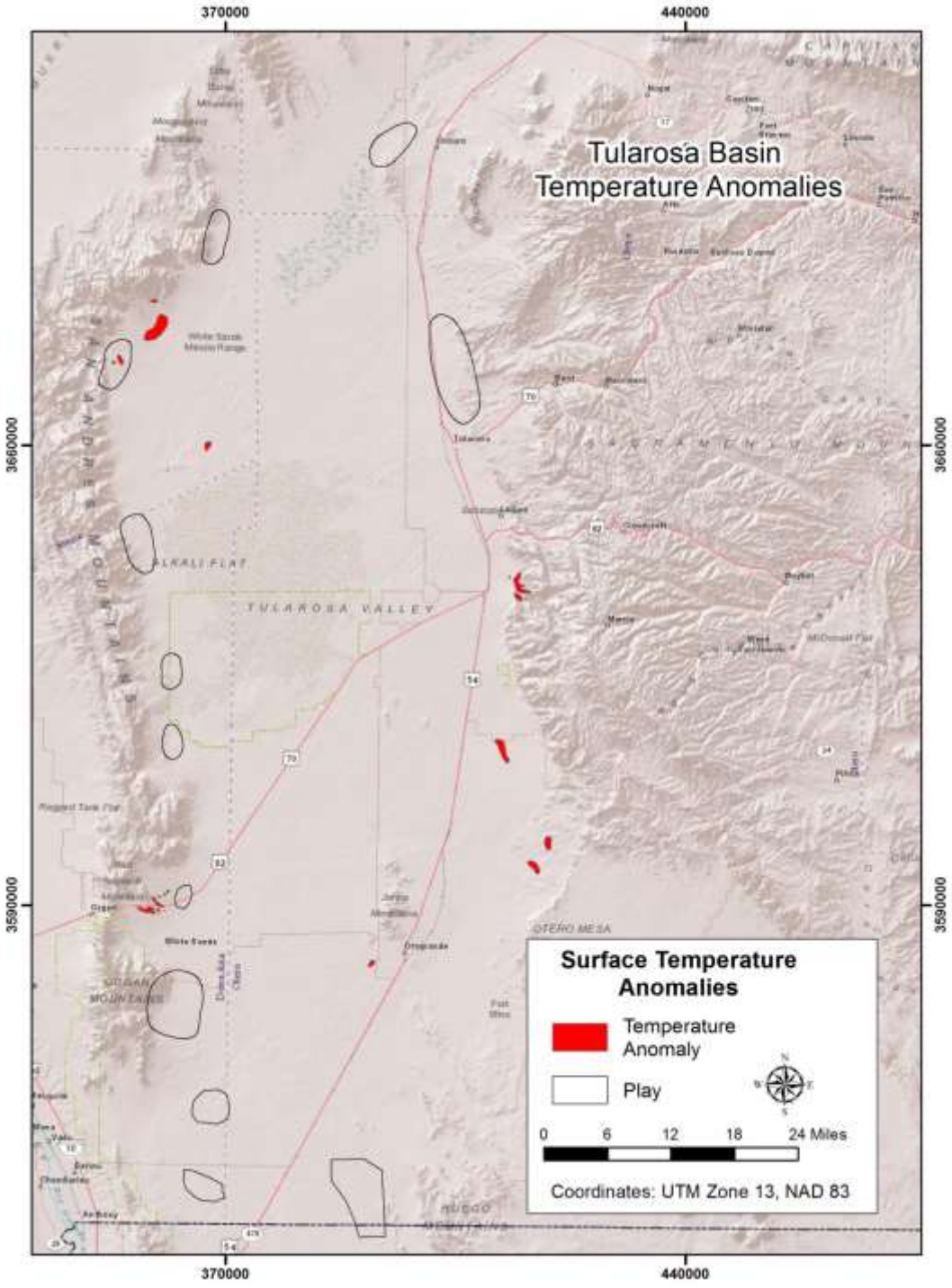

Figure 1. Surface temperature anomalies mapped from ASTER nighttime surface temperature data.

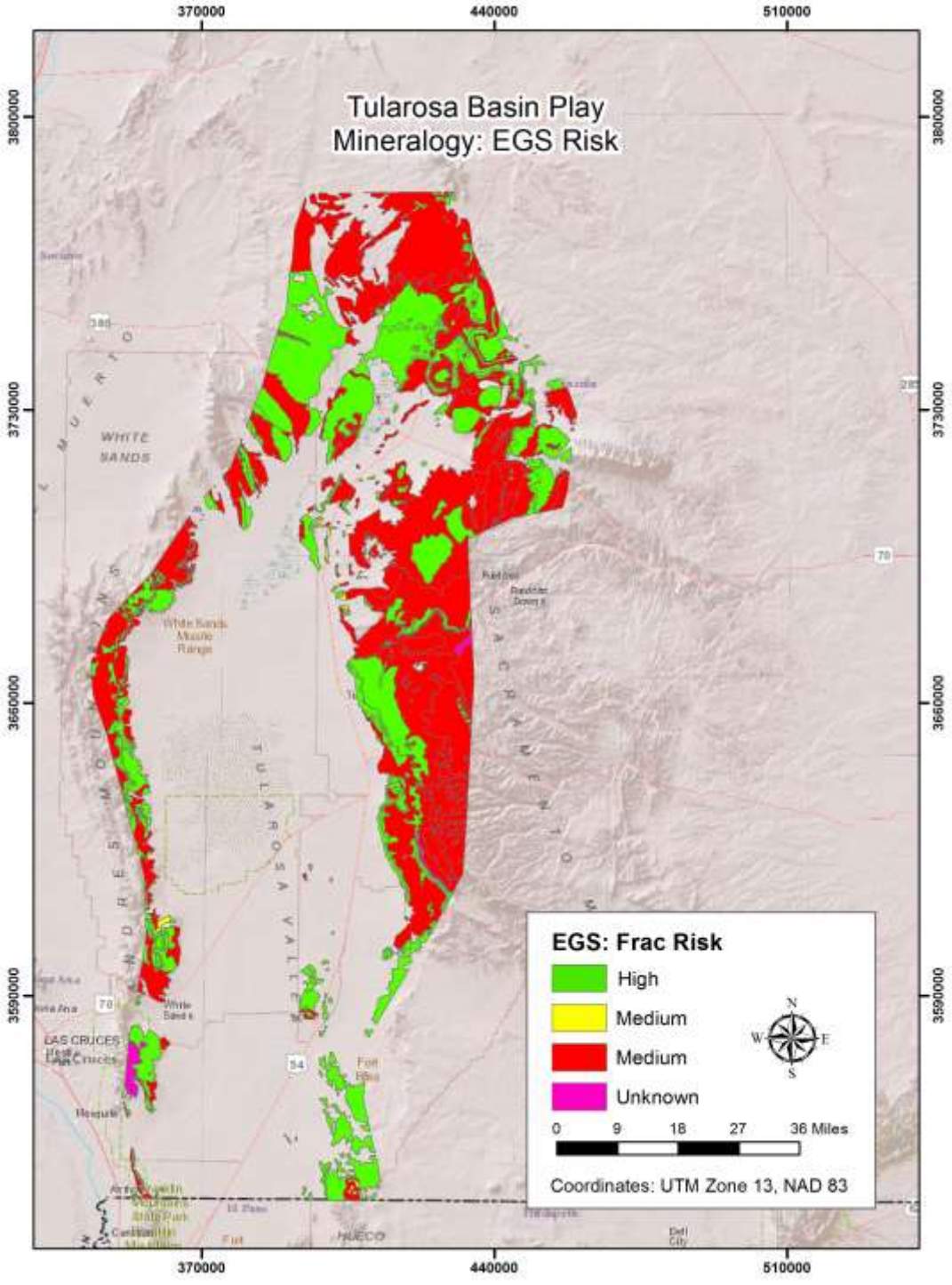

Figure 2. EGS risk based up rock brittleness suggested by ASTER multispectral image analysis.

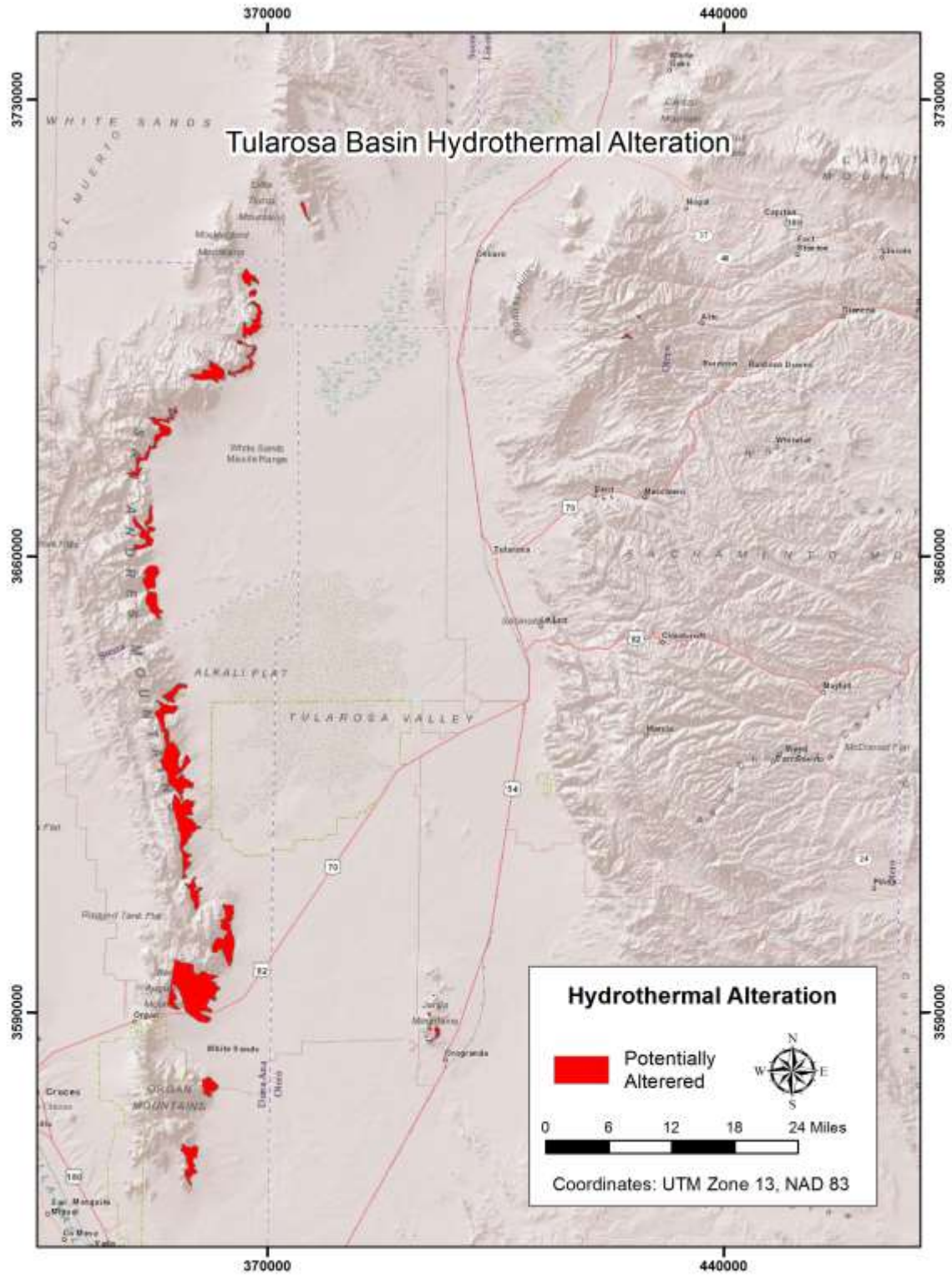

Figure 3. Hydrothermal alteration suggested by ASTER multispectral image analysis. The extensive areas on the west side of the valley are related to Mesoproterozoic granite, and may be from weathering or hydrothermal alteration or both.

Geophysical Profiles of the Tularosa Basin

Basement Structure

In order to achieve a general understanding of the basins structure we constructed 12 east-west cross sections (across the basin) and one longitudinal cross-section (north-south) using contours created from regional magnetic intensity and Bouguer gravity anomaly data obtained from PACES, University of El Paso, Texas. The locations of these geophysical profiles are shown in Figures 1 and 2.

These profiles show relative highs and lows in the geophysical properties across and along the Tularosa basin. These geophysical highs and lows indicate heterogeneities in the basin arising from rock properties (density and magnetic differences) and/or fault-bounded structural highs. In other words, a simplistic view of the Tularosa basin merely as a Tertiary rift graben filled with sediments and bounded by structural highs on the east and west margin of the basin is not realistic. This region has experienced a long and complex geological history with different thermo-tectonic episodes, and the following Figures exhibit some of this complexity.

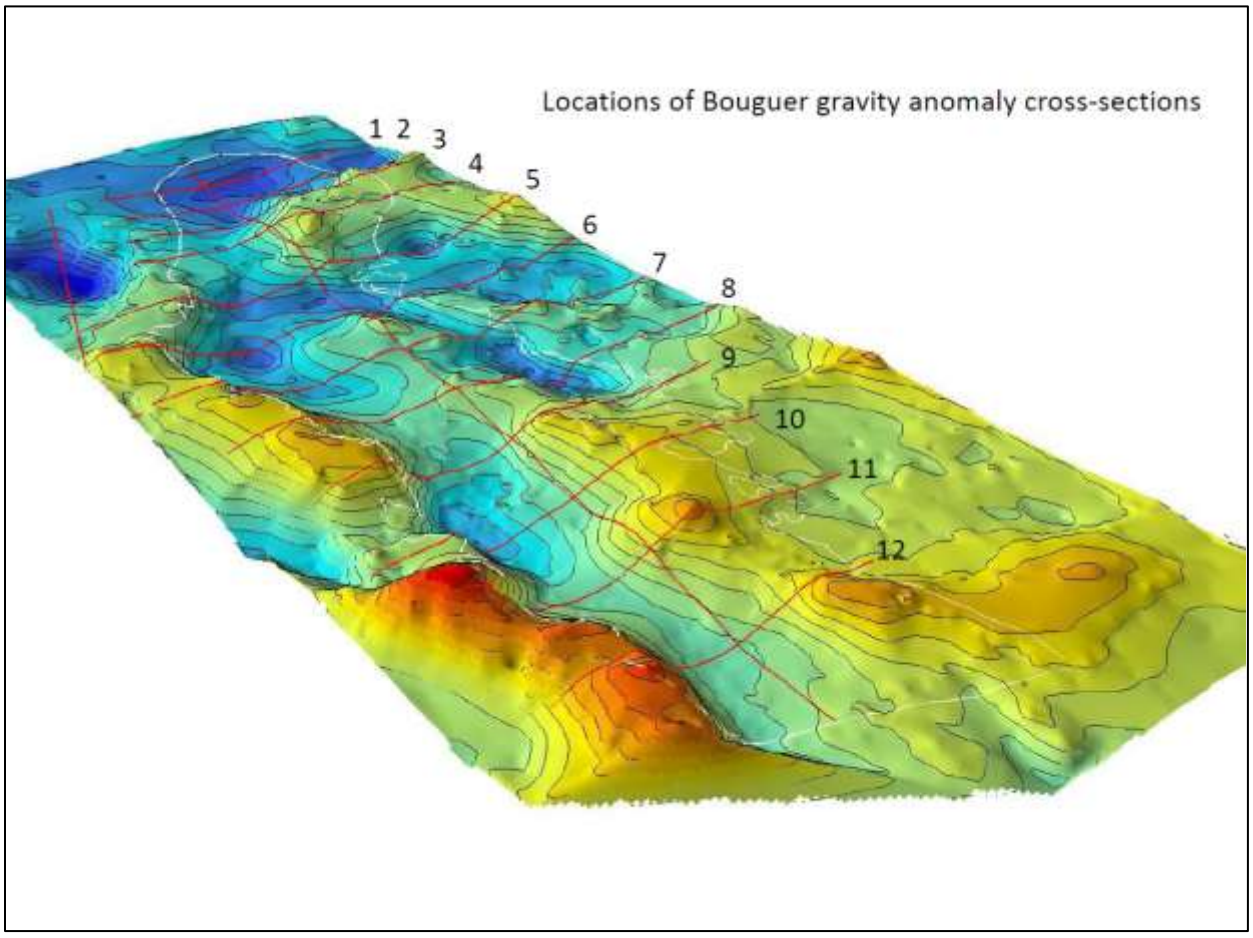

Figure 1. Locations of east-west cross sections for Bouguer gravity anomaly contours. Several sub-basins can be noted in this graphic.

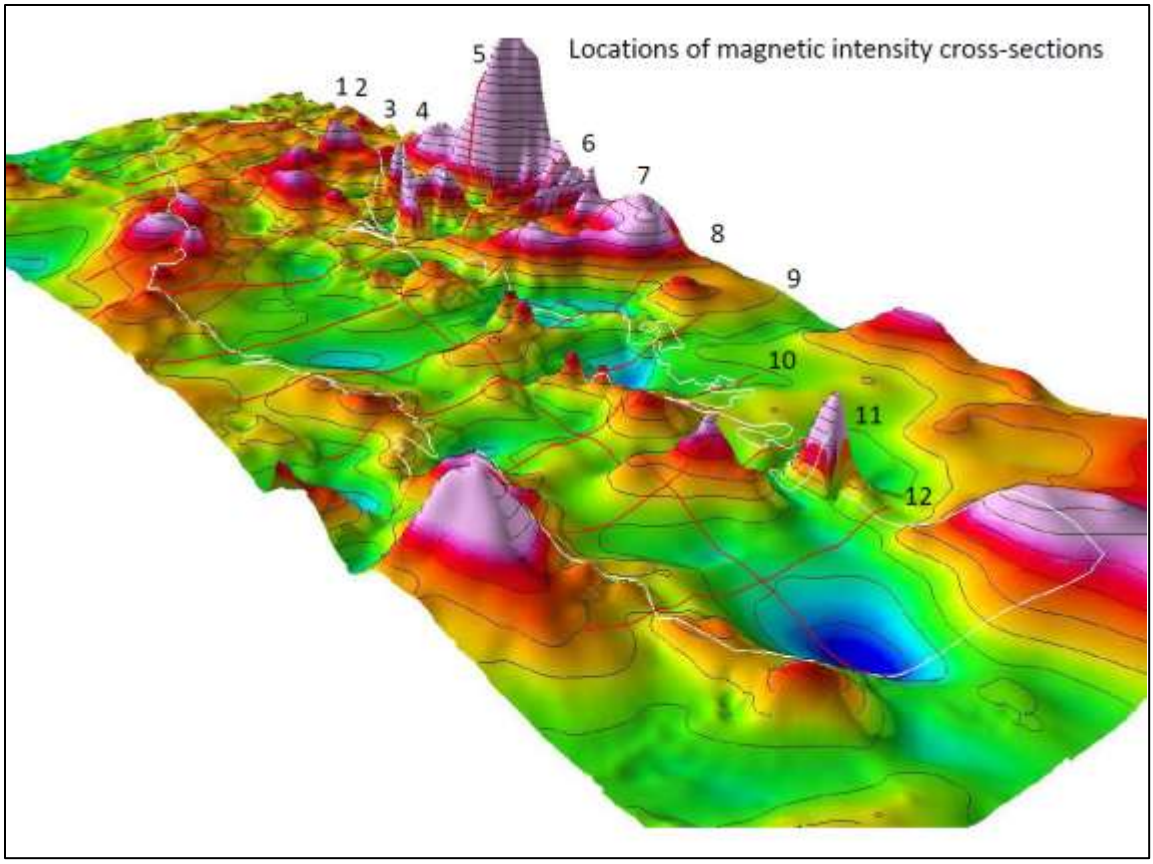

Figure 2. Locations of east-west cross sections for magnetic intensity contours, again indicating the presence of several sub-basins.

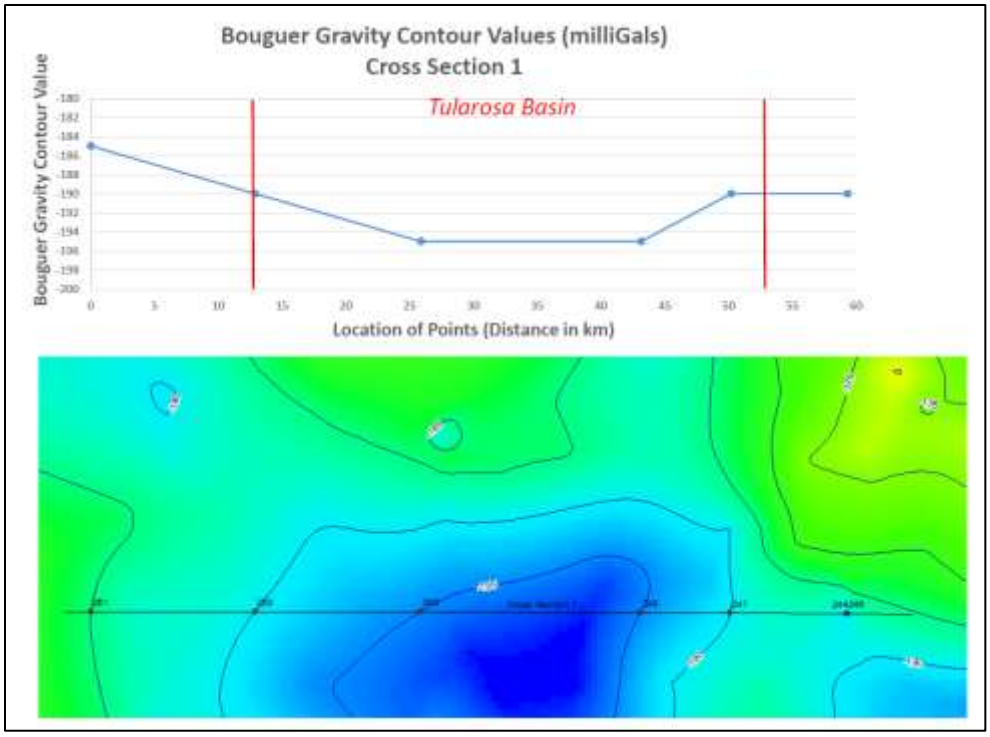

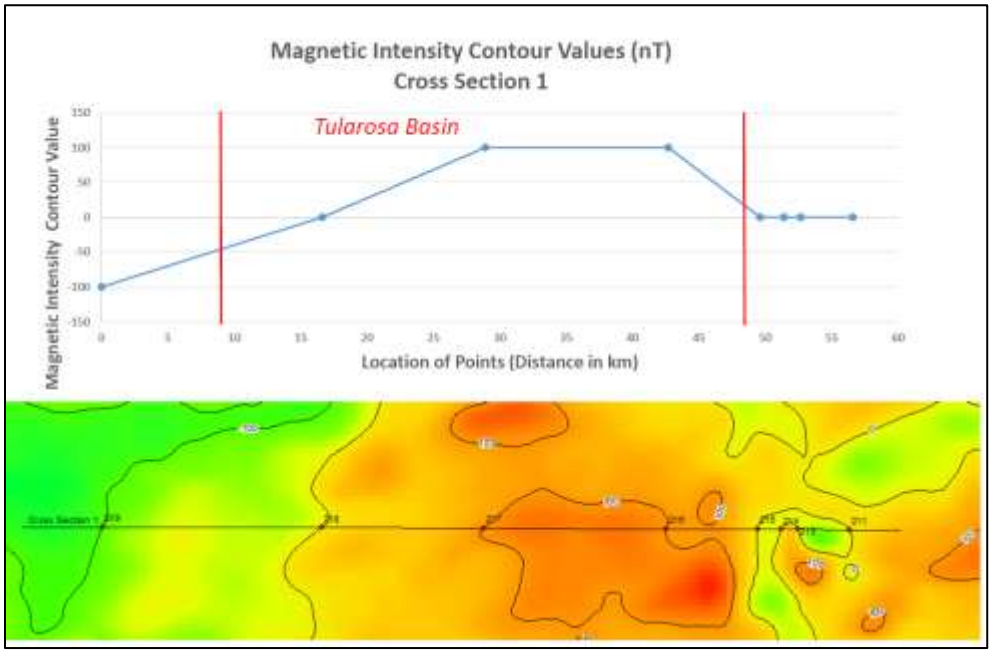

Figure 3. The east-west gravity cross-section (top) shows a relatively simple extensional basin profile. The bottom magnetic cross-section shows a high that is the inverse of the gravity profile, perhaps indicating a down-dropped tertiary intrusive.

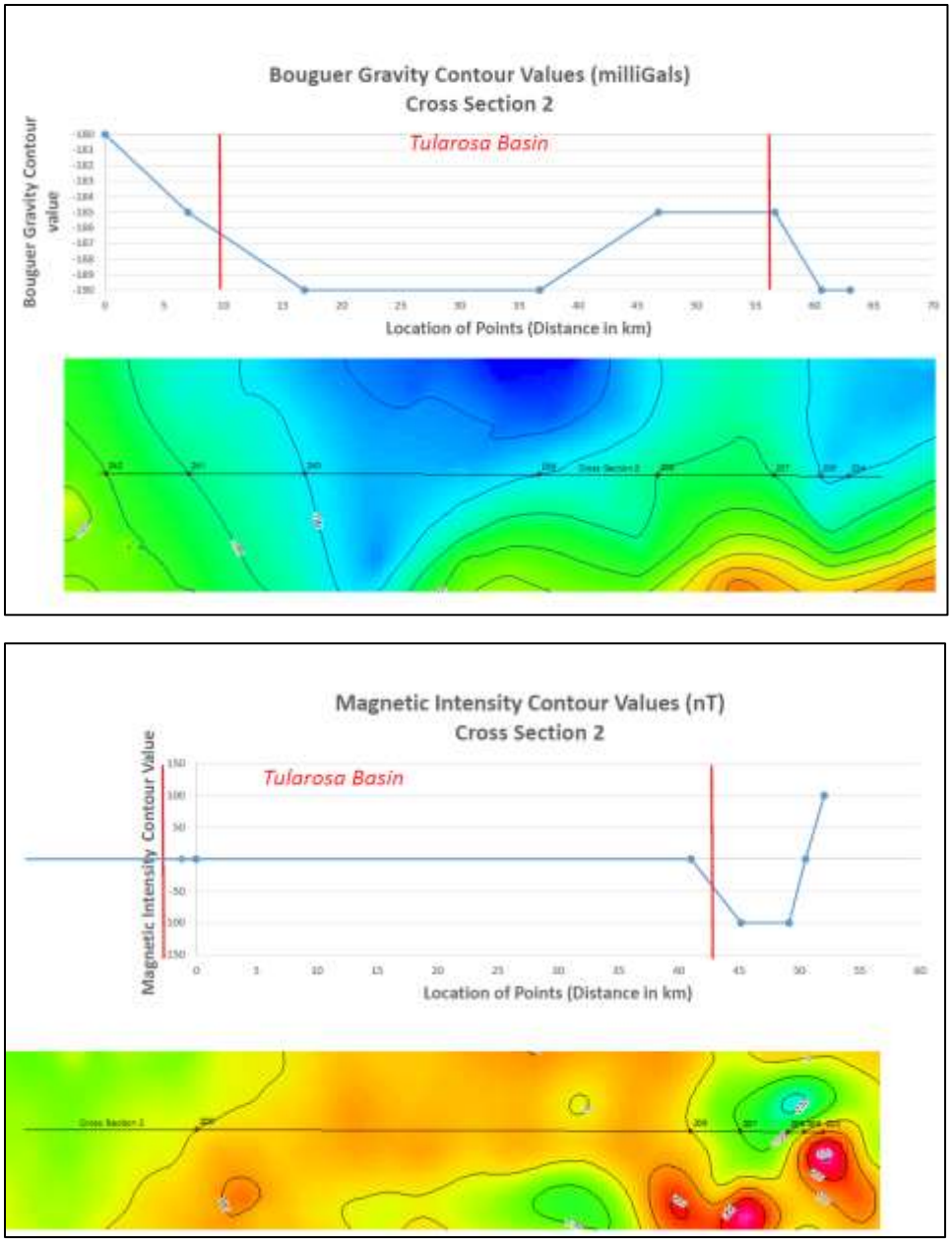

Figure 4. A gravity high (top) on the east side of the basin suggests a horst-like structure just outboard of the northern Sacramento Range that may be buried glide-block of primarily low-magnetic mineral sedimentary rock as suggested by the magnetic low covering part of the same area (bottom). The generally flat nature of the magnetic profile suggests a paucity of magnetic minerals and a sedimentary section in this part of the basin.

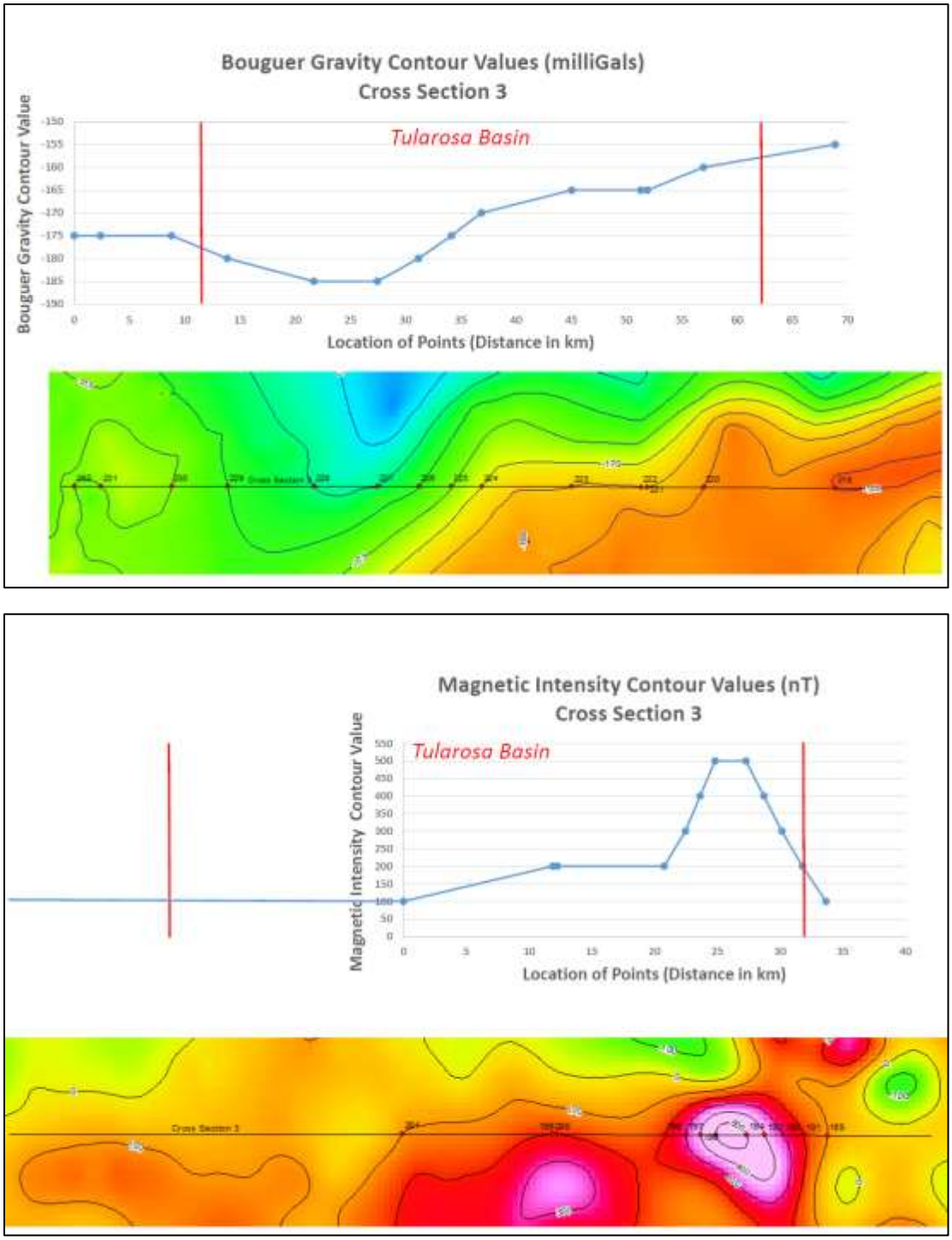

Figure 5. The gravity profile (top) suggest two west-dipping normal faults, one bounding the Sacramento Range and one out-board of the range, as well as an east-dipping normal fault bounding the basin on the west. The magnetic data (bottom) once again peaks on the east side of the cross-section suggestion intrusive rock, which is faulted (fault correlates with gravity fault). As the magnetic data cross-section slopes to the west it crosses a Quaternary basalt flow which may cause the moderate high prior to dropping off to the west.

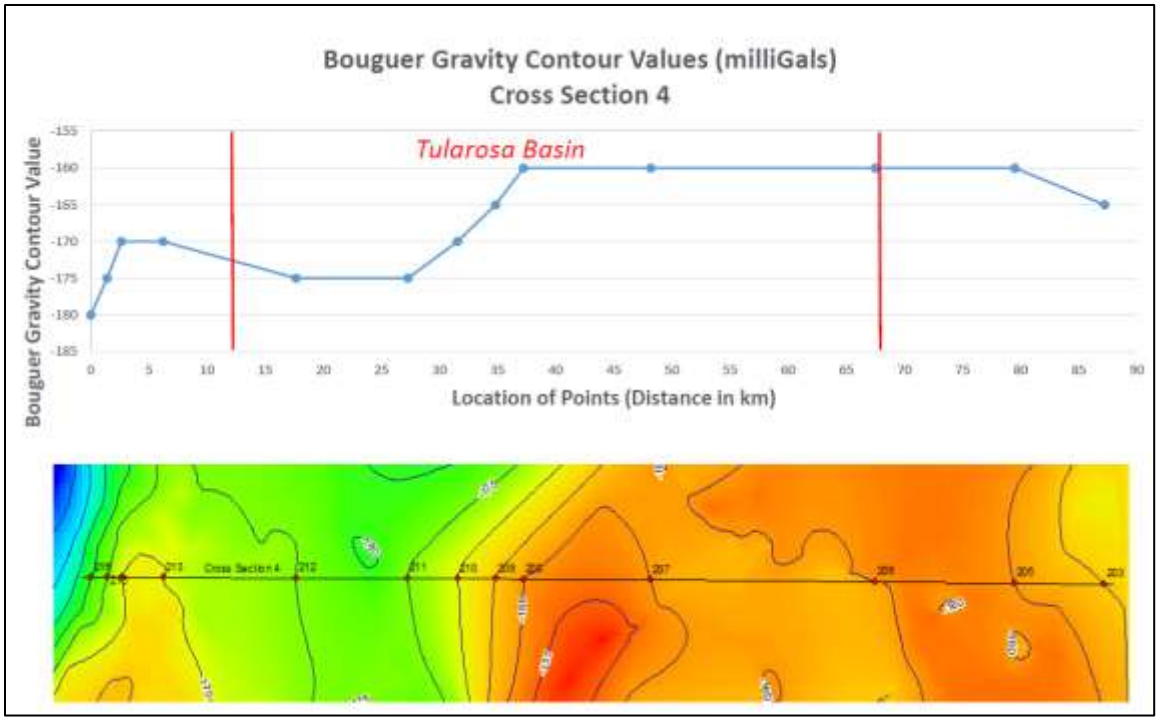

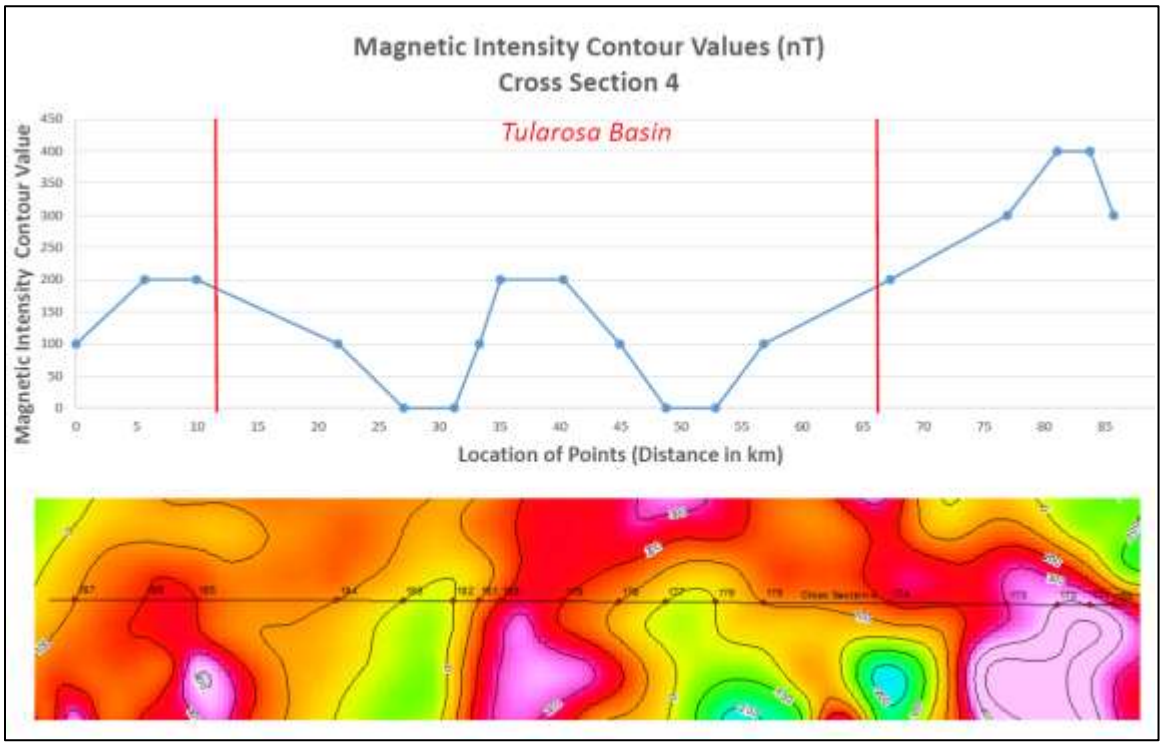

Figure 6. The gravity profile (top) shows a narrowing of the basin with a distinctive west-dipping fault bounding the east side of the valley and possibly another west-dipping fault on the western margin of the profile. The Magnetic data show a prominent high that may represent mafic magma chamber rocks related to the Quaternary basalt flow that this profile crosses.

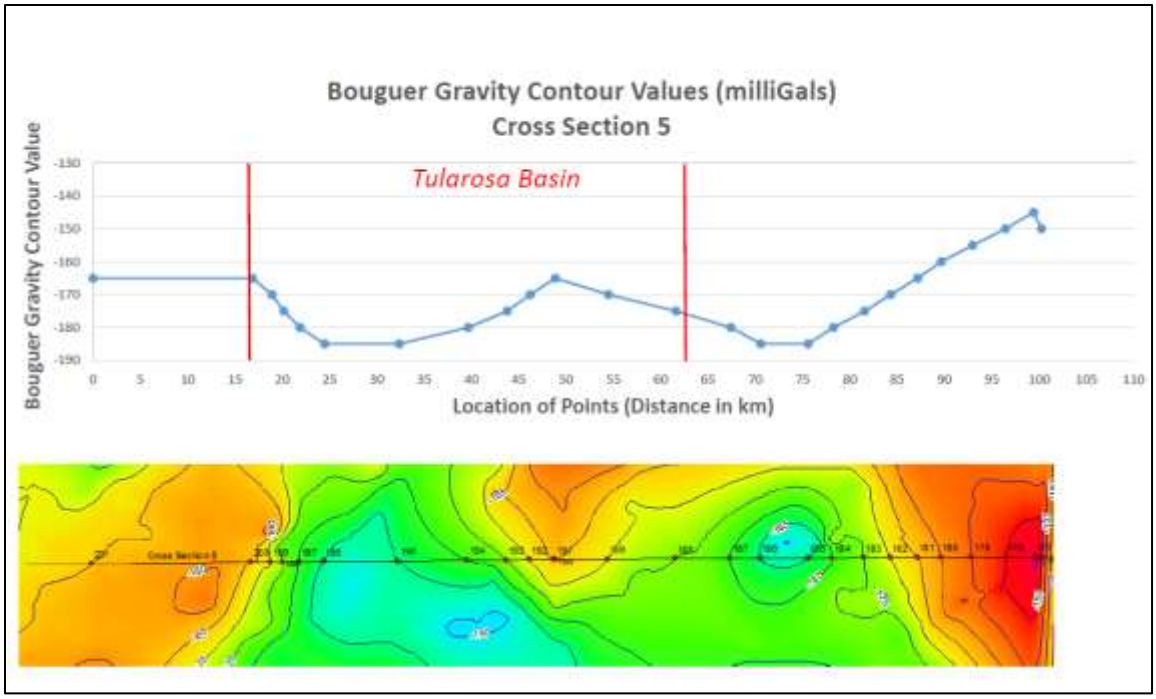

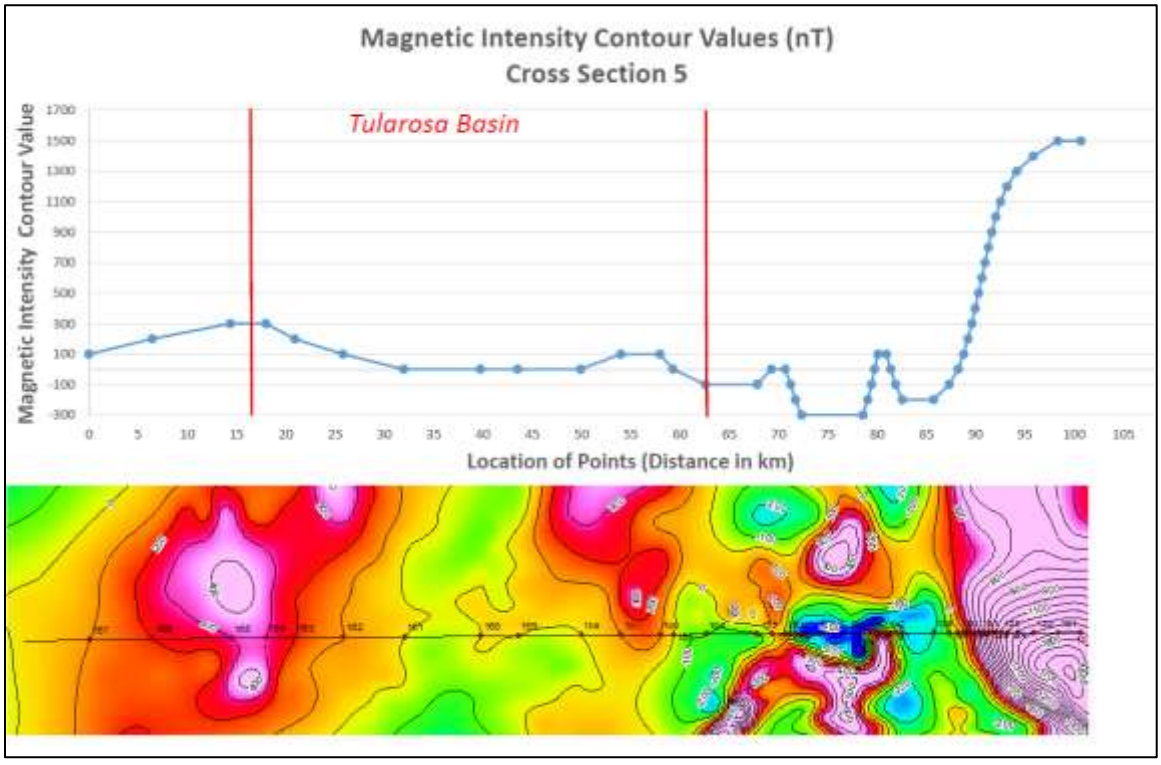

Figure 7. Both the gravity (top) and magnetic data (bottom) suggest the location of basin-bounding faults and what may be the southern margin of the mafic magma chamber related to the Quaternary basalt flow.

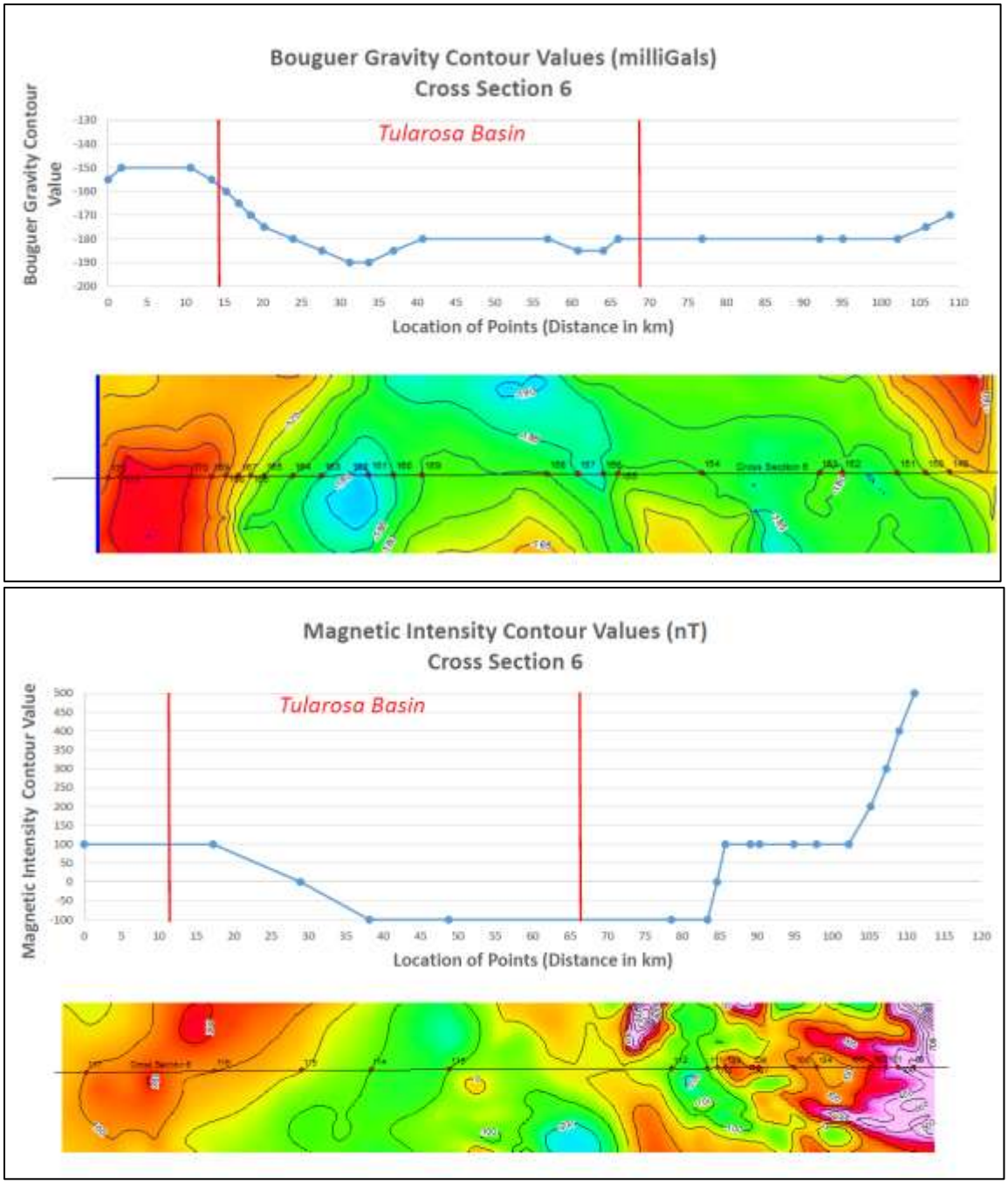

Figure 8. The gravity data profile (top) is relatively flat along the eastern basin margin with only a slight dip. This may be related to relatively young fault propagation of the Sacramento Range bounding faults in this area – a location where fault-tips are coalescing producing critical stress. A basement high is also apparent in the gravity profile. A well-developed east-dipping fault along the western basin margin is suggested by both data profiles.

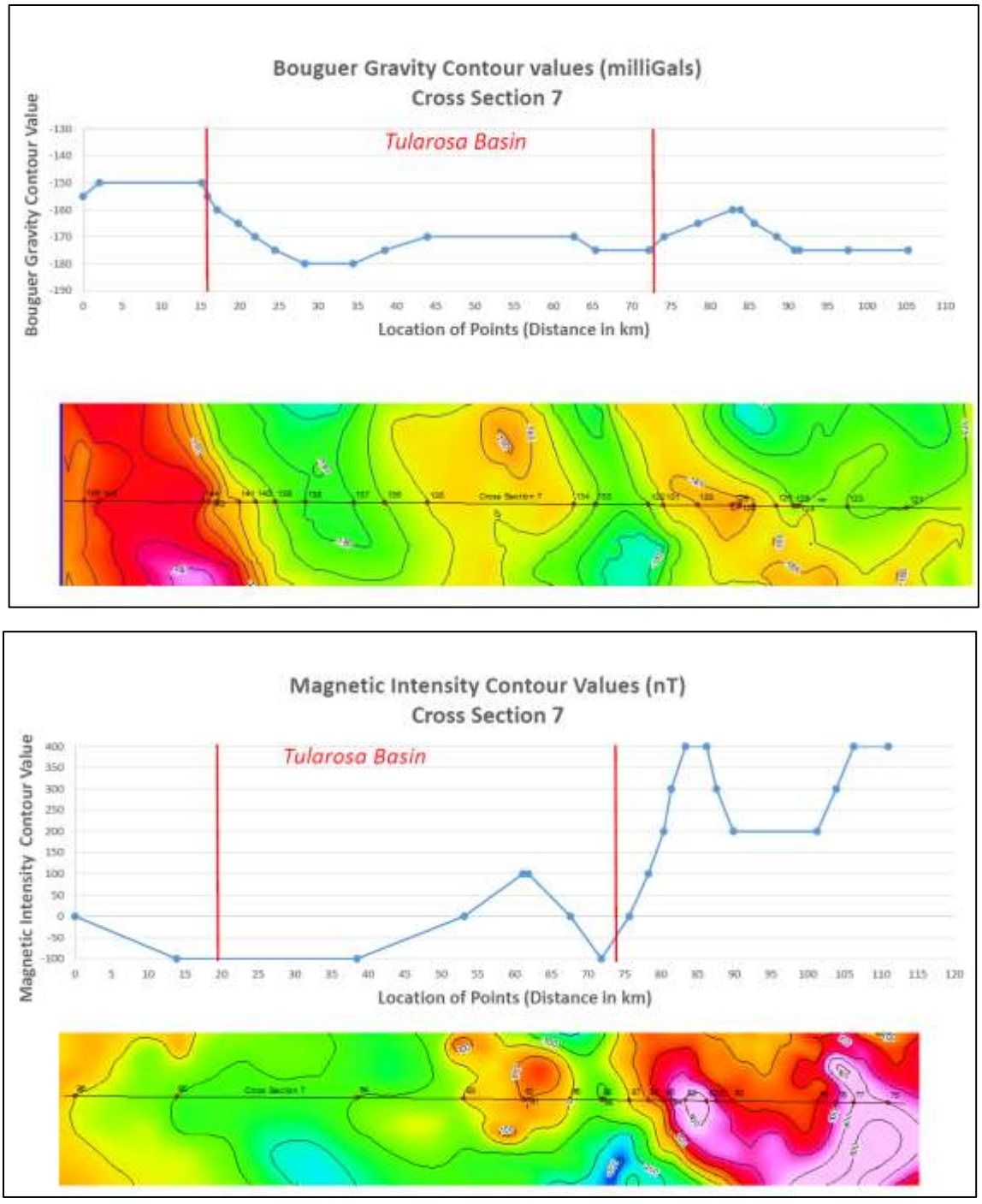

Figure 9. The gravity profile (top) again suggests normal faults bounding both the eastern and western margins of the basin. The basement high is more prominent than in Figure 8 suggesting a buried horst with faulting conjugate to the basin bounding faults. A magnetic high across part of the horst suggests that a portion of its lithology consist of volcanic, volcaniclastic, or intrusive rock. Both datasets suggest a basin flexure in this area, with fault-strikes changing from a predominantly NE direction to a NNW direction.

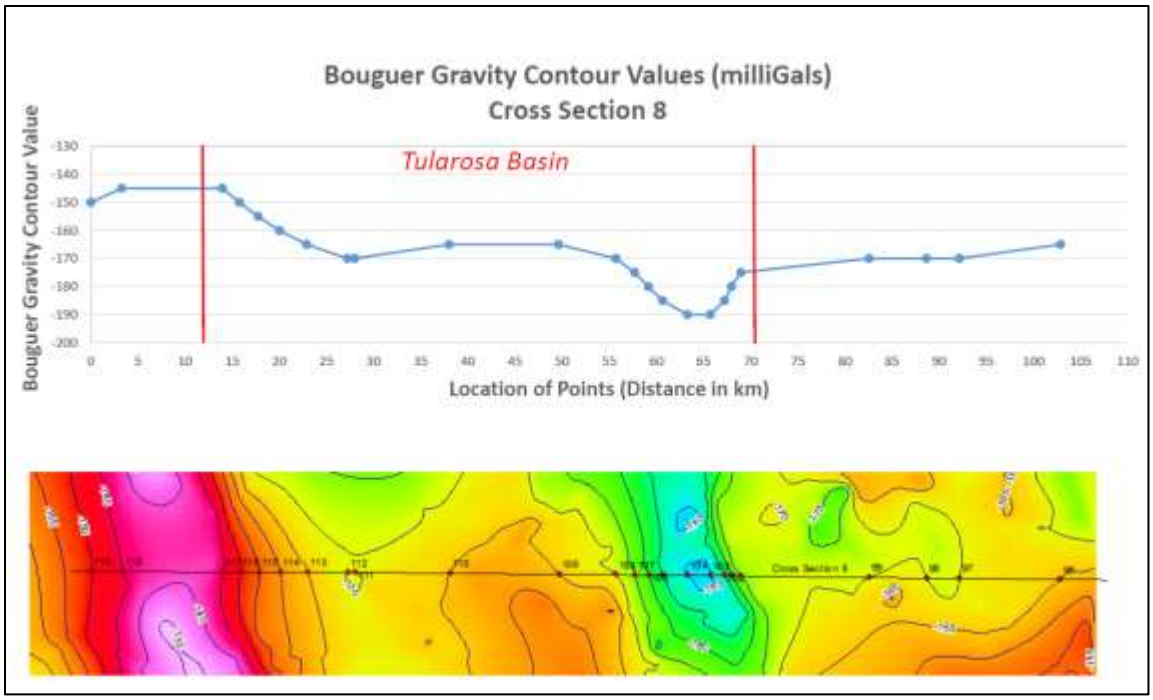

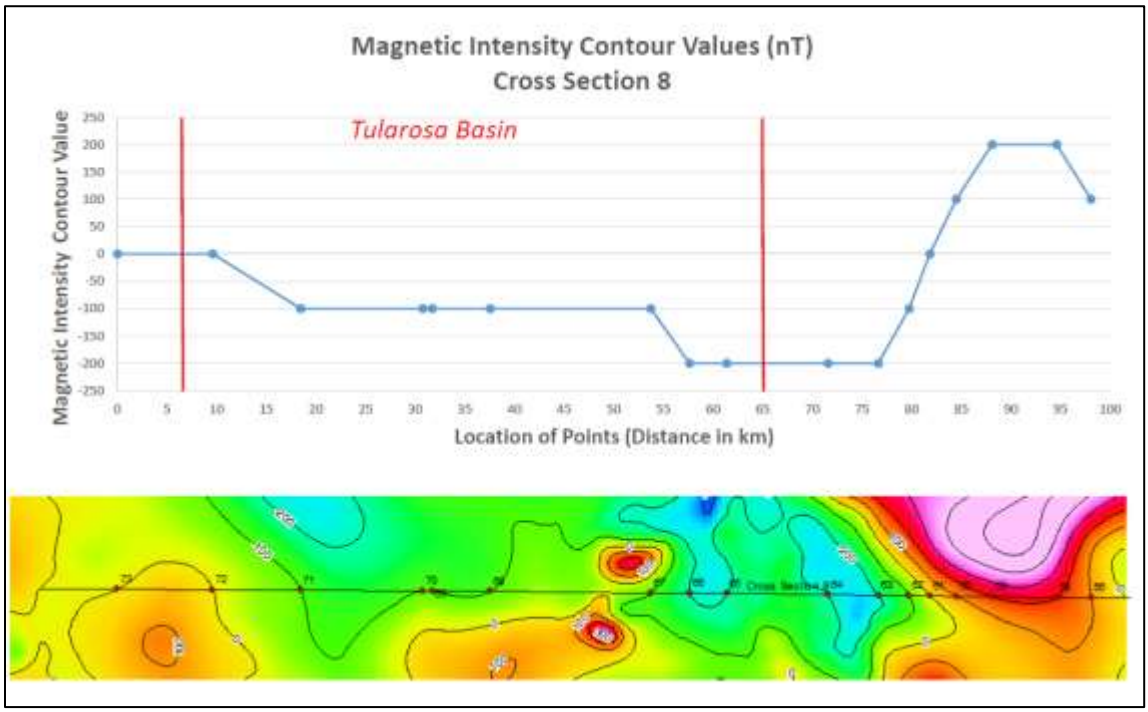

Figure 10. The gravity profile (top) continues to suggest a basement high, which may be an extension of the horst postulated in Figure 9. This is also suggested by the magnetic profile (bottom), although the western edge is truncated.

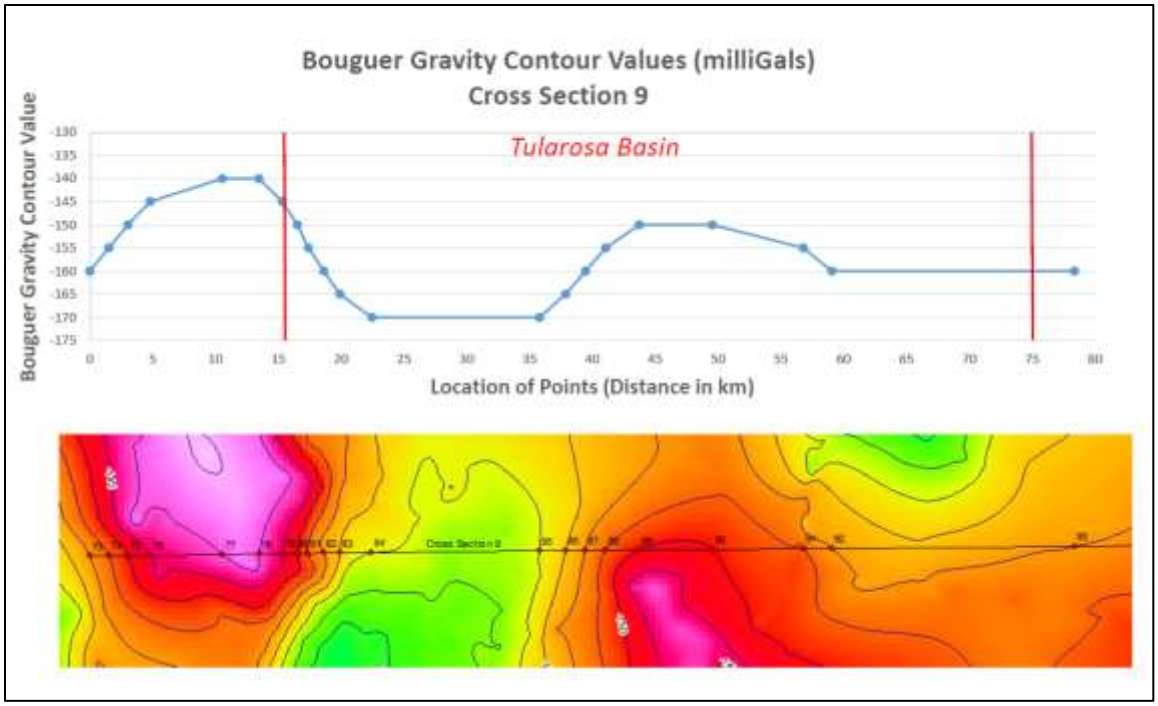

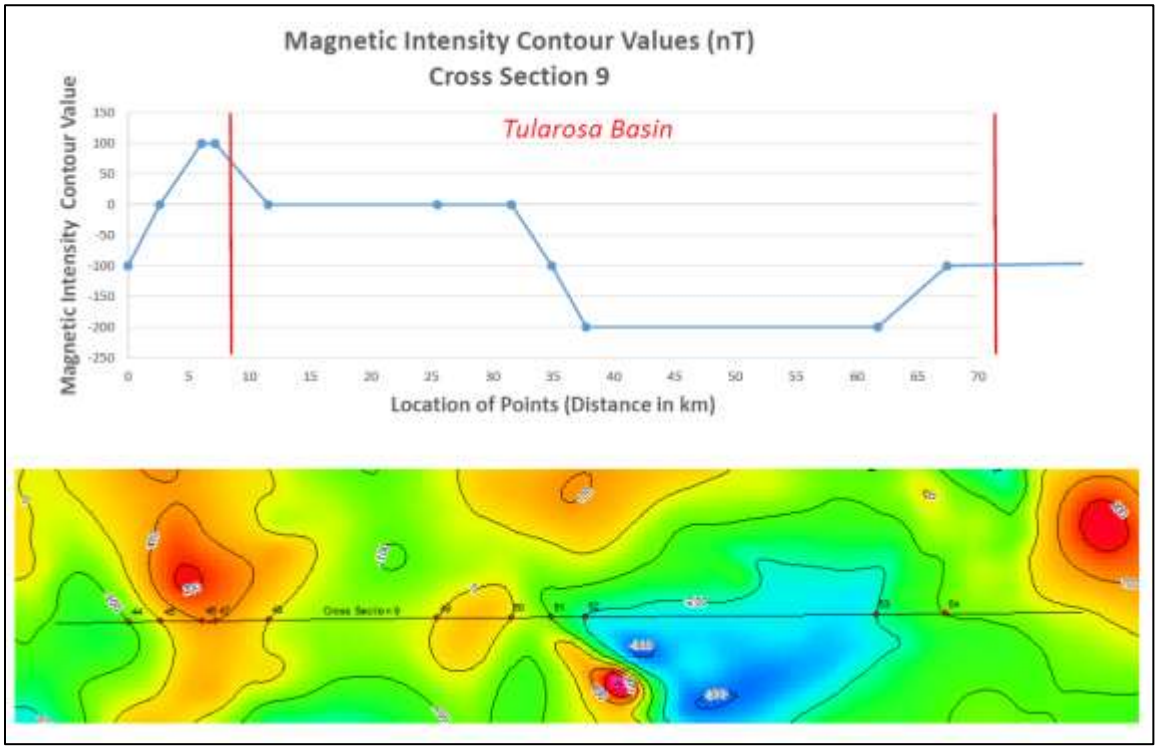

Figure 11. The gravity profile (top) again suggests well developed basin-bounding fault systems. The magnetic profile (bottom) suggests a transition from buried volcanic/intrusive rock to sedimentary rock to the east.

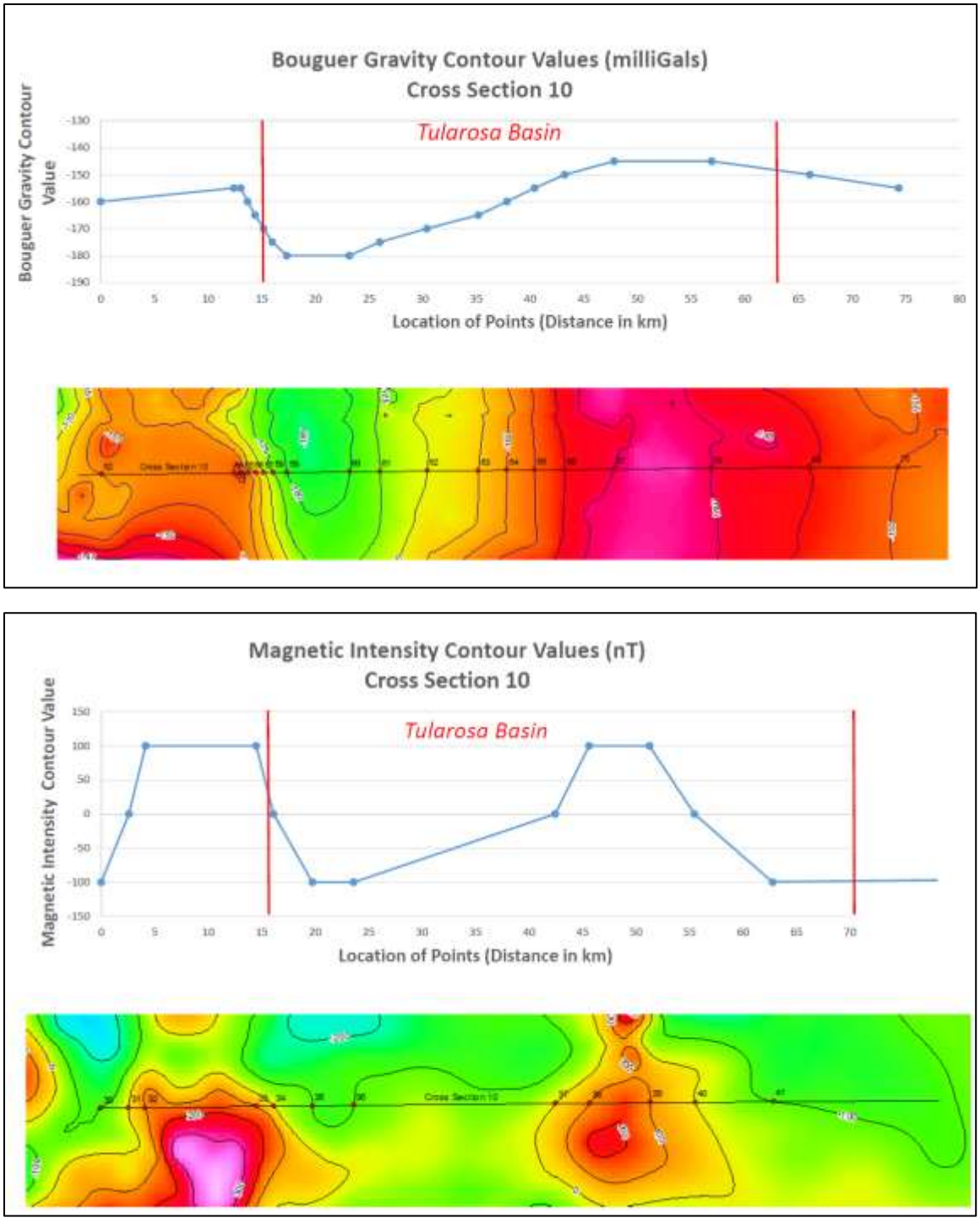

Figure 12. These profiles cross near the southern terminus of the Sacramento Range. The gravity profile has a steep gradient on the western basin margin, but the gradient on the eastern margin is significantly more gentle, suggesting less fault offset. The significant magnetic high on the eastern side of the bottom profile suggests an intrusion in the Sacramento Range and that seen to the west may result from Paleoproterozoic igneous rocks in the San Andreas Range.

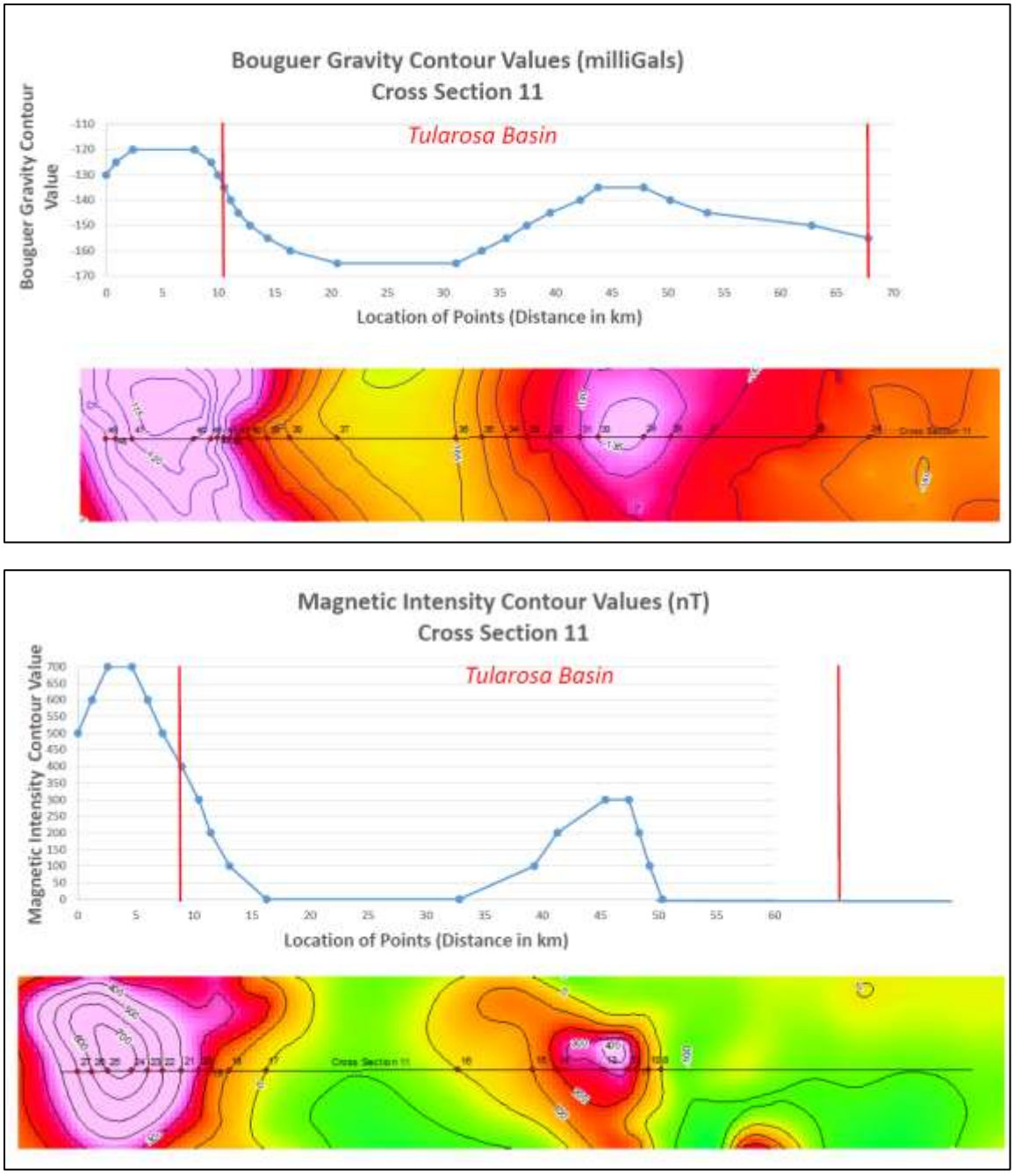

Figure 13. The profiles in this figure cross the basin between the San Andreas and Franklin Mountains. Both the gravity (top) and the Magnetic (bottom) data define basin-bounding normal faults.

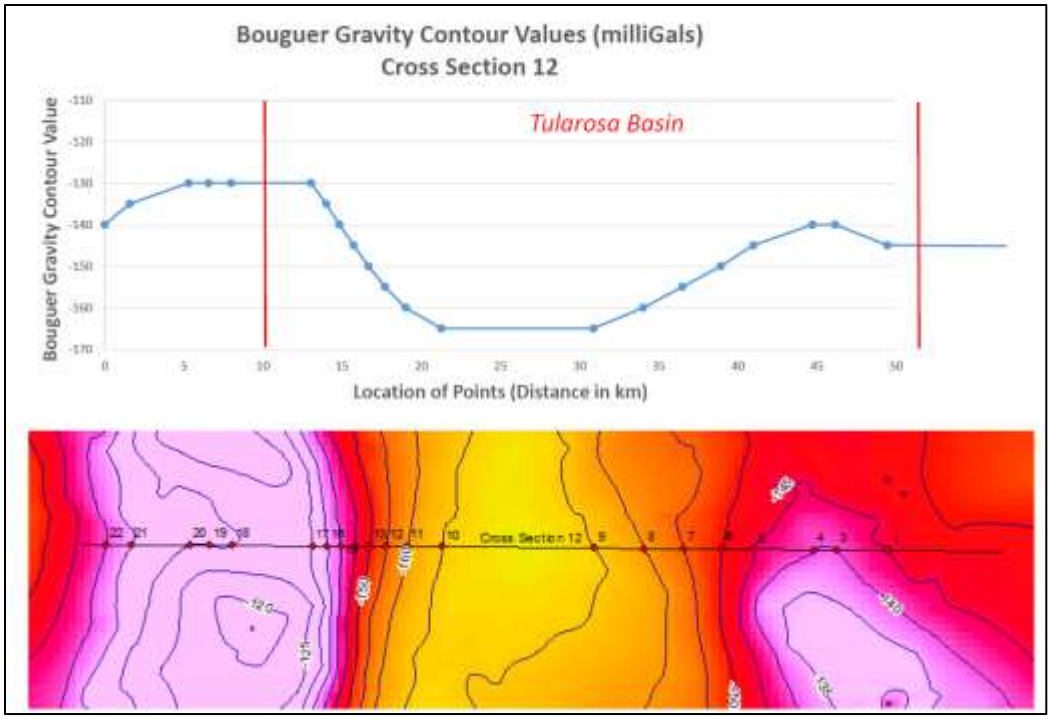

Figure 14. The profiles in this figure cross the basin between near the center of the Franklin Mountains. The gravity profile once again defines basin-bounding normal faults.

North to South Geophysical Profiles of Tularosa Basin

We also constructed north-south profiles of the Tularosa basin using Bouguer gravity anomaly and magnetic intensity counter values. Since these cross sections are free from the east-west margin topographic effects of the basin, they even better depict the heterogeneity in rock properties within and along the basin from north to south. Four such geophysical "highs" are identified to exist approximately at spatial intervals of (A) 50-90 km (A), 125-135 km (B), 170-190 km (C), and 220-240 km (D), as measured from the northern limit of the basin. In all of these localities, both Bouguer gravity and magnetic intensity show relatively higher values (compared to the surrounding areas in the basin) indicating the presence of higher density and more magnetic rocks. These heterogeneous localities seem to be "basement highs" of "more magnetic rocks" which may be mafic intrusions (dikes) and/or fault-bounded basement highs. Interestingly these features appear to strike in an east-west direction perpendicular to the general north-south trend of the basin. The heterogeneous nature of rocks within the basin and the basement underlying the basin has critical impact on the structural configuration, fracture permeability, heat flow of the Tularosa basin. Therefore, more detailed modeling of these geophysical data will be important in Phase II, especially given that there is also scarcity of well data from the basin.

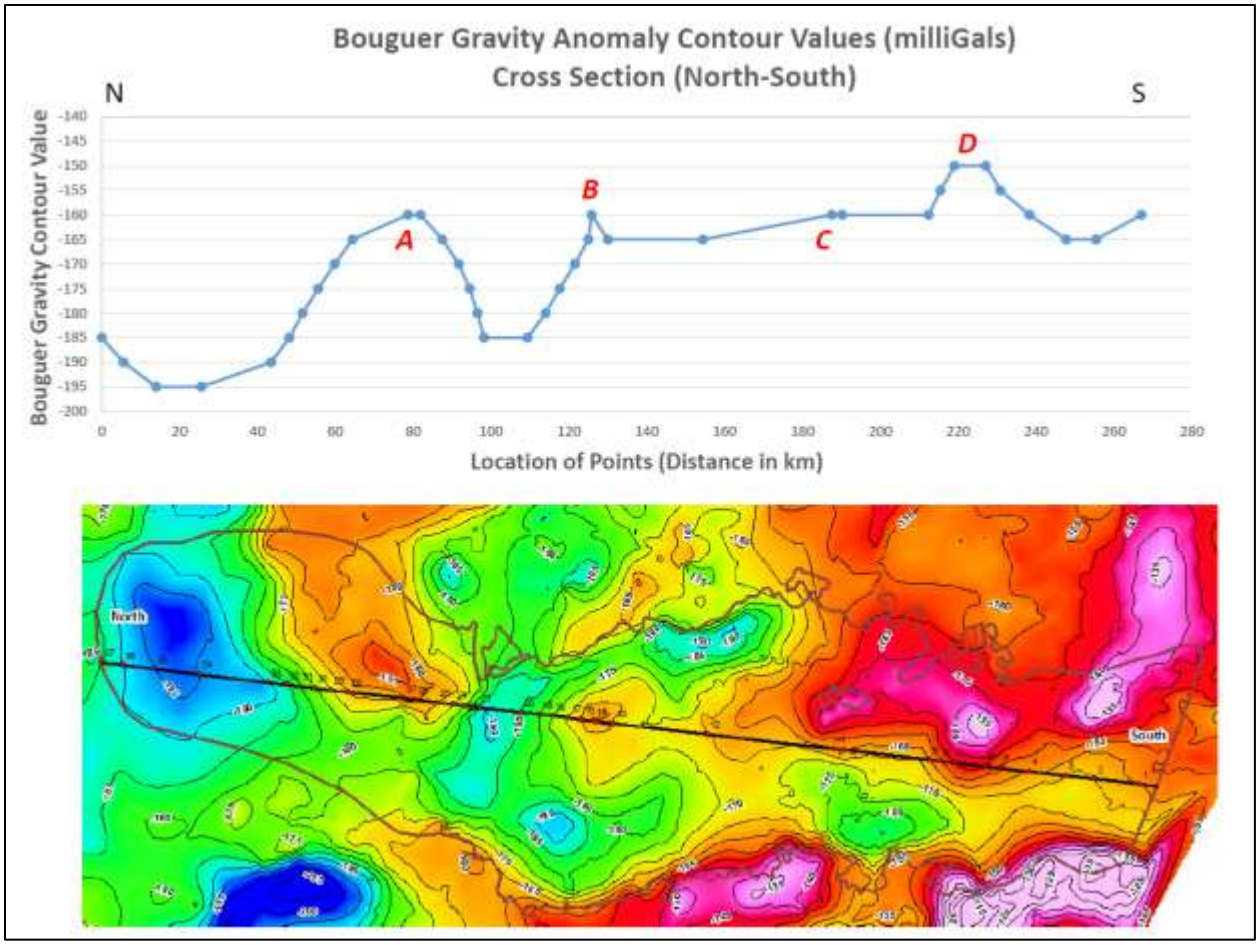

Figure 15. A north-south cross-section of Bouguer gravity anomaly (in milliGals) across the Tularosa basin

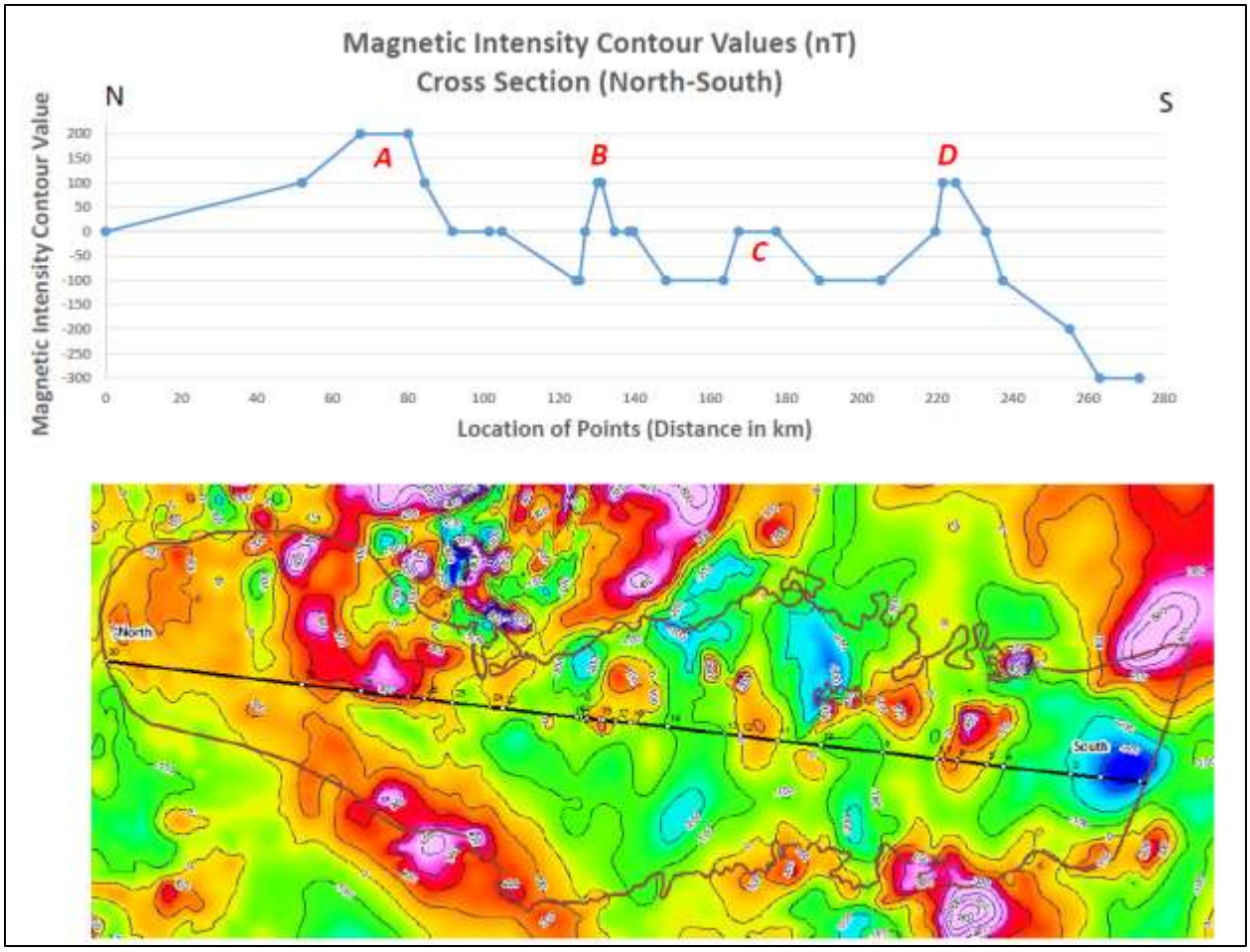

Figure 16. A north-south cross-section of magnetic intensity (in nanno-Tesla) across the Tularosa basin

BIBLIOGRAPHY

Bibliographic Database: Tularosa Basin and Rio Grande Rift, New Mexico

Adams, D.C. and Keller, G.R. (1994) Crustal Structure and Basin Geometry in South-Central New Mexico, *in* Keller G.R. and Cather, S.M., eds., *Basins of the Rio Grande Rift: Structure, Stratigraphy, and Tectonic Setting*, Geological Society of America Special Paper, No. 291, p. 241-256.

Albrecht, M. (2011) *Innovative Exploration Techniques for Geothermal Assessment at Jemez Pueblo, New Mexico*, U.S. Department of Energy, Division of Geothermal Energy, 16 p.

Aldrich, M.J. and Dethier, D.P. (1990) Stratigraphic and tectonic evolution of the northern Espanola basin Rio Grande
Rift, New Mexico, *Geological Society of America Bulletin*, Vol. 102, p. 1695-1705.

Aldrich, M.J., Chapin, C.E., and Laughlin, A.W. (1986) Stress History and Tectonic Development of the Rio Grande Rift, New Mexico, *Journal of Geophysical Research*, Vol. 91, No. B6, p. 6199-6211.

Aldrich, M.J., Jr. (1986) Tectonics of the Jemez Lineament in the Jemez Mountains and Rio Grande Rift, *Journal of Geophysical Research*, Vol. 91, No. B2, p. 1753-1762.

Ander, M.E. (1981) Geophysical Study of the Crust and Upper Mantle beneath the Central Rio Grande Rift and Adjacent Great Plains and Colorado Plateau, United States Department of Energy, University of California, 218 p.

Anderson, O.J. and Jones, G.E. (1994) Geologic Map of New Mexico, 1:500,000, New Mexico Bureau of Mines and Mineral Resources Open File Report, No. 408, 32 p.

Ankeny, L.A. and Braile, L.W. (1986) Upper Crustal Structure beneath the Jemez Mountains Volcanic Field, New Mexico, Determined by Three-Dimensional Simultaneous Inversion of Seismic Refraction and Earthquake Data, *Journal of Geophysical Research*, Vol. 91, No. B6, p. 6188-6198.

Aprea, C.M., Hildebrand, S., Fehler, M., et al. (2002) Three-dimensional Kirchhoff migration: Imaging of the Jemez volcanic field using teleseismic data, *Journal of Geophysical Research*, Vol. 107, No. B10, p. 15 p.

Armstrong, C., Dutrow, B.L., Henry, D.J., et al. (2013) Provenance of volcanic clasts from the Santa Fe Group, Culebra graben of the San Luis Basin, Colorado: A guide to tectonic evolution, *in* Hudson, M.R. and Grauch, V.J.S., *New Perspectives on Rio Grande Rift Basins: From Tectonics to Groundwater*, *The Geological Society of America Special Paper*, No. 494, p. 21-46.

Atkinson, P.G. and Gulati, M.S. (1979) Status Report on Geothermal Development in the Valles Caldera, New Mexico, Union Oil Co., p. 257-259.

Averill, M.G. and Miller, K.C. (2013) Upper crustal structure of the southern Rio Grande rift: A composite record of rift and pre-rift tectonics, *in* Hudson, M.R. and Grauch, V.J.S., eds., *New Perspectives on Rio Grande Rift Basins: From Tectonics to Groundwater*, *The Geological Society of America Special Paper*, No. 494, p. 463-474.

Bailey, R.A. and Ross, C.S. (1969) Stratigraphic Nomenclature of Volcanic Rocks in the Jemez Mountains, New

Mexico, *Contributions to Stratigraphy, New stratigraphic names and revisions in nomenclature of upper Tertiary and Quaternary volcanic rocks in the Jemez Mountains*, Geological Survey Bulletin 1274, 19 p.

Bailey, R.A., Smith, R.L., and Ross, C.S. (1961) Outline of the geology of the Jemez Mountains, New Mexico, New Mexico Geological Society, Twelfth Field Conference, p. 139-143.

Baldridge, W.S. (1978) Petrology and Petrogenesis of Plio-Pleistocene Basaltic Rocks from the Central Rio Grande Rift, New Mexico, and Their Relation to Rift Structure, *in* Riecker, R.E., eds., *Rio Grande Rift: Tectonics and Magmatism*, American Geophysical Union, p. 323-354.

Baldridge, W.S. and Olsen, K.H. (1989) The Rio Grande Rift, *American Scientist*, Vol. 77, No. 3, p. 240-247.

Baldridge, W.S., et al. (1984) Rio Grande Rift: Problems and Perspectives, *New Mexico Geological Society Guidebook, 35th Field Conference*, 13 p.

Baldridge, W.S., Olsen, K.H., and Callender, J.F. (2015) Multimodal Geothermal Development in the Tularosa Basin, NM, *Fortieth Workshop on Geothermal Reservoir Engineering*, Stanford University, 7 p.

Barker, D.S. (1978) Cenozoic Magmatism in the Trans-Pecos Province: Relation to the Rio Grande Rift, *in* Riecker, R.E., eds., *Rio Grande Rift: Tectonics and Magmatism*, American Geophysical Union, p. 382-392.

Barroll, M.W. and Reiter, M. (1990) Analysis of the Socorro Hydrogeothermal System: Central New Mexico, *Journal of Geophysical Research*, Vol. 95, No. B13, p. 21949-21963.

Barrow, R. and Keller, G.R. (1994) An Integrated Geophysical Study of the Estancia Basin, Central New Mexico, *in* Keller G.R. and Cather, S.M., eds., *Basins of the Rio Grande Rift: Structure, Stratigraphy, and Tectonic Setting*, *The Geological Society of America Special Paper*, No. 291, p. 171-186.

Barse, K.A., McDonald, M.R., and Crowell, A.M. (2012) Evaluation of the Geothermal Potential in the Rio Grande Rift: Truth or Consequences, New Mexico, GRC Transactions, Vol. 36, p. 1315-1320.

Barton, C.A. and Zoback, M.D. (1988) In-Situ Stress Orientation and Magnitude at the Fenton Geothermal Site, New Mexico, Determined from Wellbore Breakouts, *Geophysical Research Letters*, Vol. 15, No. 5, p. 467-470.

Beck, W.C. and Chapin, C.E. (1994) Structural and Tectonic Evolution of the Joyita Hills, Central New Mexico: Implications of Basement Control on Rio Grande Rift, *in* Keller G.R. and Cather, S.M., eds., *Basins of the Rio Grande Rift: Structure, Stratigraphy, and Tectonic Setting*, *The Geological Society of America Special Paper*, No. 291, p. 187-206.

Berglund, H.T., Sheehan, A.F., Murray, M.H., et al. (2012) Distributed deformation across the Rio Grande Rift, Great Plains, and Colorado Plateau, *Geology*, Vol. 40, No. 1, p. 23-26.

Birch, F.S. (1982) Gravity models of the Albuquerque basin, Rio Grande rift, New Mexico, *Geophysics*, Vol. 47, No. 8, p. 1185-1197.

Blanchard, W.G., Jr. and Davis, M.J. (1929) Permian Stratigraphy and Structure of Parts of Southeastern New Mexico
and South-western Texas, *AAPG Bulletin*, Vol. 13, p. 957-995.

Bowsher, A.L. (1991) Some effects of the Precambrian basement on the development of the Sacramento Mountains,
Geology of the Sierra Blanca, Sacramento, and Capitan Ranges, New Mexico, Annual NMGS Fall Field Conference Guidebooks, New Mexico Geological Society, p. 81-89.

Boyd, T., et al. (2011) The feasibility of Geothermal Potential in the Rio Grande Rift Area of New Mexico and Texas, *GHC Bulletin*, p. 10-16.

Bridwell, R.J. and Anderson, C.A. (1980) *Thermomechanical Models of the Rio Grande Rift, Los Alamos Scientific Laboratory*, U.S. Department of Energy, 24 p.

Brister, B.S. and Gries, R.R. (1994) Tertiary Stratigraphy and Tectonic Development of the Alamosa Basin (Northern San Luis Basin) Rio Grande Rift, South-Central Colorado, *in* Keller G.R. and Cather, S.M., eds., *Basins of the Rio Grande Rift: Structure, Stratigraphy, and Tectonic Setting*, *The Geological Society of America Special Paper*, No. 291, p. 39-58.

Broadhead, R.F. (2003) Petroleum Geology of the McGregor Range Otero County, New Mexico, *New Mexico Bureau of Geology and Mineral Resources, Search and Discovery Article*, No. 10052, 13 p.

Brocher, T.M. (1981) Shallow Velocity Structure of the Rio Grande Rift North of Socorro, New Mexico: A Reinterpretation, *Journal of Geophysical Research*, Vol. 86, No. B6, p. 4960-4970.

Brown, C.D. and Phillips, R.J. (1999) Flexural rift flank uplift at the Rio Grande rift, New Mexico, *Tectonics*, Vol. 18, No. 6, p. 1275-1291.

Brown, L.D., Krumhansl, P.A., Chapin, C.E., et al. (1978) Cocorp Seismic Reflection Studies of the Rio Grande Rift, *in* Riecker, R.E., eds., *Rio Grande Rift: Tectonics and Magmatism*, American Geophysical Union, p. 169-184.

Brown, L.D., Kaufman, S., and Oliver, J.E. (1983) Cocorp Seismic Traverse across the Rio Grande Rift, *Seismic Expression of Structural Styles: A Picture and Work Atlas, Studies in Geology 15*, Vol. 2, 6 p.

Brown, L.L. and Caffall, N.M. (1993) Paleomagnetism and tectonic interpretations of the Taos Plateau Volcanic Field, Rio Grande Rift, New Mexico, *Journal of Geophysical Research*, Vol. 98, No. B12, p. 22401-22413.

Broxton, D.E. and Vaniman, D.T. (2005) Geologic Framework of a Groundwater System on the Margin of a Rift Basin, Pajarito Plateau, North-Central New Mexico, Los Alamos National Laboratory, *Vadose Zone Journal*, Vol. 4, p. 522-550.

Caine, J.S. and Minor, S.A. (2009) Structural and geochemical characteristics of faulted sediments and inference on the role of water in deformation, Rio Grande Rift, New Mexico, *GSA Bulletin*, Vol 121, No. 9-10, p. 1325-1340.

Callender, J.F. (1978) Evaluation of geothermal potential of Rio Grande rift and Basin and Range province, New Mexico, U.S. Geological Survey, 263 p.

Cape, C.D., McGeary, S., and Thompson, G.A. (1983) Cenozoic normal faulting and the shallow structure of the Rio Grande rift near Socorro, New Mexico, *Geological Society of America Bulletin*, Vol. 94, p. 3-14.

Carciumaru, D. and Ortega, R. (2011) On the origin of low angle normal faulting in the Southern Rio Grande Rift, *Geofisica Internacional*, p. 177-190.

Carter, K.F. and Winter, C.I. (1995) Fractal nature and scaling of normal faults in the Espanola Basin, Rio Grande rift, New Mexico: implications for fault growth and brittle strain, *Journal of Structural Geology*, Vol. 17, No. 6, p. 863-873.

Cather, S.M., Karlstrom, K.E., Timmons, J.M., et al. (2006) Palinspastic reconstruction of Proterozoic basement related aeromagnetic features in north-central New Mexico: Implications for Mesoproterozoic to late Cenozoic tectonism, *Geosphere*, Geologic Society of America, Vol. 2, No. 6, p. 299-323.

Cather, S.M., Chamberlin, R.M., Chapin, C.E., et al. (1994) Stratigraphic Consequences of Episodic Extension in the Lemitar Mountains, Central Rio Grande Rift, *in* Keller G.R. and Cather, S.M., eds., *Basins of the Rio Grande Rift: Structure, Stratigraphy, and Tectonic Setting*, *The Geological Society of America Special Paper*, No. 291, p. 157-170.

Chaimov, T.A. (1988) A 3-D Seismic Modeling Study of the Ladron Horst near Socorro, New Mexico, *Geophysical Research Letters*, Vol. 15, No. 11, p. 1207-1210.

Chamberlin, R.M. (2001) Waning-Stage Eruptions of the Oligocene Socorro Caldera, Central New Mexico, *Volcanology in New Mexico, New Mexico Museum of Natural History and Science Bulletin*, p. 69-77.

Chamberlin, R.M. and McIntosh, W.C. (2007) Chronology and structural control of Late Cenozoic volcanism in the Loma Creston quadrangle, southern Jemez volcanic field, New Mexico, *Geology of the Jemez Region II, New Mexico Geological Society 58th Annual Fall Field Conference Guidebook*, p. 248-261.

Chamberlin, R.M., McIntosh, W.C., and Chapin, C.E. (2003) Oligocene calderas, mafic lavas and radiating mafic dikes of the Socorro-Magdalena magmatic system, Rio Grande rift, New Mexico: surface expression of a miniplume?, Bureau of Geology and Mineral Resources, New Mexico Tech, 5 p.

Chapin, C.E. (1978) Evolution of the Rio Grande Rift: A Summary, *in* Riecker, R.E., eds., *Rio Grande Rift: Tectonics and Magmatism*, American Geophysical Union, p. 1-6.

Chapin, C.E. and Cather, S.M. (1994) Tectonic Setting of the Axial Basins of the Northern and Central Rio Grande Rift, *in* Keller G.R. and Cather, S.M., eds., *Basins of the Rio Grande Rift: Structure, Stratigraphy, and Tectonic Setting, The Geological Society of America Special Paper*, No. 291, p. 5-26.

Clarkson, G. and Reiter, M. (1984) Analysis of Terrestrial Heat-Flow Profiles Across the Rio Grande Rift and Southern Rocky Mountains in Northern New Mexico, *New Mexico Geological Society Guidebook, 35th Field Conference*, p. 39-44.

Collins, E.W. and Raney, J.A. (1994) Tertiary and Quaternary Tectonics of the Hueco Bolson, Trans-Pecos Texas and Chihuahua, Mexico, *in* Keller G.R. and Cather, S.M., eds., *Basins of the Rio Grande Rift: Structure, Stratigraphy, and Tectonic Setting*, *The Geological Society of America Special Paper*, No. 291, p. 265-282.

Connell, S.D., Smith, G.A., Geissman, J.W., et al. (2013) Climatic controls on nonmarine depositional sequences in the Albuquerque Basin, Rio Grande rift, north-central New Mexico, *in* Hudson, M.R. and Grauch, V.J.S., eds., *New Perspectives on Rio Grande Rift Basins: From Tectonics to Groundwater*, *The Geological Society*

of America Special Paper, No. 494, p. 383-426.

Cook, F.A., McCullar, D.B., Decker, E.R., et al. (1978) Crustal Structure and Evolution of the Southern Rio Grande Rift, *in* Riecker, R.E., eds., *Rio Grande Rift: Tectonics and Magmatism*, American Geophysical Union, p. 195-208.

Cooper, J.R. (2006) Igneous Intrusions and Thermal Evolution in the Raton Basin, CO-NM: Contact Metamorphism and Coal-Bed Methane Generation, University of Missouri-Columbia Thesis, 249 p.

Copeland, P., Murphy, M.A., Dupre, W.R., et al. (2011) Oligocene Laramide deformation in southern New Mexico and its implications for Farallon plate geodynamics, *Geosphere*, Geological Society of America, Vol. 7, No. 5, p. 1209-1219.

Cordell, L. (1978) Regional geophysical setting of the Rio Grande rift, *Geological Society of America Bulletin*, Vol. 89, p. 1073-1090.

Cordell, L. (1982) Extension in the Rio Grande Rift, *Journal of Geophysical Research*, Vol. 87, No. B10, p. 8561-8569.

Cordell, L., Zorin, Y.A., and Keller, G.R. (1991) The Decompensative Gravity Anomaly and Deep Structure of the Region of the Rio Grande Rift, *Journal of Geophysical Research*, Vol. 96, No. B4, p. 6557-6568.

Cordell, L., Long, C.L., and Jones, D.W. (1985) Geophysical Expression of the Batholith beneath Questa Caldera, New Mexico, *Journal of Geophysical Research*, Vol. 90, No. B13, p. 11263-11269.

Crumpler, L.S. (2001) Volcanism in New Mexico: An Overview, *Volcanology in New Mexico, New Mexico Museum of Natural History and Science Bulletin*, p. 17-29.

Crumpler, L.S. and Aubele, J.C. (2001) Volcanoes of New Mexico: An Abbreviated Guide for Non-Specialists, *Volcanology in New Mexico, New Mexico Museum of Natural History and Science Bulletin*, p. 5-15.

Culbertson, J.K. (1967) Evidence of Secondary Circulation in an Alluvial Channel, *Geological Survey Research 1967, Chapter D, Geological Survey Professional Paper*, No. 575-D, p. D214-D216.

Daggett, P.H., Keller, G.R., Morgan, P., et al. (1986) Structure of the Southern Rio Grande Rift from Gravity Interpretation, *Journal of Geophysical Research*, Vol. 91, No. B6, p. 6157-6167.

Dahal, S., McDonald, M.R., Bubach, B., et al. (2012) Evaluation of Geothermal Potential of Lighting Dock KGRA, New Mexico, GRC Transactions, Vol. 36, p. 638-640.

D'Alfonso, D., Hardwick, C., Hollingshaus, B., et al. (2011) *Geothermal Potential of the Rio Grande Rift: A Critical Assessment*, University of Utah, 50 p.

Darton, N.H. (1920) *Geothermal Data of the United States*, Department of the Interior, United States Geological Survey, 97 p.

Davidson, M.E. (2000) *Seismic Modeling of the Valles Caldera, Jemez Mountains, New Mexico*, Purdue University Thesis, ProQuest, UMI Dissertation Publishing, 250 p.

Davis, T.L. and Stoughton, D. (1978) Interpretation of Seismic Reflection Data from the Northern San Luis Valley,

South-Central Colorado, *in* Riecker, R.E., eds., *Rio Grande Rift: Tectonics and Magmatism*, American Geophysical Union, p. 185-194.

De Voogd, B., Serpa, L., and Brown, L. (1988) Crustal extension and magmatic processes: COCORP profiles from Death Valley and the Rio Grande rift, *Geological Society of America Bulletin*, Vol. 100, p. 1550-1567.

Decker, E.R. and Smithson, S.B. (1975) Heat Flow and Gravity Interpretation Across the Rio Grande Rift in Southern New Mexico and West Texas, *Journal of Geophysical Research*, Vol. 80, No. 17, p. 2542-2552.

Dethier, D.P. and Martin, B.A. (1984) Geology and Structure along part of the Northeast Jemez Mountains, New Mexico, *Rio Grande Rift: Northern New Mexico, New Mexico Geological Society Guidebook, 35th Field Conference*, p. 145-150.

Dickerson, P.W. (2013) Tascotal Mes transfer zone-An element of the Border Corridor transform system, Rio Grande
rift of West Texas and adjacent Mexico, *in* Hudson, M.R. and Grauch, V.J.S., eds., *New Perspectives on Rio Grande Rift Basins: From Tectonics to Groundwater*, *The Geological Society of America Special Paper*, No. 494, p. 475-500.

Dickerson, P.W. and Muehlberger, W.R. (1994) Basins in the Big Bend Segment of the Rio Grande Rift, Trans-Pecos Texas, *in* Keller G.R. and Cather, S.M., eds., *Basins of the Rio Grande Rift: Structure, Stratigraphy, and Tectonic Setting*, *The Geological Society of America Special Paper*, No. 291, p. 283-297.

Doughty, P.T. (2003) Clay Smear seals and fault sealing potential of an exhumed growth fault, Rio Grande rift, New Mexico, *AAPG Bulletin*, Vol. 87, No. 3, p. 427-444.

Drenth, B.J., Grauch, V.J.S., and Rodriguez, B.D. (2013) Geophysical constraints on Rio Grande rift structure in the central San Luis Basin, Colorado and New Mexico, *in* Hudson, M.R. and Grauch, V.J.S., eds., *New Perspectives on Rio Grande Rift Basins: From Tectonics to Groundwater*, *The Geological Society of America Special Paper*, No. 494, p. 75-100.

Eardley, A.J. (1963) Relation of Uplifts to Thrusts in Rocky Mountains, Backbone of the Americas: Tectonic History from Pole to Pole, American Association of Petroleum Geologists, p. 209-219.

Easley, E., Garchar, L., Bennett, M. et al. (2011) Investigation of Geothermal Resource Potential in the Northern Rio Grande Rift, Colorado and New Mexico, *GRC Transactions*, Vol. 35, p. 761-768.

Easley, E., Garchar, L., Bennett, M. et al. (2011), A Geochemical and Isotopic Study of Two Geothermal Prospects in the Rio Grande Rift, Colorado and New Mexico, *The Mountain Geologist*, Vol. 48, No. 4, p. 95-106.

Eaton, G.P. (1978) A Plate-Tectonic Model for Late Cenozoic Crustal Spreading in the Western United States, *in* Riecker, R.E., eds., *Rio Grande Rift: Tectonics and Magmatism*, American Geophysical Union, p. 7-32.

Elston, W.E. (2001) The Ignimbrite Flareup in Southwestern New Mexico: What Have we Learned these Last 50 Years, *Volcanology in New Mexico, New Mexico Museum of Natural History and Science Bulletin*, p. 49
67.

Elston, W.E. and Bornhorst, T.J. (1978) The Rio Grande Rift in Context of Regional Post-40 M.Y. Volcanic and Tectonic Events, *in* Riecker, R.E., eds., *Rio Grande Rift: Tectonics and Magmatism*, American

Geophysical Union, p. 416-438.

Faust, C.R., Mercer, J.W., and Thomas, S.D. (1984) Quantitative Analysis of Existing Conditions and Production Strategies for the Baca Geothermal System, New Mexico, *Water Resources Research*, Vol. 20, No. 5, p. 601-618.

Ferguson, J.F., Baldridge, W.S., Braile, L.W., et al. (1995) Structure of the Espanola Basin, Rio Grande Rift, New Mexico, from SAGE seismic and gravity data, *New Mexico Geological Society fall Field Conference 1995*, Los Alamos National Laboratory, United States Department of Energy, 20 p.

Fialko, Y. and Simons, M. (2001) Evidence for on-going inflation of the Socorro magma body, New Mexico, From Interferometric Synthetic Aperture Radar imaging, *Geophysical Research Letters*, Vol. 28, No. 18, p. 3549-3552.

Finger, J.T. and Jacobson, R.D. (1997) *Fort Bliss Exploratory Slimholes: Drilling and Testing*, Sandia National Laboratories, United States Department of Energy, 181 p.

Fischer, H.B. (1967) Transverse Mixing in a Sand-Bed Channel, *Geological Survey Research 1967, Chapter D, Geological Survey Professional Paper*, No. 575-D, p. D267-D272.

Fleischmann, D.J. (2006) *Geothermal Resource Development Needs in New Mexico*, Geothermal Energy Association for the U.S. Department of Energy, 30 p.

Gao, W. (2006) *Upper Mantle Seismic Structure beneath the Central Rio Grande Rift and beneath Eastern Mexico and their Implications*, The University of Texas at Austin Dissertation, 218 p.

Gao, W., Grand, S.P., Baldridge, W.S., et al. (2004) Upper Mantle Convection Beneath the Central Rio Grande Rift, *Journal of Geophysical Research*, Vol. 109, No. B3, 50 p.

Gardner, J.N. and Goff, F. (1986) Stratigraphic relations and lithologic variations in the Jemez Volcanic Field, New Mexico, *Journal of Geophysical Research*, Vol. 91, No. B2, p. 1763-1778.

Gardner, J.N., Lavine, A., WoldeGabriel, G., et al. (1999) Structural Geology of the Northwestern Portion of Los Alamos National Laboratory, Rio Grande Rift, New Mexico: Implications for Seismic Surface Rupture Potential from TA-3 to TA-55, Los Alamos National Laboratory, United States Department of Energy, 112 p.

Gardner, J.N., Goff, F., Goff, S., et al. (1987) Core Lithology Valles Caldera #1, New Mexico, Los Alamos National Laboratory, United States Department of Energy, 273 p.

Goff, F. (2002) Geothermal Potential of the Valles Caldera, New Mexico, *GHC Bulletin*, p. 7-12.

Goff, F. and Gardner, J.N. (1994) Evolution of a Mineralized Geothermal System, Valles Caldera, New Mexico, *Economic Geology*, Vol. 89, p. 1803-1832.

Goff, F. and Gardner, J.N. (2004) Late Cenozoic Geochronology of Volcanism and Mineralization in the Jemez Mountains and Valles Caldera, North Central New Mexico, *The Geology of New Mexico, A Geologic History*, New Mexico Geological Society, p. 295-312.

Goff, F. and Shevenell, L. (1987) Travertine deposits of Soda Dam, New Mexico, and their implications for the age and evolution of the Valles caldera hydrothermal system, *Geological Society of America Bulletin*, Vol. 99, p. 292-302.

Goff, F., Shevenell, L., and Gardner, J.N. (1988) The Hydrothermal Outflow Plume of Valles Caldera, New Mexico, and a Comparison with Other Outflow Plumes, *Journal of Geophysical Research*, Vol. 93, No. B6, p. 6041-6058.

Goff, F., Gardner, J., Rosemary, V., et al. (1985) Geochemistry and Isotopes of Fluids from Sulphur Springs, Valles Caldera, New Mexico, *Journal of Volcanology and Geothermal Research*, Elsevier Science Publishers B.V., Vol 23, p. 273-297.

Goff, F., McCormick, T., Trujilo, P.E., Jr., et al. (1982) Geochemical Data for 95 Thermal and Nonthermal Waters of the Valles Caldera-Southern Jemez Mountains Region, New Mexico, Los Alamos National Laboratory, 51 p.

Golombek, M.P. (1983) Geology, structure, and tectonics of the Pajarito fault zone in the Espanola basin of the Rio Grande rift, New Mexico, *Geological Society of America Bulletin*, Vol. 94, p. 192-205.

Golombek, M.P. (1981) Geometry and rate of extension across the Pajarito fault zone, Espanola basin, Rio Grande rift, northern New Mexico, *Geology*, Vol. 9, p. 21-24.

Gornitz, V. (1982) Volcanism and the Tectonic Development of the Rio Grande Rift and Environs, New Mexico – Colorado, from Analysis of Petrochemical Data, *The Mountain Geologist*, Vol. 19, No. 2, p. 41-58.

Goteti, R., Mitra, G., Becene, A., et al. (2013) Three-dimensional finite-element modeling of fault interactions in rift scale normal fault systems: Implications for the late Cenozoic Rio Grande rift of north-central New Mexico, *in* Hudson, M.R. and Grauch, V.J.S., eds., *New Perspectives on Rio Grande Rift Basins: From Tectonics to Groundwater*, *The Geological Society of America Special Paper*, No. 494, p. 157-184.

Grant, P.R., Jr. (1982) Geothermal Potential in the Albuquerque Area, New Mexico, *New Mexico Geological Society Guidebook, 33rd Field Conference*, p 325-331.

Grauch, V.J.S. and Connell, S.D. (2013) New perspectives on the geometry of the Albuquerque Basin, Rio Grande rift, New Mexico: Insights from geophysical models of rift-fill thickness, *in* Hudson, M.R. and Grauch, V.J.S., eds., *New Perspectives on Rio Grande Rift Basins: From Tectonics to Groundwater*, *The Geological Society of America Special Paper*, No. 494, p. 427-462.

Grauch, V.J.S. and Hudson, M.R. (2007) Guides to understanding the aeromagnetic expression of faults in sedimentary basins: Lessons learned from the central Rio Grande rift, New Mexico, *Geosphere*, Geological Society of America, Vol. 3, No. 6, p. 596-623.

Grauch, V.J.S., Phillips, J.D., Koning, D.J., et al. (2009) Geophysical Interpretations of the Southern Espanola Basin, New Mexico, That Contribute to Understanding Its Hydrogeologic Framework, U.S. Department of the Interior, U.S. Geologic Survey, 87 p.

Gries, J.C. (1978) Problems of Delineation of the Rio Grande Rift into the Chihuahua Tectonic Belt of Northern Mexico, *in* Riecker, R.E., eds., *Rio Grande Rift: Tectonics and Magmatism*, American Geophysical Union, p. 107-114.

Grigsby, C.O. (1984) Geochemical Behavior of a Hot Dry Rock Geothermal Reservoir, Rio Grande Rift: Northern New Mexico, *New Mexico Geological Society Guidebook, 35th Field Conference*, p. 265-270.

Hagstrum, J.T. and Lipman, P.W. (1986) Paleomagnetism of the structurally deformed Latir volcanic field, northern New Mexico: Relations to formation of the Questa caldera and development of the Rio Grande rift, *Journal of Geophysical Research*, Vol. 91, No. B7, p. 7383-7402.

Hagstrum, J.T., Lipman, P.W., and Elston, D.P. (1982) Paleomagnetic evidence bearing on the structural development
on the Latir Volcanic Field near Questa, New Mexico, *Journal of Geophysical Research*, Vol. 87, No. B9, p. 7833-7842.

Hamblock, J.M., Adronicos, C.L., Miller, K.C., et al. (2007) A composite geologic and seismic profile beneath the southern Rio Grande rift, New Mexico, based on xenolith mineralogy, temperature, and pressure, *Tectonophysics*, Vol. 442, p. 14-48.

Harder, V., Morgan, P., and Swanberg, C.A. (1980) Geothermal Resources in the Rio Grande Rift: Origins and Potential, *Geothermal Resources Council, Transactions*, Vol. 4, p. 61-64.

Harlan, S.S. and Geissman, J.W. (2009) Paleomagnetism of Tertiary intrusive and volcaniclastic rocks of the Cerrillos Hills and surrounding region, Expanola Basin, New Mexico, U.S.A.: Assessment and implications of vertical-axis rotations associated with extension of the Rio Grande rift, *Lithosphere*, Vol. 1, No. 3, p. 155-173.

Harrison, R.W. (1994) Winston Graben: Stratigraphy, Structure, and Tectonic Setting, *in* Keller G.R. and Cather, S.M., eds., *Basins of the Rio Grande Rift: Structure, Stratigraphy, and Tectonic Setting*, *The Geological Society of America Special Paper*, No. 291, p. 227-240.

Harrison, T.M., Morgan, P., and Blackwell, D.D. (1986) Constraints on the age of heating at the Fenton Hill Site, Valles Caldera, New Mexico, *Journal of Geophysical Research*, Vol. 91, No. B2, p. 1899-1908.

Hawley, J. (1999) Overview of the Hydrogeology of the Northern Rio Grande Basin - Colorado, New Mexico, and Texas, WRRI Conference Proceedings, 24 p.

Hawley, J.W., Haase, C.S., and Lozinsky, R.P. (1994) An Underground View of the Albuquerque Basin, *The Water Future of Albuquerque and Middle Rio Grande Basin*, New Mexico Water Resources Research Institute, p. 37-55.

Heiken, G., Goff, F., Stix, J., et al. (1986) Intracaldera volcanic activity, Toledo Caldera and Embayment, Jemez Mountains, New Mexico, *Journal of Geophysical Research*, Vol. 91, No. B2, p. 1799-1815.

Heiken, G., Goff, F., Gardner, J.N., et al. (1990) The Valles/Toledo Caldera Complex, Jemez Volcanic Field, New Mexico, *Annual Rev. Earth Planetary Science*, Vol. 18, p. 27-53.

Hermance, J.F. (1979) Toward Assessing the Geothermal Potential of the Jemez Mountains Volcanic Complex: A Telluric-Magnetotelluric Survey, Los Alamos National Laboratory, United States Department of Energy, 86 p.

Hermance, J.F. and Pedersen, J. (1980) Deep structure of the Rio Grande Rift: A magnetotelluric interpretation, *Journal of Geophysical Research*, Vol. 85, No. B7, p. 3899-3912.

Herrick, C.L. (1900) The Geology of the White Sands of New Mexico, *The Journal of Geology*, Vol. 8, No. 2, p. 112-128.

Hills, J.M. (1970) Late Paleozoic Structural Directions in Southern Perpian Basin, West Texas and Southeastern New Mexico, *The American Association of Petroleum Geologists Bulletin*, Vol. 54, No. 10, p. 1809-1827.

Hoffer, J.M. (2001) Geology of Potrillo Maar, Southern New Mexico and Northern Chihuahua, Mexico, *Volcanology in New Mexico, New Mexico Museum of Natural History and Science Bulletin*, p. 137-140.

Hoffer, J.M. (2001) Geology of the West Potrillo Mountains, *Volcanology in New Mexico, New Mexico Museum of Natural History and Science Bulletin*, p. 141-145.

Holt, B. and Ghormley, E.L. (1976) Energy Conversion and Economics for Geothermal Power Generation at Heber, California, Valles Caldera, New Mexico, and Raft River, Idaho - Case Studies, *Geothermal Energy Conversion and Economics - Case Study*, Electric Power Research Institute, 114 p.

House, M.A., Kelley, S.A., and Roy, M. (2003) Refining the footwall cooling history of a rift flank uplift, Rio Grande rift, New Mexico, *Tectonics*, Vol. 22, No. 5, 18 p.

Huang, L. and Albrecht, M. (2011) Seismic and Magneto-Telluric Imaging for Geothermal Exploration at Jemez Pueblo in New Mexico, *Thirty-Sixth Workshop on Geothermal Reservoir Engineering, Stanford University,* Los Alamos National Laboratory, Los Alamos Geothermal Technology Center, 6 p.

Hudson, M.R., Grauch, V.J.S., and Minor, S.A. (2008) Rock magnetic characterization of faulted sediments with associated magnetic anomalies in the Albuquerque Basin, Rio Grande rift, New Mexico, *GSA Bulletin*, Vol. 120, No. 5/6, p. 641-658.

Huff, G.F. (2004) Simulation of Ground-Water Flow in the Basin-Fill Aquifer of the Tularosa Basin, South-Central New Mexico, Predevelopment through 2040, *USGS Scientific Investigations Report*, No. 2004-5197, 108 p.

Ingersoll, R.V., Cavazza, W., Baldridge, W.S., et al. (1990) Cenozoic sedimentation and paleotectonics of north central New Mexico: Implications for initiation and evolution of the Rio Grande rift, *Geological Society of America Bulletin*, Vol. 102, p. 1280-1296.

Jiracek, G.R. (1974) Geophysical Studies in the Jemez Mountains Region New Mexico, *New Mexico Geological Society Guidebook, 25th Field Conference*, p. 137-144.

Jiracek, G.R., Ander, M.E., and Holcombe, H.T. (1978) Magnetotelluric Soundings of Crustal Conductive Zones in Major Continental Rifts, *in* Riecker, R.E., eds., *Rio Grande Rift: Tectonics and Magmatism*, American Geophysical Union, p. 209-222.

Johnson, C.M. (1991) Large-scale crustal formation and lithosphere modification beneath Middle to Late Cenozoic calderas and volcanic fields, western North America, *Journal of Geophysical Research*, Vol. 96, No. B8, p. 13485-13507.

Johnson, C.M. and Thompson, R.A. (1991) Isotopic composition of Oligocene mafic volcanic rocks in the Northern Rio Grande Rift: Evidence for contributions of ancient intraplate and subduction magmatism to evolution of

lithosphere, *Journal of Geophysical Research*, Vol. 96, No. B8, p. 13593-13608.

Johnson, P.S., Koning, D.J., and Partey, F.K. (2013) Shallow groundwater geochemistry in the Espanola Basin, Rio Grande rift, New Mexico: Evidence for structural control of a deep thermal source, *in* Hudson, M.R. and Grauch, V.J.S., eds., *New Perspectives on Rio Grande Rift Basins: From Tectonics to Groundwater*, The Geological Society of America Special Paper, No. 494, p. 261-302.

Jones, D., Chu, S., Barghouty, L., et al. (2013) Magnetotelluric Investigation of Structures Related to a Geothermal Anomaly in the Buckman Well field in the Rio Grande Rift, New Mexico, American Geophysical Union, Vol. 2013, 1 p.

Jurdy, D.M. and Brocher, T.M. (1980) Shallow velocity model of the Rio Grande rift near Socorro, New Mexico, *Geology*, Vol. 8, p. 185-189.

Kaufman, G. (2013) Innovative Exploration Techniques for Geothermal Assessment at Jemez Pueblo, New Mexico, U.S. Department of Energy, Division of Geothermal Energy, 18 p.

Keller, G.R. and Baldridge, W.S. (1999) The Rio Grande rift: A geological and geophysical overview, *Rocky Mountain Geology*, Vol. 34, No. 1, p. 121-130.

Keller, G.R., Braile, L.W., and Schlue, J.W. (1978) Regional Crustal Structure of the Rio Grande Rift from Surface Wave Dispersion Measurements, *in* Riecker, R.E., eds., *Rio Grande Rift: Tectonics and Magmatism*, American Geophysical Union, p. 115-126.

Kelley, S.A. and Duncan, I.J. (1986) Late Cretaceous to middle Tertiary tectonic history of the northern Rio Grande Rift, New Mexico, *Journal of Geophysical Research*, Vol. 91, No. B6, p. 6246-6262.

Kelley, S.A., Kempter, K.A., McIntosh, et al. (2013) Syndepositional deformation and provenance of Oligocene to Lower Miocene sedimentary rocks along the western margin of the Rio Grande rift, Jemez Mountains, New Mexico, *in* Hudson, M.R. and Grauch, V.J.S., eds., *New Perspectives on Rio Grande Rift Basins: From Tectonics to Groundwater*, *The Geological Society of America Special Paper*, No. 494, p. 101-124.

Kelley, S.A., McIntosh, W.C., Goff, F., et al. (2013) Spatial and temporal trends in pre-caldera Jemez Mountains volcanic and fault activity, *Geosphere*, Geological Society of America, Vol. 9, No. 3, p. 614-646.

Kelley, S.A., Osburn, G.R., and Kempter, K.A. (2007) Geology of Canon de San Diego, southwestern Jemez Mountains, north-central New Mexico, *Geology of the Jemez Region II, New Mexico Geological Society 58th Annual Fall Field Conference Guidebook*, p. 169-138.

Kelley, V.C. (1978) Tectonics, Middle Rio Grande Rift, New Mexico, *in* Riecker, R.E., eds., *Rio Grande Rift: Tectonics and Magmatism*, American Geophysical Union, p. 57-70.

Kellogg, K.S. (1999) Neogene basins of the northern Rio Grande rift: partitioning and asymmetry inherited from Laramide and older uplifts, *Tectonophysics*, Vol. 305, p. 141-152.

Kil, Y. and Wendlandt, R.F. (2006) Depleted and enriched mantle processes under the Rio Grande rift: spinel peridotite xenoliths, *Contributions to Mineralogy and Petrology*, p. 135-151.

Kil, Y. and Wendlandt, R.F. (2004) Pressure and temperature evolution of upper mantle under the Rio Grande Rift,

Contributions to Mineralogy and Petrology, p. 265-280.

King, D. and Metcalfe, E. (2013) Rift Zones as a Case Study for Advancing Geothermal Occurrence Models, AAAS Science and Technology Policy Fellow, 11 p.

Klenner, R., McDonald, M.R., Dahal, S., et al. (2011) Evaluation of the Geothermal Potential in the Rio Grande Rift: San Luis Basin, Colorado and New Mexico, *The Mountain Geologist*, Vol. 48, No. 4, p. 107-119.

Kluth, C.F. and Schaftenaar, C.H. (1994) Depth and Geometry of the Northern Rio Grande Rift in the San Luis Basin, South-Central Colorado, *in* Keller G.R. and Cather, S.M., eds., *Basins of the Rio Grande Rift: Structure, Stratigraphy, and Tectonic Setting*, *The Geological Society of America Special Paper*, No. 291, p. 27-38.

Koning, D.J., Grauch, V.J.S., Connell, S.D., et al. (2013) Structure and tectonic evolution of the eastern Espanola Basin, Rio Grande rift, north central New Mexico, *in* Hudson, M.R. and Grauch, V.J.S., eds., *New Perspectives on Rio Grande Rift Basins: From Tectonics to Groundwater*, *The Geological Society of America Special Paper*, No. 494, p. 185-220.

Landman, R.L. and Flowers, R.M. (2013) (U-Th)/He thermochronologic constraints on the evolution of the northern Rio Grande Rift, Gore Range, Colorado, and implications for rift propagation models, *Geosphere*, Vol. 9, No. 1, p. 170-187.

Larsen, S., Reilinger, R., and Brown, L. (1986) Evidence of Ongoing Crustal Deformation Related to Magmatic Activity near Socorro, New Mexico, *Journal of Geophysical Research*, Vol. 91, No. B6, p. 6283-6292.

Lawton, T.F. and McMillan, N.J. (1999) Arc abandonment as a cause for passive continental rifting: Comparison of the Jurassic Mexican Borderland rift and the Cenozoic Rio Grande rift, *Geology*, Vol. 27, No. 9, p. 779-782.

Lewis, C.J. and Baldridge, W.S. (1994) Crustal Extension in the Rio Grande Rift, New Mexico: Half Grabens, Accommodation Zones, and Shoulder Uplifts in the Ladron Peak-Sierra Lucero Area, *in* Keller G.R. and Cather, S.M., eds., *Basins of the Rio Grande Rift: Structure, Stratigraphy, and Tectonic Setting*, *The Geological Society of America Special Paper*, No. 291, p. 135-156.

Lewis, C.J., Gardner, J.N., Schultz-Fellenz, E.S., et al. (2009) Fault interaction and along-strike variation in throw in the Pajarito fault system, Rio Grande rift, New Mexico, *Geosphere*, Vol. 9, No. 3, p. 252-269.

Lipman, P.W. and McIntosh, W.C. (2008) Eruptive and noneruptive calderas, northeastern San Juan Mountains, Colorado: Where did the ignimbrites come from?, *GSA Bulletin*, Vol. 120, No. 7/8, p. 771-795.

Lipman, P.W. and Mehnert, H.H. (1978) The Taos Plateau Volcanic Field, Northern Rio Grande Rift, New Mexico, *in* Riecker, R.E., eds., *Rio Grande Rift: Tectonics and Magmatism*, American Geophysical Union, p. 289-312.

Lipman, P.W., Mehnert, H.H., and Naeser, C.W. (1986) Evolution of the Latir Volcanic Field, Northern New Mexico, and Its Relation to the Rio Grande Rift, as Indicated by Potassium-Argon and Fission Track Dating, *Journal of Geophysical Research*, Vol. 91, No. B6, p. 6329-6345.

Lipman, P.W., Logatchev, N.A., Zorin, Y.A., et al. (1989) Intracontinental rift comparisons: Baikal and Rio Grande Rift Systems, *Eos*, Vol. 70, No. 19, p. 578-579.

Lisenbee, A.L. (2013) Multistage Laramide deformation in the area of the southern Santa Fe embayment (Rio Grande
rift) north-central New Mexico, *in* Hudson, M.R. and Grauch, V.J.S., eds., *New Perspectives on Rio Grande Rift Basins: From Tectonics to Groundwater*, *The Geological Society of America Special Paper*, No. 494, p. 239-260.

Lozinsky, R.P. (1994) Cenozoic Stratigraphy, Sandstone Petrology, and Depositional History of the Albuquerque Basin, Central New Mexico, *in* Keller G.R. and Cather, S.M., eds., *Basins of the Rio Grande Rift: Structure, Stratigraphy, and Tectonic Setting*, *The Geological Society of America Special Paper*, No. 291, p. 73-82.

Lucas, S.G. (2001) The Age of Mammals and the Age of Volcanoes in New Mexico: An Outline of the Cenozoic\ Geology and Paleontology of the State, *Volcanology in New Mexico, New Mexico Museum of Natural History and Science Bulletin*, p. 30-48.

Machette, M.N. (1986) History of Quaternary Offset and Paleoseismicity along the La Jencia Fault, Central Rio Grande Rift, New Mexico, *Bulletin of the Seismological Society of America*, Vol. 76, No. 1, p. 259-272.

Machette, M.N., Thompson, R.A., Marchetti, D.W., et al. (2013) Evolution of ancient Lake Alamosa and integration of the Rio Grande during the Pliocene and Pleistocene, *in* Hudson, M.R. and Grauch, V.J.S., eds., *New Perspectives on Rio Grande Rift Basins: From Tectonics to Groundwater*, *The Geological Society of America Special Paper*, No. 494, p. 1-20.

Mack, G.H. and Leeder, M.R. (1999) Climatic and Tectonic Controls on Alluvial-Fan and Axial-Fluvial Sedimentation in the Plio-Pleistocene Palomas Half Graben, Southern Rio Grande Rift, *Journal of Sedimentary Research*, Vol. 69, No. 3, p. 635-652.

Mack, G.H. and Seager, W.R. (1990) Tectonic control on facies distribution of the Camp Rice and Palomas Formations (Pliocene-Pleistocene) in southern Rio Grande rift, *Geological Society of America Bulletin*, Vol. 102, p. 45-53.

Mack, G.H. and Seager, W.R. (1995) Transfer zones in the southern Rio Grande rift, *Journal of the Geological Society*, London, Vol. 152, p. 551-560.

Mack, G.H., Jones, M.C., Tabor, N.J., et al. (2012) Mixed Geothermal and Shallow Meteoric Origin of Opal and Calcite Beds in Pliocene Lower Pleistocene Axial-Fluvial Strata, Southern Rio Grande Rift, Rincon Hills, New Mexico, U.S.A., *Journal of Sedimentary Research*, Vol. 82, No. 8, p. 616-631.

Mack, G.H., Cole, D.R., and Trevino, L. (2000) The distribution and discrimination of shallow, authigenic carbonate in the Pliocene Pleistocene Palomas Basin, southern Rio Grande rift, *GSA Bulletin*, Vol. 112, No. 5, p. 643-656.

Mack, G.H., Leeder, M., Perez-Arlucea, M., et al. (2011) Tectonic and climatic controls on Holocene channel migration, incision and terrace formation by the Rio Grande in the Palomas half graben, southern Rio Grande Rift, USA, Department of Geological Sciences, *Sedimentology*, Vol. 58, p. 1065-1086.
Mack, G.H., James, W.C., and Salyards, S.L., (1994) Late Pliocene and Early Pleistocene Sedimentation as Influenced by Intrabasinal Faulting, Southern Rio Grande Rift, *in* Keller G.R. and Cather, S.M., eds., *Basins of the Rio Grande Rift: Structure, Stratigraphy, and Tectonic Setting*, *The Geological Society of America Special Paper*, No. 291, p. 257-264.

Mack, G.H., Seager, W.R., and Leeder, M.R. (2003) Synclinal-horst basins: examples from the southern Rio Grande rift and southern transition zone of southwestern New Mexico, USA, *Basin Research*, Vol. 15, p. 365-377.

Mailloux, B.J., Person, M., Kelley, S., et al. (1999) Tectonic controls on the hydrogeology of the Rio Grande Rift, New Mexico, *Water Resources Research*, Vol. 35, No. 9, p. 2641-2659.

Maldonado, F., Miggins, D.P., Budahn, J.R., et al. (2013) Deformational and erosional history for the Abiquiu and contiguous area, north central New Mexico: Implications for formation of the Abiquiu embayment and a discussion of new geochronological and geochemical analysis, *in* Hudson, M.R. and Grauch, V.J.S., eds., *New Perspectives on Rio Grande Rift Basins: From Tectonics to Groundwater*, *The Geological Society of America Special Paper*, No. 494, p. 125-156.

Manley, K. (1978) Stratigraphy and Structure of the Espanola Basin, Rio Grande Rift, New Mexico, *in* Riecker, R.E., eds., *Rio Grande Rift: Tectonics and Magmatism*, American Geophysical Union, p. 71-86.

Manley, K. (1984) Brief summary of the Tertiary geologic history of the Rio Grande rift in northern New Mexico, *New Mexico Geologic Society, 35th Annual Fall Field Conference Guidebook*, p. 63-66.

Mattick, R.E. (1967) A Seismic and Gravity Profile across the Hueco Bolson, Texas, Geological Survey Research 1967, Chapter D, *Geological Survey Professional Paper*, No. 575-D, p. D85-D91.

May, S.J. and Russell, L.R. (1994) Thickness of the Syn-Rift Santa Fe Group in the Albuquerque Basin and Its Relation to Structural Style, *in* Keller G.R. and Cather, S.M., eds., *Basins of the Rio Grande Rift: Structure, Stratigraphy, and Tectonic Setting, The Geological Society of America Special Paper*, No. 291, p. 113-124.

May, S.J., Kelley, S.A., and Russell, L.R. (1994) Footwall Unloading and Rift Shoulder Uplifts in the Albuquerque Basin: Their Relation to Syn-Rift Fanglomerates and Apatite Fission-Track Ages, *in* Keller G.R. and Cather, S.M., eds., *Basins of the Rio Grande Rift: Structure, Stratigraphy, and Tectonic Setting*, *The Geological Society of America Special Paper*, No. 291, p. 125-134.

McCalpin, J.P. (2005) Late Quaternary activity of the Pajarito fault, Rio Grande rift of northern New Mexico, USA, *Tectonophysics*, Vol. 408, p. 213-236.

McMillan, N.J., Dickin, A.P., and Haag, D. (2000) Evolution of magma source regions in the Rio Grande rift, southern New Mexico, *GSA Bulletin*, Vol. 112, No. 10, p. 1582-1593.

Meinzer, O.E. and Hare, R.F. (1915) Geology and Water Resources of Tularosa Basin, New Mexico, Department of the Interior, *United States Geological Survey Water-Supply Paper*, No. 343., 317 p.

Meyer, J. and Foland, K.A. (1991) Magmatic-tectonic interaction during early Rio Grande rift extension at Questa, New Mexico, *Geological Society of America Bulletin*, Vol. 103, p. 993-1006.

Meyer, J. and Foland, K.A. (1991) A geophysical model of the Espanola Basin, Rio Grande Rift, New Mexico, *Geological Society of America Bulletin*, Vol. 103, p. 993-1006.

MicroGeophysics Corporation (1977) *Crustal Seismic - Refraction Investigations of the Geothermal Potential in the Central Rocky Mountains*, United States Geological Survey, 14 p.

Minor, S.A., Hudson, M.R., Caine, J.S., et al. (2013) Oblique transfer of extensional strain between basins of the

middle Rio Grande rift, New Mexico: Fault kinematic and paleostress constraints, *in* Hudson, M.R. and Grauch, V.J.S., eds., *New Perspectives on Rio Grande Rift Basins: From Tectonics to Groundwater*, *The Geological Society of America Special Paper*, No. 494, p. 345-382.

Morgan, P. and Witcher, J.C. (2011) Geothermal Resources along the Southern Rocky Mountains and the Rio Grande Rift, *The Mountain Geologist*, Vol. 48, No. 4, p. 81-93.

Morgan, P., Harder, V., Swanberg, C.A., et al. (1981) A groundwater convection model for Rio Grande rift geothermal
resources, *Geothermal Resource Council*, Vol. 5, p. 228-231.

Morgan, P., Seager, W.R., and Golombek, M.P. (1986) Cenozoic Thermal, Mechanical and Tectonic Evolution of the Rio Grande Rift, *Journal of Geophysical Research*, Vol. 91, No. B6, p. 6263-6276.

Morton, E.A. and Bilek, S.L. (2014) Limited Dynamic Earthquake Triggering in the Socorro Magma Body Region, Rio Grande Rift, New Mexico, *Bulletin of the Seismological Society of America*, Vol. 104, No. 5,
p. 2182-2193.

Moucha, R., Forte, A.M., Rowley, D.B., et al. (2008) Mantle convection and the recent evolution of the Colorado Plateau and the Rio Grande Rift valley, *Geology*, Geological Society of America, Vol. 36, No. 6, p. 439-442.

Mozley, P.S. and Davis, J.M. (2005) Internal structure and mode of growth of elongate calcite concretions: Evidence for small-scale, microbial induced, chemical heterogeneity in groundwater, *GSA Bulletin*, Vol.
117, No. 11/12, p. 1400-1312.

Muehlberger, W.R., Belcher, R.C., and Goetz, L.K. (1978) Quaternary faulting in Trans-Pecos Texas, *Geology*, Vol. 6, p. 337-340.

Murphy, H.D., Tester, J.W., Grigsby, C.O., et al. (1981) Energy Extraction from Fractured Geothermal Reservoirs in Low-Permeability Crystalline Rock, *Journal of Geophysical Research*, Vol. 86, No. B8, p. 7145-7158.

Nielson, D.L. and Hulen, J.B. (1984) Internal Geology and Evolution of the Redondo Dome, Valles Caldera, New Mexico, *Journal of Geophysical Research*, Vol. 89, No. B10, p. 8695-8711.

Nishimura, T., Fehler, M., Baldridge, W.S., et al. (1996) Heterogeneous structure around the Jemez volcanic field, New Mexico, USA, as inferred from the envelope inversion of active-experiment seismic data, *Geophysical Journal*, Vol. 131, p. 667-681.

O'Donnell, T.M., Miller, K.C., and Witcher, J.C. (2001) A seismic and gravity study of the McGregor geothermal system, southern New Mexico, *Geophysics*, Vol. 66 No. 4, p. 1002-1014.

Olsen, K.H., Braile, L.W., Stewart, J.N., et al. (1986) Jemez Mountains volcanic field, New Mexico: Time term interpretation of the CARDEX seismic experiment and comparison with Bouguer gravity, *Journal of Geophysical Research*, Vol. 91, No. B6, p. 6175-6187.

Olsen, K.H., Keller, G.R., and Stewart, J.N. (1978) Crustal Structure Along the Rio Grande Rift from Seismic Refraction Profiles, *in* Riecker, R.E., eds., *Rio Grande Rift: Tectonics and Magmatism*, American Geophysical Union, p. 127-144.

Orr, B.R. and Myers, R.G. (1986) Water Resources in Basin-Fill Deposits in the Tularosa Basin, New Mexico, U.S. Geological Survey Water-Resources Investigations Report, No. 85-94

Parker, E.C., Davis, P.M., Evans, J.R., et al. (1984) Upwarp of anomalous asthenosphere beneath the Rio Grande rift,
Nature, Vol. 312, p. 354-356.

Pearse, J. and Fialko, Y. (2010) Mechanics of active magmatic intraplating in the Rio Grande Rift near Socorro, New Mexico, *Journal of Geophysical Research*, Vol. 115, 16 p.

Pearson, C. and Goff, F. (1981) Schlumberger Resistivity Study of the Jemez Springs Region of Northwestern New Mexico, *Geothermal Resource Council*, Vol. 5, p. 119-122.

Pepin, J., Person, M., Phillips, F., et al. (2015) Deep fluid circulation within crystalline basement rocks and the role of hydrologic windows in the formation of the Truth or Consequences, New Mexico low-temperature geothermal system, *Geofluids*, Vol. 15, p. 139-160.

Perez-Arlucea, M., Mack, G., and Leeder, M. (2000) Reconstructing the ancestral (Plio-Pleistocene) Rio Grande in its active tectonic setting, southern Rio Grande rift, New Mexico, USA, *Sedimentology*, Vol. 47, p. 701-720.

Perry, F.V., Baldridge, W.S., and DePaolo, D.J. (1988) Chemical and isotopic evidence for lithospheric thinning beneath the Rio Grande rift, *Nature*, Vol. 332, p. 432-434.

Peters, T.J., Menzies, M., Thirlwall, M., et al. (2007) Zuni-Bandera volcanism, Rio Grande, USA - Melt Formation in garnet- and spinel-facies mantle straddling the asthenosphere-lithosphere boundary, *Lithos*, Vol. 102, p. 295-315.

Peterson, C. and Roy, M. (2005) Gravity and Flexure Models of the San Luis, Albuquerque, and Tularosa Basin in the Rio Grande rift, New Mexico, and Southern Colorado, *56th Field Conference Guidebook, Geology of the Chama Basin*, New Mexico Geological Society, p. 105-114.

Phillips, F.M., Goff, F., Vuataz, F., et al. (1984) 36CL as a Tracer in Geothermal Systems: Example from Valles Caldera, New Mexico, *Geophysical Research Letters*, Vol. 11, No. 12, p. 1227-1230.

Porreca, C., Selverstone, J., and Samuels, K. (2006) Pyroxenite xenoliths from the Rio Puerco volcanic field, New Mexico: Melt metasomatism at the margin of the Rio Grande rift, *Geosphere*, Vol. 2, No. 7, p. 333-351.

Raatz, W.D. (2005) *Devonian Shelf to Basin Facies Distributions and Source Rock Potential, South-central and Southwestern New Mexico*, New Mexico Bureau of Geology and Mineral Resources Open File Report, No. 484, 38 p.

Ramberg, I.B. and Smithson, S.B. (1975) Gridded fault patterns in a late Cenozoic and a Paleozoic continental rift, *Geology*, Vol. 3, p. 201-205.

Ramberg, I.B., Cook, F.A., and Smithson, S.B. (1978) Structure of the Rio Grande rift in southern New Mexico and West Texas based on gravity interpretation, *Geological Society of America Bulletin*, Vol. 89, p. 107-123.

Rawling, G.C. and Goodwin, L.B. (2006) Structural record of the mechanical evolution of mixed zones in faulted poorly lithified sediments, Rio Grande rift, New Mexico, USA, *Journal of Structural Geology*, Vol. 28, p. 1623-1639.

Rawling, G.C. and Goodwin, L.B. (2006) Structural of the mechanical evolution of mixed zones in faulted poorly lithified sediments, Rio Grande rift, New Mexico, USA, *Journal of Structural Geology*, Vol 28, p. 1623-1639.

Reilinger, R.E., Brown, L.D., and Oliver, J.E. (1978) Recent Vertical Crustal Movements from Leveling Observations in the Vicinity of the Rio Grande Rift, *in* Riecker, R.E., eds., *Rio Grande Rift: Tectonics and Magmatism*, American Geophysical Union, p. 223-236.

Reiter, M. (2005) Subsurface temperatures and crustal strength changes within the seismogenic layer at Arroyo del coyote in the Socorro seismic area, central Rio Grande Rift, New Mexico, *GSA Bulletin*, Vol. 117, No. 3/4, p. 307-318.

Reiter, M., Chamberlin, R.M., and Love, D.W. (2010) New data reflect on the thermal antiquity of the Socorro magma body locale, Rio Grande Rift, New Mexico, *Lithosphere*, Vol. 2, No. 6, p. 447-453.

Reiter, M., Edwards, C.L., Hartman, H., et al. (1975) Terrestrial Heat Flow along the Rio Grande Rift, New Mexico and Southern Colorado, *Geological Society of America Bulletin*, Vol. 86, p. 811-818.

Reiter, M., Eggleston, R.E., Broadwell, B.R., et al. (1986) Estimates of Terrestrial Heat Flow From Deep Petroleum Tests Along the Rio Grande Rift in Central and Southern New Mexico, *Journal of Geophysical Research*, Vol. 91, No. B6, p. 6225-6245.

Reiter, M., Shearer, C., and Edwards, C.L. (1978) Geothermal anomalies along the Rio Grande rift in New Mexico, *Geology*, Vol. 6, No. 2, p. 85-88.

Reiter, M., Mansure, A.J., and Shearer, C. (1978) Geothermal Characteristics of the Rio Grande Rift with the Southern Rocky Mountain Complex, *in* Riecker, R.E., eds., *Rio Grande Rift: Tectonics and Magmatism*, American Geophysical Union, p. 253-268.

Ricketts, J.W., Karlstrom, K.E., Priewisch, A., et al. (2014) Quaternary extension in the Rio Grande rift at elevated strain rates recorded in travertine deposits, central New Mexico, *Lithosphere*, Vol. 6, p. 3-16.

Ricketts, J.W., Karlstrom, K.E., and Kelley, S.A. (2015) Embryonic core complexes in narrow continental rifts: The importance of low-angle normal faults in the Rio Grande rift of central New Mexico, *Geosphere*, Geologic Society of America, Vol. 11, No. 2, p. 425-444.

Riley, P.R., Goodwin, L.B., and Lewis, C.J. (2010) Controls on fault damage zone width, structure, and symmetry in the Bandelier Tuff, New Mexico, *Journal of Structural Geology*, Vol 32, p. 766-780.

Rinehart, E.J., Sanford, A.R., and Ward, R.M. (1978) Geographic Extent and Shape of an Extensive Magma Body at Midcrustal Depths in the Rio Grande Rift near Socorro, New Mexico, *in* Riecker, R.E., eds., *Rio Grande Rift: Tectonics and Magmatism*, American Geophysical Union, p. 237-253.

Rodriguez, B.D. and Sawyer, D.A. (2013) Geophysical constraints on Rio Grande rift structure and stratigraphy from magnetotelluric models and borehole resistivity logs, northern New Mexico, *in* Hudson, M.R. and

Grauch, V.J.S., eds., *New Perspectives on Rio Grande Rift Basins: From Tectonics to Groundwater*, *The Geological Society of America Special Paper*, No. 494, p. 323-344.

Rowe, M.C. and Lassiter, J.C. (2009) Chlorine enrichment in central Rio Grande Rift basalt melt inclusions: Evidence for subduction modification of the lithospheric mantle, *Geology*, Geological Society of America, Vol. 37, No. 5, p. 439-442.

Rowe, M.C., Lassiter, J.C., and Goff, K. (2015) Basalt volatile fluctuations during continental rifting: An example from the Rio Grande Rift, USA, *Geochemistry, Geophysics, Geosystems*, American Geophysical Union, p. 1254-1273.

Roy, M., MacCarthy, J.K., and Selverstone, J. (2005) Upper mantle structure beneath the eastern Colorado Plateau and Rio Grande rift revealed by Bouguer gravity, seismic velocities, and xenolith data, *An Electronic Journal of the Earth Sciences*, AGU, Geochemical Society, Vol. 6, No. 10, 19 p.

Ruhe, R.V. (1962) Age of the Rio Grande Valley in Southern New Mexico, *The Journal of Geology*, Vol. 70, No. 2, p. 151-167.

Ruhl, C., Bilek, S.L., and Stankova-Pursley, J. (2010) Relocation and characterization of the August 2009 microearthquake swarm above the Socorro magma body in the central Rio Grande Rift, *Geophysical Research Letters*, American Geophysical Union, Vol. 37, No. 23, 4 p.

Ruleman, C.A., Thompson, R.A., Shroba, R.R., et al. (2013) Late Miocene-Pleistocene evolution of a Rio Grande rift subbasin, Sunshine Valley Costilla Plain, San Luis Basin, New Mexico and Colorado, *in* Hudson, M.R. and Grauch, V.J.S., eds., *New Perspectives on Rio Grande Rift Basins: From Tectonics to Groundwater*, *The Geological Society of America Special Paper*, No. 494, p. 47-74.

Russell, L.R. and Snelson, S. (1994) Structure and Tectonics of the Albuquerque Basin Segment of the Rio Grande Rift: Insights from Reflection Seismic Data, *in* Keller G.R. and Cather, S.M., eds., *Basins of the Rio Grande Rift: Structure, Stratigraphy, and Tectonic Setting*, *The Geological Society of America Special Paper*, No. 291, p. 83-112.

Russell, L.R. and Snelson, S. (1994) Structural Style and Tectonic Evolution of the Albuquerque Basin Segment of the Rio Grande Rift, New Mexico, U.S.A., *Interior Rift Basin*, *American Association of Petroleum Geologists Memoir 59*, p. 205-258.

Ryder, R.T. (1983) *Petroleum Potential of Wilderness Lands, New Mexico*, United States Department of the Interior, Geological Survey, 38 p.

Salyards, S.L., Ni, J.F., and Aldrich, J., Jr. (1994) Variation in Paleomagnetic Rotations and Kinematics of the North Central Rio Grande Rift, New Mexico, *in* Keller G.R. and Cather, S.M., eds., *Basins of the Rio Grande Rift: Structure, Stratigraphy, and Tectonic Setting*, The Geological Society of America Special Paper, No. 291, p. 59-72.

Sanford, A. (1983) Magma Bodies in the Rio Grande Rift in Central New Mexico, *New Mexico Geological Society Guidebook, 34th Field Conference*, p. 123-125.

Sanford, A.R., Budding, A.J., Hoffman, J.P., et al. (1972) *Seismicity of the Rio Grande Rift in New Mexico*, New Mexico State Bureau of Mines and Mineral Resources, 23 p.

Sanford, A.R., Olsen, K.H., and Jaksha, L.H. (1978) Seismicity of the Rio Grande Rift, *in* Riecker, R.E., eds., *Rio Grande Rift: Tectonics and Magmatism*, American Geophysical Union, p. 145-168.

Sass, J.H. and Morgan, P. (1988) Conductive heat flux in VC-1 and the thermal regime of Valles Caldera, Jemez Mountains, New Mexico, *Journal of Geophysical Research*, Vol. 93, No. B6, p. 6027-6039.

Savage, J.C., Lisowski, M., and Prescott, W.H. (1980) Geodetic Measurement of Horizontal Deformation across the Rio Grande Rift Near Socorro, New Mexico, *Journal of Geophysical Research*, Vol. 85, No. B12, p. 7215-7220.

Schlue, J.W. and Aster, R.C. (1996) A lower crustal extension to a midcrustal magma body in the Rio Grande Rift, New Mexico, *Journal of Geophysical Research*, Vol. 101, No. B11, p. 25283-25291.

Schlue, J.W. and Hostettler, K.K. (1987) Evidence from Rayleigh Wave Data for Magma in an Upper Crustal Dike in the Albuquerque-Belen Basin of the Rio Grande Rift, New Mexico, *Journal of Geophysical Research*, Vol. 92, No. B9, p. 9281-9292.

Schneider, R.V. and Keller, G.R. (1994) Crustal Structure of the Western Margin of the Rio Grande Rift and Mogollon-Datil Volcanic Field, Southwestern New Mexico and Southeastern Arizona, *in* Keller G.R. and Cather, S.M., eds., *Basins of the Rio Grande Rift: Structure, Stratigraphy, and Tectonic Setting*, *The Geological Society of America Special Paper*, No. 291, p. 207-226.

Seager, W.R. and McCurry, M. (1988) The Cogenetic Organ Cauldron and Batholith, South Central New Mexico: Evolution of a Large-Volume Ash Flow Cauldron and Its Source Magma Chamber, *Journal of Geophysical Research*, Vol. 93, No. B5, p. 4421-4433.

Seager, W.R. and Morgan, P. (1978) Rio Grande Rift in Southern New Mexico, West Texas, and Northern Chihuahua,
in Riecker, R.E., eds., *Rio Grande Rift: Tectonics and Magmatism*, American Geophysical Union, p. 87-106.

Self, S., Goff, F., Gardner, J.N., et al. (1986) Explosive Rhyolitic volcanism in the Jemez Mountains: Vent locations, caldera development and relation to regional structure, *Journal of Geophysical Research*, Vol. 91, No. B2, p. 1779-1798.

Semken, S.C. (2001) The Navajo Volcanic Field, Volcanology in New Mexico, *New Mexico Museum of Natural History and Science Bulletin*, p. 79-83.

Shafike, N.G. and Flanigan, K.G. (1999) Hydrologic modeling of the Estancia Basin, New Mexico, *Albuquerque Geology, Annual NMGS Fall Field Conference Guidebooks*, New Mexico Geological Society, p. 81-89.

Sheetz, K.E. and Schlue, J.W. (1992) Inferences for the Socorro magma body from teleseismic receiver functions, *Geophysical Research Letters*, Vol. 19, No. 18, p. 1867-1870.

Shevenell, L., Goff, F., Vuataz, F., et al. (1987) Hydrogeochemical Data for Thermal and Nonthermal Waters and Gases of the Valles Caldera- Southern Jemez Mountains Region, New Mexico, Los Alamos National Laboratory, United States Department of Energy, 51 p.

Sinno, Y.A., Daggett, P.H., Keller, G.R., et al. (1986) Crustal Structure of the Southern Rio Grande Rift Determined

From Seismic Refraction Profiling, *Journal of Geophysical Research*, Vol. 91, No. B6, p. 6143-6156.

Slack, P.D., Davis, P.M., Baldridge, W.S., et al. (1996) The upper mantle structure of the central Rio Grande rift region from teleseismic P and S wave travel time delays and attenuation, *Journal of Geophysical Research*, Vol. 101, No. B7, p. 16003-16023.

Slate, J.L., et al. (2013) Upper Neogene tephrochronologic correlations of the Espanola Basin and Jemez Mountains volcanic field, northern Rio Grande rift, north-central New Mexico, *in* Hudson, M.R. and Grauch, V.J.S., eds., *New Perspectives on Rio Grande Rift Basins: From Tectonics to Groundwater*, *The Geological Society of America Special Paper*, No. 494, p. 303-322.

Smith, D.L. and Jones, R.L. (1978) Thermal Anomaly in Northern Mexico: An Extension of the Rio Grande Rift?, *in* Riecker, R.E., eds., *Rio Grande Rift: Tectonics and Magmatism*, American Geophysical Union, p. 269-278.

Smith, G.A. (2001) Development of a Pyroclastic Apron Adjacent to Rhyolite Domes in a Subsiding Basin: Upper Miocene Peralta Tuff, Jemez Mountains, New Mexico, *Volcanology in New Mexico, New Mexico Museum of Natural History and Science Bulletin*, p. 85-96.

Smith, G.A., McIntosh, W., and Kuhle, A.J. (2001) Sedimentologic and geomorphic evidence for seesaw subsidence of the Santo Domingo accommodation-zone basin, Rio Grande rift, New Mexico, *GSA Bulletin*, Vol. 113, No. 5, p. 561-574.

Smith, G.A., Moore, J.D., and McIntosh, W.C. (2002) Assessing Roles of Volcanism and Basin Subsudence in Causing Oligocene-Lower Miocene Sedimentation in the Northern Rio Grande Rift, New Mexico, U.S.A., J*ournal of Sedimentary Research*, Vol. 72, No. 6, p. 836-848.

Smith, L.N., Lucas, S.G., and Elston, W.E. (1985) Paleogene Stratigraphy, Sedimentation and Volcanism of New Mexico, *Cenozoic Paleogeography of the West-Central United States, The Rocky Mountain Section SEPM (Society for Sedimentary Geology)*, p. 293-315.

Smith, R.R. (1978) Early Rift Magmatism at Spanish Peaks, Colorado, *in* Riecker, R.E., eds., *Rio Grande Rift: Tectonics and Magmatism*, American Geophysical Union, p. 313-322.

Sosa, A., Thompson, L., Velasco, A.A., et al. (2014) 3-D structure of the Rio Grande Rift from 1-D constrained joint inversion of receiver functions and surface wave dispersion, *Earth and Planetary Science Letters*, Vol. 402, p. 127-137.

Spence, W. (1990) A Tomographic Glimpse of the Upper Mantle Source of Magmas of the Jemez Lineament, New Mexico, *Journal of Geophysical Research*, Vol. 95, No. B7, p. 10829-10849.

Spohn, T. and Schubert, G. (1982) Convective thinning of the lithosphere: A mechanism for the initiation of continental rifting, *Journal of Geophysical Research*, Vol. 87, No. B6, p. 4669-4681.

Steck, L.K., Thurber, C.H., Fehler, M.C., et al. (1998) Crust and upper mantle P wave velocity structure beneath Valles Caldera, New Mexico: Results from the Jemez teleseismic tomography experiment, *Journal of Geophysical Research*, Vol. 103, No. B10, p. 24301-24320.

Stix, J., Pearson, C., Vuataz, F., et al. (1982) Geology, Resistivity, and Hydrogeochemistry of the Ojo Caliente Hot

Springs Area, Northern New Mexico, *Geothermal Resources Council, Transactions*, Vol. 6, p. 55-58.

Sussman, A.J., Lewis, C.J., Masin, S.N., et al. (2011) Paleomagnetism of the Quaternary Bandelier Tuff; implications for the tectonic evolution of the Espanola Basin, Rio Grande Rift, *Lithosphere*, Vol. 3, No. 5, p. 328-345.

Swanberg, C.A. (1978) Chemistry of Thermal and Nonthermal Groundwaters in the Rio Grande Rift and Adjacent Tectonic Provinces, *in* Riecker, R.E., eds., *Rio Grande Rift: Tectonics and Magmatism*, American Geophysical Union, p. 279-288.

Swanberg, C.A. and Morgan, P. (1980) The Silica Heat Flow Interpretation Technique: Assumptions and Applications, *Journal of Geophysical Research*, Vol. 85, No. B12, p. 7206-7214.

Tandon, K., Brown, L., and Hearn, T. (1999) Deep structure of the northern Rio Grande rift beneath the San Luis basin (Colorado) from a seismic reflection survey: implications for rift evolution, *Tectonophysics*, Vol. 302, p. 41-56.

Tappa, M.J., Coleman, D.S., Mills, R.D., et al. (2011) The plutonic record of a silicic ignimbrite from the Latir volcanic field, New Mexico, *Geochemistry, Geophysics, Geosystems*, American Geophysical Union, 16 p.

Tomczyk, T. and Morgan, P. (1987) Evaluation of the thermal regime of the Valles Caldera, New Mexico, U.S.A., by downward continuation of temperature data, *Tectonophysics*, Elsevier Science Publishers B.V., Vol. 134, p. 339-345.

Towle, J.N. (1980) New evidence for magmatic intrusion beneath the Rio Grande rift, New Mexico, *Geological Society of America Bulletin*, Vol. 91, p. 626-630.

Townsend, D.A. and Sonder, L.J. (2001) Rheologic controls of buoyancy-driven extension of the Rio Grande rift, *Journal of Geophysical Research*, Vol. 106, No. B8, p. 16515-16523.

Trainer, F.W. (1974) Ground water in the southwestern part of the Jemez Mountains volcanic region, New Mexico, *New Mexico Geological Society 25th Annual Fall Field Conference Guidebook*, p. 337-345.

Trainer, F.W. and Lyford, F.P. (1979) Geothermal Hydrology in the Rio Grande Rift, North-Central New Mexico, *New Mexico Geological Society Guidebook, 30th Field Conference*, p. 299-306.

Trainer, F.W., Rogers, R.J., and Sorey, M.L. (2000) Geothermal Hydrology of Valles Caldera and the Southwestern Jemez Mountains, *New Mexico, U.S. Geological Survey, Water-Resources Investigations Report 00-4067*, 115 p.

Turbeville, B.N. and Self, S. (1988) San Diego Canyon Ignimbrites: Pre-Bandelier Tuff Explosive Rhyolitic Volcanism in the Jemez Mountains, New Mexico, *Journal of Geophysical Research*, Vol. 93, No. B6, p. 6148-6156.

Tweto, O. (1978) The Rio Grande Rift System in Colorado, *in* Riecker, R.E., eds., *Rio Grande Rift: Tectonics and Magmatism*, American Geophysical Union, p. 33-56.

van Wijk, J., van Hunen, J., and Goes, S. (2008) Small-scale convection during continental rifting: Evidence from the Rio Grande rift, *Geology*, The Geological Society of America, Vol. 36, No. 7, p. 575-578.

Vernon, J.H. and Riecker, R.E. (1989) Significant Cenozoic faulting, east margin of the Espanola Basin, Rio Grande rift, New Mexico, *Geology*, Vol. 17, p. 230-233.

Vuataz, F.D. and Goff, F. (1986) Isotope geochemistry of thermal and nonthermal waters in the Valles Caldera, Jemez Mountains, Northern New Mexico, *Journal of Geophysical Research*, Vol. 91, No. B2, p. 1835-1853.

Vuataz, F.D., Goff, F., Fouillac, C., et al. (1988) A strontium isotope study of the VC-1 core hole and associated hydrothermal fluids and rocks from Valles Caldera, Jemez Mountains, New Mexico, *Journal of Geophysical Research*, Vol. 93, No. B6, p. 6059-6067.

Ward, R.M., Schlue, J.W., and Sanford, A.R. (1981) Three-dimensional velocity anomalies in the upper crust near Socorro, New Mexico, *Geophysical Research Letters*, Vol. 8, No. 6, p. 553-556.

Warren, R.G., Kudo, A.M., and Keil, K. (1978) Geochemistry of Lithic and Single-Crystal Inclusions in Basalt and a Characterization of the Upper Mantle-Lower Crust in the Engle Basin, Rio Grande Rift, New Mexico, *in* Riecker, R.E., eds., *Rio Grande Rift: Tectonics and Magmatism*, American Geophysical Union, p. 393-415.

Weir, J.E., Jr. (1965) Geology and Availability of Ground Water in the Northern Part of the White Sands Missile Range and Vicinity New Mexico, United States Department of the Interior, Geological Survey, 82 p.

Wendlandt, R.F., Baldridge, W.S., and Neumann, E.R. (1991) Modification of Lower Crust by Continental Rift Magmatism, *Geophysical Research Letters*, Vol. 18, No. 9, p. 1759-1762.

White, A.F., Delany, J.M., Truesdell, A., et al. (1984) Fluid Chemistry of the Baca Geothermal Field, Valles Caldera, New Mexico, *New Mexico Geological Society Guidebook, 35th Field Conference, Rio Grande Rift: Northern New Mexico*, p. 257-263.

Williams, A.J., Crossey, L.J., Karlstrom, K.E., et al. (2013) Hydrogeochemistry of the Middle Rio Grande aquifer system - Fluid mixing and salinization of the Rio Grande due to fault inputs, *Chemical Geology*, Vol. 351, p. 281-298.

Williams, R.T. and Rodriguez, B.D. (2002) Magnetotelluric Data in the Middle Rio Grande Basin, Albuquerque Volcanoes, New Mexico, U.S. Department of the Interior, U.S. Geologic Survey, 90 p.

Williams, R.T., Goodwin, L.B., Mozley, P.S., et al. (2015) Tectonic controls on fault zone flow pathways in the Rio Grande rift, New Mexico, USA, *Geology*, Geologic Society of America, Vol. 43, No. 8, p. 723-726.

Wilson, D., Aster, R., West, M., et al. (2005) Lithospheric structure of the Rio Grande rift, *Nature*, Vol. 433, p. 851-855.

Wilson, D., Aster, R., Ni, J., et al. (2005) Imaging the seismic structure of the crust and upper mantle beneath the Great Plains, Rio Grande Rift, and Colorado Plateau using receiver functions, *Journal of Geophysical Research*, Vol. 110, 14 p.

Witcher, J.C. (1995) Geothermal Resource Data Base, New Mexico, Southwest Technology Development Institute, 32 p.

Witcher, J.C. (2002) *Field Studies of Geothermal Reservoirs Rio Grande Rift, New Mexico*, United States Department of Energy, 10 p.

Witcher, J.C. (2001) Deep Production Well for Geothermal Direct-Use Heating of a Large CommercialGreenhouse, Radium Springs, Rio Grande Rift, New Mexico, United States Department of Energy, 29 p.

Witcher, J.C. (2002) Geothermal Energy in New Mexico, *GHC Bulletin*, p. 2-10.

Withjack, M.O. and Schlische, R.W. (2002) Rift-Basin Structure and Its Influence on Sedimentary Systems, *Sedimentation in Continental Rifts, Society for Sedimentary Geology Special Publication*, No. 73, p. 57-81.

WoldeGabriel, G., Koning, D.J., Broxton, D., et al. (2013) Chronology of volcanism, tectonics, and sedimentation near the western boundary fault of the Espanola Basin, Rio Grande rift, New Mexico, *in* Hudson, M.R. and Grauch, V.J.S., eds., *New Perspectives on Rio Grande Rift Basins: From Tectonics to Groundwater*, *The Geological Society of America Special Paper*, No. 494, p. 221-238.

Woldegabriel, G., Warren, R.G., Broxtoni, D.E., et al. (2001) Episodic Volcanism, Petrology, and Lithostratigraphy of the Pajarito Plateau and Adjacent Areas of the Espanola Basin and the Jemez Mountains, *Volcanology in New Mexico, New Mexico Museum of Natural History and Science Bulletin*, p. 97-129.

Wolff, J.A., Rowe, M.C., Teasdale, R., et al. (2005) Petrogenesis of Pre-caldera Mafic Lavas, Jemez Mountains Volcanic Field (New Mexico, USA) *Journal of Petrology*, Vol. 46, No. 2, p. 407-439.

Woodward, L.A. (1977) Rate of crustal extension across the Rio Grande Rift near Albuquerque, New Mexico, *Geology*, Vol. 5, p. 269-272.

Woodward, L.A. and Duchene, H.R. (1975) Geometry of Sierrita fault and its bearing on tectonic development of the Rio Grande rift, New Mexico, *Geology*, Vol. 3, p. 114-116.

Zimbelman, J.R. and Johnston, A.K. (2001) Improved Topography of the Carrizozo Lava Flow: Implications for Emplacement Conditions, *Volcanology in New Mexico, New Mexico Museum of Natural History and Science Bulletin*, p. 131-136.

Zimmerman, C. and Kudo, A.M. (1978) Geochemistry of Andesites and Related Rocks, Rio Grande Rift, New Mexico, *in* Riecker, R.E., eds., *Rio Grande Rift: Tectonics and Magmatism*, American Geophysical Union, p. 355-381.

Appendix B
PFA Associated Data

Table 2. WoE Training Sites

Name	Power Plant	State
Baltazor Hot Springs	No	Nevada
Bog Hot Springs	No	Nevada
Howard Hot Springs	No	Nevada
East Pinto Hot Springs	No	Nevada
Soldier Meadow Hot Springs	No	Nevada
Double Hot Springs	No	Nevada
Trego Hot Springs	No	Nevada
Gerlach Hot Springs	No	Nevada
San Emidio Hot Springs	Yes	Nevada
Bradys Hot Spring	Yes	Nevada
Patua Hot Springs	No	Nevada
Walleys Hot Springs	No	Nevada
McLeod Ranch Hot Springs	No	Nevada
Smith Creek Hot Springs	No	Nevada
Tungsten Mountain	No	Nevada
Dixie Meadows Hot Springs	No	Nevada
Hot Springs Ranch	No	Nevada
Jersey Valley Hot Springs	Yes	Nevada
Sou Hot Springs	No	Nevada
Leach Hot Springs	No	Nevada
Kyle Hot Springs	No	Nevada
Bass Hot Spring	No	Nevada
Buffalo Valley Hot Springs	No	Nevada
Golconda Hot Springs	No	Nevada
Carlin Hot Springs	No	Nevada
Beowawe/PP	Yes	Nevada
Cresent Valley Hot Springs	No	Nevada
Dann Hot Springs	No	Nevada
Bruffeys Hot Springs	No	Nevada
Upper Hot Creek Ranch springs	No	Nevada
Bartholomae Hot Springs	No	Nevada
Walti Hot SPrings	No	Nevada
Cherry Creek Hot Springs	No	Nevada
Hot Creek Springs	No	Nevada
Three Mile Spring	No	Nevada
Hot Sulpur Springs/Tuscorora	Yes	Nevada
Mineral Hot Springs	No	Nevada
Joseph Hot Springs	No	Utah
Red Hill Hot Springs	No	Utah

Cove Fort PP	Yes	Utah
Meadow Hatton Hot Springs	No	Utah
Roosevelt Hot Springs	Yes	Utah
Abraham Hot Springs	No	Utah
McGinness Hills	Yes	Nevada
Hondo Hot Springs	No	New Mexico
Gila Hot Springs	No	New Mexico
Souse Springs	No	New Mexico
T or C Warm Spring	No	New Mexico
Ponce de Leon Hot Spring	No	New Mexico
Jemez Pueblo Indian Hot Spring	No	New Mexico

Appendix C
Methodology Flow Charts

Deterministic Geothermal Play Fairway Analysis (PFA):
Petroleum Industry Logic

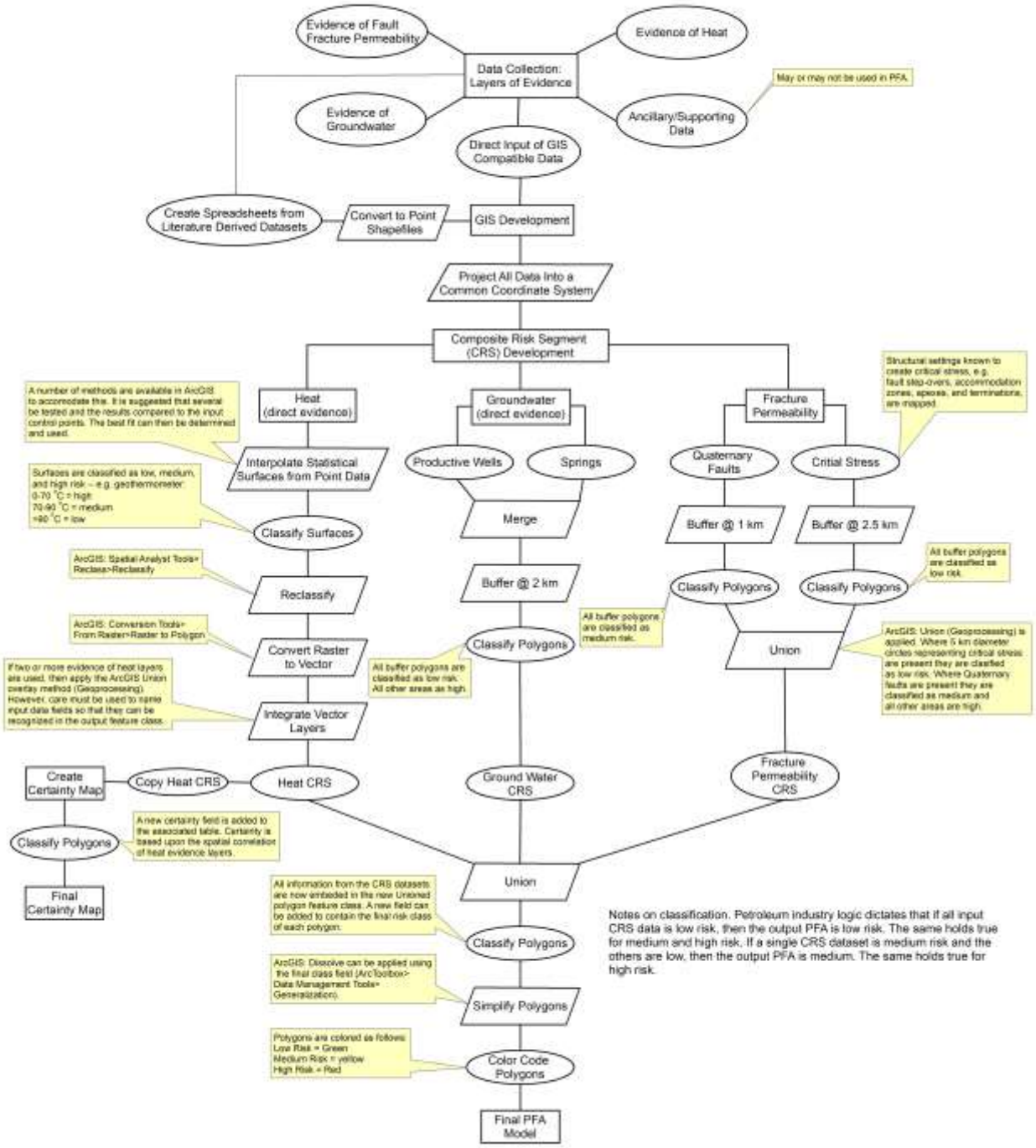

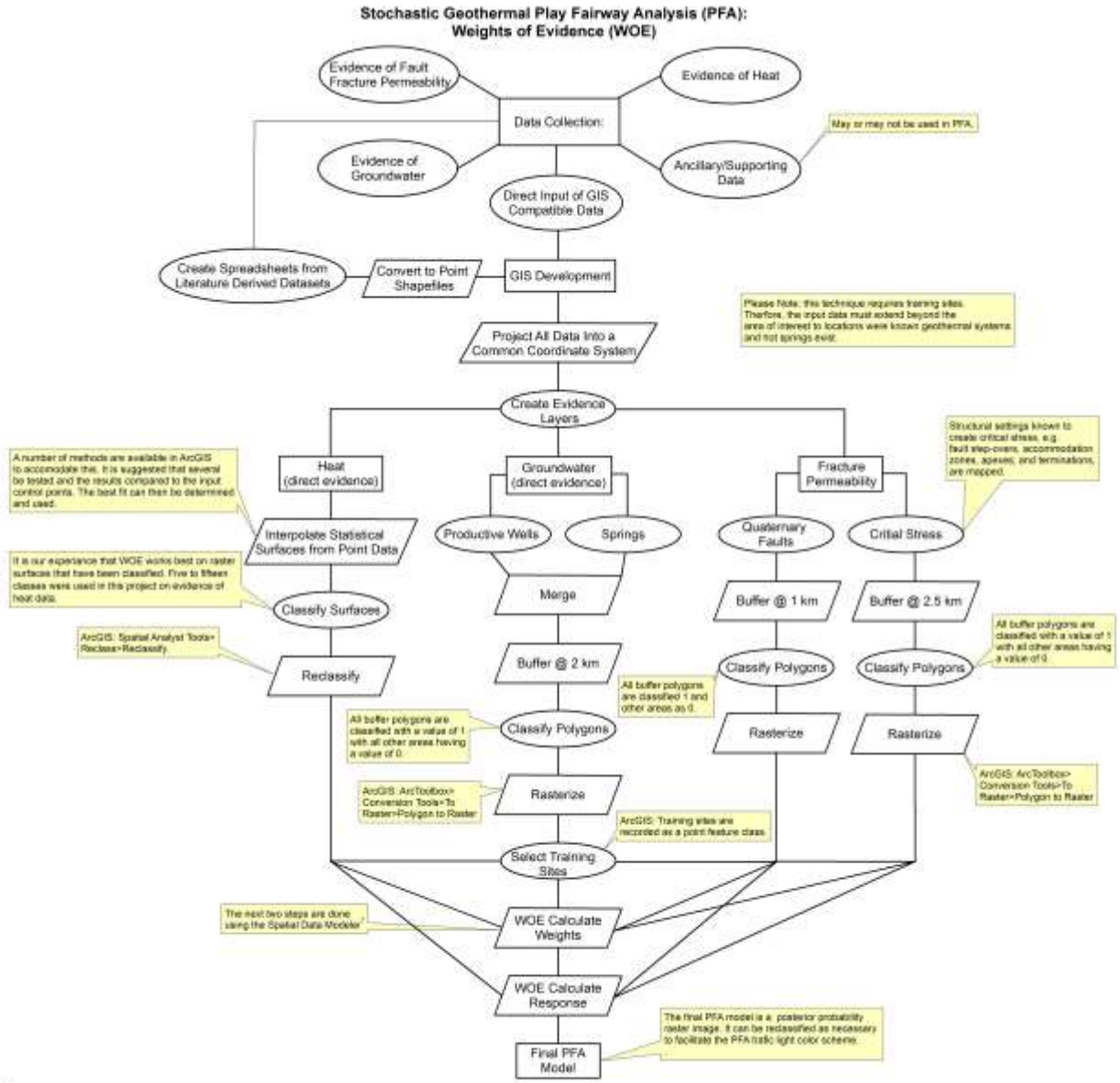

[1]Sawatzky, D.L., Raines, G.L. , Bonham-Carter, G.F., and Looney, C.G., 2009, Spatial Data Modeller (SDM): ArcMAP 9.3 geoprocessing tools for spatial data modelling using weights of evidence, logistic regression, fuzzy logic and neural networks. http://arcscripts.esri.com/details.asp?dbid=15341.

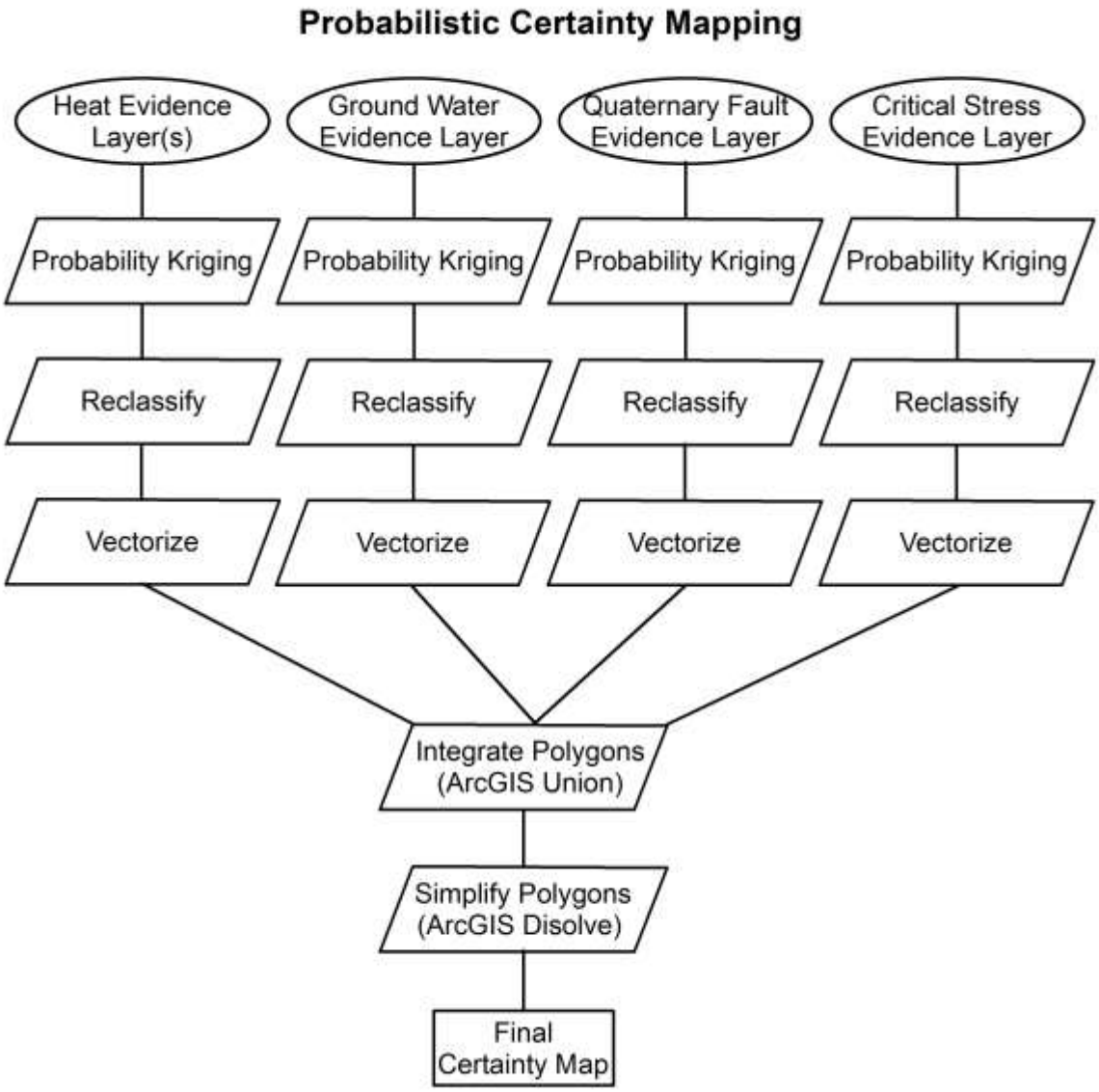
Probabilistic Certainty Mapping
Heat Evidence Layer(s)
Ground Water Evidence Layer
Quaternary Fault Evidence Layer
Critical Stress Evidence Layer
Probability Kriging
Probability Kriging
Probability Kriging
Probability Kriging
Reclassify
Reclassify
Reclassify
Reclassify
Vectorize
Vectorize
Vectorize
Vectorize
Integrate Polygons (ArcGIS Union)
Simplify Polygons (ArcGIS Disolve)
Final Certainty Map

The Convergence of Heat, Groundwater & Fracture Permeability:

Innovative Play Fairway Modelling Applied to the Tularosa Basin

DOE Contract #DE-EE0006730

PHASE 2 PROJECT REPORT

May 31, 2017

Submitted By:

Ruby Mountain Inc.

Salt Lake City ■ El Paso ■ Seattle ■ Newport Beach

and

EGI Energy & Geoscience Institute AT THE UNIVERSITY OF UTAH

The Convergence of Heat, Groundwater & Fracture Permeability:

Innovative Play Fairway Modelling Applied to the Tularosa Basin

PHASE 2 PROJECT REPORT

This report summarizes the activities and key findings of the project team occurring during Phase 2 (primarily from August 2016 – May 2017) of the Tularosa Basin Geothermal Play Fairway Analysis Project. Questions regarding the contents of this document should be directed to: RMI Senior Project Manager Carlon R. Bennett at carlonbennett@gmail.com

Submitted By:

Ruby Mountain Inc.

Carlon R. Bennett, Project Manager
2373 East 1300 South, Salt Lake City, UT 84108
801-538-5003 ● rubymountaininc.com

and the

EGI Energy & Geoscience Institute
AT THE UNIVERSITY OF UTAH

Gregory D. Nash, Ph.D. Principal Investigator
423 Wakara Way #300, Salt Lake City, UT 84108
801-581-5126 ● egi.utah.edu

TABLE OF CONTENTS

ACKNOWLEDGEMENTS

Ruby Mountain Inc. and EGI wish to thank the following individuals and organizations for their cooperation, support and assistance throughout the implementation of Phase 2 of this project:

- U.S. Department of Energy (DOE) Geothermal Technologies Office (GTO) for its financial support, oversight, and guidance through Contract # DE-EE0006730;
- Fort Bliss Directorate of Public Works (DPW), Environmental Division (DPW-E), Range Operations and Office of the Staff Judge Advocate;
- White Sands Missile Range;
- Aerospace Data Facility Southwest (ADF-SW);
- Johnson Space Center/NASA - White Sands Test Facility.

PROJECT TEAM

Ruby Mountain Inc.

- Carlon R. Bennett, PFA Project Manager
- Jon Lear, RMI Principal
- Jesus Daniel Aguilar, Administrative Assistant to the Project Manager

Energy & Geoscience Institute at the University of Utah

- Gregory Nash, Ph.D., Project Principal Investigator
- Phil Wannamaker, Ph.D., Research Professor
- Stuart Simmons, Ph.D. Research Professor
- Rasoul B. Sorkhabi , Ph.D., Research Professor
- Virginia Maris, Ph.D., Post Doc.
- Adam Brandt, Student Research Assistant
- Brian Pfaff, Student Research Assistant

U.S. Navy Geothermal Program Office

- Michael Lazaro, Navy Geothermal Division Director
- Kelly Blake, P.G., Geologist
- Andrew Sabin, Ph.D., P.G., Geologist
- Saundra Anderson, GPO Business Manager

Utah Geologic Survey

- Mark Gwynn, P.G., Geologist
- Christian Hardwick, P.G., Geophysicist
- Jodi Patterson, UGS Financial Manager

Barker Engineering

- Benjamin Barker, P.E., Special Project Consultant

Quantech Geoscience, Ltd.

- Jeff Nichols, Debbie Ramlal and Jeff Violette

The Convergence of Heat, Groundwater & Fracture Permeability:

Innovative Play Fairway Modelling Applied to the Tularosa Basin

Greg Nash[1], Carlon Bennett[2], Stuart Simmons[1], Kelly Blake[3], Christian Hardwick[4], Mark Gwynn[4], Rasoul Sorkhabi[1], Virginia Maris[1], Phil Wannamaker[1], Andrew Sabin[3], Adam Brandt[1], Brian Pfaff[1]

[1]Energy & Geoscience Institute at the University of Utah, [2]Ruby Mountain, Inc., [3]Navy Geothermal Program Office, [4]Utah Geological Survey

---

1.0 OVERVIEW

1.1 Introduction

This Phase 2 Report for the Tularosa Basin Play Fairway Analysis (PFA) Project is submitted to the U.S. Department of Energy (DOE) in fulfillment of requirements of Contract #DE-EE0006730 which was awarded to develop a methodology for, and conduct, a Geothermal Play Fairway Analysis in the Tularosa Basin located in South-Central New Mexico and Far West Texas. Ruby Mountain Inc. (RMI) is the prime contractor to DOE under the grant award. The Energy and Geoscience Institute (EGI) at the University of Utah is the prime subcontractor to RMI. This report summarizes primary activities and key findings of the project team occurring during second phase work from July 2016 – May 2017.

1.2 Phase 2 Planning and Work

Phase two work successfully fulfilled our three main objectives: (1) fill in data needed for play fairway analysis (PFA) which was missing or sparse in identified Phase 1 plays; (2) collect local datasets in high priority areas; and, (3) become more familiar with the geology of all identified plays. As importantly, our second phase efforts continue to demonstrate that the play fairway methodology developed by our team, while complex, has the unique ability to be easily understood by decision makers of all varieties – having been well received by both military leadership and energy staff at several installations.

The project team's Phase 2 work plan consisted primarily of the following:

1. Field geology
    a. Geological reconnaissance at low priority plays
    b. Mapping, with an emphasis on structure, at high priority plays
2. Gravity data surveys and infill at high priority plays
3. Shallow temperature (2m) surveys at high priority plays
4. Existing well water sampling for chemical analyses and geothermometry
5. Temperature logging in existing wells
6. A magnetotelluric survey at McGregor Range to support future drilling
7. New PFA model development

It was originally anticipated that water chemistry and/or temperature gradient data would be collected from each play regardless of priority, with the exception of McGregor Range, for which a relatively rich

data set already exists. However, in reality, wells were not accessible in all plays during our Phase 2 data collection period. Figure 1 shows plays for which new data were collected.

1.3 Study Area

The Tularosa Basin is a graben located in the southern Rio Grande Rift (Fig. 2). The study area covers approximately 7,700 miles^2, much of which is underexplored. Several factors went into the selection of the Tularosa Basin. It was primarily chosen because it is a challenging, yet ideal test bed to evaluate effectiveness of PFA.

The basin is home to several military installations including White Sands Missile Range (WSMR) and Fort Bliss, which are the first and second largest U.S. Army bases in the United States, together covering more than 10,000 km^2 of southcentral New Mexico and Far West Texas. Both installations have been cooperative throughout our geothermal exploration efforts and have expressed an interest in developing any geothermal resource which may be proven viable.

Additionally, the Aerospace Data Facility Southwest (ADF-SW) located at the Johnson Space Center's White Sands Test Facility on the western side of the Organ Mountains requested to join Phase 2 of the Tularosa Basin PFA effort in summer of 2016 and provided funding for the RMI project team to begin exploration on the western side of the Organ Mountains. The DOE agreed to the addition and ADF-SW provided funding to supplement the existing DOE project grant. The RMI team provided a 20 percent cost share to the ADF-SW funding and was able to bring some economic efficiency to the effort by reducing mobilization/de-mobilization costs for teams already working in the field on the eastern side of the Organ Mountain Range. Geothermal development throughout the basin can help the military achieve its Net Zero Energy goals and installation resiliency objectives.

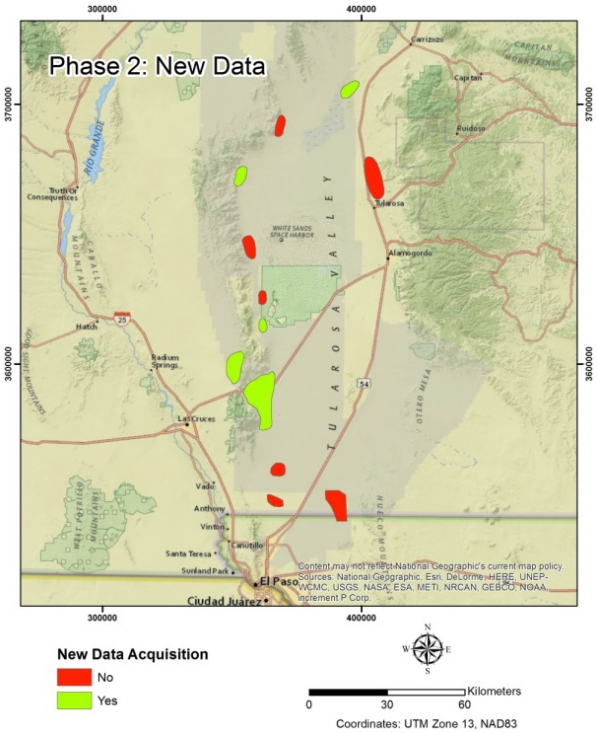

Figure 1. New data collection in plays.

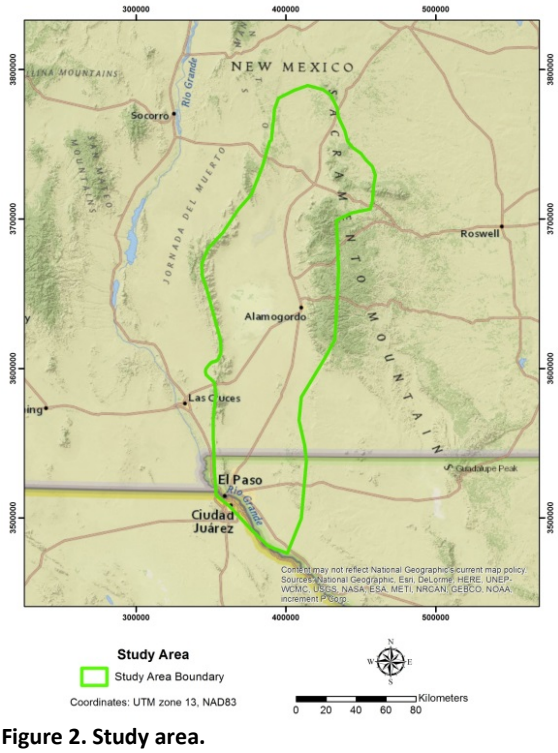

Figure 2. Study area.

2.0 PHASE 2 ACCOMPLISHMENTS

2.0.1 Geology

The study area encompassing the Organ, San Agustin, San Andres, and Sacramento Mountains underwent basement uplift during the early Cenozoic Laramide orogeny. The San Andres, San Agustin, and Sacramento mountains are composed largely of Paleozoic carbonates and quartzite, with local outcrops of Proterozoic granite, and Mesozoic sandstones and conglomerates. The Organ Mountains are predominated by Oligocene granitic rock. Tertiary volcanic rocks are also present locally throughout much of the area. A generalized stratigraphic column can be seen in Appendix A.

Based on mapping and observations reported by Seager (1981), we suggest that the area near the WSMR main cantonment was formed by oroclinal bending during the Laramide. This area was later associated with the emplacement of the 33-Ma Organ Batholith. Basin-and-Range type extension was then superimposed on the Laramide uplift, creating a large number of normal faults bounding grabens and half-grabens. Oroclinal bending structures have often found to be areas of structural complexity and focused strain (e.g., Marshak, 2004). In many areas, extensional basins associated with oroclinal bending are characterized by high heat flow; e.g., Rhine Graben (Pribnow and Clauser, 2000).

Remote sensing and surface mapping have revealed the presence of Quaternary fault systems in the study area. Seager (1981), for instance, documents varying heights of scarps cut by several generations of Quaternary fans. Certain geological features make the study area in this project favorable for geothermal systems: (1) the shallow-level Precambrian and Tertiary igneous rock complex help conduct basement heat flow; (2) structural complexity and focused strain indicates the presence of a networks of structures of medium to small size; (3) active (Quaternary) tectonics suggests structures that are still fluid conductive in some areas (not healed by long-term geological processes); and (4) rift tectonics and magmatism tend to elevate geothermal gradient.

To further advance our knowledge of the area geology, all low priority plays were visited and geologic features of interested noted. One of the priorities in this reconnaissance was to try to identify surficial geothermal features, such as fossil sinters and hydrothermal alteration. Hydrothermal alteration was observed in a small area, along what is believed to be a Quaternary fault, in San Agustin Mountains a few miles north of the WSMR main cantonment. Areas of alteration were also observed in the San Andreas Range; however, these are likely related to the Proterozoic granite that is part of the Laramide thrust package. In the south-eastern corner of the ADFSW play, pervasive silicification of Paleozoic carbonates was noted and several limestone beds in the adjacent range were silicified at different stratigraphic levels suggesting sporadic pulses of hydrothermal actively. This was found to be a structurally complex area containing several copper deposits that attest to past structurally-controlled hydrothermal activity.

Within the high priority areas in WSMR, the Main Cantonment area and adjoining HTA area to the north, several previously unmapped faults were identified. Additionally, numerous mafic, rhyolitic, and granitic pegmatite dikes occur in Proterozoic granite in these areas, which appear to be structurally controlled. The mafic dikes are sometimes accompanied by copper mineralization. New structural details discovered during this work will be discussed further in the gravity data section later in the report.

2.0.2 Water Chemistry and Geothermometry

Geochemical analyses were obtained on shallow groundwater samples (~120 m depth) within the study area. The samples were collected by the Utah Geological Survey in the period November 20 to December 15, 2016, from flowing wells either from storage tanks or from a tap the wellhead (Fig. 3). They were delivered to EGI and then sent out to three separate labs for chemical and isotopic analyses.

2.0.2.1 Methods & Results

Well waters were collected into three different types of containers depending on the methods of analysis. Untreated waters were collected in glass bottles fitted with a rubber tube and hose clamp. These bottles are designed to be over-filled with water and then clamped to prevent loss of aqueous carbon dioxide. The waters were analyzed for bicarbonate (HCO_3) and pH via automated alkalinity titration at the Utah Department of Health lab in Salt Lake City.

Treated samples were collected in acid washed Nalgene bottles (250 ml) for analyses of major anions and cations (Li, Na, K, Ca, Mg, SiO_2, Cl, F, SO_4). These waters were treated in the field first by filtering (0.45 µm) and then by acidification (2.5 mls 10% HNO_3) to preserve the solutes. These samples were analyzed in the Department of Earth Sciences, University of Minnesota. The cations (Li, Na, K, Ca, Mg, SiO_2) were analyzed by ICP-OES and the anions (Cl, F, SO_4) were analyzed by ion chromatography.
Untreated water samples were also collected in 30 ml glass bottles with a screw cap to determine the oxygen (18O/16O) and hydrogen (D/H) isotope ratios. The isotope ratios were measured via mass spectrometers in the SIRFER lab at the University of Utah.

2.0.2.2 Interpretation

The stable isotope compositions of the waters plot as a coherent continuous linear trend that coincides with local ground water (Fig. 4), with the exception of SC-2 (Stallion Range Control Center). The variation in isotopic compositions for all samples reflect fractionation effects due to latitude and/or elevation which is commonly seen in cold shallow groundwaters. Thus the outlying position of SC-2 simply suggests that it comes from percolation of rainwater and/or snowmelt, which entered the ground water system at a higher elevation relative to the rest of the samples. None of the waters show a positive-shift to the right of meteoric water line, as is typical of deeply circulated thermal waters that have been subject to re-equilibration due to high temperature (100-300°C) water-rock interaction.

The waters are near neutral pH (6-7), and the Cl-HCO_3-SO_4 ternary plot (Fig. 5) shows that most of the waters are rich in bicarbonate and/or sulfate. The most sulfate-rich waters are ORC, SC-2 and 100-C-365, whereas the only chloride-rich water is WSRM up-range Herbie well.

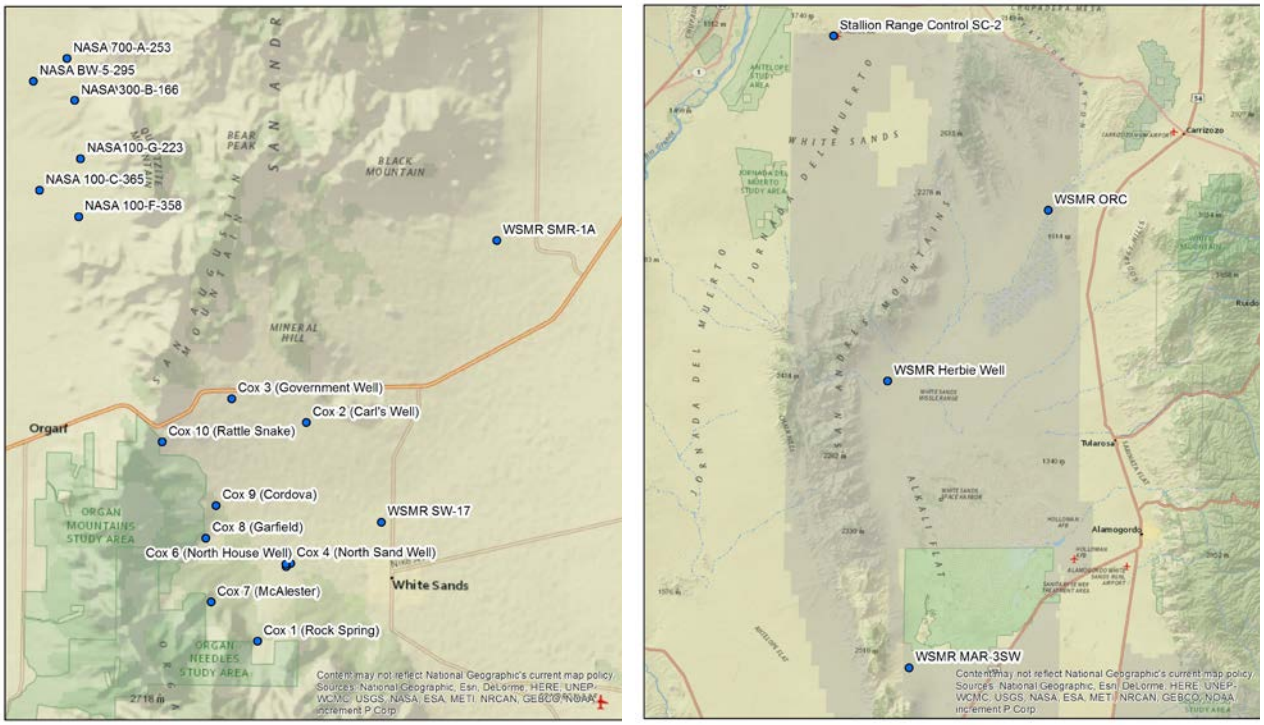

Figure 3. Wells sampled for water chemistry: WSMR main cantonment/ ADF-SW/NASA (left) and WSMR up-range (right).

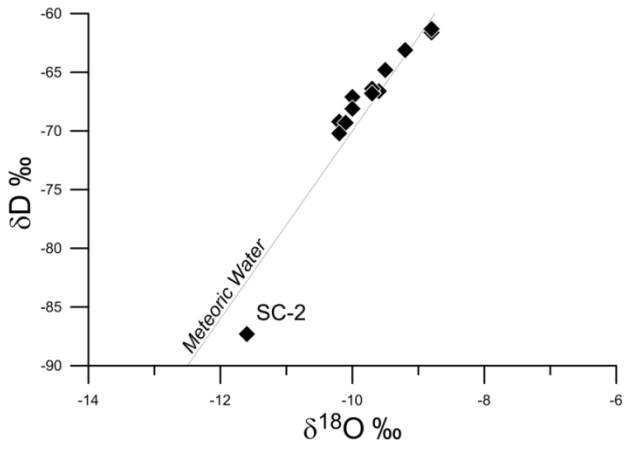

Figure 4. Hydrogen versus oxygen isotope values of groundwaters compared to the global meteoric water line. Their coincidence indicates that groundwater comes from local rain and snowmelt.

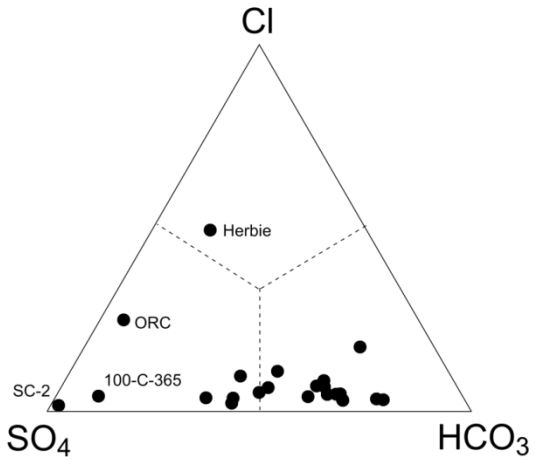

Figure 5 (right). Cl-HCO_3-SO_4 ternary plot, showing the predominance of bicarbonate in samples.

The Na-Ca-Mg ternary plot (Fig. 6) shows that most of the waters are rich in calcium, with the exception of BW-5-295 and 100-C-365, which are dominated by sodium. The absolute concentrations of calcium and magnesium range from 30-570 mg/kg and 5-175 mg/kg, respectively, and the co-variation in results plot in a rough linear trend (Fig. 7). Such high calcium and magnesium concentrations are unusual for

thermal waters, and like the stable isotope data, there is no strong evidence that any of the waters were subjected to high-temperature water-rock interaction.

As for geothermometry, the most reliable values are based on the concentrations of aqueous silica (10-50 mg/kg), which when compared to quartz-SiO_2 solubility (Fournier, 1991). These suggest equilibration temperatures in the range from 40 to 100 °C (Fig. 8). The quartz-SiO_2 geothermometer has broad applicability that includes low to high temperature resources that are hosted by a diverse range of rock types. By contrast, the K-Mg geothermometer yields cooler equilibration temperatures, whereas the Na-K geothermometer yields much hotter equilibration temperatures, but these calculated values are likely to be less reliable, given the high concentrations of aqueous calcium and magnesium. The quartz geothermometers were added to the existing PFA dataset and used for the development of the revised heat composite risk segment.

Well samples MAR-3SW, SC-2, SMR-1A and SW-17 have the hottest measured temperatures of ~25°C, whereas their quartz-SiO_2 equilibration temperatures are in the range of 70-90°C (Fig. 9). The physical and chemical measurements suggest that areas in the vicinity of these wells may be promising sites for future investigation. Sundance Engineering (2015) reports Well SW-17 as having a CO_2-N_2 geothermometer of 127.8 ^{o}C.

2.0.3 2m Temperature Surveys

These surveys were done by the Navy Geothermal Program Office (GPO). Data were collected over parts of ADF-SW/NASA and WSMR plays. The specific type of deployment used for this survey has been applied previously by the University of Nevada Reno's GBCGE and the Navy GPO (Coolbaugh et al., 2007, Sladek et al., 2007, Kratt et al., 2010, Lazaro et al., 2011, Skord et al., 2011).

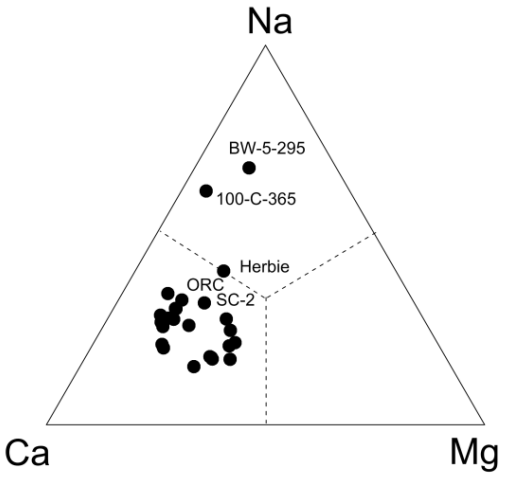

Figure 6. Na-Ca-Mg ternary plot, showing the predominance of calcium in samples.

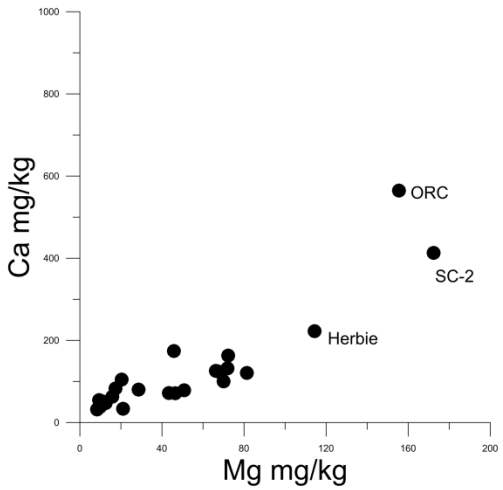

Figure 7. Calcium versus Mg concentrations in samples.

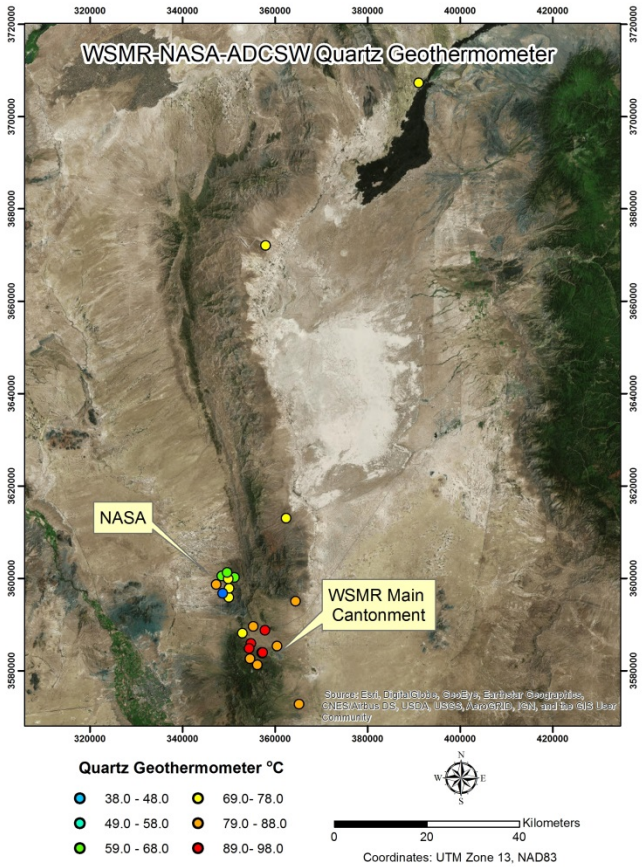

Figure 8. Quartz geothermometer results.

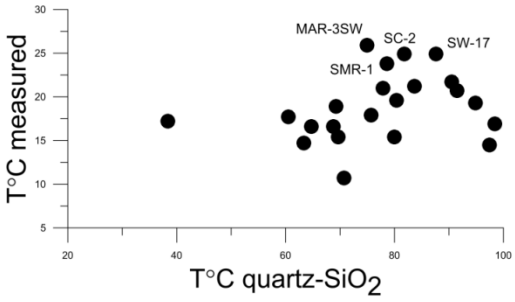

Figure 9. A comparison of calculated quartz-SiO2 solubility equilibration temperature versus measured field sampling temperatures.

The GPO collected thirty-eight 2m probe points at ADF-SW/NASA between December 8th and December 11th, 2016 (Fig. 9). The data were collected by driving a 5/8" diameter, 2 meter long, hollow probe into the ground using a pneumatic hammer. A thermistor was then inserted down the probe and left to equilibrate for at least an hour before the shallow temperature was read and recorded. All of the points were accessed using either a truck or side by side ATV via existing roads. From January 6th through the 10th, ninety-one points were collected at WSMR employing the same methodology (Fig. 10). Both areas had locations with very shallow bedrock (usually ~0.25 meters depth) where the probe could not be installed. This is the reason for uneven spacing in some locations between points at both survey sites.

Base stations were established at both sites to facilitate temperature measurements throughout the duration of the survey that can be used to correct for seasonal changes. If more 2m probes are collected at these two plays in the future, these same base stations should be re-occupied to ensure consistent seasonal corrections in the data.

2.0.3.1 Base Station Correction

Base stations were located in the middle of each survey for ease of access (Fig. 10). For both base stations, the same thermistor was used to be consistent across both surveys. Base station readings were collected at the beginning of each day, in the middle of each day, and at the end of each day. These data were used to determine a seasonal bias by taking an average for the base station at each time interval; morning (AVG_{BM}), day (AVG_{BD}), night (AVG_{BN}). This value was then added to each base measurement to calculate a correction value ($Corr_{BM}$). This correction was applied to each 2m probe measurement (2m

PM) to correct for a seasonal bias. AVG_B varied per day, time of day and per depth measurement (1m, 1.5m and 2m).

Base station average: $(Base_M + Base_M + Base_M)/3 = AVG_{BM}$
Correction coefficient: $AVG_{BM} + Base_M = Corr_{BM}$
Corrected value: $Corr_{BM}$ + 2m PM=Corr2mProbe

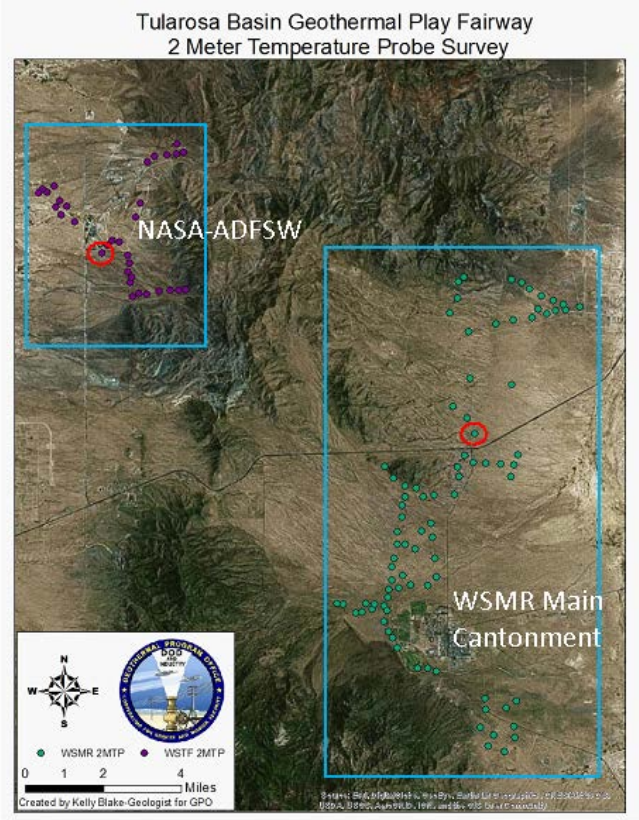

Figure 10. 2m probe points collected during December, 2016 and January, 2017. The purple dots are the points on ADF-SW/NASA and the green dots are the points on WSMR. The base stations are circled in red. The blue boxes represent the areas in Figures 3 and 4.

Thermistor Calibration and Correction

All thermistors were calibrated prior to deployment. Using a hot plate and distilled water in the GPO wet lab. Thermistor 1(T1) was used to determine the temperature of the heated distilled water. Every other thermistor (e.g., TX where X is the number of the thermistor) was then placed in the heated distilled water to measure temperature. The measured temperature of each thermistor (TX) was then subtracted from T1 to determine a corrected value (TX_{CORR}) for each thermistor. This thermistor correction was applied to every measurement. The thermistor correction (TX_{CORR}) was added to the base station corrections (Corr2mProbe) to yield thermistor calibrated and corrected temperatures (Corr2mProbeTX).

$$T1-TX=TX_{CORR}$$
$$TX_{CORR} + Corr2mProbe = Corr2mProbeTX$$

2.0.3.2 Albedo and Topographic Slope Aspect Correction

Both the albedo of the surface and the ground slope where the probe measurement is taken are known to influence shallow ground temperature measurements (Sladek et al., 2009, Coolbaugh et al., 2010).

ASTER (Advanced Spaceborne Thermal Emmision and Reflection) imagery and Digital Elevation Model (DEM) data are used to correct for albedo and slope, respectively. For this survey, however, neither was found to have an effect on the data so these corrections were not applied.

2.0.3.3 RESULTS

After data corrections were performed, the values of Corr2mProbeTX for 1meter, 1.5 meters and 2 meters were used to create statistical surfaces using the natural neighbor method in ArcGIS (Figs. 11 and 12). Contoured 2m probe measurements at WSMR illustrate several clusters of high and low temperatures and a broad north to south alignment in the central and western margin of the investigated region (Fig. 11). The highest temperature Quartz geothermometers are just outside of the survey area; however, the 2 meter data contours vector toward these high values in the southwestern area of the survey.

At all three depths, the higher temperature anomaly follows the mapped Quaternary fault. There also seems to be a spreading out of temperature that begins where the western bend in the mapped fault occurs. This area is also very sandy. The larger area of anomalous high temperatures may be a product of structure and lithology.

At the ADFSW/NASA, the maximum temperature at 2 meters depth is about one degree Fahrenheit warmer than at WSMR. In Fig. 12, the 1 meter, 1.5 meter and 2 meter temperature contours and quartz geothermometer temperatures are mapped. There are no previously mapped Quaternary faults in this area. In the 1 meter temperature map, the anomalous high temperatures are along the range front. There is also a higher temperature lineation striking northwest from the southern extent of the survey. The 1.5 meter temperatures are warmer across the entire area. In the 2 meter temperature data, the hotter areas are more concentrated to the southern extent of the survey and along the northwest trend seen in the 1 meter data. At all three depths, a patch of anomalous temperatures were found in the western area of the survey, which coincides with the hottest quart geothermometer.

These surveys were done to help determine if anomalous heat was present in local areas, but not used in the PFA, which covers a much larger area.

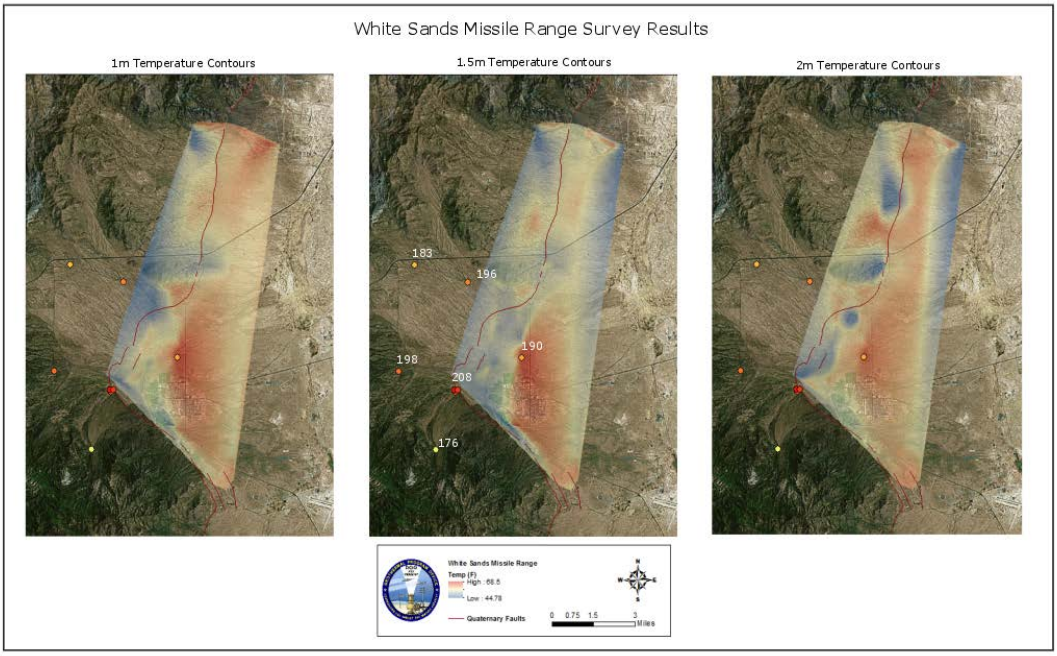

Figure 11. WSMR 2-meter temperature probe natural neighbor interpolation for 1m, 1.5m, and 2 depths. Quartz geothermometer temps are given in Fahrenheit on the 1.5 meter map (^{o}F). Red indicates higher temps and blue lower temps.

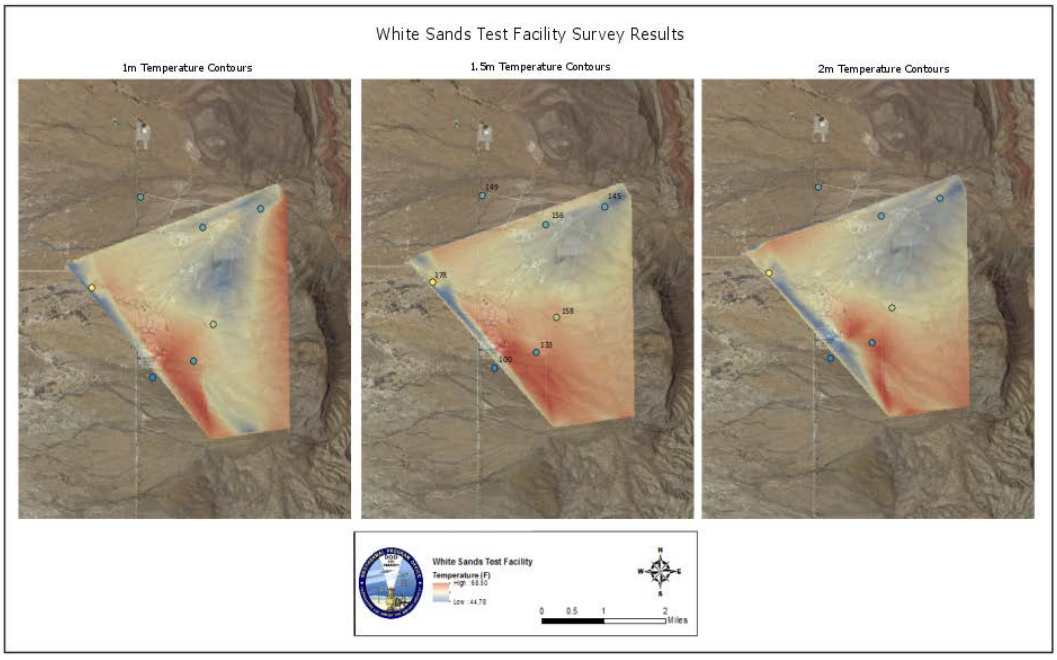

Figure 12. Natural neighbor interpolation for ADFSW/NASA temperatures at 1m, 1.5m, and 2m depths. Quartz geothermometer temperatures are labeled in the 1.5 meter map (^{o}F). Red indicates higher temps and blue lower temps.

2.0.4 Temperature Logging in Existing Wells

Temperature-depth profiles were measured and recorded at four ADF-SW/NASA monitor wells and eight White Sands Missile Range (WSMR) wells (Fig. 13) of varying types using high-precision

temperature logging equipment. The logging gear consists of a thermister probe attached to a reel-mounted, four-conductor, cable. Measurement accuracy is ±0.01°C. Because the probe equilibrates quickly in the water column, temperatures were measured at 2 m intervals in these zones. In contrast, measurements made above the water column take much longer due to slow equilibration times, and can be affected by

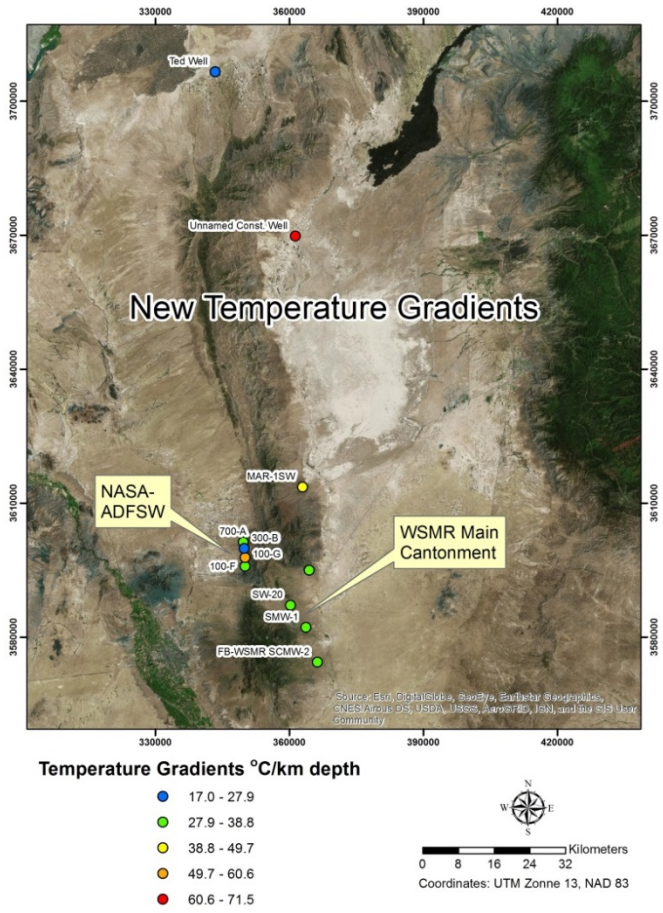

Figure 13. Temperature gradient results from existing wells.

transient air currents, especially near the top of the well, that diminish accuracy. Therefore, measurements in the air column were taken at coarser intervals (typically 5-25 m), depending on depth to water and the time available for logging a given well.

The ADF-SW/NASA monitor wells are pumped occasionally using low-volume pumps to obtain water samples, but none had been pumped for at least several weeks prior to temperature logging. The pumps in these wells were carefully removed to minimize disturbance of the static water and air columns that might affect temperature measurements. These wells were then left static for several days to re-equilibrate from any disturbance caused by removing the pumps. Therefore, it was assumed that all the wells were at static formation temperatures when logged. The pumps were reinstalled after logging and water samples were taken for geothermal analysis. Well depths ranged from 54.9 to 115.3 m. The profiles in these wells appear to be primarily conductive in nature and are generally similar (Fig. 14). Gradients from the linear segments at the bottom of each well range from about 22°C/km (well 300-B-166) to 59°C/km (well 100-G-223). Multiplying typical thermal conductivity values for the reported

lithology at the bottom of each well suggests that heat flow is lowest in well 300-B-166 (40 mW/m^2) and highest in well 100-G-223 (100 mW/m^2). Heat flow values for wells 700-A-253 and 100-F-358 are approximately 70 and 90 mW/m^2 respectively. However, thermal conductivity can vary greatly, so the uncertainty in these heat flow estimates may be on the order of ±20% or more. The reason for the much lower heat flow in well 300-B-166 is unclear, but could be related to cooler groundwater flow or greater uncertainties in thermal conductivity estimates or reported lithologies.

The WSMR wells consisted of monitor wells, primary water supply wells that are normally pumped, but had the pumps removed for maintenance/well rehabilitation, abandoned supply wells used for construction projects, and a supply test well. Most of these wells can be considered as "wells of opportunity" and were logged based more on accessibility than location. Locations ranged from south of the main WSMR cantonment to the Stallion Range Control area in the northern part of the WSMR range. A number of additional wells were checked for logging suitability that could not be logged for various

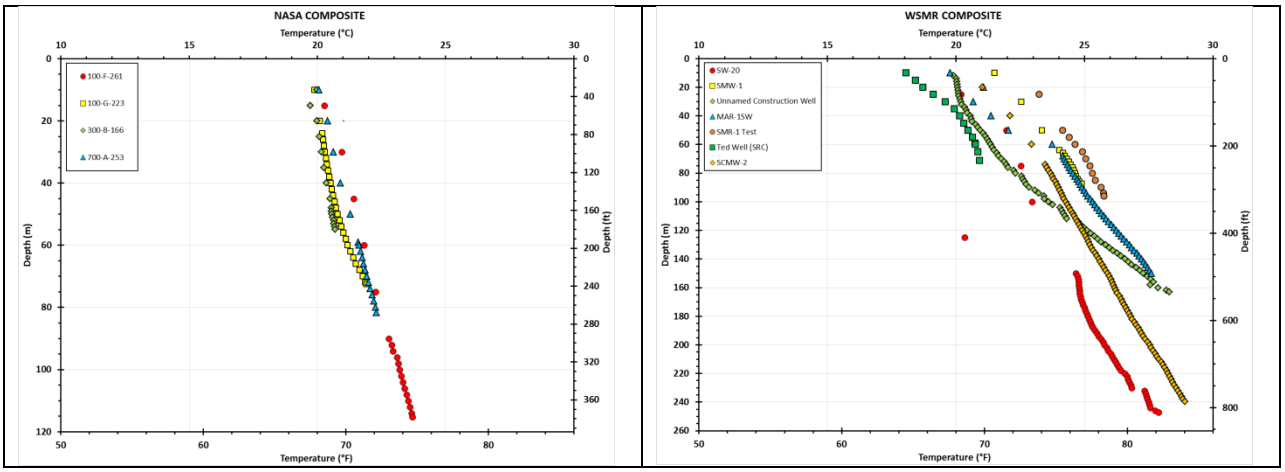

Figure 14 . ADF-SW/NASA (left) and WSMR (right) temperature log composites.

reasons. As far as could be determined, all of the wells had been static for quite some time and were assumed to be at thermal equilibrium. However, it is possible that pumping the SMR-1 supply well about 35 m from the logged SMR-1 Test well could cause a thermal disturbance. Unlike the ADF-SW/NASA wells, pumps are not installed in the WSMR monitor wells that were logged, so there were no issues with disturbing the wells prior to logging. Sample intervals varied in the same way and for the same reasons as in the WSTF wells. The temperature-depth plots are much more varied than those of the WST wells (Fig. 14). Profiles for all of the wells appear to be primarily conductive. An apparent equipment malfunction near the bottom of SW-20 is likely responsible for a small positive shift. These data were added to the PFA dataset and used for the heat CRS.

2.0.5 Gravity Data Acquisition & Analysis

A gravity survey was conducted by the Utah Geological Survey (UGS) in the Tularosa, New Mexico study area to delineate basement/subsurface structures. A total of 189 new gravity stations (Fig. 15) were acquired during the 2016 field season. Field measurements were made using a Scintrex CG-5 Autograv (precision of 1 µGal, accuracy of 5 µGal) following the methods of Gettings and others (2008) and using an absolute gravity base station located near Salt Lake City. Elevation control was established through post-processing of data collected by Trimble GeoXH GPS equipment for a minimum duration of 10 minutes and processed using Pathfinder Office Software tied to local CORS GPS base stations. We report

better than 10 cm vertical accuracy for all stations. Based on the vertical gravity gradient (0.3086 mGal/m) this procedure results in a gravity accuracy of better than 0.03 mGal (30 μGal).

Initial processing of the gravity data was followed by the calculation of terrain corrections, the Complete Bouguer gravity anomaly (CBGA), the horizontal gravity gradient. Inner-zone terrain corrections (0 to 67 m) were calculated by hand based on field terrain surveys using the methods of Gettings(2017). Outer-zone terrain corrections were computed using the methods of Gettings (2017) for each station from 67 m to 166.7 km using 90 m Shuttle Radar Topography Mission (SRTM) elevation data. CBGA values were computed using the methods outlined in Hinze et. al (2005). UGS gravity data were combined with legacy data from the Pan American Center for Earth and Environmental Studies (PACES, http://research.utep.edu/default.aspx?tabid=37229) to improve data coverage. Gravity anomaly and outer-zone terrain correction values were recalculated for the legacy data using the above methods before merging with newly collected UGS data. We conducted a gravity survey in the study area to delineate basement/subsurface structures.

Simplified 2D gravity model of a transect (Appendix B) in the study area was created using a variable thickness sedimentary layer overlying bedrock. The gravity anomaly values along the transect were adjusted for regional effects using low-order polynomials and subsequently modeled using the Semi-Automated Marquardt Inversion code (SAKI) of Webring (1985). The sediment and bedrock density contrasts were held constant for specific interval depths (for sediment layers) and based on estimated values from local geological information, samples, and drill logs of equivalent geographic areas containing sedimentary basins. A density-depth profile was developed using deep well data and densities were assigned in 500 m intervals for the basin fill as follows: 2.0, 2.16, 2.235, 2.31, 2.385, and 2.395 g/cm^3. Bedrock unit for the Tularosa study area was assigned a density value of 2.67 g/cm^3.

Bedrock outcrops on the margins of the valley and interpretations from geologic maps were used as depth-to-bedrock control points for the model to check layer density picks. The profile shows asymmetric basin comprised of a more steeply-dipping interface on the west side of the valley compared to more gently-dipping interfaces on the east side. The basin fill thickness at this location is estimated at a maximum just shy of 1.6 km near the center of the cross-section where the maximum gravity signal is approximately 27 m/Gal. Further north, the gravity anomaly signal is larger indicating sediments are potentially thicker. On the east side of the Organ mountains the gravity anomaly shows the start of a similar signal amplitude in the Tularosa Basin. However, accurate measurements would be required further to the east in order to constrain the Tularosa basin anomaly and have better controls for a future basin model.

Figure 16 below shows study area faults. A prominent Quaternary fault scarp is found curving through the WSMR main cantonment and then running north. Most of the other faults shown in this figure were interpreted from the gravity data.

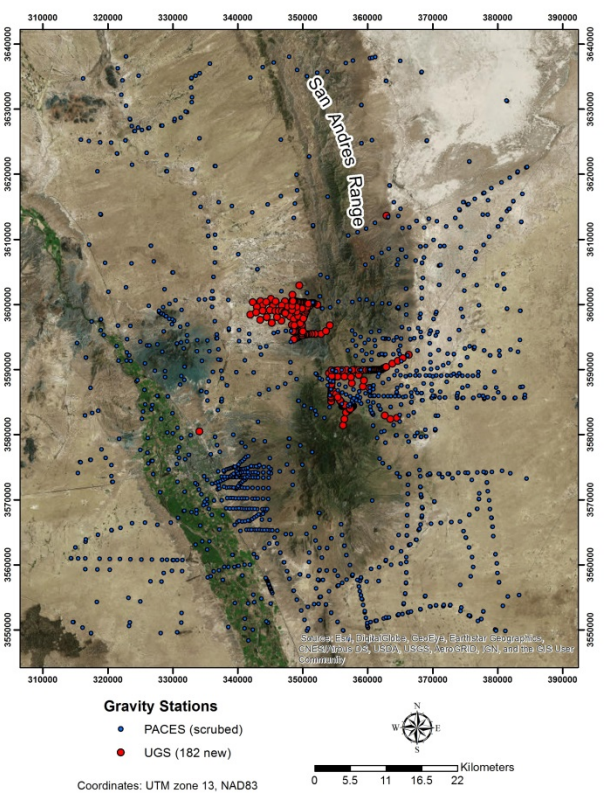

Figure 15. New and legacy gravity stations used for structural analysis.

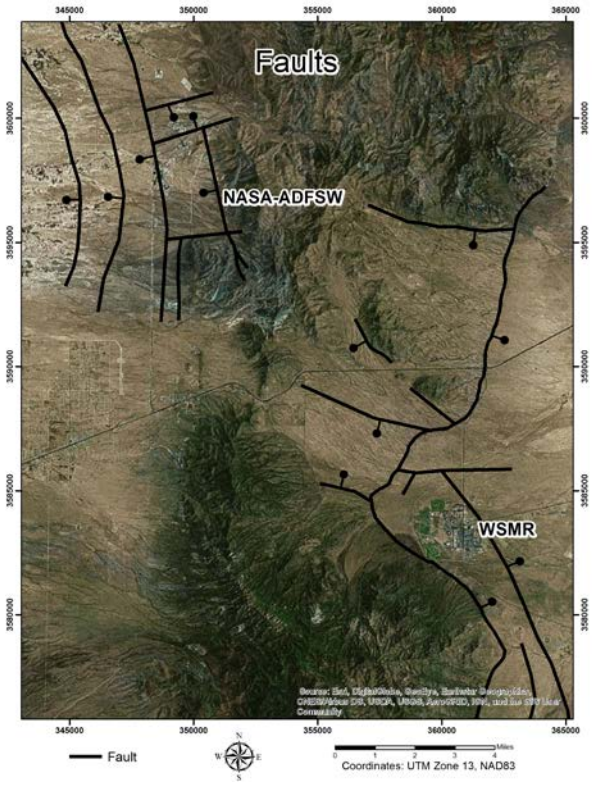

Figure 16. WSMR and ADF-SW/NASA area faults, many of which were interpreted from gravity data.

2.0.6 Magnetotelluric Survey: McGregor Range

A magnetotelluric (MT) survey was done at McGregor Range on Fort Bliss, to help better characterize the area of validation well 56-5, which was drilled by Ruby Mountain Inc. under a DOE ARRA grant. Well 56-5 showed good promise during drilling when several hot water entries were encountered. This well will be flow-tested toward the end of this project, and if adequate flow is achieved, a 0.25 MWe test plant will be installed. The MT survey was run looking forward to the possibility of future development and the potential need to site additional production wells.

To this end, a 56 station survey was conducted by Quantec Geoscience during January, 2017. The data were then submitted to EGI where inversion modelling was accomplished. This is detailed in Appendix B. We interpret this data as showing a NW trending conductor that may be related to hydrothermal alteration on a mapped Quaternary fault. This system was not well understood prior to this survey and may be a target for future drilling (Fig. 17).

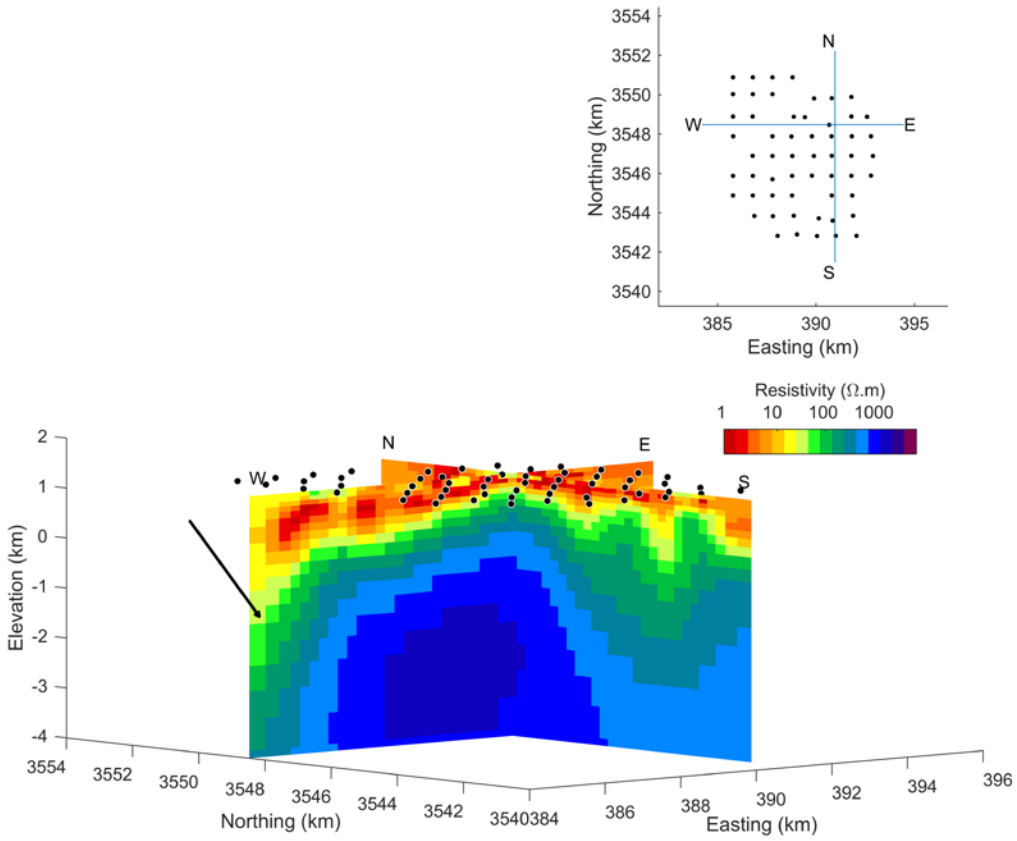

Figure 17. A conductive zone, indicated by the arrow, is believed to be a Quaternary fault system that may be a source of geothermal fluid and a target for future drilling.

3.0 PFA Model Development

Our Phase 1 Play Fairway Analyses (PFA) used a deterministic method based upon petroleum industry logic (Fraser et al., 2001) and the probabilistic Weights of Evidence method (Sawatzky et al, 2009; Coolbaugh, 2003; Bonham-Carter, 1994). The models were based upon (1) the heat of the Earth, (2) fault related fracture permeability, and (3) the presence of ground water. The heat and water data used in these models was collected from public databases, local governments, and literature. Upon exhausting these sources, enough data was present to create the PFAs, although significant expanses of the study area were data poor or devoid of data. Fault related fracture permeability was considered to be areas along and adjacent to Quaternary fault systems and areas of critical stress (Faulds et al., 2006, 2010, 2013). Zones of critical stress were mapped using geomorphological characteristics along with gravity and aeromagnetic data interpretation. Phase 1 PFA analyses identified 12 plays (Fig. 18). The plays were then prioritized based upon economic analyses, land status, and proximity to transmission lines. Phase 2 PFA models were developed in a generally similar manner. However, new data acquired as part of this project were added.

3.0.1 Phase 2 Deterministic Play Fairway Analysis: Petroleum Logic Approach

3.0.1.1 Heat of the Earth CRS

The methods used in Phase 2 closely follow those detailed in our Phase 1 report, with the notable exception that in Phase 1 the 2011 SMU Geothermal Laboratory Heat Flow Map of the Coterminous United States (Blackwell et al., 2011) was used for heat flow. For Phase 2, this data was thought to be overly generalized due to the small scale of the map. Therefore, the SMU Geothermal Laboratory heat flow data were re-interpolated over the study area. Additionally, new quartz geothermeters and temperature gradient data, acquired during Phase 2, were added to Phase 1 datasets which were re-interpolated. All data locations can be viewed in Fig. 19. The resultant raster grids were then classified as follows and vectorized as discussed in detail in our Phase 1 report.

Temperature gradients: 0 ^{o}C/km – 60 ^{o}C/km = High Risk; 60 ^{o}C/km – 80 ^{o}C/km = Medium Risk; >80 ^{o}C/km = Low Risk

Quartz Geothermometer: 0 ^{o}C – 60 ^{o}C = High Risk; 60 ^{o}C – 80 ^{o}C = Medium Risk; >80 ^{o}C = Low Risk

Heat flow was digitized as vector data directly from the SMU 2011 heat flow map (Blackwell et al., 2011). It was classified as follows (mW/m^2): 55 – 70 = High Risk; 70 – 85 = Medium Risk >85 = Low Risk

The final heat CRS was then created through the fusion of the three heat vector layers. The results can be observed on (Fig. 20).

3.1.2 Fracture Permeability CRS

This CRS was developed using Quaternary faults and zones of critical stress (Fig. 21) (Faulds et al., 2006, 2010, 2013). Quaternary faults were derived from the USGS Quaternary Fault and Fold Database of the United States. These data were clipped to fit the study area and then buffered at a distance of 1 km. The resultant polygons were then all classified as Medium Risk. Quaternary faults and recent seismic actively are known to be related to permeability in geothermal systems, but fault slippage can both open and

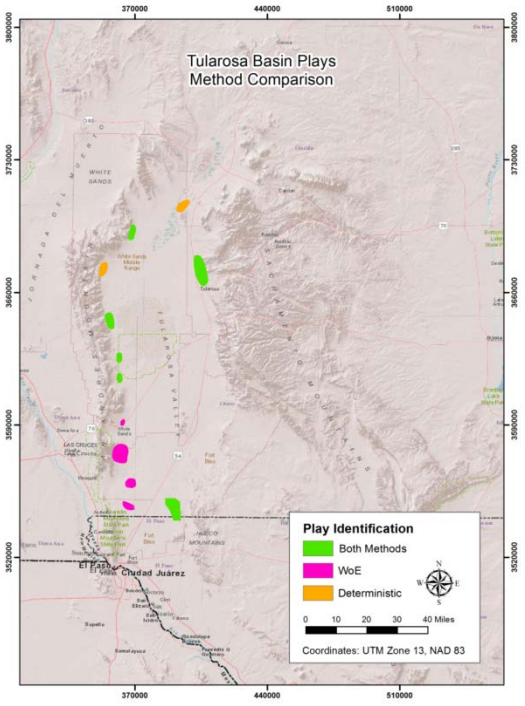

Figure 18. Plays identified in Phase 1 and a comparison of the methods which identified them.

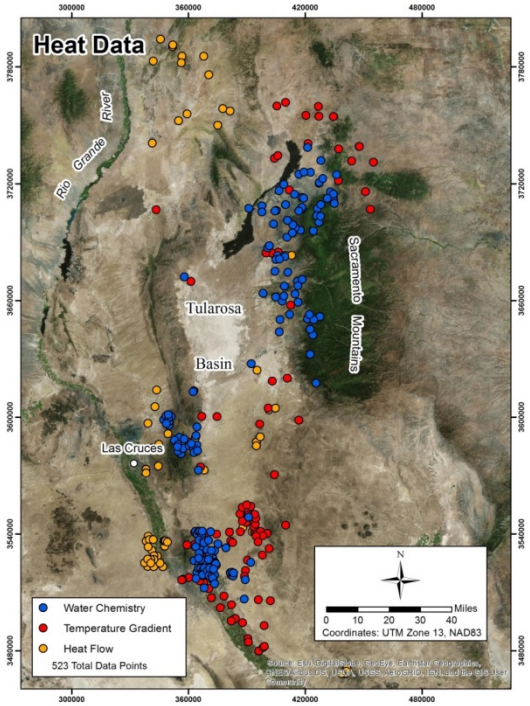

Figure 19. Datasets representing the heat of the Earth. Note that the data types are generally spatially separate.

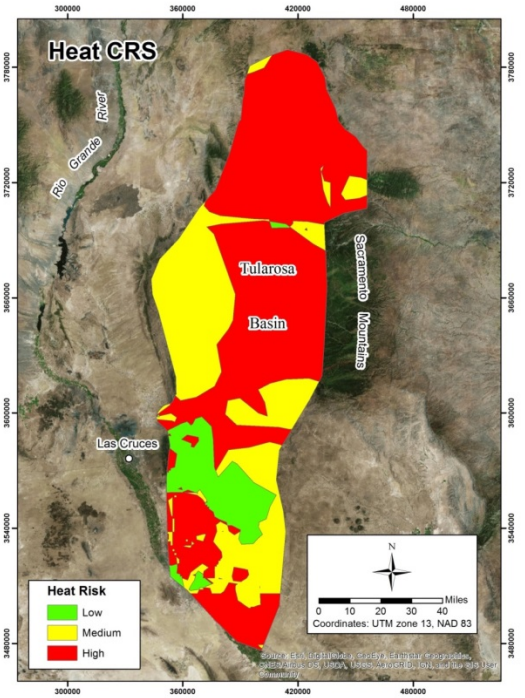

Figure 20. Heat CRS: fusion of heat flow, temperature gradient, and quartz conditional geothermometer data.

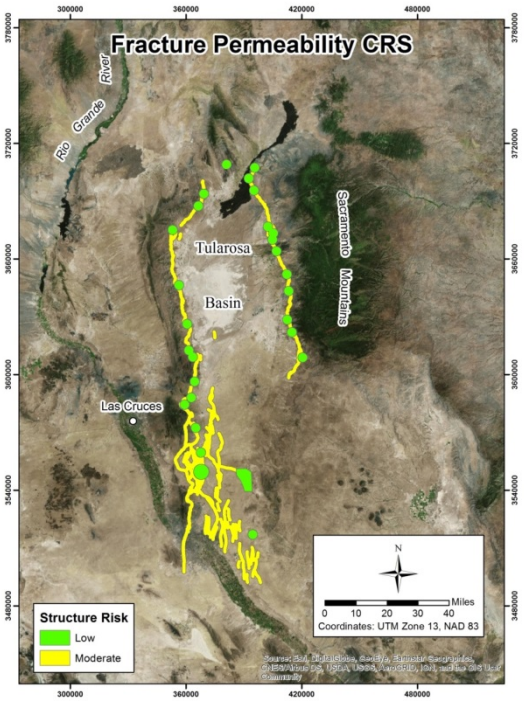

Figure 21. Fracture permeability CRS: Quaternary faults @ 1 km buffer (each side of fault) and 5 km diameter zones of critical stress. Areas within the study area that are not colored are high risk.

close fractures. Therefore, we believed that Quaternary faults needed to be represented, but not as Low Risk. Zones of critical stress form in structural settings such as fault step-overs, tips, apexes, intersections, ramp relays, and accommodation zones. Critical stress zones were mapped using aerial photography, Bouguer gravity, and total magnetic data interpretation. Each zone was considered to be encompassed within a 5 km diameter buffer circle, except where evidence indicated that a larger area may be impacted. Resultant polygons were classified as Low Risk (Fig. 21).

3.0.1.3 Ground Water CRS

Ground water appears to be well distributed in the Tularosa Basin based upon producing wells (New Mexico Office of the State Engineer – POD waters). Additionally, Pleistocene Lake Otero occupied the west central part of the basin providing deep aquifer recharge. There are also numerous water wells not found in the POD database located at WSMR and ADF-SW/NASA. It was found during Phase 1 that water was of little consequence in the PFA due to its availability. Therefore, the Phase 2 deterministic PFA did not use a ground water CRS.

3.0.1.4 Final Petroleum Industry Logic PFA

The final deterministic PFA was created through an overlay of the heat of the Earth and fracture permeability CRS layers (Fig. 22). This PFA contains 7 plays, whereas the Phase 1 PFA deterministic model that produced 8 plays. This was due to the re-interpolation of heat flow data, which eliminated some broadly interpolated high heat flow areas in the west-central and northwestern part of the basin.

3.0.1.5 Certainty

Certainty has many factors including data quality and spatial distribution. Because all of the data used in Phase 1, which also constitutes the majority of data used for Phase 2, came from public databases and literature, we can only assume that it is of high quality. The newly acquired data used in Phase 2 modeling were collected using best known industry practices.

Spatial distribution is critical due to inherent error which propagates between widely spaced data points during interpolation. Therefore, data points were buffered at a 5 km radius with the results being incorporated into the model to show areas of no data, which are low certainty (Fig 23.). This reduced the number of plays to six through the elimination of a play which was based solely upon interpolation. Simple kriging probability was also used, at a threshold of 0.8, for certainty as follows: 0.0-0.6 = low certainty, 0.6-0.8 = medium certainty and 0.8-1.0 = high certainty for heat CRS input data (Fig. 24). Only three plays fell into the high certainty category. The availability of water was also considered, although not as an input CRS, through an overlay shown in Fig. 25, which shows water within all low risk areas.

3.0.2 Stochastic Play Fairway Analysis: Weights of Evidence Approach

The weights of evidence (WoE) method used for the Phase 1 was again applied to the revised Phase 2 data. The use of this technique was based on work done by Moghaddam et al. (2013), where they found it to be the superior stochastic method, out of several tested, for geothermal exploration model development. This technique examines multiple layers of evidence, which makes it ideal for this work. It first calculates weights for each evidential layer based upon the spatial relationships of training points,

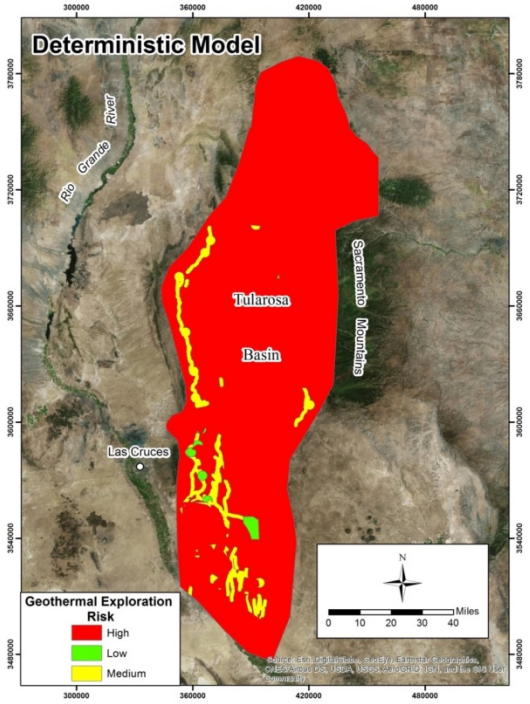

Figure 22. Deterministic petroleum industry logic PFA model suggesting seven potential plays.

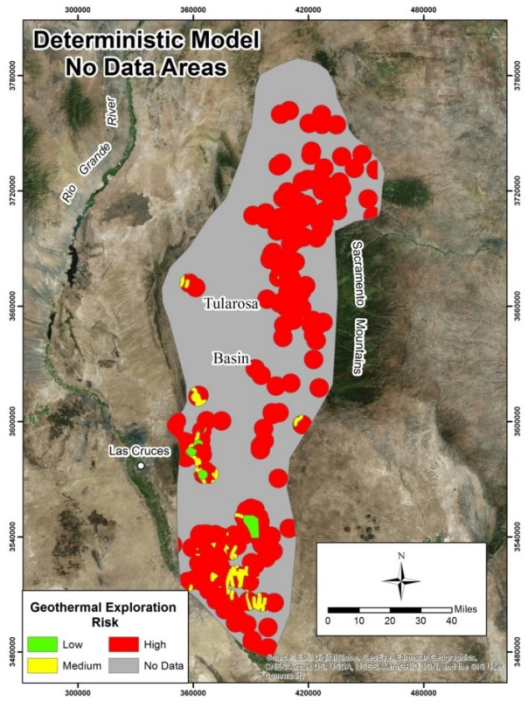

Figure 23. Areas of no data (gray) in relation to PFA results.

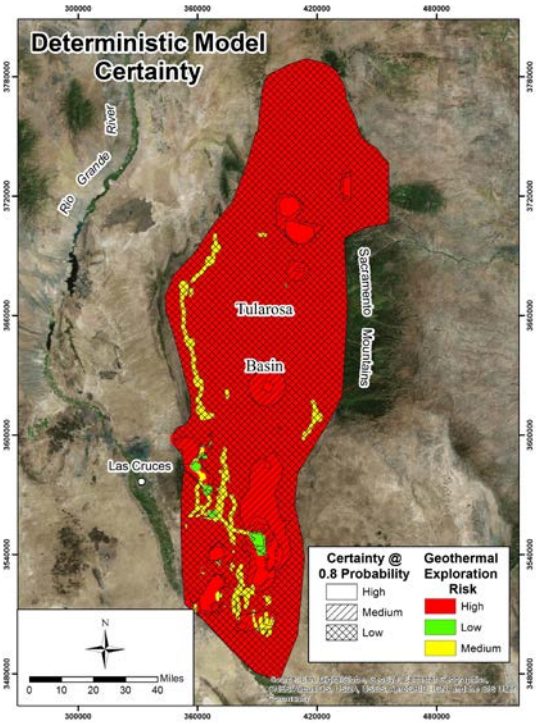

Figure 24. Certainty based upon a 0.8 cutoff on CRS simple kriging probability models.

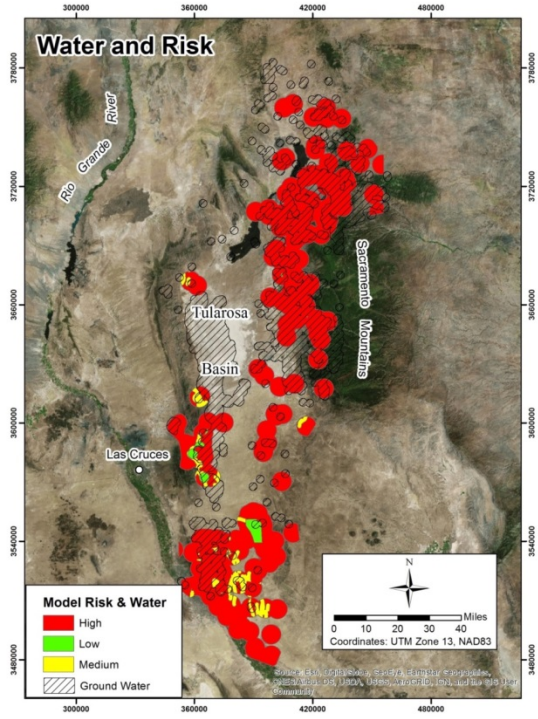

Figure 25. PFA with no data zones removed and the water resource layer added. Water is available within all low risk areas.

which are located at known geothermal systems and hot springs, and then produces a posterior probability raster surface, a certainty raster surface, and other related statistics.

A problem applying this method was encountered for the Tularosa Basin where a lack of training sites existed. There is only one partially proven geothermal system in the area and no hot springs exist. This was addressed by creating regional statistical surfaces, for training use, that covered Nevada, Utah, and New Mexico. This gave access to ample training sites. Spatial Data Modeler was used for the WoE analysis (Sawatzky et al., 2009).

3.0.2.1 WoE Layers of Evidence

In Phase 1, water chemistry data, from the Great Basin Groundwater Geochemical Database from the Nevada Bureau of Mining and Geology (http://www.nbmg.unr.edu/Geothermal/GeochemDatabase.html) and additional data from the Oregon Institute of Technology Geo-Heat Center (http://www.oit.edu/orec/geo-heat-center), were compiled into an ArcGIS shapefile. Redundant points were removed and the quartz (conductive) geothermometer (Fournier, 1991) calculated. The IDW interpolation method was then applied to the quartz geothermometers using ArcGIS to create a regional raster statistical surface. The same process was also applied to heat flow and temperature gradient data originating from the SMU Geothermal Laboratory (http://www.smu.edu/dedman/academics/programs/geothermallab). Extrapolation was allowed into areas with no data for the evidential layers. However, training sites were only chosen in data rich areas where the statistical surfaces were very accurate.

For Phase 2, raster IDW statistical surfaces, specific to the Tularosa Basin project area, created for the deterministic model using newly acquired data as well as data collected during Phase 1, were integrated onto the regional surfaces discussed above to update them (Fig. 26). The datasets were then classified, using standard deviations of the mean, to: Heat Flow = 16 classes, Temperature Gradients = 12 classes and Quartz Geothermometers = 13 classes).

Fault related fracture permeability was represented by zones of critical stress (Fig. 27). These originated from the Faulds Structural Inventory of Great Basin Geothermal Systems and Definition of Favorable Structural Settings (http://en.openei.org/datasets/dataset/structural-inventory-of-great-basin-geothermal-systems-and-definition-of-favorable-structural-setti2) for Nevada and Utah and were mapped by the PI in New Mexico. These data were considered to be binary (critical stress zone = 1, all other areas = 0) in the layer of evidence. Training points are shown in Fig. 28. Ground water was not used as a layer of evidence for the same reason given in the deterministic model section earlier in this report.

The final WoE post probability model overlain with the WoE confidence layer is shown in Fig. 29. It was not anticipated that high probabilities would be produced for the Tularosa Basin due to the placement of training points at known systems that were generally high enthalpy and this was the case. McGregor Range at Fort Bliss, the only know geothermal system in the area, had the highest probability within the study area.

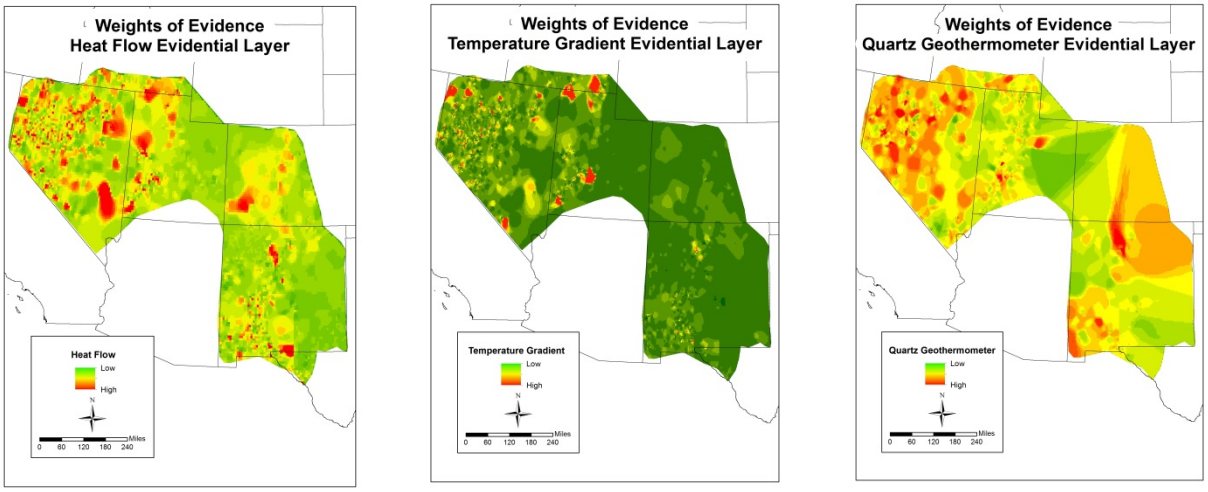

Figure 26. Evidential layers for heat. Please note that no data were used for eastern Utah or Colorado so data covering these areas are interpolations. Training points were located in data rich areas in Nevada, New Mexico, and Utah.

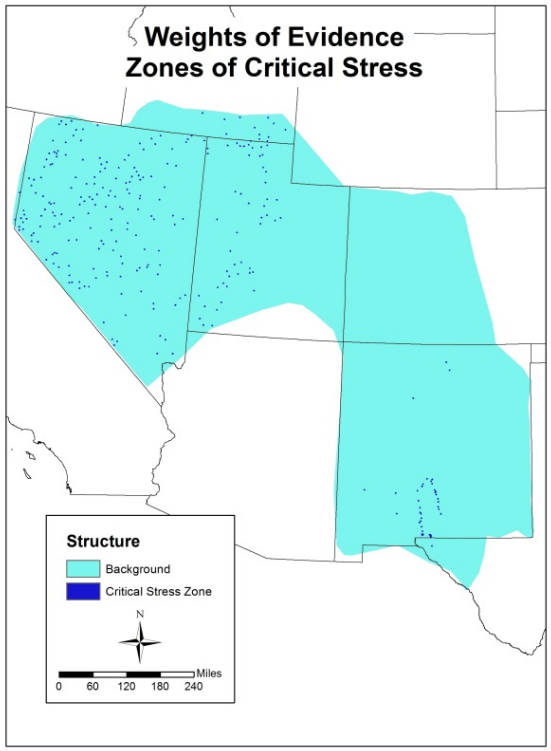

Figure 27 . Zones of critical stress layer of evidence.

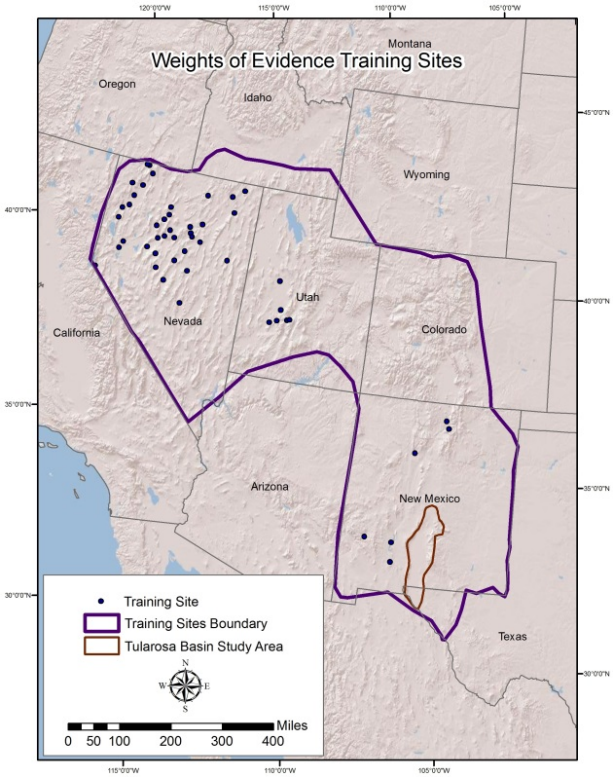

Figure 28. Training points used in WoE analysis.

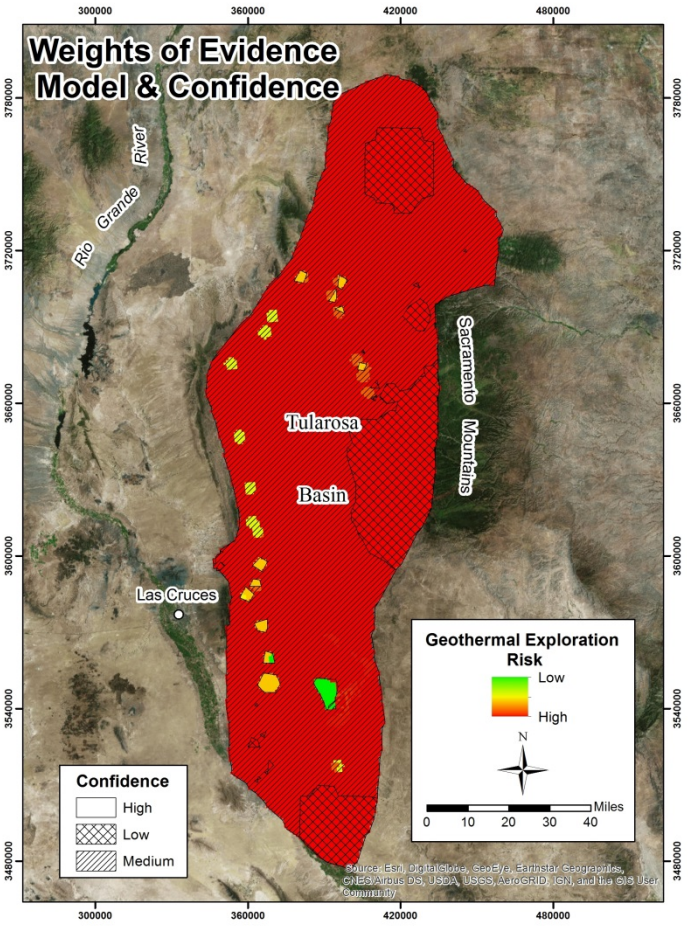

Figure 29. WoE post probability model overlain with the WoE confidence layer. Red areas have 0.0 probability. McGregor Range at Fort Bliss had the highest probability in the study area. It too, however, has the most available data.

3.0.3 Final Plays

Plays from the deterministic model were chosen primarily on being located in low risk areas. Plays from the WoE model were chosen primarily on having probability values that were greater than background. Certainty was then considered and a play had to have high certainty either from (1) kriging probability or (2) WoE confidence. Finally, each play had to be at least partially within a 5km radius of data. The final play map can be seen in Fig. 30.

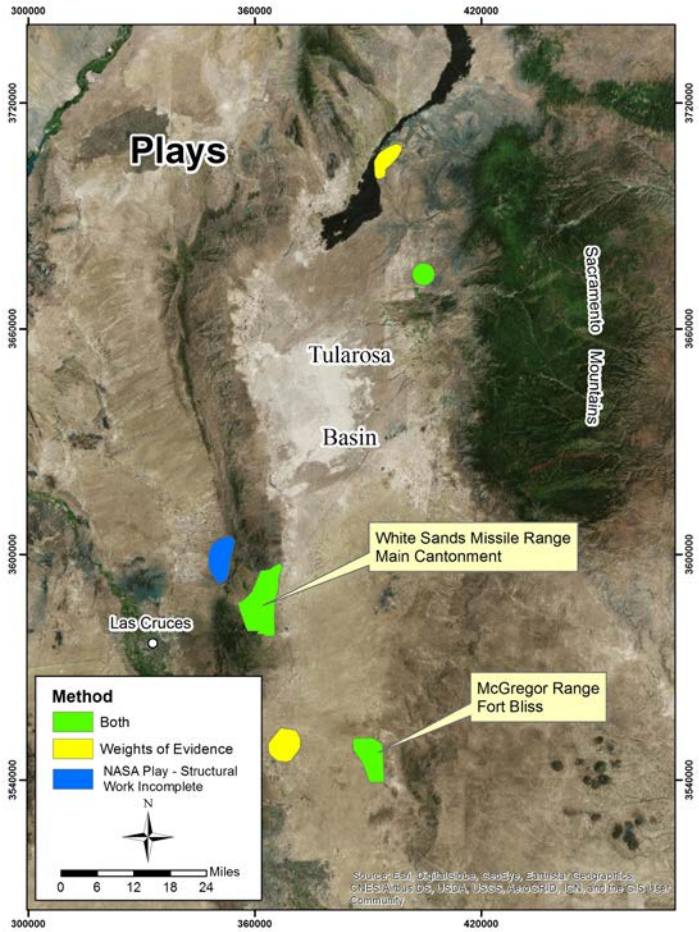

Figure 30. Final Phase 2 play map showing the methods used to choose the plays. Most of the plays were chosen by both methods.

Phase 2 resulted in a significantly reduced number of plays from those produced in Phase 1 (Fig. 31). This was in part due to the re-interpolation of heat flow data, as previously mentioned, which resulted in lower values over part of the study area and because of the application of certainty and areas of no data in a conservative manner. Additionally, the plays were prioritized (Fig. 32) as follows: (1) if both PFA methods indicated the presence of a play and all methods of certainty were high the play was considered high priority; (2) if both PFA methods indicated the presence of a play an only a single method of certainty was high, the play was considered medium priority; and (3) if a single PFA method indicated the presence of a play and a single method indicated high certainty the play was ranked as low priority. This leaves the McGregor Range and WSMR Main Cantonment plays as the highest priorities.

The ADF-SW/NASA play (colored blue on Figs. 30, 31 & 32) was in the low risk category on the deterministic heat CRS, however, no zone of critical stress in a Quaternary fault system has yet been positively identified and since quartz geothermometers suggest increasing heat toward the west part of the play further heat validation is warranted. This work at this play is funded by the U. S. Air Force. It is

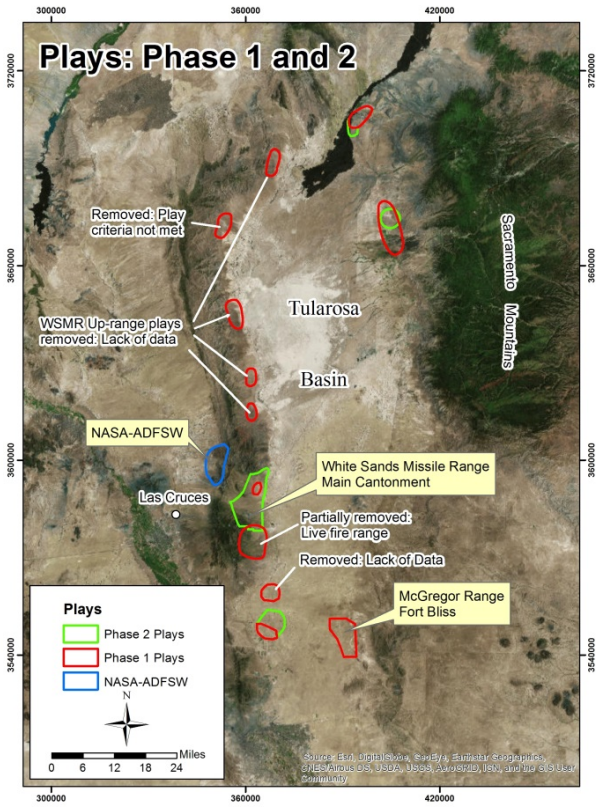

Figure 31. Play comparison between Phase 1 and Phase 2.

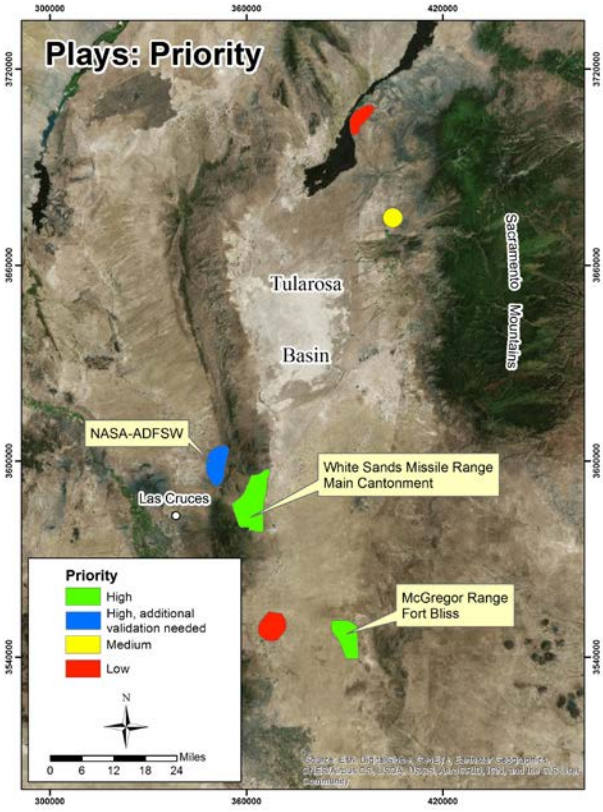

Figure 32. Phase 2 play prioritization.

anticipated that additional data will become available to complete this work. If a zone of critical stress can be confirmed, it will become a PFA high priority play.

4.0 Conclusions

New data, collected during Phase 2, representing the heat of the Earth, in the high priority areas at WSMR and ADF-SW/NASA add evidence of geothermal systems. Quartz geothermometers in the WSMR Main Cantonment area suggest temperatures as high as 98 ^{o}C (Fig. 8). Although data suggests significant ground water mixing, this is one of the highest quartz geothermometers found in the study area. Several nearby wells also have similar, but slightly lower, quartz geothermometers. This is unique within the study area where there are a few spotty similarly high values, but no other known clusters exist. In comparison, the geothermal validation well 56-5 at McGregor Range, Fort Bliss, has a quartz geothermometer of 94 ^{o}C. Additionally, the shallow (2m) temperature survey at WSMR had a spatially correlative temperature anomaly projecting toward this cluster. The shallow temperature survey also exhibited temperature anomalies that correlated well with the Quaternary fault system and showed interesting clusters near the northern and southern extent of the survey (Fig. 33). Temperature logging of existing wells generally did not indicate high temperature gradients. This may be due to the influx of cold ground water. Unfortunately, the choice of wells for logging was generally based upon availability and the spatial relationship with the Quaternary fault system was not optimal. However, a gradient of 71.5 ^{o}C/km was found at an unnamed construction well up-range at WSMR. This area did not become a

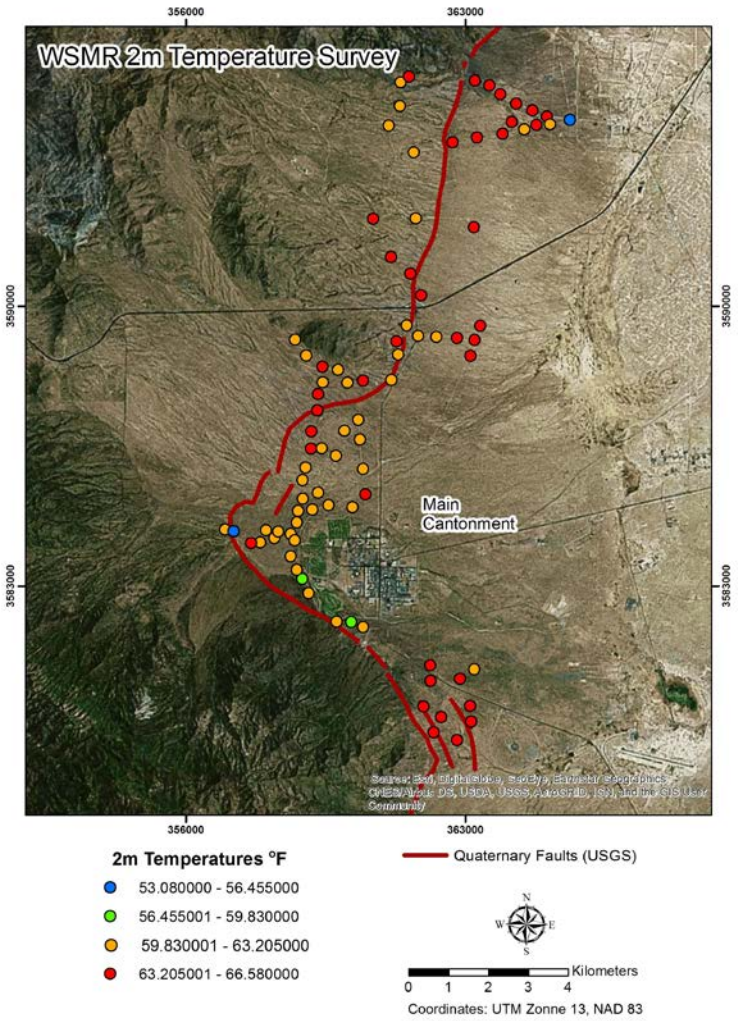

Figure 32. WSMR shallow temperature survey results.

play because this was lower than the allowed threshold. However, it is believed that more work may be warranted in this area in the future.

Structural interpretation from gravity data has provided new insights both at WSMR and ADF-SW/NASA. New faults have been interpreted including en echelon faults outboard of the range-fronts at ADF-SW/NASA at WSMR. Intersecting and interconnecting faults have also been mapped that may be creating zones of critical stress. This is especially prominent at WSMR where structural remnants of oroclinal bending likely influenced the propagation and linkage of the San Andres and Organ fault systems. Additionally, seismic profiles, provided by NASA, suggest that en echelon faults offset buried Quaternary sediments at ADF-SW/NASA, raising the stakes at this play.

Finally, while there is not 100% certainty that there is a geothermal system at any of the plays identified in our study, with the exception of McGregor Range, we believe that the probability has been significantly raised. The WSMR main cantonment area shows good promise. Therefore, we recommend drilling 1000' deep temperature gradient holes in this area for validation. The ADF-SW/NASA play is also beginning to show promise and we assume that additional funds will become available from the Air

Force to advance this area. Other areas in the Tularosa Basin may also have geothermal systems, such as the Rhodes Canyon play, where the unnamed construction well had a relatively high temperature gradient. Additionally, the geochemistry of wells MAR-3SW, SC-2, and SMR1A suggest the possibility of geothermal activity in their respective areas. However, data is sparse to nonexistent over much of the study area, but it is hoped that this study will provide information that will help guide future exploration.

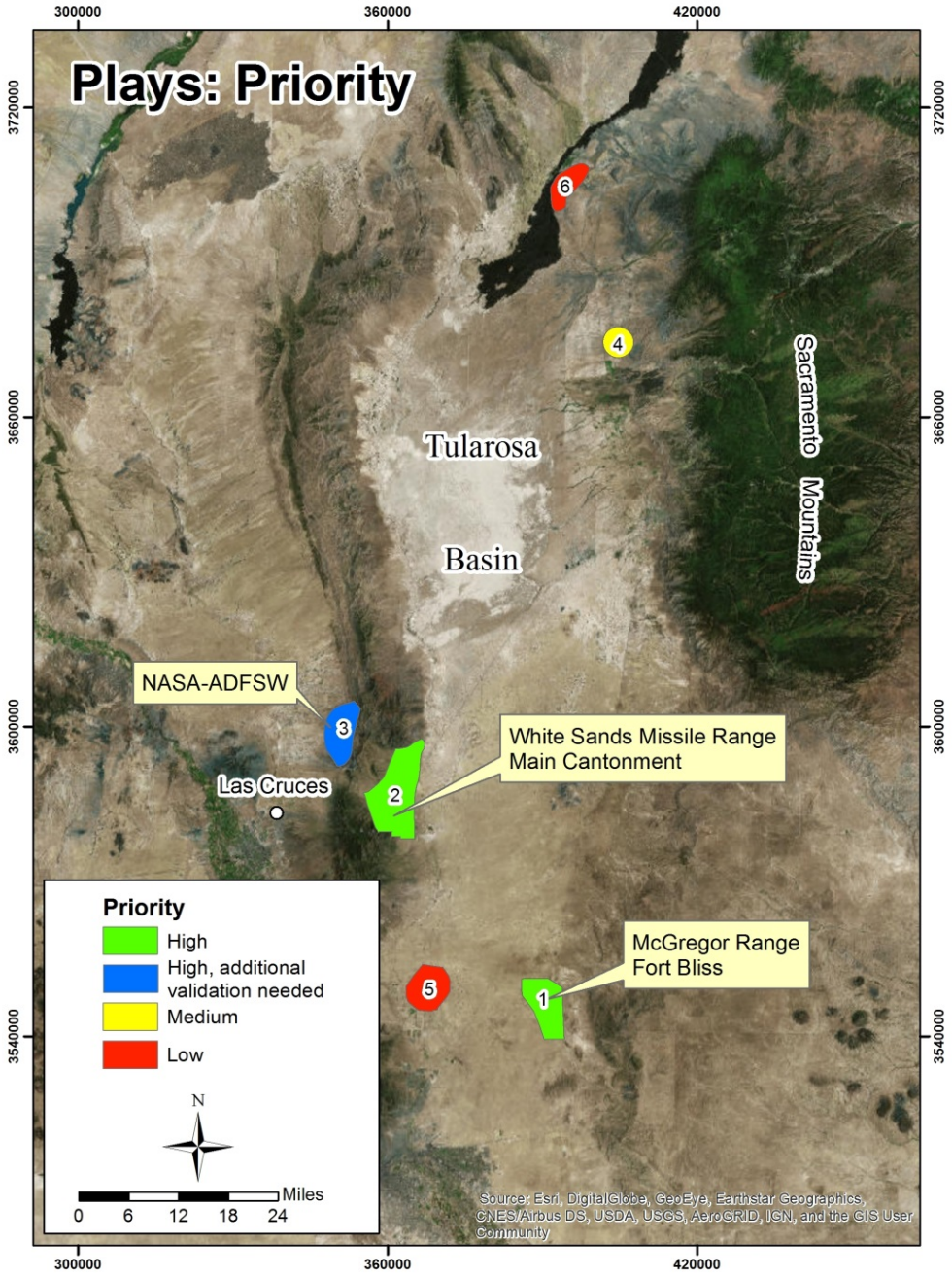

Figure 33. Ranked plays following Phase 2.

References

Bonham-Carter, G., 1994. Geographic information systems for geoscientists: modelling with GIS. Pergamon press.

Broadhead, R.F., 2003, Petroleum geology of the McGregor Range Otero County, New Mexico. AAPG Search and Discovery Article #10052.

Coolbaugh, M. F., 2003: the prediction and detection of geothermal systems at regional and local scales in Nevada using a geographic information system and thermal infrared imagery. Dissertation, University of Nevada, 172 p.

Coolbaugh, M., Sladek, C., Faulds, J., Zehner, R., and Oppliger, G. "Use of Rapid Temperature Measurements at a 2-Meter Depth to Augment Deeper Temperature Gradient Drilling," Thirty-Second Workshop on Geothermal Reservoir Engineering, January 2007.

Coolbaugh, M., Sladek, C. and Kratt, C. "Compensation for Seasonal and Surface Affects of Shallow (Two-Meter) Temperature Measurements," Geothermal Resource Council Transactions, Volume 34, 2010.

Faulds, J., M. Coolbaugh, G. S. Vice, and M. L. Edwards, 2006. Characterizing structural controls of geothermal fields in the northwestern Great Basin: A Progress Report, GRC *Transactions,* v. 30, p. 69-76.

Faulds, J., M. Coolbaugh, V. Bouchot, I. Moeck, and K. Oguz, 2010. Characterizing Structural Controls of Geothermal Reservoirs in the Great Basin, USA, and Western Turkey: Developing Successful Exploration Strategies in Extended Terranes, *Proceedings*, World Geothermal Congress, Bali, Indonesia, p. 1-10.

Faulds, J. E., N. H. Hinz, C. Kreemer, and M. Coolbaugh, 2012. Regional patterns of geothermal activity in the Great Basin region, western USA: Correlation with strain rates, GRC *Transactions*, v. 36, p. 897- 901.

Faulds, J. E., N. H. Hinz, G. M. Dering, and D. L. Siler, 2013. The hybrid model – the most accommodating structural setting for geothermal power generation in the Great Basin, western USA: *GRC Transactions*, 37, 3-10.

Fournier, R. O., 1991, Water geothermometers applied to geothermal energy; in Applications of Geochemistry in Geothermal Reservoir Development, UNITAR-UNDP (ed. F. D'Amore), p. 37-69.

Fraser, A. J., 2001, Vining, B.A. & Pickering, S. C. (eds) Petroleum Geology: From Mature Basins to New Frontiers – Proceedings of the 7th Petroleum Geology Conference, 791–800. DOI: 10.1144/0070791# Petroleum Geology Conferences Ltd. Published by the Geological Society, London, p. 791-800.

Gettings, P. (2017), Ph.D. thesis, University of Utah.

Gettings, P., D. S. Chapman, and R. Allis (2008), Techniques, analysis, and noise in a Salt Lake Valley 4D gravity experiment, Geophysics, 73 (6), WA71–WA82.

Geochemistry in Geothermal Reservoir Development, UNITAR-UNDP (ed. F. D'Amore), p. 119-144.
Hinze, W. J., et al. (2005), New standards for reducing gravity data: The North American gravity database, Geophysics, 70 (4), J25–J32.

Harder, V.M., 1982, Oil and Gas Potential of the Tularosa Basin-Otero Platform Area, Otero County, New Mexico. M.S. Thesis, University of Texas at El Paso, 90 p.

King, W.E., and Harder, V.M., 1985, Oil and Gas Potential of the Tularosa Basin-Otero Platform Area, Otero County, New Mexico. New Mexico Bureau of Mines & Mineral Resources, Socorro, Circular 198, 37 p.

Kottlowski, F.E., 1975. Stratigraphy of the San Anders Mountains in south-central New Mexico. In: Las Cruces County. Seager, W.R., Clemens, R.E., Callender, J.F. (eds.), New Mexico Geological Society 26th Annual Fall Field Conference Guidebook, pp. 95-104.

Lazaro, M., Page, C., Tiedeman, A., Sabin, A., Bjornstad, B., Alm, S., Meade, D., Shoffner, J., Mitchel, K., Crowder, B. and Halsey, G."United States Department of the Navy Geothermal Exploration Leading to Shallow and Intermediate Drilling at Hawthorne Ammunition Depot, Hawthorne, NV," Geothermal Resource Council Transactions, Volume 34, 2010.

Lazaro, M., Alm, S., Tiedeman, A., Page, C., Meade, D., Shoffner, J., Bucher, K. "Department of the Navy Geothermal Exploration on Naval Air Station Fallon (NASF) Managed Lands in Dixie Valley, Nevada," Geothermal Resource Council, Volume 35, 2011.

Marshak, S. (2004) Salients, recesses, arcs, oroclines, and syntaxes – a review of ideas concerning the formation of map-view curves in fold-thrust belts. In K.R. McClay (ed.) AAPG Memoir 52, p. 131-156.

Pribnow, D., and Clauser, C. (2000) Heat and fluid flow at the Soultz hot dry rock system in the Rhine graben. Proceedings World Geothermal Congress, Kyushu-Tohoku, Japan, May 28-June 10, 2000, p. 3835-3840.

Seager, W.R. (1981) Geology of Organ Mountains and southern San Andres Mountains, New Mexico. New Mexico Bureau of Mines & Mineral Resources Memoir 26, 97 p. plus 5 maps sheets.

Sladek, C., Coolbaugh, M. and Zehner, R. "Development of 2-Meter Soil Temperature Probes and Results of Temperature Survey Conducted at Desert Peak, Nevada, USA," Geothermal Resource Council Transactions, Volume 31, 2007.

Sawatzky, D.L., Raines, G.L., Bonham-Carter, G.F., and Looney, C.G., 2009, Spatial Data Modeler (SDM): ArcMAP 9.3 geoprocessing tools for spatial data modelling using weights of evidence, logistic regression, fuzzy logic and neural networks. http://arcscripts.esri.com/details.asp?dbid=15341.

Skord, J., Sladek, C., Coolbaugh, M., Cashman, P., Lazaro, M. and Kratt, C. "2-M Probe Survey at Dixie Valley Geothermal Area," Geothermal Resource Council Transaction, Volume 35, 2011.

Sundance Engineering, 2015, Final geothermal exploration report at White Sands Missile Range New Mexico, U.S. Army Corps of Engineers Contract No. W912PP-14-P-0076, 77 p.

Webring, M. W. (1985), SAKI–a Fortran program for generalized linear inversion of gravity and magnetic profiles, Open-File Report 85-122, U.S. Geological Survey, 104p.

APPENDIX A: General Stratigraphy

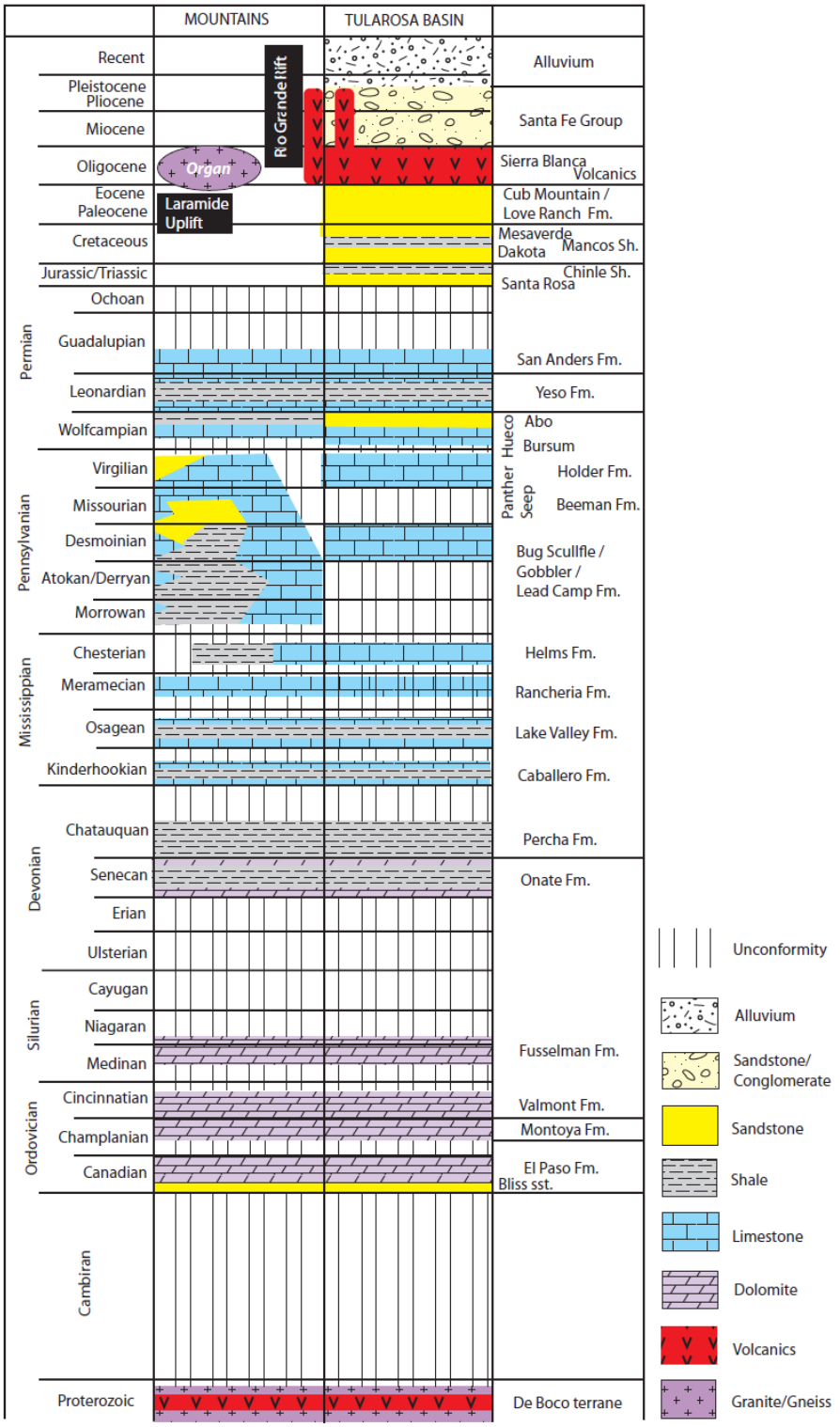

A simplified stratigraphy of the Tularosa Basin and bordering mountains in southern New Mexico (modified from Seager, 1981; Harder, 1982; King and Harder, 1985; and Broadhead, 2003).

APPENDIX B: Gravity Transect

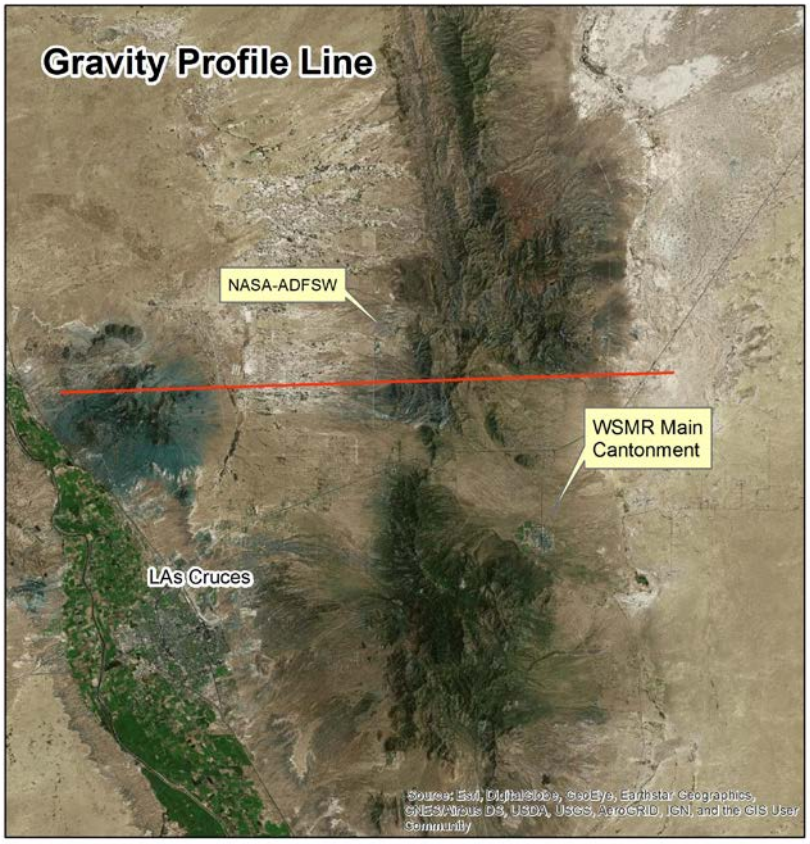

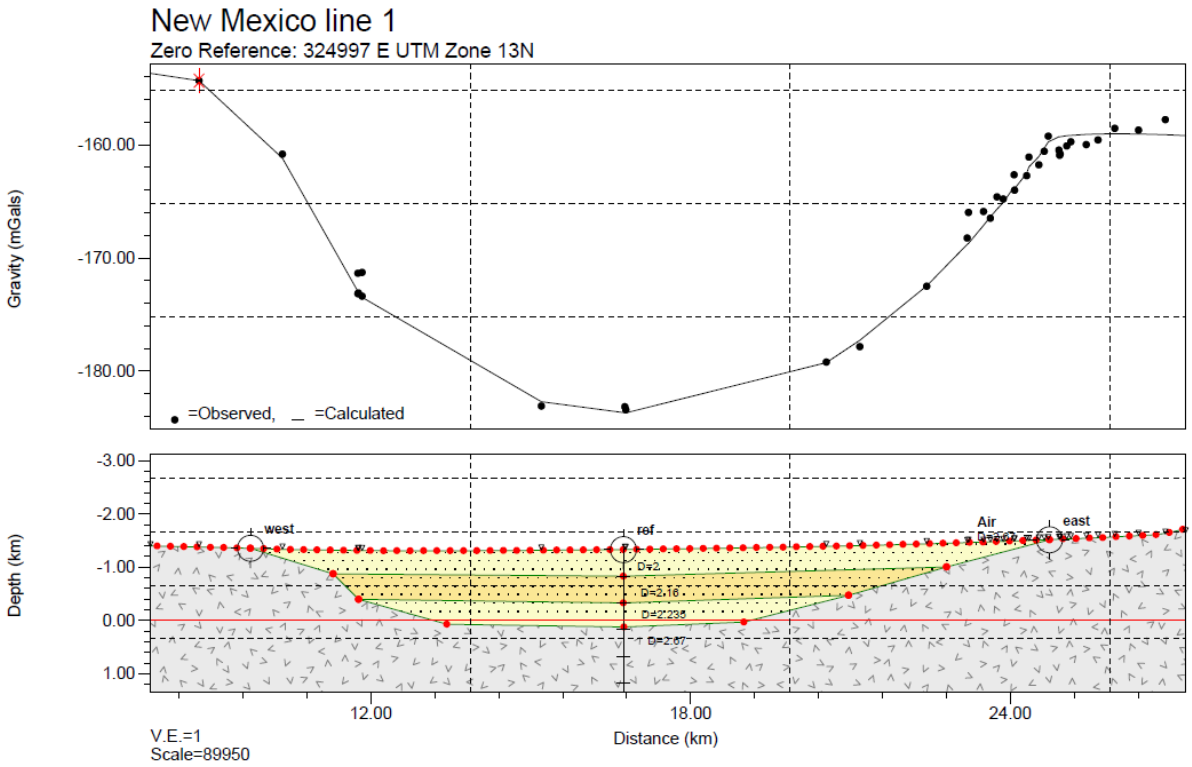

APPENDIX C: MT Inversions

Two inversions were carried out, the first using only 16 (every other) of the 31 frequencies used for the second inversion. From a starting nRMS near 12, nRMS values close to 1 were obtained by Model 11, in both inversions, from a 25 Ωm starting halfspace.

Topography

- Source: USGS (2006), Shuttle Radar Topography Mission, 1 Arc Second scene SRTM_ ffB01_p032r038, Filled Finished-B 2.0, Global Land Cover Facility, University of Maryland, College Park, Maryland, February 2000.
    - ftp://ftp.glcf.umd.edu/glcf/SRTM/WRS2_Tiles/p032/SRTM_ffB01_p032r038

Mesh

- 82 (north) x 80 (east) x 61 (vertical) FE cells; 13 layers of air (z-node #14 is earth surface).
- Deformed vertically to mimic the surface topography at z-layer=14 nodes.
- 78 x 76 x 46 inversion parameters (272,688)
- Background elevation set to 1250 m asl.

Data Weights

- Kzx and Kzy are not included in the inversion.
- $$\text{data weight for } Z_{ij} \text{ at frequency ifr} = \max\begin{cases} 5\% \cdot \left|Z_{ij}(ifr)\right| \\ 5\% \cdot \dfrac{\left|Z_{xy}(ifr) - Z_{yx}(ifr)\right|}{2} \\ \text{originally assigned data weight} \end{cases}$$

Model Weights

- Model weights are determined by the following scheme:
    - For each layer *iz*, consider parameters *j* immediately beneath and surrounding each receiver. Calculate
        - $MeanW_{iz} = \left(\dfrac{\sqrt{\sum (S_j)^2}}{\#} \right)_{iz}$; $S_j = \left(\dfrac{\sqrt{diagF^T F}}{cellvolume} \right)_j$
        - $MaxW_{iz} = \max(S_j)_{iz}$.
    - Determine shallowest layer for which $MaxW_{iz} \le 2 \times MeanW_{iz}$; set $MaxW_{ref} = MaxW_{iz}$. Should $MaxW_{ref}$ not be defined by a user-specified *iz*, the specified *iz* is used to determine $MaxW_{ref}$.
    - For each layer, model weight applied laterally: $W_L(iz) = 1 + \dfrac{MaxW_{iz}}{MaxW_{ref}}$

model weight applied vertically: $W_V(iz) = 1 + 10\%\left(\frac{MaxW_{iz}}{MaxW_{ref}}\right)$.

- Note model weights are calculated for the starting model and held fixed for the inversion.
- Note model weights are scaled by the average volume of the cells within a user-specified region-of-interest (ROI).

Smoothness Regularization Calculation

- $\lambda = nRMS \cdot ndiagJ \cdot \kappa$
  - $ndiagJ = \frac{\sum\left(J_{.j}^T J_{.j}\right)}{\#j}$. If *ndiagJ* increases from one iteration to the next, the smaller value is used.
  - $nRMS = \sqrt{\sum\left(\frac{d_{obs} - d_{pre}}{d_w}\right)^2 / \#d}$
  - κ = 0.001; specified in the input file. If nRMS does not reduce by at least 5% from one iteration to the next, the value of κ is halved.

Parameter-step stabilizer Epsilon:

- = 0.0000001; specified in the input file; applied only to the region of interest (NOT all diagonal entries).

APPENDIX D: Well Test Report

October 23, 2020

To: Carlon Bennett
Sr. Project Manager, Ruby Mountain, Inc.

From Benjamin Barker, Ph.D.
Principal, Barker Engineering

Addendum Report on October 2019 Flow Testing of Well RMI 56-5, McGregor Range

Summary

Well RMI 56-5 was drilled from May 17 to June 23, 2013 to a depth of 3,030 feet. A string of slotted 7 inch casing was set in 8.75 inch hole on bottom fill at 3,017 feet to complete the well. Pump testing was not possible with the equipment and budget available at the time, but encouraging results were obtained from observations during drilling. On October 1-10, 2019 the Ruby Mountain (RMI) team returned to the McGregor Range to flow test the well and gather as much evidence as possible about its condition and potential.

A principal objective of the October 2019 campaign was to verify that well RMI 56-5 is still in usable condition. RMI also wished to validate or improve upon the 2016 productivity estimates. The work was successful on both counts, as the well demonstrated water temperatures beyond expectations and flow performance consistent with the 2016 calculations. We also observed exceptional community support for Fort Bliss. Several local contractors stepped up to cope with unexpected events, any one of which could have exhausted the limited funds available for this testing and curtailed the project early.

Preparation

The well site of RMI 56-5 proved to be fertile ground for natural vegetation growth in the three years since drilling. An El Paso construction company, LB & Sons, Inc., was engaged in September 2019 to restore the containment berm and remove the bushes that had taken root on the site. They also touched up the approach ramp from the tank trail on the north side of the site that serves as the access road. LB & Sons' work was done efficiently and no difficulties were encountered with site stability or preparation during the job.

The Las Cruces branch of Rain For Rent (R4R) was contracted to supply a water metering and disposal system. On October 1, 2019 the R4R crew mobilized a roadable 21,000 gallon closed top tank to the site.

The tank outlet hoses were connected to a diesel-engine powered centrifugal pump, which was placed within its own containment pan (Figure 1). The pump output was routed through a positive displacement totalizing water meter (Figure 2) and then to a 300 foot slotted irrigation pipe for dispersal (Figure 3). The tank and drill rig are shown in Figure 4.

Figure 1. DV100C pump

Figure 2. Totalizing water meter

Figure 3. Water pump and dispersal field

Figure 4. Drilling rig with water tank behind

The water dispersal field was selected to spread water over a previously disturbed area in small streams to avoid erosion, and downslope from nearby roads. It was designed in collaboration with the Fort Bliss environmental group and McGregor Range management, with the guidance of RMI. RMI obtained all the necessary permits and made introductions that were essential to get the job done in a timely manner.

The original plan was for the drilling company, Hydrotech Drilling of Alamagordo, to mobilize to the site simultaneously with R4R to facilitate hooking up lines. Unfortunately, lightning storms and heavy rains near Ruidoso required Hydrotech to stand down for their workers' safety. By the time roads had dried enough to move the rig, nearly a week had passed. Hydrotech was finally able to bring its Ingersoll-Rand T3W rig to the RMI 56-5 site on October 8.

Downhole instrumentation to measure drawdown and water temperature presented a conundrum. The maximum temperature measured in 2016 was 200 F at 3,000 ft, which would require higher temperature tools than were available within the available budget. However, the well had been idle for three years, the shallowest water in 2016 was about 180 F, and cooler water could be expected to migrate from shallower strata. We concluded there was a chance that the early part of the flow test could be recorded with relatively inexpensive groundwater monitoring memory tools. To this end, we rented two TROLL 700 instruments from In-Situ Inc., of Fort Collins, CO. The maximum rated operating temperature of these tools is 176 F (80 C). A copy of the brochure for these tools is appended. Hydrotech Drilling fabricated a chamber to hold the tools below the air injection level in the well (Figures 5, 6). The cords in the left photo are tethers for removing the tools from the close-fitting inner chamber of the slotted sub.

Figure 5. Inner chamber holding tools

Figure 6. Assembled sub with air slots above

Testing Operations

When Hydrotech Drilling arrived on location, their crew required only 3-1/2 hours to rig up and prepare tools for running in the hole (Figure 6). That took place mid-day on October 8 and operations were essentially completed within 48 hours thereafter in four test sequences. The test sequences are listed below, while the detailed timing of steps is recorded in the Activity Log which follows.

- Sequence 1
  - Ran pressure and temperature memory tools to 500 ft subsurface, 16 ft below the depth of the last measured water table depth in 2016.
  - Injected air at nominal 900 SCFM to lift water. After 16 minutes noted large quantities of steam condensate and stopped the air injection.
  - Retrieved memory tools.
- Sequence 2
  - Ran open ended drill pipe to 840 ft and resumed air injection for 18 hrs.
- Sequence 3
  - Ran in open ended to 900 ft and resumed air injection for 1 hr 25 min.
- Sequence 4
  - Ran in open ended to 1,000 ft and resumed air injection for 3 hr.

TABLE 1: Activity log of Well RMI 56-5 well test

DATE	TIME	SURVEY min	REMARKS (all depths measured in feet from ground level)
10/1/2019	1000		MIRU R4R 21,000 gal covered tank, DV100 diesel pump, totalizing water flow meter and 300 ft slotted irrigation pipe.
10/2-7/2019	-		waiting on weather (Hydrotech Drilling delayed by storms)
10/8/2019	1000		MIRU Hydrotech Drilling I-R T3W rig.
SEQUENCE 1			
10/8/2019	1300	0	attempted to sound static water level w/capacitance tape. (operator stated he suspects 370 ft reading was erroneously shallow due to wet casing) Started clocks in memory tools.
"	1328	28	made up 4 in. drill pipe sub for dual P,T memory tools.
"	1332	32	begin RIH w/dual P,T memory tools.
"	1410	70	stopped RIH @ 480 ft.
"	1430	90	rigged air injection line to wellhead and water flow line to tank.

10/8/2019	1433	93	began air injection 900 cfm.
"	1449	109	measured water temp 115 F at tank bottom drain.
"	1449	109	noted copious steam condensate venting from tank. Estimated surface water temperature with IR thermometer 160 F.
"	1450	110	water in tank est 1050 gal. Stopped air, POH with P,T tools.
"	1528	148	recovered P,T tools. Max T 181 F @ 480 ft (tool rated to 176 F).
SEQUENCE 2			
10/8/2019	1615		RIH w/open ended drill pipe.
"	1800		hung drill pipe @ 840 ft, began air injection.
10/8-9/2019			[continued air-lift water production overnight]
10/9/2019	1200		shut off air.
SEQUENCE 3			
10/9/2019	1202		RIH to 900 ft.
"	1245		resumed air injection.
"	1410		shut off air.
SEQUENCE 4			
10/9/2019	1412		RIH to 1,000 ft.
"	1500		resumed air injection, standpipe pressure 220 psig.
"	1800		shut off air.
"	1801		vented wellhead to atmosphere, began inflow recovery test.
"	1810		completed inflow recovery test.
"	1814		vented well to tank. Secured well and rig for the night.
"			[drill pipe left at 1,000 ft, connected by hose to water tank]
DEMOBILIZE			
10/10/2019	0730		began rigging down R4R.
"	0900		rinsed minor sand from R4R tank @ Patriot Road standpipe.
"	1215		Hydrotech began POH and laying down 4 in drill pipe.
"	1253		completed POH.
"	1256		loaded out drill pipe from derrick, laid down derrick.
"	1320		sounded water level @ 550 ft w/capacitance tape, repeated measurements twice w/same result.
"	1400		reinstalled wellhead, fence. Cleared McGregor Range.

Results

Sequence 1

The temperature and pressure recording tool records are appended to this report as Table 4 following the Conclusions. The data is displayed in Figure 7, below. Several features of the data are noteworthy:

- The agreement between the two tools is excellent.
- The temperature at the top of the static water column exceeded the 176 F tool rating before the airlift started.
- The water table was encountered before air injection at a shallower depth than in 2016.
- The pressure response of the tools is much faster than the temperature response.
- Both tools registered unstable two-phase flow during the air injection during minutes 93-110.
- Minimal pressure drawdown over sequence interval.

Figure 7. Pressure and Temperature data recorded during Sequence 1

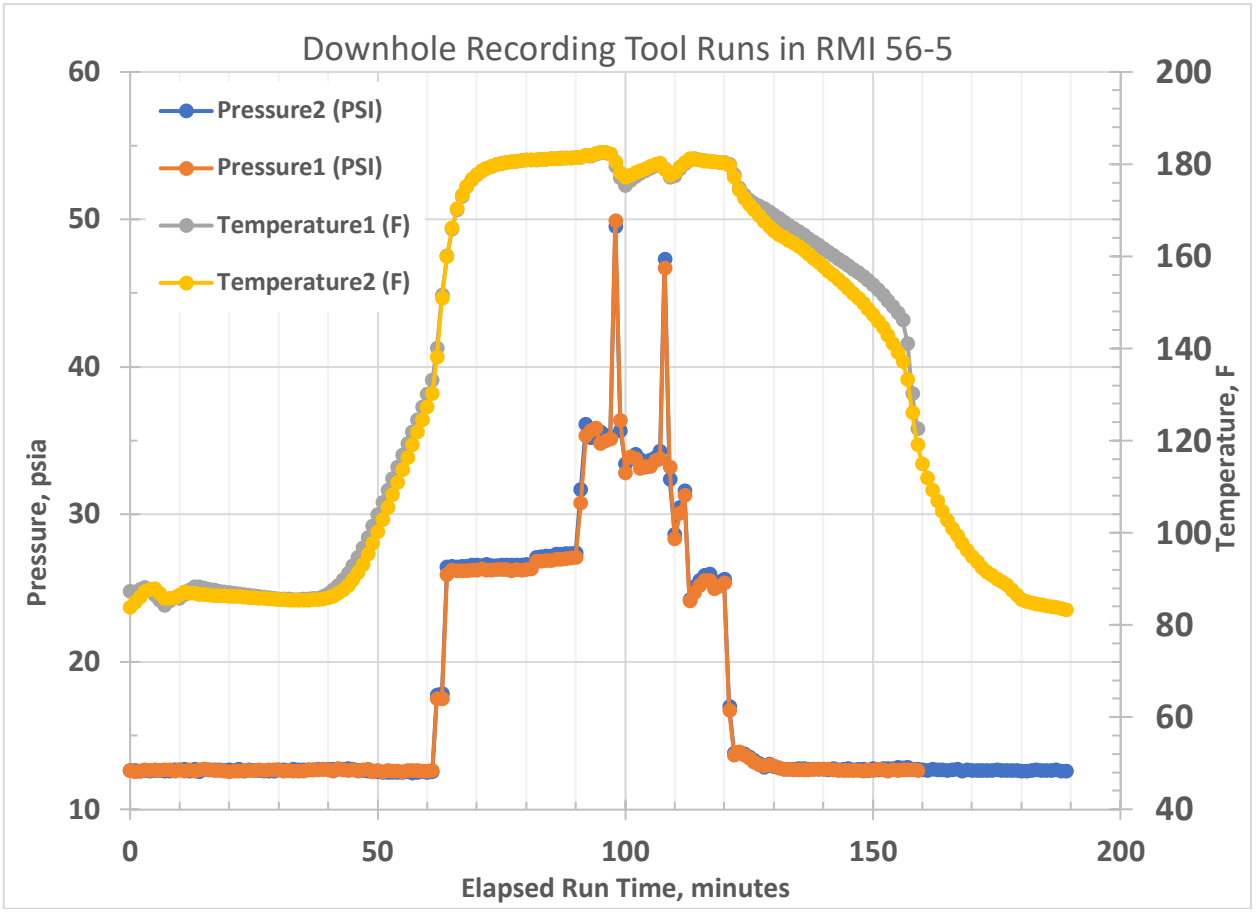

Sequences 2-4

Figure 8. Flow rate data recorded during Sequences 2-4

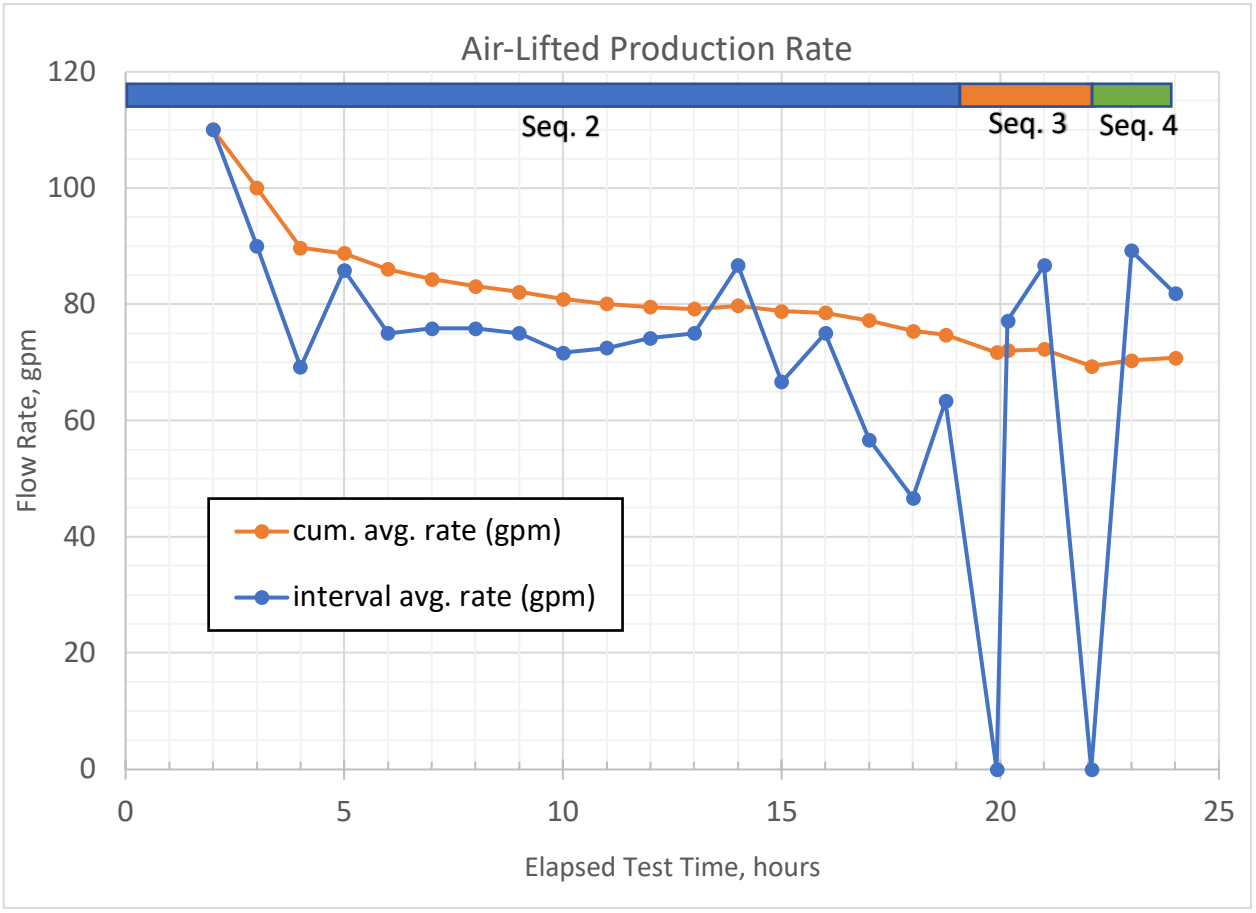

The objective in Sequence 2 was to observe whether a stable drawdown could be achieved. In fact, from hours 6-13 the production rate stabilized at 75.8 gpm, compared to an initial rate of 110 gpm. This time period spanned the coolest hours from midnight until dawn when the outside air temperature was about 73 F. After sunrise, temperatures quickly climbed back close to 90 F and the air compressor performance began to degrade due to intercooler limitations, requiring a reduction in air injection rate.

The Sequence 3 and 4 objectives were to verify that adequate pumping submergence had been achieved in Sequence 2, and to see whether deeper injection would materially affect rate. Although the compressor was still affected by the ambient temperature in the hottest part of the day, production was established at deeper air injection points of 900 and 1,000 ft. The slightly higher production rates in Sequences 3 and 4 compared to the Sequence 2 stabilized rate of 75.8 gpm confirms that there was adequate submergence in Sequence 2.

Analysis

The data recorded downhole and on the surface during Sequence 1 show a static water table higher than in 2016 and remarkably little drawdown during production. The water collected in the tank during almost 16 minutes of air lifting amounted to approximately 1050 gal, for an average rate of 65 gpm. The pressure measured below the air injection point in the well increased with injection, indicating that the water level was not drawn down to the tool depth and the pressure required to lift the two-phase column of fluid in the annulus around the drill pipe was being sensed in addition to the submergence. The water level measured immediately after venting the injected air and the collapse of the fluid column is the closest estimate available of the drawdown at that rate. The resulting initial estimate of well productivity is shown below in Table 2.

The initial estimate of productivity is dependent on volumetric metering in the first 5% of tank fill, which is the least accurate. A better estimate of initial production rate may be obtained from the first hour of metered flow in Sequence 2, 110 gpm. From the discussion above of Sequence 2 in relation to Figure 8, the production rate stabilized at 75.8 gpm after about four hours. Applying this ratio of initial to stable rates yields the final estimates of stable PI in Table 2.

TABLE 2: Water Table Depth & Productivity Index (PI)

	Instrument 1	Instrument 2	Avg.	Remark
Pressure, minutes 67-71, psia	26.22	26.51	26.36	before air lift
Pressure, minutes 115-120, psia	25.26	25.61	25.44	after air lift
Static water level, ft subsurface	437.7	437.0	437.3	before air lift
Drawdown, psi	0.95	0.91	0.93	
Drawdown, ft (180 F density)	2.26	2.15	2.21	60.578 lb/ft^3
Initial PI, gpm/psi (Seq. 1 avg.)			69.9	@65 gpm
Initial PI, gpm/ft			31.6	
Initial PI, l/s/m			6.55	@4.1 l/s
ratio of stable/initial rate, Seq. 2			0.59	65/110 gpm
Est. stable PI, gpm/ft			18.7	
Est. stable PI, l/s/m			3.87	

As a consistency check on the reasonableness of our measurements, we compared the 2019 flow rates with predictions made using the methodology of the "Multiservice Procedures For Well-Drilling Operations," FM 5-484, Chapter 8. We found the measured rates well within the manual's uncertainty limits. Although FM 5-484 has been superceded by TM 3-34.49, the relevant section to this study has not materially changed. Chapter 8-1(3) presents a chart-based method using as variables the water table depth, submergence of air pipe and drawdown to calculate the air flow needed to lift a gallon of water. Since we knew the water table depth and the flow rates of air and water, we used the method to estimate the drawdown and effective submergence. An abridged table of contents for the Field Manual, and a complete copy of its Chapter 8 with charts, is appended to this report.

For comparison with 2016, the static water level then was 484 ft below surface, 47 ft deeper than in 2019. The best estimate of PI was about 0.36 l/s/m, only 9.3% of the 2019 value in Table 2. This is dramatically higher productivity than the estimate we obtained during drilling. Table 3 shows the practical effects of the differences in estimates upon completion in 2016 and based on the 2019 results.

TABLE 3: Comparison of 2016 and 2019 Estimates

Item	2016 estimate	2019 estimate
static water level, subsurface	484 ft	437 ft
drawdown for 500 gpm	287 ft	26.7 ft
rate for 100 ft drawdown	174 gpm	1873 gpm
rate for 800 ft pump set depth	288 gpm	3,983 gpm
Energy flux available	7-10 MWt	>34 MWt

The 2019 estimate of available energy flux assumes 180 F water production and a rejection temperature of 120 F. That is almost certainly an underestimate, as the water at 120 F would still have utility for space heating, and 180 F is the minimum logged temperature in the well. Bottom hole temperatures exceed 200 F and a mixture hotter than 180 F is probable.

Conclusion

The question we posed for the purpose of this Addendum, is what effect does the 2019 test information have on the likely utility of well RMI 56-5 for geothermal energy use? The short answer is that the 2019 results not only validate the 2016 conclusion of commerciality, they suggest the possibility that the McGregor Range resource is significantly bigger than previously understood. The obvious conclusion is that well RMI 56-5 is not only an attractive candidate for entry-level development, but it may be capable of supplying much of the Range thermal energy needs on its own.

The 2016 crew that drilled RMI 56-5 had extensive experience using the same rig and equipment to drill water wells for US Army Fire Support Bases in Afghanistan. The drillers opined that this well would most likely be capable of supplying 300-500 gpm on a continuous basis, and could do better with further well "development," or cleaning.

This estimate was more optimistic than the 2016 drawdown and buildup tests results we cited above and published in Table 1 of the November 2014 Final Project Report for DOE Contract #DE-EE0002827. The results of the latest test suggest that the well does, indeed, have at least as much potential as it appeared to the drillers when they were completing it. The rise in static water level is significant, as is the very small drawdown observed during production. It appears that some natural cleanup of the well has occurred during its three years of natural convection in a closed wellbore. A complete pump test is still a cautious and necessary step before committing to a major development project, but the latest results leave little doubt that well RMI 56-5 taps a valuable energy source on the McGregor Range.

TABLE 4: Temperature and Pressure recorded by downhole memory tools
Sheet 1 of 5

Tool1 s/n:	543986						
Tool2 s/n:	543989						
		Run t					
Date	Time	min	P1, psia	T1, F	P2, psia	T2, F	Activity
10/8/19	1:00:00 PM	0	12.649	87.322	12.624	83.799	surface
10/8/19	1:01:00 PM	1	12.569	87.138	12.623	84.909	surface
10/8/19	1:02:00 PM	2	12.601	87.715	12.598	86.050	surface
10/8/19	1:03:00 PM	3	12.666	88.098	12.641	87.365	surface
10/8/19	1:04:00 PM	4	12.644	87.414	12.603	87.738	surface
10/8/19	1:05:00 PM	5	12.685	86.417	12.647	87.873	surface
10/8/19	1:06:00 PM	6	12.651	85.341	12.635	86.856	surface
10/8/19	1:07:00 PM	7	12.665	84.297	12.599	85.731	surface
10/8/19	1:08:00 PM	8	12.686	85.218	12.607	85.721	surface
10/8/19	1:09:00 PM	9	12.615	85.957	12.673	85.874	surface
10/8/19	1:10:00 PM	10	12.675	85.829	12.665	86.521	surface
10/8/19	1:11:00 PM	11	12.599	86.604	12.708	87.181	surface
10/8/19	1:12:00 PM	12	12.698	87.602	12.577	86.955	surface
10/8/19	1:13:00 PM	13	12.577	88.331	12.746	86.842	surface
10/8/19	1:14:00 PM	14	12.687	88.243	12.559	86.673	surface
10/8/19	1:15:00 PM	15	12.719	87.964	12.709	86.550	surface
10/8/19	1:16:00 PM	16	12.665	87.721	12.683	86.455	surface
10/8/19	1:17:00 PM	17	12.649	87.543	12.686	86.364	surface
10/8/19	1:18:00 PM	18	12.657	87.300	12.690	86.380	surface
10/8/19	1:19:00 PM	19	12.577	87.196	12.651	86.375	surface
10/8/19	1:20:00 PM	20	12.557	87.051	12.665	86.251	surface
10/8/19	1:21:00 PM	21	12.589	86.861	12.625	86.194	surface
10/8/19	1:22:00 PM	22	12.575	86.728	12.706	86.129	surface
10/8/19	1:23:00 PM	23	12.631	86.591	12.609	86.054	surface
10/8/19	1:24:00 PM	24	12.631	86.456	12.670	85.961	surface
10/8/19	1:25:00 PM	25	12.634	86.331	12.628	85.912	surface
10/8/19	1:26:00 PM	26	12.667	86.191	12.659	85.815	surface
10/8/19	1:27:00 PM	27	12.617	86.021	12.614	85.766	surface
10/8/19	1:28:00 PM	28	12.681	85.900	12.608	85.671	surface
10/8/19	1:29:00 PM	29	12.682	85.769	12.583	85.637	surface
10/8/19	1:30:00 PM	30	12.669	85.694	12.666	85.548	surface
10/8/19	1:31:00 PM	31	12.573	85.662	12.663	85.495	surface
10/8/19	1:32:00 PM	32	12.632	85.601	12.629	85.425	RIH
10/8/19	1:33:00 PM	33	12.574	85.544	12.703	85.392	RIH
10/8/19	1:34:00 PM	34	12.599	85.525	12.681	85.391	RIH
10/8/19	1:35:00 PM	35	12.582	85.589	12.674	85.396	RIH
10/8/19	1:36:00 PM	36	12.662	85.607	12.680	85.429	RIH
10/8/19	1:37:00 PM	37	12.687	85.724	12.692	85.436	RIH
10/8/19	1:38:00 PM	38	12.693	85.844	12.744	85.499	RIH

TABLE 4: Temperature and Pressure recorded by downhole memory tools
Sheet 2 of 5

Tool1 s/n:	543986						
Tool2 s/n:	543989						
		Run t					
Date	Time	min	P1, psia	T1, F	P2, psia	T2, F	Activity
10/8/19	1:39:00 PM	39	12.705	86.195	12.718	85.650	RIH
10/8/19	1:40:00 PM	40	12.670	86.801	12.746	85.877	RIH
10/8/19	1:41:00 PM	41	12.600	87.591	12.716	86.252	RIH
10/8/19	1:42:00 PM	42	12.764	88.613	12.725	86.827	RIH
10/8/19	1:43:00 PM	43	12.691	89.804	12.722	87.574	RIH
10/8/19	1:44:00 PM	44	12.631	91.192	12.756	88.536	RIH
10/8/19	1:45:00 PM	45	12.661	92.804	12.738	89.767	RIH
10/8/19	1:46:00 PM	46	12.609	94.657	12.659	91.312	RIH
10/8/19	1:47:00 PM	47	12.666	96.748	12.619	93.191	RIH
10/8/19	1:48:00 PM	48	12.725	98.935	12.586	95.290	RIH
10/8/19	1:49:00 PM	49	12.561	101.486	12.606	97.654	RIH
10/8/19	1:50:00 PM	50	12.643	103.972	12.557	100.153	RIH
10/8/19	1:51:00 PM	51	12.546	106.549	12.504	102.818	RIH
10/8/19	1:52:00 PM	52	12.630	109.172	12.520	105.501	RIH
10/8/19	1:53:00 PM	53	12.607	111.788	12.502	108.255	RIH
10/8/19	1:54:00 PM	54	12.611	114.302	12.503	110.964	RIH
10/8/19	1:55:00 PM	55	12.570	116.859	12.491	113.702	RIH
10/8/19	1:56:00 PM	56	12.633	119.383	12.538	116.381	RIH
10/8/19	1:57:00 PM	57	12.622	121.898	12.480	119.068	RIH
10/8/19	1:58:00 PM	58	12.619	124.548	12.496	121.809	RIH
10/8/19	1:59:00 PM	59	12.575	127.280	12.569	124.552	RIH
10/8/19	2:00:00 PM	60	12.577	130.048	12.514	127.283	RIH
10/8/19	2:01:00 PM	61	12.659	133.071	12.533	130.233	RIH
10/8/19	2:02:00 PM	62	17.490	140.020	17.771	138.085	RIH
10/8/19	2:03:00 PM	63	17.500	151.635	17.829	150.923	RIH
10/8/19	2:04:00 PM	64	25.905	160.034	26.437	159.951	RIH
10/8/19	2:05:00 PM	65	26.234	165.924	26.488	166.144	RIH
10/8/19	2:06:00 PM	66	26.168	170.026	26.426	170.296	RIH
10/8/19	2:07:00 PM	67	26.189	172.942	26.464	173.185	RIH
10/8/19	2:08:00 PM	68	26.189	175.103	26.470	175.195	RIH
10/8/19	2:09:00 PM	69	26.208	176.595	26.552	176.672	RIH
10/8/19	2:10:00 PM	70	26.204	177.709	26.568	177.658	RIH
10/8/19	2:11:00 PM	71	26.288	178.476	26.515	178.477	RIH
10/8/19	2:12:00 PM	72	26.231	179.074	26.599	179.067	@500 SS
10/8/19	2:13:00 PM	73	26.236	179.501	26.500	179.490	@500 SS
10/8/19	2:14:00 PM	74	26.258	179.854	26.521	179.878	@500 SS
10/8/19	2:15:00 PM	75	26.256	180.136	26.577	180.081	@500 SS
10/8/19	2:16:00 PM	76	26.253	180.331	26.562	180.301	@500 SS
10/8/19	2:17:00 PM	77	26.172	180.498	26.583	180.485	@500 SS

TABLE 4: Temperature and Pressure recorded by downhole memory tools
Sheet 3 of 5

Tool1 s/n:	543986						
Tool2 s/n:	543989						
		Run t					
Date	Time	min	P1, psia	T1, F	P2, psia	T2, F	Activity
10/8/19	2:18:00 PM	78	26.244	180.604	26.562	180.608	@500 SS
10/8/19	2:19:00 PM	79	26.230	180.771	26.575	180.738	@500 SS
10/8/19	2:20:00 PM	80	26.280	180.837	26.616	180.795	@500 SS
10/8/19	2:21:00 PM	81	26.294	180.891	26.583	180.844	@500 SS
10/8/19	2:22:00 PM	82	26.801	180.929	27.097	180.914	@500 SS
10/8/19	2:23:00 PM	83	26.828	181.003	27.123	180.990	@500 SS
10/8/19	2:24:00 PM	84	26.868	181.052	27.182	181.060	@500 SS
10/8/19	2:25:00 PM	85	26.870	181.147	27.178	181.149	@500 SS
10/8/19	2:26:00 PM	86	26.942	181.173	27.315	181.166	@500 SS
10/8/19	2:27:00 PM	87	26.954	181.244	27.294	181.195	@500 SS
10/8/19	2:28:00 PM	88	26.975	181.277	27.355	181.257	@500 SS
10/8/19	2:29:00 PM	89	27.027	181.328	27.353	181.293	@500 SS
10/8/19	2:30:00 PM	90	27.092	181.377	27.366	181.385	@500 SS
10/8/19	2:31:00 PM	91	30.764	181.412	31.665	181.412	@500 SS
10/8/19	2:32:00 PM	92	35.303	181.821	36.103	181.878	@500 SS
10/8/19	2:33:00 PM	93	35.654	181.649	35.187	181.874	@500 SS
10/8/19	2:34:00 PM	94	35.849	182.142	35.818	182.298	@500 SS
10/8/19	2:35:00 PM	95	34.803	182.412	35.577	182.499	@500 SS
10/8/19	2:36:00 PM	96	34.987	182.420	35.375	182.464	@500 SS
10/8/19	2:37:00 PM	97	35.097	182.071	35.191	182.109	@500 SS
10/8/19	2:38:00 PM	98	49.889	179.481	49.501	180.423	@500 SS
10/8/19	2:39:00 PM	99	36.351	177.008	35.673	178.117	@500 SS
10/8/19	2:40:00 PM	100	32.830	175.345	33.415	177.074	@500 SS
10/8/19	2:41:00 PM	101	33.901	176.393	33.770	177.544	@500 SS
10/8/19	2:42:00 PM	102	33.779	177.263	34.082	178.046	@500 SS
10/8/19	2:43:00 PM	103	33.123	177.919	33.737	178.484	@500 SS
10/8/19	2:44:00 PM	104	33.243	178.520	33.214	178.953	@500 SS
10/8/19	2:45:00 PM	105	33.238	179.115	33.674	179.450	@500 SS
10/8/19	2:46:00 PM	106	33.634	179.549	33.866	179.855	@500 SS
10/8/19	2:47:00 PM	107	33.772	179.886	34.282	180.106	@500 SS
10/8/19	2:48:00 PM	108	46.671	178.986	47.295	178.784	@500 SS
10/8/19	2:49:00 PM	109	33.184	177.068	32.353	177.559	@500 SS
10/8/19	2:50:00 PM	110	28.319	177.454	28.631	178.019	POH
10/8/19	2:51:00 PM	111	30.056	178.909	30.455	179.299	POH
10/8/19	2:52:00 PM	112	31.279	180.035	31.610	180.378	POH
10/8/19	2:53:00 PM	113	24.117	180.853	24.207	181.128	POH
10/8/19	2:54:00 PM	114	24.696	181.163	25.086	181.068	POH
10/8/19	2:55:00 PM	115	25.165	180.874	25.515	180.852	POH
10/8/19	2:56:00 PM	116	25.501	180.663	25.874	180.647	POH

TABLE 4: Temperature and Pressure recorded by downhole memory tools
Sheet 4 of 5

Tool1 s/n:	543986						
Tool2 s/n:	543989						
		Run t					
Date	Time	min	P1, psia	T1, F	P2, psia	T2, F	Activity
10/8/19	2:57:00 PM	117	25.517	180.571	25.952	180.575	POH
10/8/19	2:58:00 PM	118	24.954	180.483	25.280	180.413	POH
10/8/19	2:59:00 PM	119	25.109	180.336	25.421	180.304	POH
10/8/19	3:00:00 PM	120	25.337	180.293	25.603	180.213	POH
10/8/19	3:01:00 PM	121	16.732	179.888	16.962	179.608	POH
10/8/19	3:02:00 PM	122	13.675	177.619	13.807	177.056	POH
10/8/19	3:03:00 PM	123	13.912	174.697	13.845	174.295	POH
10/8/19	3:04:00 PM	124	13.684	173.185	13.755	172.503	POH
10/8/19	3:05:00 PM	125	13.475	172.123	13.539	171.189	POH
10/8/19	3:06:00 PM	126	13.215	171.404	13.314	169.991	POH
10/8/19	3:07:00 PM	127	13.036	170.823	13.100	168.852	POH
10/8/19	3:08:00 PM	128	12.924	170.270	12.838	167.600	POH
10/8/19	3:09:00 PM	129	13.047	169.571	13.093	166.464	POH
10/8/19	3:10:00 PM	130	12.927	168.885	12.905	165.430	POH
10/8/19	3:11:00 PM	131	12.796	168.186	12.806	164.667	POH
10/8/19	3:12:00 PM	132	12.742	167.451	12.741	164.089	POH
10/8/19	3:13:00 PM	133	12.726	166.728	12.708	163.413	POH
10/8/19	3:14:00 PM	134	12.661	165.991	12.706	162.773	POH
10/8/19	3:15:00 PM	135	12.685	165.260	12.766	162.073	POH
10/8/19	3:16:00 PM	136	12.661	164.565	12.749	161.303	POH
10/8/19	3:17:00 PM	137	12.698	163.848	12.742	160.457	POH
10/8/19	3:18:00 PM	138	12.710	163.112	12.712	159.526	POH
10/8/19	3:19:00 PM	139	12.727	162.335	12.741	158.602	POH
10/8/19	3:20:00 PM	140	12.736	161.604	12.717	157.674	POH
10/8/19	3:21:00 PM	141	12.722	160.864	12.687	156.751	POH
10/8/19	3:22:00 PM	142	12.694	160.115	12.752	155.813	POH
10/8/19	3:23:00 PM	143	12.644	159.386	12.689	154.915	POH
10/8/19	3:24:00 PM	144	12.646	158.646	12.740	153.913	POH
10/8/19	3:25:00 PM	145	12.631	157.916	12.768	152.945	POH
10/8/19	3:26:00 PM	146	12.646	157.166	12.693	151.899	POH
10/8/19	3:27:00 PM	147	12.652	156.406	12.714	150.822	POH
10/8/19	3:28:00 PM	148	12.604	155.577	12.704	149.719	POH
10/8/19	3:29:00 PM	149	12.660	154.706	12.640	148.543	surface
10/8/19	3:30:00 PM	150	12.647	153.744	12.755	147.313	surface
10/8/19	3:31:00 PM	151	12.703	152.700	12.696	145.951	surface
10/8/19	3:32:00 PM	152	12.700	151.545	12.768	144.459	surface
10/8/19	3:33:00 PM	153	12.612	150.345	12.757	142.845	surface
10/8/19	3:34:00 PM	154	12.681	149.022	12.777	141.030	surface
10/8/19	3:35:00 PM	155	12.645	147.632	12.844	139.142	surface

TABLE 4: Temperature and Pressure recorded by downhole memory tools
Sheet 5 of 5

Tool1 s/n:	543986						
Tool2 s/n:	543989						
		Run t					
Date	Time	min	P1, psia	T1, F	P2, psia	T2, F	Activity
10/8/19	3:36:00 PM	156	12.679	146.149	12.810	137.148	surface
10/8/19	3:37:00 PM	157	12.676	141.088	12.842	133.234	surface
10/8/19	3:38:00 PM	158	12.672	130.201	12.718	126.023	surface
10/8/19	3:39:00 PM	159	12.628	122.623	12.736	119.062	surface
10/8/19	3:40:00 PM	160			12.678	114.948	surface
10/8/19	3:41:00 PM	161			12.655	111.843	surface
10/8/19	3:42:00 PM	162			12.703	109.174	surface
10/8/19	3:43:00 PM	163			12.672	106.837	surface
10/8/19	3:44:00 PM	164			12.668	104.663	surface
10/8/19	3:45:00 PM	165			12.655	102.707	surface
10/8/19	3:46:00 PM	166			12.671	100.925	surface
10/8/19	3:47:00 PM	167			12.715	99.325	surface
10/8/19	3:48:00 PM	168			12.578	97.723	surface
10/8/19	3:49:00 PM	169			12.673	96.241	surface
10/8/19	3:50:00 PM	170			12.624	94.864	surface
10/8/19	3:51:00 PM	171			12.622	93.633	surface
10/8/19	3:52:00 PM	172			12.653	92.464	surface
10/8/19	3:53:00 PM	173			12.618	91.483	surface
10/8/19	3:54:00 PM	174			12.628	90.718	surface
10/8/19	3:55:00 PM	175			12.694	89.916	surface
10/8/19	3:56:00 PM	176			12.618	89.353	surface
10/8/19	3:57:00 PM	177			12.621	88.698	surface
10/8/19	3:58:00 PM	178			12.658	87.545	surface
10/8/19	3:59:00 PM	179			12.644	86.457	surface
10/8/19	4:00:00 PM	180			12.586	85.527	surface
10/8/19	4:01:00 PM	181			12.612	85.039	surface
10/8/19	4:02:00 PM	182			12.619	84.843	surface
10/8/19	4:03:00 PM	183			12.691	84.565	surface
10/8/19	4:04:00 PM	184			12.643	84.392	surface
10/8/19	4:05:00 PM	185			12.645	84.137	surface
10/8/19	4:06:00 PM	186			12.633	83.971	surface
10/8/19	4:07:00 PM	187			12.674	83.775	surface
10/8/19	4:08:00 PM	188			12.574	83.531	surface
10/8/19	4:09:00 PM	189			12.615	83.320	surface

In-Situ
YOUR EYES IN THE FIELD

Level TROLL® 400, 500 & 700 Data Loggers

GET WATER LEVEL DATA THE WAY YOU WANT IT, WHEN YOU WANT IT WITH INDUSTRY-LEADING WATER LEVEL/PRESSURE AND TEMPERATURE DATA LOGGERS. BY PARTNERING WITH IN-SITU, YOU RECEIVE DURABLE LEVEL TROLL® DATA LOGGERS THAT PROVIDE YEARS OF SERVICE, ACCURATE RESULTS, INTUITIVE SOFTWARE, AND REAL-TIME FUNCTIONALITY. USE THE VUSITU™ MOBILE APP TO MANAGE YOUR DATA ON YOUR SMARTPHONE OR TABLET.

BE EFFECTIVE

- **Increase productivity:** Reduce training and installation time with In-Situ's intuitive software platform and integrated components. Patented twist-lock connectors, included on Level TROLL Data Loggers and RuggedCable® Systems, ensure error-free deployments.
- **Streamline data management:** Use the VuSitu Mobile App to consolidate all site information on your smartphone, and tag data with site photos and GPS coordinates. Simply connect the instrument to a Wireless TROLL Com or power pack, launch the mobile app, and start reading results. Simplify instrument setup, reduce errors and get the most out of your data with Log Setup Assistant and Panoramic Live Data. Log data to your smartphone and download results in a standard Universal Data File format.
- **Set up real-time networks:** Access data 24/7 and receive event notifications when you connect data loggers to Tube and Cube Telemetry Systems, HydroVu Data Services, or other third-party data collection platforms.

BE RELIABLE

- **Deploy in all environments:** Install loggers in fresh water, saltwater, and contaminated waters. Solid titanium and sealed construction outperforms and outlasts specially coated data loggers.
- **Log accurate data:** Get optimal accuracy under all operating conditions. Sensors undergo a 3D, NIST-traceable factory calibration across the full pressure and temperature range. For applications requiring the highest levels of accuracy, use a vented (gauged) system.
- **Get long-lasting operation:** Reduce trips to the field with low-power loggers that typically operate for 10 years.

TOTAL FIELD SUPPORT

- **Receive 24/7 technical support and online resources.**
- **Order data loggers and accessories from the In-Situ website.**
- **Get guaranteed 7-day service for maintenance (U.S.A. only).**

Applications:

- **AQUIFER CHARACTERIZATION: SLUG & PUMPING TESTS**
- **COASTAL: TIDAL, WETLAND & ESTUARY STUDIES**
- **HYDROLOGIC EVENTS: STORM SURGE & FLOOD CONTROL SYSTEMS**
- **LONG-TERM, REAL-TIME GROUNDWATER & SURFACE WATER MONITORING**
- **MINING & REMEDIATION**

www.in-situ.com

CALL OR CLICK TO PURCHASE OR RENT
1-800-446-7488 (toll-free in U.S.A. and Canada)
970-498-1500 (U.S.A. and international)

GENERAL	LEVEL TROLL 400	LEVEL TROLL 500	LEVEL TROLL 700	LEVEL BaroTROLL
TEMPERATURE RANGES[1]	Operational: -20 to 80° C (-4 to 176° F) Storage: -40 to 80° C (-40 to 176° F) Calibrated: -5 to 50° C (23 to 122° F)	Operational: -20 to 80° C (-4 to 176° F) Storage: -40 to 80° C (-40 to 176° F) Calibrated: -5 to 50° C (23 to 122° F)	Operational: -20 to 80° C (-4 to 176° F) Storage: -40 to 80° C (-40 to 176° F) Calibrated: -5 to 50° C (23 to 122° F)	Operational: -20 to 80° C (-4- to 176° F) Storage: -40 to 80° C (-40 to 176° F) Calibrated: -5 to 50° C (23 to 122° F)
DIAMETER	1.83 cm (0.72 in.)	1.83 cm (0.72 in.)	1.83 cm (0.72 in.)	1.83 cm (0.72 in.)
LENGTH	21.6 cm (8.5 in.)	21.6 cm (8.5 in.)	21.6 cm (8.5 in.)	21.6 cm (8.5 in.)
WEIGHT	124 g (0.27 lb)	124 g (0.27 lb)	124 g (0.27 lb)	124 g (0.27 lb)
MATERIALS	Titanium body; Delrin® nose cone	Titanium body; Delrin nose cone	Titanium body; Delrin nose cone	Titanium body; Delrin nose cone
ENVIRONMENTAL RATING	IP68 with cable attached IP67 without cable attached	IP68 with cable attached IP67 without cable attached	IP68 with cable attached IP67 without cable attached	IP68 with cable attached IP67 without cable attached
OUTPUT OPTIONS	Modbus/RS485, SDI-12, 4 to 20 mA	Modbus/RS485, SDI-12, 4 to 20 mA	Modbus/RS485, SDI-12, 4 to 20 mA	Modbus/RS485, SDI-12, 4 to 20 mA
BATTERY TYPE & LIFE[2]	3.6V lithium; 10 years or 2M readings	3.6V lithium; 10 years or 2M readings	3.6V lithium; 10 years or 2M readings	3.6V lithium; 10 years or 2M readings
EXTERNAL POWER	8 to 36 VDC	8 to 36 VDC	8 to 36 VDC	8 to 36 VDC
MEMORY Data records[3] Data logs	2.0 MB 120,000 50 logs	2.0 MB 120,000 50 logs	4.0 MB 250,000 50 logs	1.0 MB 60,000 2 logs
FASTEST LOGGING RATE	2 per second	2 per second	4 per second	1 per minute
FASTEST OUTPUT RATE	Modbus: 2 per second SDI-12 & 4 to 20 mA: 1 per second	Modbus: 2 per second SDI-12 & 4 to 20 mA: 1 per second	Modbus: 2 per second SDI-12 & 4 to 20 mA: 1 per second	Modbus: 2 per second SDI-12 & 4 to 20 mA: 1 per second
LOG TYPES	Linear, Fast Linear, and Event	Linear, Fast Linear, and Event	Linear, Fast Linear, Linear Average, Event, Step Linear, True Logarithmic	Linear
SOFTWARE	Android™: VuSitu through Google Play™ or Amazon® App Store; iOS: VuSitu through Apple® App Store; Windows®: Win-Situ 5, Data Services: HydroVu			
SENSOR TYPE/MATERIAL	**PIEZORESISTIVE; TITANIUM**	**PIEZORESISTIVE; TITANIUM**	**PIEZORESISTIVE; TITANIUM**	**PIEZORESISTIVE; TITANIUM**
RANGE	Absolute (non-vented) 30 psia: 11 m (35 ft) 100 psia: 60 m (197 ft) 300 psia: 200 m (658 ft) 500 psia: 341 m (1120 ft)	Gauged (vented) 5 psig: 3.5 m (11.5 ft) 15 psig: 11 m (35 ft) 30 psig: 21 m (69 ft) 100 psig: 70 m (231 ft) 300 psig: 210 m (692 ft) 500 psig: 351 m (1153 ft)	Absolute (non-vented) 30 psia: 11 m (35 ft) 100 psia: 60 m (197 ft) 300 psia: 200 m (658 ft) 500 psia: 341 m (1120 ft) 1000 psia: 693 m (2273 ft) Gauged (vented) 5 psig: 3.5 m (11.5 ft) 15 psig: 11 m (35 ft) 30 psig: 21 m (69 ft) 100 psig: 70 m (231 ft) 300 psig: 210 m (692 ft) 500 psig: 351 m (1153 ft)	30 psia (usable up to 16.5 psi; 1.14 bar)
BURST PRESSURE	Max. 2x range; burst > 3x range	Max. 2x range; burst > 3x range	Max. 2x range; burst > 3x range	Vacuum/over-pressure above 16.5 psi damages sensor
ACCURACY	±0.05% FS from -5 to 50° C	±0.05% FS from -5 to 50° C	±0.05% FS from -5 to 50° C	±0.05% FS from -5 to 50° C
LONG-TERM STABILITY[4]	<0.1% FS	<0.1% FS	<0.1% FS	<0.1% FS
RESOLUTION	±0.005% FS or better	±0.005% FS or better	±0.005% FS or better	±0.005% FS or better
UNITS OF MEASURE	Pressure: psi, kPa, bar, mbar, mmHg, inHg, cmH20, inH20 Level: in., ft, mm, cm, m	Pressure: psi, kPa, bar, mbar, mmHg, inHg, cmH20, inH20 Level: in., ft, mm, cm, m	Pressure: psi, kPa, bar, mbar, mmHg, inHg, cmH20, inH20 Level: in., ft, mm, cm, m	Pressure: psi, kPa, bar, mbar, mmHg, inHg, cmH20, inH20
TEMPERATURE SENSOR	**SILICON**	**SILICON**	**SILICON**	**SILICON**
ACCURACY	±0.1° C	±0.1° C	±0.1° C	±0.1° C
RESOLUTION	0.01° C or better	0.01° C or better	0.01° C or better	0.01° C or better
UNITS OF MEASURE	Celsius or Fahrenheit	Celsius or Fahrenheit	Celsius or Fahrenheit	Celsius or Fahrenheit
WARRANTY[5]	**3 YEARS**	**3 YEARS**	**3 YEARS**	**3 YEARS**

NOTES: [1] Temperature range for non-freezing liquids. [2] Typical battery life when used within the factory-calibrated temperature range. [3] 1 data record = date/time plus 2 parameters logged for a total of 360,000, 750,000, and 180,000 data points. (No wrapping) [4] Includes linearity and hysteresis over 1 year. [5] Up to 5-year (total) extended warranties are available for all sensors. Delrin is a registered trademark of E.I. du Pont de Nemours and Company. Specifications are subject to change without notice.

www.in-situ.com

CALL OR CLICK TO PURCHASE OR RENT
1-800-446-7488 (toll-free in U.S.A. and Canada) • 1-970-498-1500 (U.S.A. and international)
221 East Lincoln Avenue, Fort Collins, CO 80524 USA

FM 5-484 (abridged table of contents)

MULTISERVICE PROCEDURES FOR WELL - DRILLING OPERATIONS

Table of Contents

FM 5-484
Chapter 8
Well-Performance Testing Procedures

8-1. Testing Pumps.

You will normally use the permanent pump for pump testing. If you use a temporary unit, it must be adequate to draw down the water and hold it at a prescribed flow rate for a period of hours. This test will determine the specific capacity of the well. You can estimate the yield of a small well by bailing water from the well rapidly if no pump is available. You must know the bailer's volume and count the number of times per minute the bailer is brought up full to estimate the GPM of the well. Accurately measuring drawdown is not possible during the test because the water level constantly fluctuates.

a. *Permanent Wells.* You should use two different testing procedures when a pump is available, depending on the intended use of the well and the available testing time. If the well will be a permanent installation and maintained in the future, you should conduct a detailed test. Measure the static water level in the well before testing, and measure the drawdown during the test. Conduct the test as follows:

- Pump at a rate that will lower the water in the well about one-third of the maximum drawdown possible (one-third the distance from the static water level to the top of the well screen) or about one-third of the rated capacity of the pump.

- Monitor and adjust the flow rate early in the test because as the drawdown increases the flow rate decreases.

- Continue pumping at a constant flow rate until the drawdown remains constant (about 1 to 4 hours).

- Record the flow rate, drawdown, and testing time. Initially, take readings rapidly, and then spread out the readings as the test continues. A reading schedule that doubles the time between readings is preferable. The recommended schedule is as follows: 0 (at the start of the test) 30 seconds, 1 minute, 2 minutes, 4 minutes, 8 minutes, 15 minutes, 30 minutes, 1 hour, 2 hours, 4 hours, and so forth.

- Establish the desired, constant flow rate quickly. You must record the exact time of each reading (not the intended or scheduled time). After the drawdown stabilizes (1 to 4 hours), the pumping rate should increase to a new, constant flow rate, which

will produce two-thirds of the capacity of the pump. Do not stop the pump between these test segments.

- Repeat the measurements, noting the exact time that the new flow rate was started. Try to follow the above reading schedule, starting from the time the flow rate was increased. When the drawdown stabilizes, increase the pumping rate to produce the maximum drawdown or about 90 percent of the maximum capacity of the pump. Conduct another reading schedule until the pumping level stabilizes.

You may modify the above procedure depending on well requirements and local site conditions. You should not modify the precision and accuracy of the measurements taken. Test results should

become a part of the permanent records. The results are useful for evaluating the efficiency of the well in the future and for determining the need for well rehabilitation. Calculating the GPM per foot of drawdown gives the capacity of the well. You can use this information to estimate production and to regulate the pump's flow rate to prevent dewatering of the well and possible pump damage.

b. *Temporary Wells.* Conduct a single-stage test rather than the step drawdown test. To establish the flow rate, conduct a 1- to 2-minute test to determine the GPM per foot of drawdown. Let the well return to the original static water level before testing (about 1 hour). Select a flow rate that will produce about two-thirds of the available drawdown but will not reach more than 90 percent of the pump's capacity. Conduct the test as described above, but with only one segment. When the drawdown stabilizes for the selected flow rate, stop the test.

c. *Methods.* See Chapter 4 for a description of pumps used in testing and well production.

(1) Submersible-Pump Method. Use the submersible pump in well-completion kits to pump test the water well. Set the pump deep enough to attain the maximum pumping rate and drawdown. When testing a well with a screen, set the suction of the pump above the top of the screen to prevent lowering the water level below the screen. When testing a well without a screen, try not to dewater the production part of the aquifer. For proper testing, you must have a reliable power source so that testing will not be interrupted. The power must be sufficient to drive the pump at a rated speed so that full capacity can be developed.

(2) Air-Lift Method. This method is sometimes best for military field operations, especially if the well may produce sand that could damage or reduce the life of a submersible pump. An air-lift pump has two major problems. Air turbulence could

make drawdown measuring difficult, and entrained air may cause considerable error in measuring the flow rate. After constructing an air- lift pump, check the pump capacity against the expected well yield. To conduct the test, set the pump according to the readings in Table 4-2.

An air compressor that puts out 350 cfm at 200 psi is suitable for performing most air-lift pumping operations. To determine the amount of air needed for pumping water, use the following equation or refer to Figure 8-1.

$$V = \frac{h}{\frac{C\,[\log\,(H+34)]}{43}}$$

where--

V = free air (actual) required to raise one gallon of water, in cubic feet.

h = total lift, in feet.

log = logarithmic value.

H = operating submergence, in feet.

C = constant (Table 8-1).

Table 8-1. Constants

Constant	Submergence (percent)
366	75
358	70
348	65
335	60
318	55
296	50
272	45
246	40
216	35

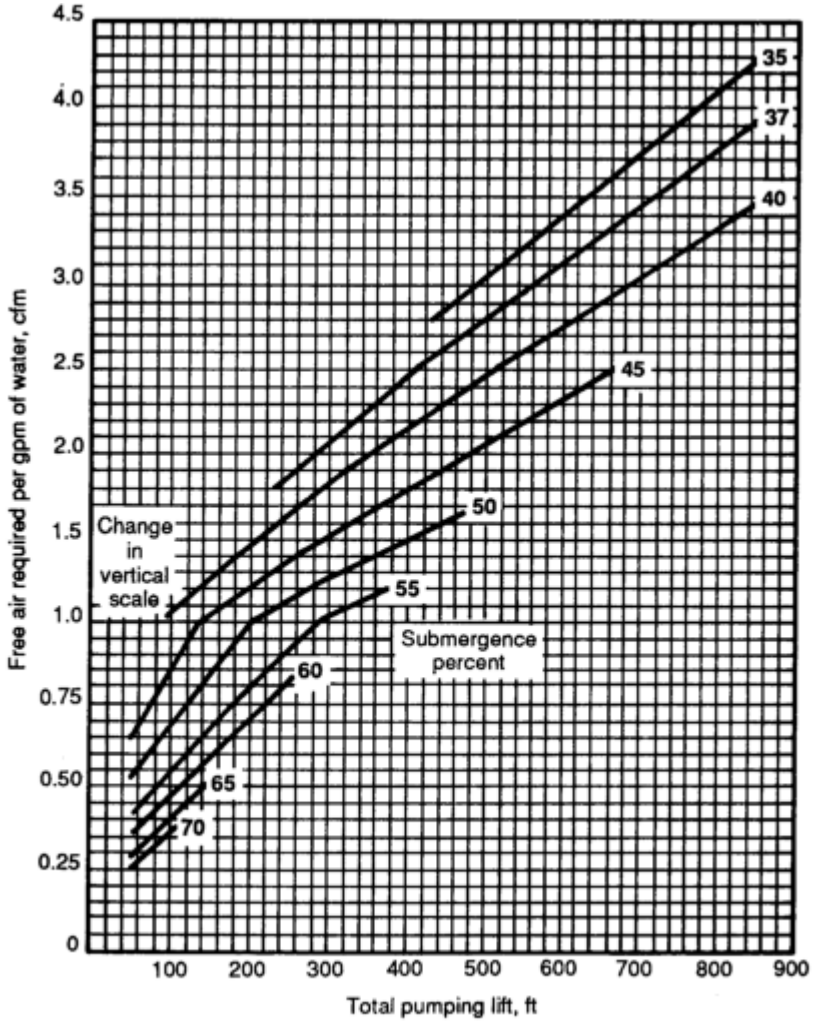

Figure 8-1. Cubic feet of air requirements for various submergences and pumping lifts

The pressure required to start pumping will be equal to the depth of water over the submerged end of the air pipe. After pumping has started, the water in the well will draw down to a working level. The air pressure required will be the total lift, in feet, from the working water level plus the friction loss in the airline. Conduct the test and try to measure flow rate and drawdown quickly. Pumping creates turbulance in the well. Use the air-line method (paragraph 8-2c) to try and measure drawdown. Because of entrained air, use the measured-container method (paragraph 8-3a) to obtain flow-rate measurements.

8-2. Measuring Water Level.

a. *Electric-Line Method.* Water levels can be measured accurately with a two-conductor, battery- powered indicator known as an M-Scope (Figure 8-2). Well-completion kits usually contain an M- Scope. The M-Scope is a battery and a meter connected in series. When the

upper wire on the tip of the M-Scope in the well touches the water, the circuit is completed and the meter gives a steady reading. Measure the amount of wire in the well to determine the depth to the water level. The wire is marked at 5-foot intervals for easy measuring.

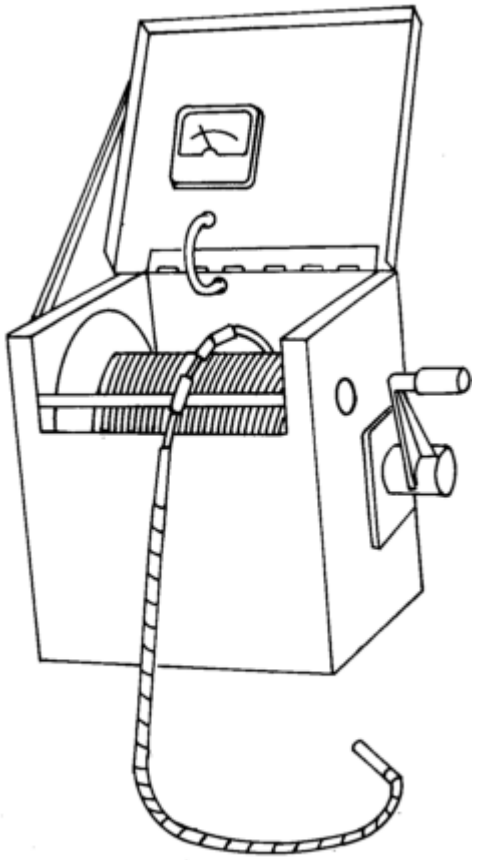

Figure 8-2. M-Scope

b. *Tape Method.* Use this method to measure the depth to the static level in a shallow well. Conduct this test as follows:

- Chalk one end of a weighted steel tape with carpenter's chalk. Lower the tape (Figure 8-3) into the well to a depth of 1 or 2 feet past the chalk. (You can use soluble felt-tip markers as an alternative to chalk.)

- Measure the wetted length of the tape and subtract the amount from the total length lowered below the reference point to obtain the water depth. This test is accurate to within 0.01 foot.

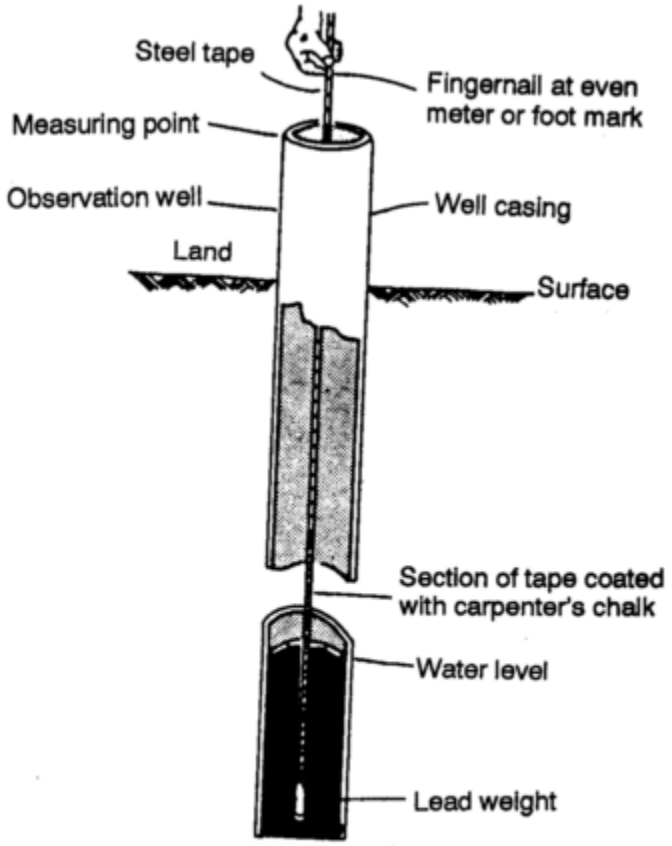

Figure 8-3. Steel-tape measurement method

c. *Air-Line Method.* You can measure the water level with an air line to follow drawdown and confirm a stable head during a test (Figure 8-4). The air line is usually 1/8- or 1/4-inch copper tubing or galvanized pipe that is long enough to extend below the lowest water level you are measuring. Fasten the air line to the pump bowls or cylinder. Install the airline with the pump. The pipe must be airtight; makeup all joints carefully. Measure the vertical length of the airline from the pressure gauge to the bottom of the line at the time of installation.

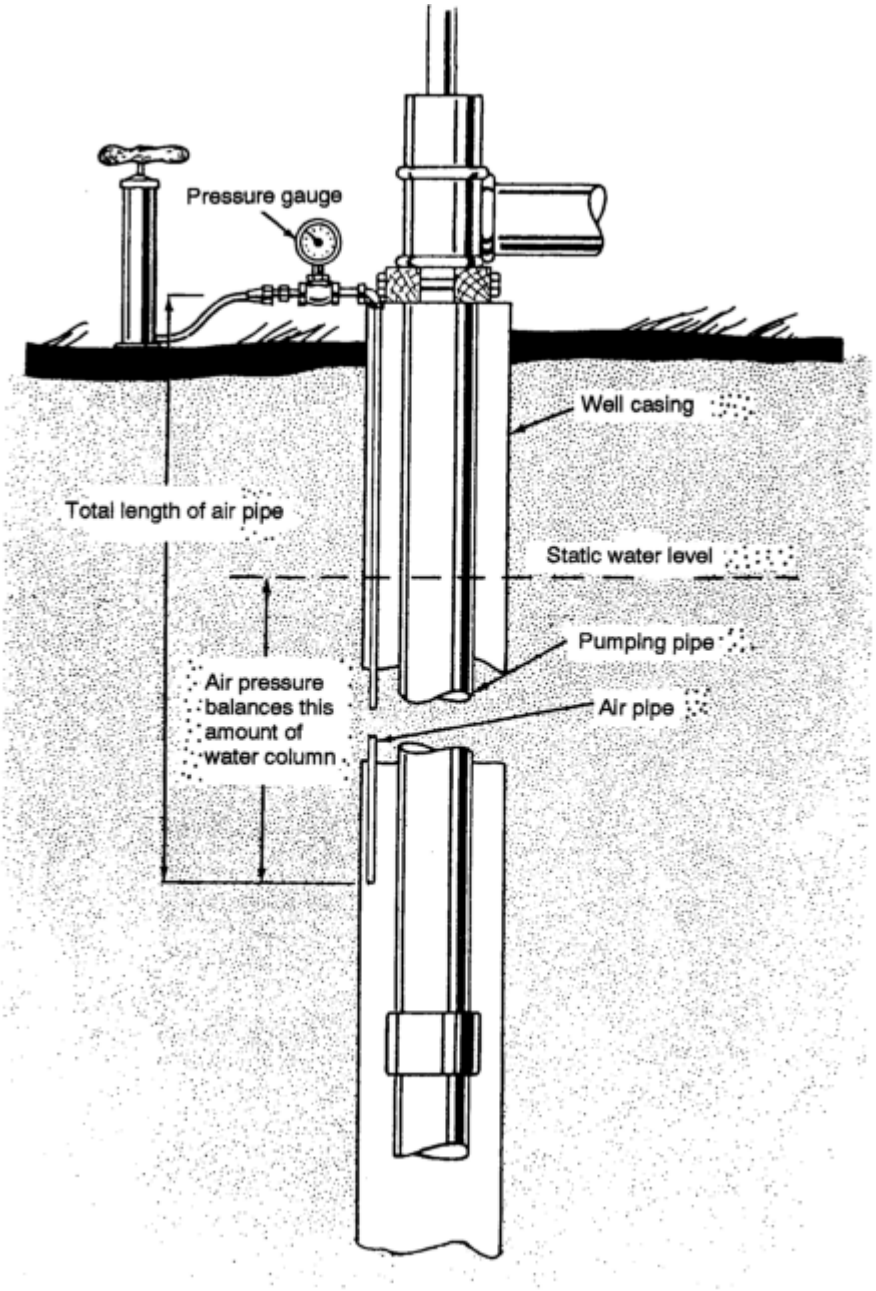

Figure 8-4. Air-line measurement method

Attach a pressure gauge to the airline at the surface with an ordinary tire valve so you can pump air into the line. Pump air into the line until you get a maximum reading. The reading should be equal to the pressure exerted by the column of water standing outside of the airline. Subtract the reading from the total vertical length of air line to get the depth to the water below the center of the gauge. Readings are measured in feet, so you may have to convert your figures.

8-3. Measuring Discharge Rate.

a. *Measured-Container Method.* You can determine the flow rate from a well or pump by measuring the time required to fill a container with a known volume. With this method, use small containers for early measurements and large containers for later measurements. Also, use an instrument, such as a stop watch, for accurate time measurements. Use the following equation:

$$FR = \frac{V(60)}{T}$$

where-- FR = flow rate, in *GPM*

V = volume, in gallons.

T = time required to fill container, in seconds.

b. *Flow-Meter Method.* A turbine-type flow meter will give an acceptable flow-rate reading. These meters are used by civilians. You can also use a totalizer-type water meter when the yield is low. Use these meters to measure the total gallons pumped and determine the flow rate. To do this, record the number of gallons that have flowed within a set amount of time and compute the flow rate.

c. *Circular-Orifice Method.* A circular-orifice meter (Figure 8-5) is a device you can make to measure discharge rates. This device gives good results and is compact and easily installed. The meter consists of a sharp-edged circular orifice at the end of a horizontal discharge pipe. The orifice is from one-half to three-fourths the diameter of the pipe. The inside of the pipe must be smooth and free from obstructions for a length of 6 feet from the orifice. The discharge pipe has a small hole on one side with a rubber-tube connection. The pipe is designed so that you can measure the pressure (head) in the discharge pipe at a distance of 2 feet from the orifice.

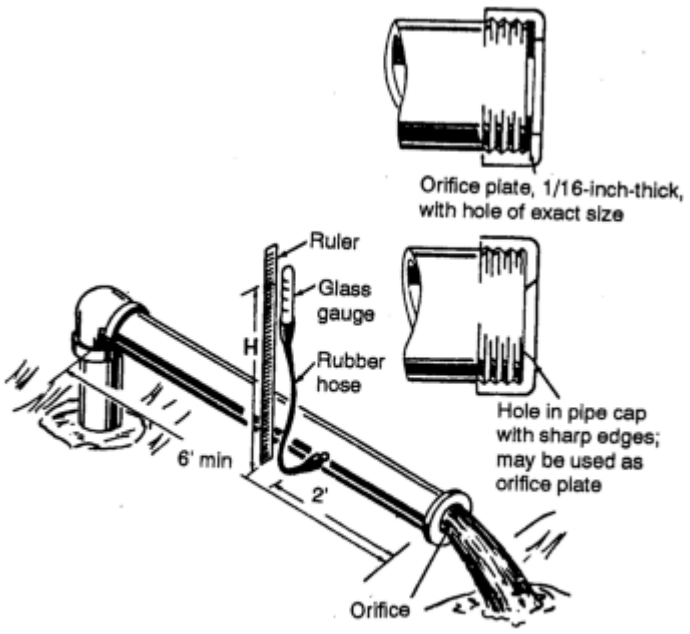

Figure 8-5. Circular-orifice flow meter

The length of hose and ruler depends on the pipe size you use (Table 8-2). The discharge pipe must be horizontal, and the stream must fall free from the orifice. The orifice must be vertical and centered in the discharge pipe. The combination of pipe and orifice diameters for a given test should be such that the head measured will be at least three times the diameter of the orifice

Table 8-2. Circular-orifice flow measurements

Head of Water in Tube Above Center of Orifice (inches)	4-inch Pipe, 2 1/2-inch Opening (GPM)	4-inch Pipe, 3-inch Opening (GPM)	6-inch Pipe, 3-inch Opening (GPM)	6-inch Pipe, 4-inch Opening (GPM)	6-inch Pipe, 5-inch Opening (GPM)	8-inch Pipe, 4-inch Opening (GPM)	8-inch Pipe, 5-inch Opening (GPM)	8-inch Pipe, 6-inch Opening (GPM)
6	62	102						
7	66	110	88					
8	70	118	94	180	350	170	280	440
9	75	126	100	190	370	180	295	465
10	80	132	106	200	390	190	310	490
12	87	145	115	220	425	210	340	540
14	94	156	125	238	460	225	370	580
16	100	168	132	253	490	240	390	620
18	106	178	140	268	520	255	415	660
20	112	188	150	283	550	270	440	695
22	118	198	158	298	575	280	460	725
25	125	210	168	318	610	300	490	780
30	138	230	182	350	670	330	540	850
35	150	250	198	375	725	360	580	920
40	160	265	210	400	780	380	620	980
45	170	280	223	425	820	400	660	1,040
50	180	300	235	450	870	425	700	1,100
60	195	325	260	490	950	465	760	1,200

d. *Open-Pipe Method.* With this method, the pipe is fully open and you measure the distance the water stream travels parallel to the pipe at a 12-inch vertical drop (Figure 8-6). Use the following procedure:

- Step 1. Measure the inside diameter of the pipe and the distance the stream travels parallel to the pipe at a 12-inch vertical drop. Your results will be in inches.

- Step 2. Estimate the flow from the pipe diameter and the distance the stream travels (Table 8-3). Your results will be in GPM.

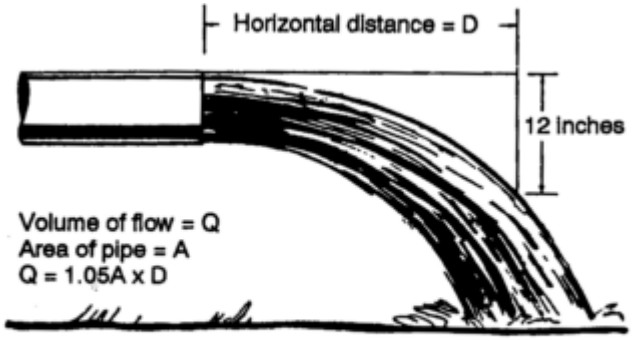

Figure 8-6. Open-pipe-flow measurement method

Table 8-3. Open-pipe-flow measurements

Pipe Diameter (inches)	Horizontal Distance (D) (inches)									
	12	14	16	18	20	22	24	26	28	30
2	41	48	55	61	68	75	82	89	96	102
3	90	105	120	135	150	165	180	195	210	225
4	150	181	207	232	258	284	310	336	361	387
6	352	410	470	528	587	645	705	762	821	880
8	610	712	813	915	1,017	1,119	1,221	1,322	1,425	1,527
10	960	1,120	1,280	1,440	1,600	1,760	1,930	2,080	2,240	2,400
12	1,378	1,607	1,835	2,032	2,286	2,521	2,760	2,980	3,210	3,430

For partially filled pipes, measure either the water depth or the freeboard. Divide the diameter by the water depth to get a percentage ratio. Measure the stream as above and calculate the discharge. The actual discharge will be, approximately, the value for a full pipe of the same diameter multiplied by the correction factor from Table 8-4.

Table 8-4. Correction factors

Percent	Factor	Percent	Factor
5	0.981	55	0.436
10	0.948	60	0.375
15	0.905	65	0.312
20	0.858	70	0.253
25	0.805	75	0.195
30	0.747	80	0.142
35	0.688	85	0.095
40	0.627	90	0.052
45	0.564	95	0.019
50	0.500	100	0.000